Dust Dynamics and Distribution in Protoplanetary Disks

Fabian Binkert

München 2023

Dust Dynamics and Distribution in Protoplanetary Disks

Fabian Binkert

Dissertation
an der Fakultät für Physik
der Ludwig–Maximilians–Universität
München

vorgelegt von
Fabian Binkert
geboren in Zürich

München, den 01-08-2023

Erstgutachter: Prof. Dr. Til Birnstiel
Zweitgutachter: Prof. Dr. Judit Szulágyi
Tag der mündlichen Prüfung: 12-10-2023

Contents

List of Figures

List of Tables

Zusammenfassung

Feinkörniger Staub ist der grundlegende Baustein von terrestrischen Planeten wie der Erde, die um junge Sterne entstehen. Gleichzeitig beeinflusst der Staub astronomische Beobachtungen, da er den Hauptbeitrag zur Opazität in den Gasscheiben leistet, die entstehende Sterne umgeben (sog. protoplanetare Scheiben). Daher sind genaue Modelle der Verteilung und Bewegung von Staub in protoplanetaren Scheiben von entscheidender Bedeutung für das Verständnis der Anfangsbedingungen der Planetenentstehung und für die Interpretation astronomischer Beobachtungen von jungen Planeten- und Sternensystemen. Dieses Thema ist besonders relevant, da neueste astronomischen Beobachtungen protoplanetarer Scheiben neue Maßstäbe in Bezug auf Auflösung und Empfindlichkeit setzen und dadurch unser derzeitiges Verständnis und unsere Modelle infrage stellen.

In dieser Arbeit präsentiere ich ein neuartiges und in sich konsistentes Modell der turbulenten Durchmischung von Staub. Das Modell bestätigt detaillierte Vorhersagen, wobei Nachteile früherer Modelle hinsichtlich der Drehimpulserhaltung, der uneindeutigen Definition der durchmischten Größe und Auswirkungen der Bahndynamik wegfallen. Somit verbessern wir die Beschreibung der Bewegung von Staub in turbulenten protoplanetaren Scheiben maßgeblich. Anschließend zeige ich auf, wie turbulente Durchmischung von Staub und andere Transportphänomene im frühen Sonnensystem, den Mangel an beständigen Kohlenstoffverbindungen, im inneren Bereich des heutigen Sonnensystems erklären kann. Im Folgenden konzentriert sich die Arbeit auf die dreidimensionale Verteilung des Staubs in protoplanetaren Scheiben in Gegenwart eines Riesenplaneten. Mithilfe von hydrodynamischen Zwei-Fluid-Simulationen (Gas + Staub) finden wir, dass ein Planet die Staubverteilung in protoplanetaren Scheiben stark beeinflusst. Wir beschreiben beobachtbare Merkmale in synthetischen Radiowellenbeobachtungen, die es erlauben, auf die Anwesenheit eines unentdeckten Riesenplaneten in einer protoplanetaren Scheibe zu schließen. Schließlich untersuchen wir die Verwirbelung von Staub durch einen Riesenplaneten, zusätzlich zur Durchmischung durch turbulentes Gas. Wir konzentrieren uns dabei auf deren kombinierte Wirkung auf die dreidimensionale Verteilung des Staubs und untersuchen Merkmale, die mit Radiowellenbeobachtungen einer protoplanetarer Scheibe beobachtbar sind und Rückschlüsse auf die Anwesenheit eines noch unentdeckten Planeten erlauben. Diese Arbeit bietet neue Einblicke in die Dynamik von Staub in turbulenten protoplanetaren Scheiben und liefert eine Erklärung für den Mangel an beständigen Kohlenstoffverbindungen im inneren Sonnensystem. Außerdem beschreiben wir mögliche beobachtbare Merkmale von noch unentdeckten Riesenplaneten in Radiowellenbeobachtungen von protoplanetaren Scheiben.

Abstract

Fine-grained dust is the fundamental building block of terrestrial planets, like Earth, that form around young stars. At the same time, the dust distribution in the gaseous disks around forming stars, so-called protoplanetary disks, influences astronomical observations, because dust is the main contributor to the opacity in protoplanetary disks. Therefore, accurate models of the distribution and dynamics of dust are critical to understanding the initial stages of planet formation and interpreting astronomical observations of forming planetary and stellar systems. This is particularly relevant because recent astronomical observations of protoplanetary disks have reached new heights in terms of resolution and sensitivity, challenging our current understanding and models.

In this thesis, I introduce a novel and self-consistent turbulent dust transport model based on a density-weighted mean-field theory that also captures non-local transport effects. The model improves upon the limitations of earlier models related to the conservation of angular momentum, the ambiguous nature of the transported quantity, and the transport effects of orbital dynamics. We therefore provide an improved description of dust dynamics in turbulent protoplanetary disks. Subsequently, I present how turbulent dust dynamics and transport in the early Solar System can explain the lack of refractory carbon in the inner Solar System today. The thesis then focuses on the three-dimensional dust distribution in protoplanetary disks in the presence of an embedded giant planet. With the help of radiative two-fluid (gas+dust) hydrodynamic simulations, we find that a planet significantly influences the dust distribution in protoplanetary disks. We identify observational signatures in synthetic radio continuum observations that hint at the potential presence of a yet undetected giant planet in a protoplanetary disk. Finally, we investigate dust stirring by a giant planet in addition to dust mixing caused by turbulent gas. We focus on the combined effects on the three-dimensional dust morphology and study observable effects of turbulent and planetary dust stirring in radio continuum observations of protoplanetary disks with an embedded planet. Our work provides novel insights into turbulent dust dynamics in protoplanetary disks and offers an explanation for the lack of refractory carbon in the inner Solar System. We also describe observational signatures of giant planets in protoplanetary disks that help with the interpretation of continuum observations. These results help guide astronomers toward the detection of forming and yet unobserved planets in protoplanetary disks.

Chapter 1

Introduction

Humans have probably always been fascinated with the origins of our world. But it was not until the 18th century that the *nebular hypothesis* was proposed (Laplace, 1798), which today is regarded as the predecessor of state-of-the-art models that describe the origin of planets, like Earth. More recently, a plethora of new observations has led to renewed interest in the origins and formation of planets and has catapulted the field to the forefront of modern astrophysics.
Current models predict the formation of planets to be closely connected to the formation of stars in a complex interplay with their galactic environment in cold, dense regions of the galaxy (e.g. McKee & Ostriker, 2007; Pineda et al., 2022). In a simplified picture, the standard process starts with a "blob", also called a *core*, of gas and fine dust grains, which exists in isolation within a star-forming region of the galaxy. The core then gravitationally contracts to form a young star that is surrounded by a rotationally supported disk of gas and dust. Within the disk, planets form from the bottom up, starting with dust grains sticking together to form centimeter-sized pebbles, which then form kilometer-sized bodies called *planetesimals*. The planetesimals then grow further to become rocky planets like Earth or attract a thick gaseous envelope to form a gas planet like Jupiter (see e.g. Evans, 1999, for a review). Despite significant progress in our understanding of the origins of worlds over the past 250 years, new questions have emerged, and many aspects remain unknown. This introductory section aims to provide a brief overview of the science of planet formation before the subsequent three chapters provide insights into the actual theory and current challenges.

Today, we understand that the interactions between stars, planets, and disks are complex and take place over a relatively brief period of time (less than ten million years). However, processes within this period set the fundamental properties of stars and planets that then endure for billions of years (Andrews, 2020). The brief period during which planets form is studied in modern research, both observationally and theoretically. Astronomical observations, from the ground and from space, provide detailed insights into structures, physical conditions, environmental dependencies, evolutionary behavior, and statistical properties of entire populations of planets outside the Solar System, so-called *exoplanets*. Observations have revealed a wealth of information on the birth and evolution of planet-forming disks and on the diversity of exoplanets. On the other hand, theoretical models provide a framework for interpreting observational data and making predictions. These models range from simple analytical descriptions to complex numerical simulations. They incorporate a range of physical and chemical processes to predict the formation and evolution of planets. By comparing theoretical model predictions with observational data, our understanding of planet formation can be tested and refined. This interplay between observations and models is particularly important in the field of planet formation because nascent planets are notoriously difficult to observe. Therefore, models must be used to infer properties of forming planets from indirect observations.
Insights gained from the aforementioned scientific approach have revealed that the path to planet

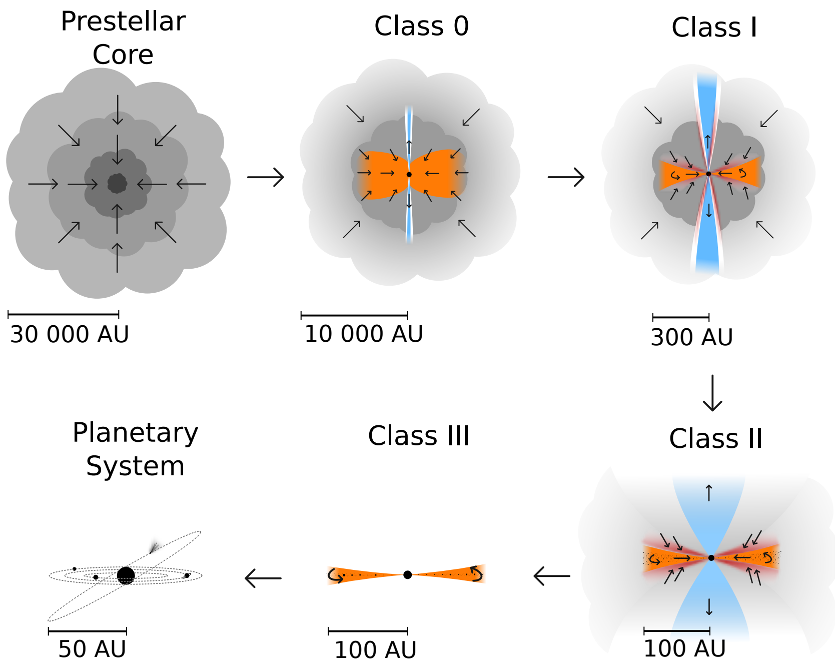

Figure 1.1: Depiction of the evolutionary stages of the star and planet formation process. (image credit: Persson, 2014a)

formation begins in the *interstellar medium* (ISM), i.e., the matter that exists between the stars in the galaxy consisting of gas and dust. Observations reveal that the ISM exhibits inhomogeneous structures across a wide range of density and velocity scales, which can seed the star and planet formation process when massive structures, of the order of $\sim 10^7 M_\odot$[1], become gravitationally bound. These massive structures inherit a high level of turbulence from the ISM which, in combination with self-gravity, causes their fragmentation into *giant molecular clouds* (GMCs) with scales of tens of parsec[2] and smaller dense clumps on pc-scales within the GMCs. Some of the densest regions created by turbulence become self-gravitating cores, which are structures on sub-parsec scales ($< 10^5$ au[3]). Some cores gravitationally collapse and are then referred to as *prestellar cores* because only they eventually form protostars. They can be regarded as the initial condition for the subsequent protostellar evolution (see e.g. the review by McKee & Ostriker, 2007).

As a prestellar core collapses, potential energy is released and transformed into kinetic energy of the gas, which in turn increases the thermal pressure of the gas and prevents further contraction. Further contraction is only possible when there is sufficient cooling and energy is released into the surrounding environment. A prestellar core also inherits some angular momentum. As a result of angular momentum conservation, it begins to rotate faster as it collapses and flattens into a disk. During this process, the majority of the mass accumulates in the center of the disk. After about $\sim 10^5$ years of evolution, the disk only contains a fraction of the mass of the central protostar and is then called *protoplanetary*. At this time, the young stellar system is still surrounded by an extended gaseous envelope, but after about 5×10^5 years, the envelope dissipates, and only the protostar surrounded by its protostellar disk remains. The protostar

---

[1] Solar mass, 1 $M_\odot = 1.98847 \times 10^{33}$ g

[2] Parsec, 1 pc $= 3.0857 \times 10^{16}$ m

[3] Astronomical unit, 1 au $= 1.4960 \times 10^{11}$ m, approximate distance from Earth to the Sun

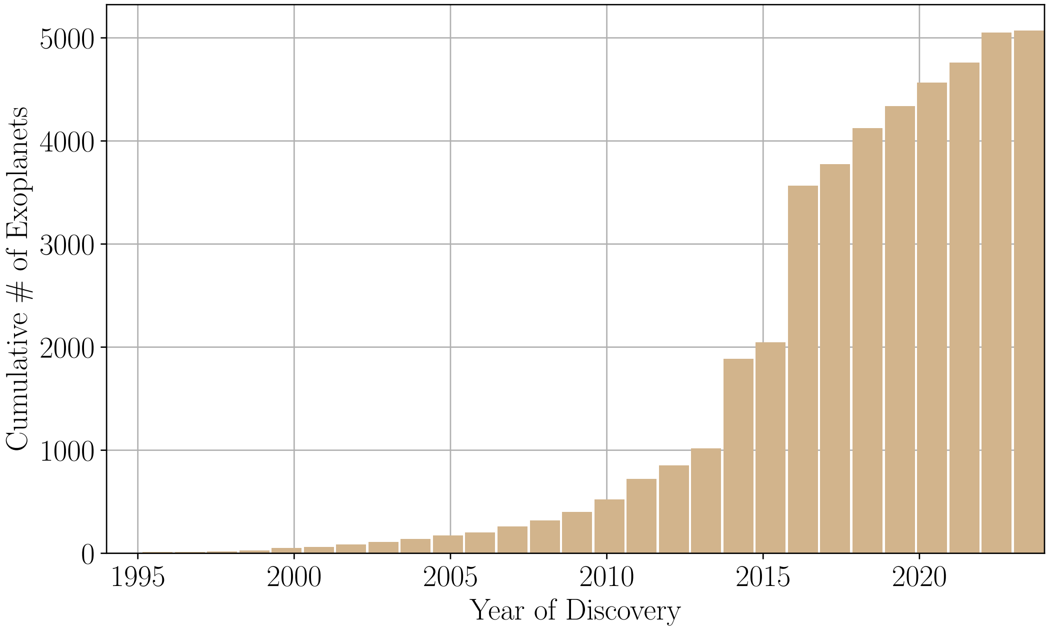

Figure 1.2: Cumulative number of confirmed exoplanets from 1995 to March 2023 (data source: `exoplanet.eu`)

at the center of the disk continues to contract until density and temperature are sufficiently high to initiate nuclear hydrogen burning. At this point, the energy created by nuclear fusion contributes to halting gravitational contraction, allowing the star to settle into a quasi-steady state. This point in evolution is regarded as the beginning of the life of the star. Figure 1.1 shows sketches of the most important stages of the formation process of a planet-hosting stellar system, which begins with a prestellar core in the first panel at the top left and ends with a mature planetary system at the bottom left.

Protoplanetary disks, which form around the young stars, serve as the material reservoirs and birthplaces of planets. They determine the initial conditions and thus, the outcomes of planet formation processes. Planetary properties, like occurrence rates, masses, formation pathways, orbital architectures, and compositions, ultimately depend on the physical properties of their natal protoplanetary disks (see e.g. Andrews, 2020, for a detailed review). Thus, understanding disk properties and evolution is equally important to understanding the planet formation process itself.

The outcome of the planet formation process can be studied in the population of detected (exo-)planets. Beyond the Solar System, this has only become technically possible within the last three decades. As of March 2023, 5076 exoplanets have been detected and their number is expected to continue growing. In Figure 1.2, we show the cumulative detections of exoplanets as a function of time, starting in 1995.

Ultimately, the goal of planet formation theory is to connect protoplanetary disks and their properties to the observed exoplanet population and explain how such a diverse population of planets forms from rotating disks of gas and dust while being fully consistent with the increasing number of observational constraints.

This thesis focuses on the distribution and dynamics of dust in the context of planet formation in protoplanetary disks. Dust is an important component of protoplanetary disks because it is the material from which all rocky bodies in planetary systems are formed (e.g., planetesimals, terrestrial planets, rocky cores of giant planets). Moreover, it contributes significantly to the continuum opacity of protoplanetary disks. Thus, the distribution of dust sensitively shapes the appearance of protoplanetary disks in astronomical observations. Understanding dust dynamics is crucial for understanding dust distribution, which in turn provides an important link between astronomical observations and the physical (and chemical) conditions present in protoplanetary disks. These conditions ultimately govern the formation of planets.

The goal of this thesis is to create a better understanding of the connection between dust dynamics and astronomical observations. The following chapters 2, 3, and 4 provide an overview of the current understanding of protoplanetary disks both from an observational and a theoretical point of view. Chapter 5 then introduces a novel turbulent dust transport model which describes the redistribution of dust in turbulent protoplanetary disks. Chapter 6 provides an explanation for the lack of refractory carbon in the inner Solar System in terms of dust transport in the protosolar disk. Chapter 7 studies the three-dimensional dust distribution in a protoplanetary disk with an embedded giant planet and links the presence of a planet to distinct observational signatures in radio-continuum observations. Chapter 8 continues the discussion from Chapter 7, and introduces subgrid turbulent dust transport to the model as introduced in Chapter 5. The thesis concludes with a summary and outlook in Chapter 9.

Chapter 2

Observational Constraints

Before reviewing the theory of disk evolution in Chapter 3 and planet formation in Chapter 4, we provide an overview of astronomical observations that provide insight into the initial and boundary conditions for the subsequent theory. In this chapter, we first discuss the historical classification of young stellar objects in Sec. 2.1, then focus on protoplanetary disk observations in Sec. 2.2, followed by exoplanet observations in Sec. 2.3 and finally address some constraints from the Solar System in Sec. 2.4.

2.1 Young Stellar Objects

The closest large star-forming regions to the Solar System, in which we observe star formation, are *Ophiuchus* (d∼120 pc), *Taurus* (d∼150 pc) and *Orion* (d∼410 pc). However, at these distances, typical protoplanetary disks span less than 1 arcsec on the sky, making spatially resolving prestellar objects challenging (for comparison, the full moon subtends about 1860 arcsec). Historically, most observational insight regarding the star formation process has come from studying the *spectral energy distribution* (SED) in unresolved observations. The SED is the distribution of flux as a function of frequency ν or wavelength λ. *Young stellar objects* (YSOs) are then classified into four different classes based on the slope of the SED in the infrared region of the spectrum. Coincidentally, the slope correlates with the evolutionary stages of YSOs (Adams et al., 1987). The four classes are defined as follows:

- **Class 0.** The SED peaks in the far infrared ($> 25\mu m$) or mm-range, with no flux detected in the near-infrared ($\sim 0.7\mu m - 5\mu m$).
- **Class I.** The SED between near- and mid-infrared wavelengths is approximately flat or rising.
- **Class II.** The SED drops noticeably between near- and mid-infrared wavelengths.
- **Class III.** The SED is effectively produced by a black body, coming from the stellar photosphere.

The shape of the SED in the different classes is illustrated in Figure 2.1.
Nowadays, Class 0 objects are identified as the least evolved, featuring a dense, optically thick envelope surrounding the protostar (see Figure 1.1). At this stage, near-infrared radiation from the central region is obscured by the envelope. A potential rotationally supported disk is thus undetectable at this stage. Only Class I objects provide direct observational evidence of disks. For this class, some radiation reaches us relatively unprocessed from the central region and is detectable at shorter wavelengths. Older Class II objects have largely accreted their envelopes, and their SEDs combine the protostellar spectrum and radiation from the surrounding disk

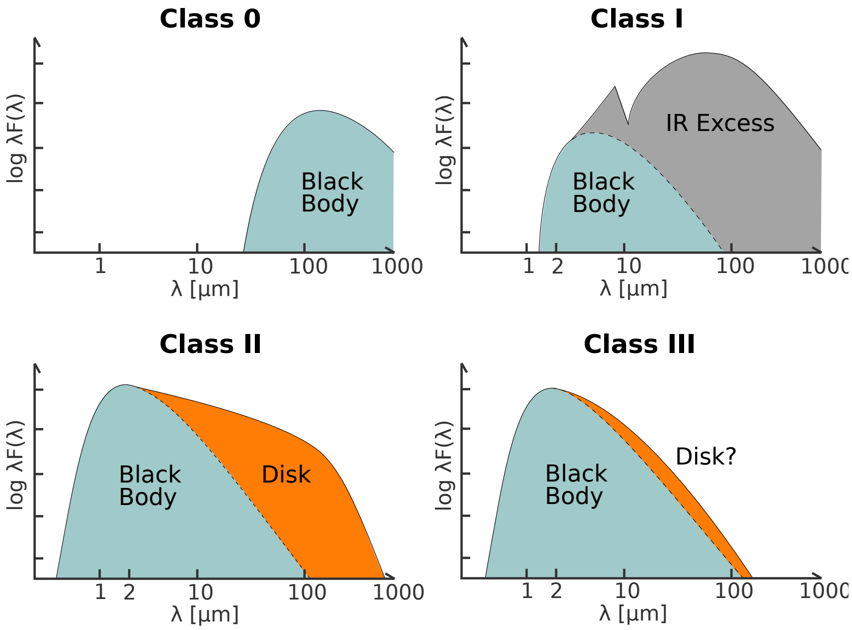

Figure 2.1: SED classification of young stellar objects based on their infrared excess. (image credit: Persson, 2014b)

at longer wavelengths. Finally, Class III objects are pre-main sequence stars that have nearly accreted all their circumstellar material.

2.2 Observations of Protoplanetary Disks

After having discussed the characteristics of unresolved observations of YSOs, we focus on resolved observations of protoplanetary disks in this section. For this, we loosely follow the content and structure of the review by Andrews (2020).

2.2.1 Observational Fundamentals

The first direct observational evidence of disks surrounding young stars came from a Hubble Space Telescope (HST) observation of the Orion nebula in the early 1990s (O'dell et al., 1993). However, beyond confirming their existence, HST's short wavelength capabilities are not well suited to probe the detailed disk structure because protoplanetary disks tend to be highly opaque at short wavelengths. Protoplanetary disks are relatively cool (< 100 K) such that their thermal emission peaks at long wavelengths in the (sub-)millimeter range of the spectrum. Therefore, the combination of small sizes (< 1 arcsec) and cool temperatures favor radio interferometry as the preferred observational tool to probe thermal emissions. Resolved disk observations at these wavelengths have only become possible at scale after the commissioning of the Atacama Large Millimeter Array (ALMA) in 2011, which has since made a great contribution to the research of young stellar systems.

Besides thermal continuum emission, there are two more observational tracers suitable for studying the structure of protoplanetary disks: Scattered light and spectral line emission. Both continuum emission and scattered light are sensitive to the physical state and distribution of solids in the disks. On the other hand, spectral line emissions trace the distribution of certain gas molecules. In Figure 2.2, we show three observations of the same disk, each using a different tracer, such that the appearance of the disk is vastly different between the observations. As each

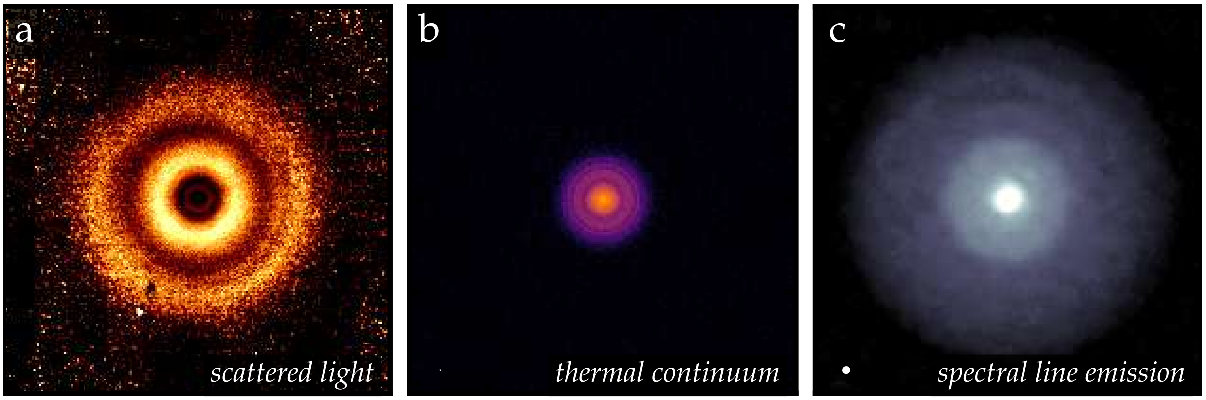

Figure 2.2: Morphologies of the TW Hya disk observed in (a) scattered light $\lambda = 1.6\ \mu m$, (b) thermal continuum $\lambda = 0.9$ mm and (c) spectral line emission of the CO J=3-2 rotational transition. All three images show the disk at the same scale. (image credit: Andrews, 2020)

tracer is sensitive to different disk components and physical conditions, they each trace different regions in a disk. Figure 2.3 shows a schematic illustration of a protoplanetary disk, highlighting the locations where each tracer commonly originates. In summary, the most important properties of each tracer are as follows:

- **Scattered Light.** Small ($\sim \mu m$-sized) dust grains suspended in the gas reflect and scatter the radiation emitted by the central star. The details of the scattering and absorption process depend on the locations, sizes, shapes, and composition of the dust grains. Scattered light is typically observed at relatively small (compared to thermal emission) near-infrared wavelengths ($\sim 0.7 - 2.2\ \mu m$), which has the advantage that disks can be observed at high resolution due to a favorable diffraction limit. One difficulty in observing scattered light emissions is that the central star also emits efficiently at these wavelengths and can outshine the emission of the disk, especially at small heliocentric distances. In Figure 2.3, the main emission region is indicated with yellow color around the disk atmosphere on the r.h.s of the illustration.

- **Continuum Emission.** Solids in the disk predominantly emit thermal radiation in the range between $\lambda \sim 1\ \mu m - 1$ cm. Thus, radio observations are well suited to observing continuum emissions. In Figure 2.3, the main emission region is indicated with purple color close to the disk midplane on the r.h.s. of the illustration. In the absence of scattering effects and assuming homogeneous temperature, the observed continuum emission intensity at frequency ν is described by the solution to the radiative transfer equation

  $$I_\nu = B_\nu(T_d)(1 - e^{-\tau_\nu}) \tag{2.1}$$

  where $B_\nu(T_d)$ is the Planck function as a function of frequency ν, dust temperature T_d, and optical depth τ_ν. The dimensionless optical depth τ_ν is defined as the integral along the line of sight of the density-weighted absorption opacity κ_ν:

  $$\tau_\nu = \int \rho_d \kappa_\nu ds \tag{2.2}$$

  Thermal emission can be optically thick and then does not leave the emission region unhindered due to the relatively large opacity provided by the dust grains at these wavelengths. If the dust emission is optical thick ($\tau_\nu \gg 1$), the observed intensity I_ν is solely a function

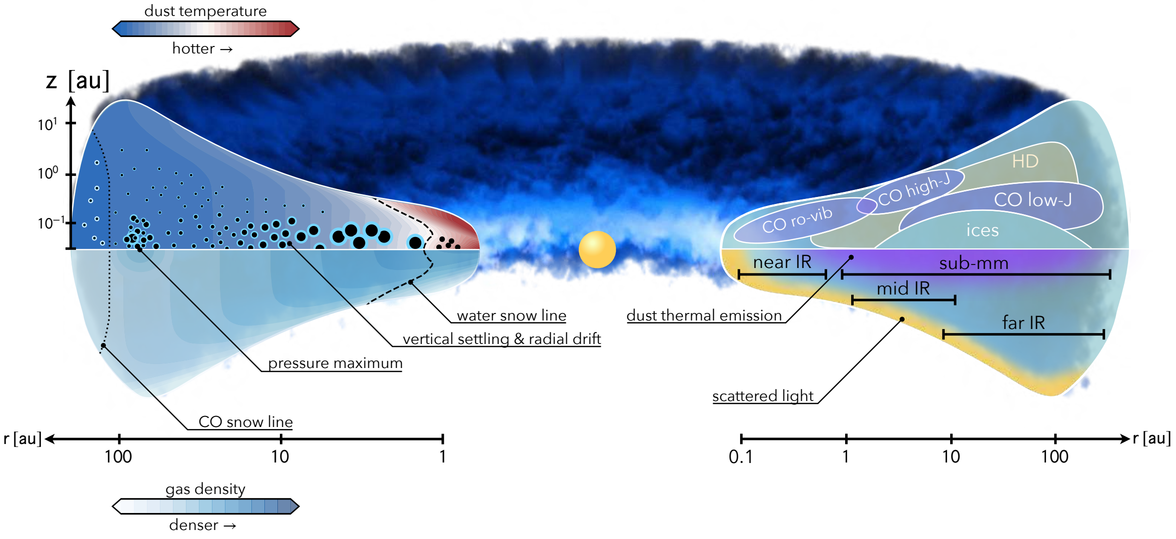

Figure 2.3: Illustration of the density and temperature structure of a protoplanetary disk. On the l.h.s., the black dots illustrate dust grains of different sizes with ice coatings beyond the snow line (dashed line). On the r.h.s, the lower part indicates the main emission regions of different wavelengths, with the main emission region of the thermal continuum emission in purple and scattered light in yellow. The upper part shows emission regions of some simple molecules. (image credit: Miotello et al., 2022)

of the dust temperature T_d:

$$I_\nu = B_\nu(T_d) \tag{2.3}$$

For optically thin emission ($\tau_\nu \ll 1$), the equation

$$I_\nu = B_\nu(T_d)\Sigma_d\kappa_\nu \tag{2.4}$$

holds, assuming the opacity is constant along the line of sight and $\Sigma_d = \int \rho_d ds$ is the dust surface density. Eq. 2.4 predicts that the observed intensity I_ν is both a function of the dust temperature T_d and the surface density Σ_d in addition to the opacity κ_ν, which is a material property. The spectral dependency of Eq. 2.4 is mainly determined by the physical properties of the solid particles[1] via the opacity (see Sec. 2.2.2). In practice, difficulties arise when inferring material properties due to degenerate parameters. Moreover, the applicability of the optically thin approximation (Eq. 2.4) is limited because large areas of protoplanetary disks can be optically thick.

- **Spectral Line Emission.** The bulk of the mass of a protoplanetary disk comes from molecular hydrogen (H_2). But, the H_2 molecule does not emit efficiently due to a lack of an electric dipole moment. Thus, the bulk of a disk is essentially invisible and there is no direct probe of its bulk mass reservoir. Instead, measurements rely on (sub-)mm

---

[1] Throughout this work, we use the term *particle* to refer to any solid constituent present in the gaseous environment of the ISM or protoplanetary disks. Their sizes can range anywhere from micron-sized dust grains to mm/cm-sized pebbles. They are distinct from *subatomic* particles common in other (astro-)physical subfields.

rotational transitions of rare tracer molecules. The upper part on the r.h.s. of Figure 2.3 illustrates the emission regions of simple molecules. Spectral line emissions can be used to probe the density and temperature structure of a disk. Moreover, spectrally resolved line emissions can be used to tomographically reconstruct the disk velocity field.

The three traces listed above have been used to observationally constrain various properties of protoplanetary disks. However, each of these tracers is subject to different limitations. Thus, it can become necessary to combine multiple tracers to obtain a complete picture. In the following section, we summarize a few of the derived properties.

2.2.2 Disk Properties

Protoplanetary disks are highly dynamic systems. Their kinematics is dominated by orbital motions (Armitage, 2011), and their detailed structure affected by magnetic fields (Turner et al., 2014), viscous transport (Lynden-Bell & Pringle, 1974, see also Sec. 3.3), pressure forces (Weidenschilling, 1977b), self-gravity (Toomre, 1964) and winds (Ercolano & Pascucci, 2017). In Chapter 3, we will discuss some of these processes in more detail. Regarding the composition, it is usually assumed that the material delivered to protoplanetary disks is similar to the precursor material in the diffuse ISM and therefore has similar properties. Specifically, it consists of 99 % (by mass) gas and 1 % dust. The dust component in the ISM generally consists of small grains with sizes $\lesssim 1\,\mu m$ (Mathis et al., 1977) and composed of silicates, graphite, and large organic molecules like *polycyclic aromatic hydrocarbons* (PAH) (Draine, 2003). In dense and cold regions of protoplanetary disks, gas molecules can freeze out onto the surfaces of these dust grains, covering them in ices (Bergin & Tafalla, 2007).

Due to the number of processes and properties involved, it is very difficult to fully characterize a protoplanetary disk. Usually, only a few fundamental properties must suffice.

Mass

The key characteristic of a protoplanetary disk is probably the distribution of mass, i.e., its density structure. But, even though insight into the detailed density structure is more desirable, the large-scale observational surveys still focus on the total disk mass because only a few disks have been spatially resolved. The total disk mass offers a fundamental constraint on disk evolution and on the mass reservoir from which planets can form.

As previously mentioned, a direct measurement of the total gas mass is difficult, whereas measuring the total dust mass is somewhat simpler (but also not easy). Although dust only contributes 1 % to the total disk mass budget, it is an important tracer for its total mass. In the optically thin limit, Eq. 2.4 provides a relationship between intensity I_ν and dust surface density Σ_d. Given an appropriate disk averaged temperature $\bar{T}_d$ and dust opacity $\bar{\kappa}_v$, the intensity can be integrated to provide the observed flux F_ν as a function of the total dust mass M_d (Hildebrand, 1983; Miotello et al., 2022)

$$F_\nu = \bar{\kappa}_\nu B_\nu(\bar{T}_d) d^{-2} M_d \tag{2.5}$$

where d is the distance between the disk and the observer. However, mass estimates derived with Eq. 2.5 are intrinsically uncertain because they rely on estimates of the mean dust temperature $\bar{T}_d$ and opacity $\bar{\kappa}_\nu$. Furthermore, estimates using Eq. 2.5 are only considered lower bounds, because some parts of the continuum emission can be optically thick. Assuming the dust mass is known, the total disk mass can then be inferred by assuming an appropriate dust-to-gas ratio. Typically, a value of 1 %, as prevalent in the ISM, is assumed (e.g. Bergin et al., 2013).

Compared to dust mass estimates based on continuum emissions, gas mass estimates based on spectral line observations are less common because the approach is observationally more challenging. A standard spectral line tracer is carbon monoxide (CO) and its isotopologues. Similarly to dust-mass estimates, a CO abundance must be assumed to infer the total gas mass

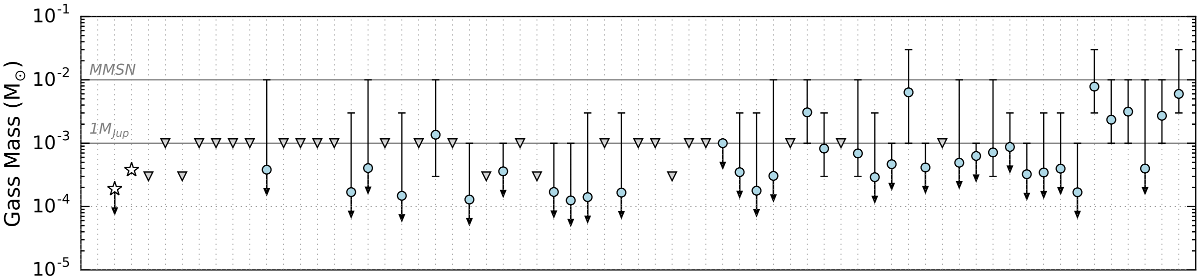

Figure 2.4: Gas mass estimates of a number of protoplanetary disks in the Lupus star-forming region using CO lines. Blue points indicate detections with associated error bars, and gray triangles indicate upper limits. The lower mass limit of the disk from which it is believed the Solar System formed, is indicated with *MMSN* (stands for Minimum Mass Solar Nebula, compare to Sec. 2.4.1). Figure adapted from Ansdell et al. (2016).

from CO-based observations, which complicates the task (see e.g. Miotello et al., 2017). Besides CO, other molecules are also frequently used as gas mass tracers (e.g., hydrogen deuteride HD). Generally, there is a high uncertainty in the disk mass determination both via gas and dust observations. In Figure 2.4 we show CO line gas mass estimates by Ansdell et al. (2016) of disks in the Lupus star-forming region. Most measurements result in a total gas mass in the range between 0.1 and 10 M_J which is considered low compared to the expected mass of the disk from which it is believed the Solar System has formed ($\gtrsim 10\ M_J$, also see Sec. 2.4.1).

For comparison, in Figure 2.5, we show the cumulative distribution of dust mass estimates of star-forming regions of different ages from Drążkowska et al. (2022). This is comparable to plotting the distribution of a single population at different evolutionary stages, as indicated by the gray *time* arrow in Figure 2.5. The median dust mass of Class 0 objects is approximately a few hundred Earth masses. The dust mass decreases rapidly towards older Class I and Class III disks. It is expected that a significant fraction of the dust either is to the central star or becomes bound in larger gravitationally bound objects within the first million years of disk evolution (Drążkowska et al., 2022). If dust is incorporated in large bodies, it is effectively hidden from observations because bodies that are larger than the observed wavelength become increasingly less efficient in their thermal emission (for a given mass of solids), making it difficult for observers to detect.

Size

Defining a physical disk size is not straightforward because most disks just taper off with increasing radius with no clear boundary. A practical approach is thus to define an effective disk size R, as the radius that encircles a fixed fraction of the total luminosity. Using this approach, and defining R such that it encircles 90 % of the luminosity, resolved mm-continuum measurements have estimated the size of approximately 200 disks to $R \approx 10 - 500$ au (Tripathi et al., 2017; Andrews et al., 2018a; Hendler et al., 2020).

Interestingly, CO-line emission extends to $100 - 500$ au (Ansdell et al., 2018), suggesting that the CO emission of individual targets stretches about twice as far as the continuum emission. The apparent size difference between continuum emission and spectral line emission is evident in the disk shown in Figure 2.2.

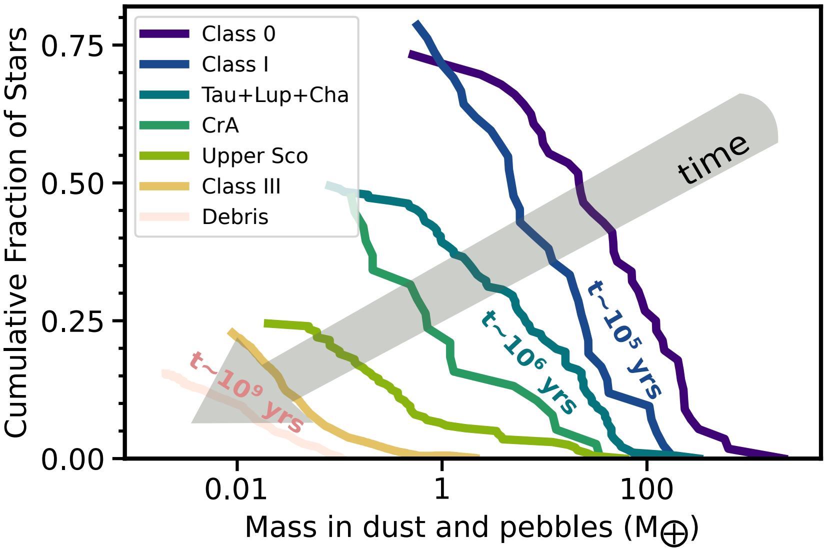

Figure 2.5: Cumulative distribution of the dust mass around young stellar objects of different ages. The typical ages of the samples are indicated. There is a clear evolutionary trend from large to low dust masses. (image credit: Drążkowska et al., 2022)

Density

In principle, spatially resolved disk observations can constrain the surface density profile of a disk. Gas surface density profiles Σ_g offer important insights into how angular momentum is transported throughout a disk (see Sec. 3), if and where planets can form (see Sec. 4) and how they will evolve. Likewise, the dust surface density profile Σ_d provides insight into the earliest stages of planet formation, and processes such as dust growth (see Chapter 4). A crude estimate suggests a radial dependence of the form $\Sigma_d \propto r^{-1}$ with values of $\Sigma_d \sim 0.001 - 1$ g/cm^2 in regions between 50 and 100 au (Andrews, 2020) with gas surface densities Σ_g roughly two orders of magnitude above that. See also Section 2.4.1 for constraints coming from the Solar System.

Lifetimes

The lifetime of a protoplanetary disk sets a strict upper limit to the timescale in which the formation of (gaseous) planets can operate. Large observational studies of nearby star-forming regions have found that the infrared excess in the SED of YSOs, which hints at the existence of a disk, disappears on a timescale of only a few million years (see e.g. the review by Hillenbrand, 2005). While the total lifetime of individual disks can vary, there seems to be an upper limit of $\sim$ 10 Myr (e.g., Mamajek et al. (2004)). The typical lifetime of a disk is likely shorter and of the order 2-5 Myr Fedele et al. (2010).

Dust Size Distribution

The small fraction of dust (by mass) contained in protoplanetary disks is the dominant contributor to the continuum absorption opacity κ_ν. The dust opacity is a pure material property and generally has the highest value at infrared wavelengths and decreases towards longer wavelengths. The opacity can be influenced by various dust properties like composition (Henning & Stognienko, 1996), shape (Bertrang & Wolf, 2017), refractive indices (Boudet et al., 2005), and the size distribution (Birnstiel, 2011), and thus influence observables. For simplicity, the wavelength dependency of the opacity is commonly approximated with a power law of the form $\kappa_\nu \propto \nu^\beta$ where the power law exponent β encodes the material properties (the parameter β can also be frequency dependent). Given this consideration, the wavelength dependence of the flux F_ν can be related to the material dependent parameter β as $F_\nu \propto \nu^\alpha$ where $\alpha = \beta + 2$ is called the *spectral index.* Multiwavelength observations can directly constrain the spectral index, which in turn sets a lower bound for the largest observed dust particle size $a_{\max}$ in the dust size distribution (Draine, 2006).

In practice, measurements find $\alpha \approx 2 - 3$ in the $\lambda \approx 2 - 3$ mm range (e.g, Ansdell et al., 2018), which, depending on the model, indicates $a_{\max} \sim 10$ cm (Birnstiel et al., 2018). This is an indication that dust grains have grown significantly since their origin in the ISM. There is also evidence that particle growth happens as early as in Class 0 objects (Galametz et al., 2019). See also the discussion in Sec. 4.3, for a theoretical view on dust growth in protoplanetary disks.

For a typical dust size distribution, one finds an absorption opacity at radio wavelengths of $\lambda = 1\,mm$ of $\kappa_{\lambda=1mm} \sim 3\,\mathrm{cm}^2/\mathrm{g}$ (Birnstiel et al., 2018). Eq. 2.2 then predicts that the disk transitions from optically thick to thin ($\tau_\nu = 1$) at a dust surface density of $\Sigma_d \sim 0.3\,\mathrm{g/cm}^2$, which for typical disks is located at around 10 au (see e.g., Eq. 2.7). Therefore, such a disk is optically thick to mm-emission in the inner region and optically thin beyond 10 au. The transition radius moves further out for emissions at smaller wavelengths.

2.2.3 Substructures

Since the progress in observational technology (interferometry, adaptive optics) allows for high-resolution radio observations of protoplanetary disks, the field has experienced a paradigm shift away from the simple picture of smooth, symmetrical disks with monotonically decreasing surface density profiles. By now, telescopes like ALMA, and also the Very Large Telescope (VLT), have revealed that protoplanetary disks are much more complex and show structures that appear in most disks on effectively all scales down to the resolution limit $\sim 1 - 5$ au (Zhang et al., 2016; Garufi et al., 2018; Andrews et al., 2018b; Andrews, 2020). The observations of substructures have led to novel insights about disk and planet formation processes and challenged previous theories. Figure 2.6 shows a gallery of ALMA continuum observations showing disks with substructures. In the remainder of this section, we will provide a brief overview of the different substructure morphologies, and in Sec. 4.6 we will discuss potential physical origins. Substructures are traditionally grouped into four categories based on their morphology:

- **Ring/Cavity.** The disk shows a primary narrow ring (usually peaking at tens of au from the central star) outside a depleted cavity.

- **Rings/Gaps.** Refers to concentric, axisymmetric alternations of intensity peaks (rings) and valleys (gaps). This morphology is the most frequent in all observed disks. In Figure 2.6, AS 209 (fifth row, third column) is a prime example of a disk with gaps and rings. Many other disks in Figure 2.6 also show rings and gaps.

- **Arcs.** Non-axisymmetric substructures that span a range of azimuth. The lower right panel of Figure 2.6 shows an observation of HD 163296 with an arc at the 8 o'clock position.

- **Spirals.** While large spiral patterns are more common in scattered light observations, there are only three known sources that exhibit spirals in the mm continuum (Pérez et al., 2016; Huang et al., 2018; Andrews, 2020). The three are IM Lup, Elias 27 and WaOph 6 (see Figure 2.6). Observed spirals have a variety of pitch angles, ranging from very open to tightly wound spirals.

The boundaries between categories are not well-defined. A single disk can contain substructures of multiple morphological types. A known problem with the observational study of substructures is the observational bias towards larger, brighter disks. An unbiased census is highly desirable, but not yet available (Andrews, 2020).

Besides observations and classification, the interpretation of substructures is another relatively new challenge. Interestingly, most of the observed substructures can be interpreted as a sign of the presence of embedded planets in the disk. However, other processes have been proposed which do not include planets. We will discuss possible explanations from a theory point of view in Sec. 4.6.

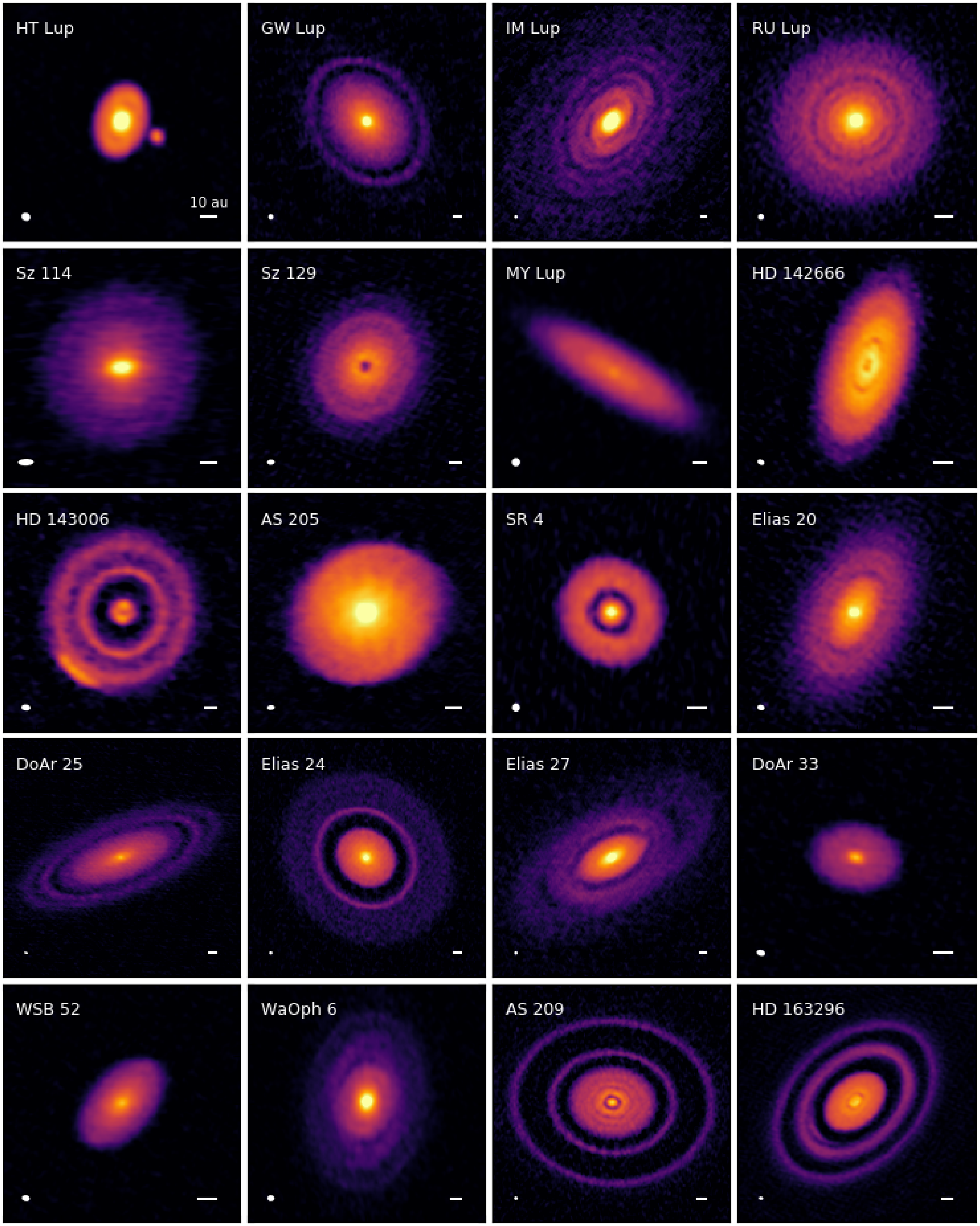

Figure 2.6: Overview of ALMA continuum emission observations as part of the Disk Substructures at High Angular Resolution Project (DSHARP). Substructures are ubiquitous. The beam size is shown in the lower-left corner. The bar in the lower-right corner represents a distance of 10 au. (image credit: Andrews et al., 2018b)

2.3 Exoplanets

In the previous sections, we discussed observations of young stellar objects and protoplanetary disks. While protoplanetary disks are the birthplaces of planets and thus provide the initial and boundary conditions for planet formation, the diverse population of mature planets represents the outcome. A complete theory of planet formation must thus be consistent with both. In this section, we will focus on the observational constraints gained from the planet population outside the Solar System, i.e., from *exoplanets*. We first introduce the typical classification and briefly review the basic concepts behind the detection of exoplanets in Sec. 2.3.1. In Sec. 2.3.2, we then provide an overview of a number of trends that can be inferred from the exoplanet population as a whole.

2.3.1 Classification and Detection

When constraining planet formation theories, of course, the planets of the Solar System must also be considered. However, we must keep in mind that, even though our Solar System provides very detailed insights, it is not necessarily representative of the planet formation process and only constitutes one specific outcome around one particular star. We will specifically discuss Solar System constraints in Sec. 2.4.

Planets outside the Solar System had long been theorized but had not been observationally confirmed until 1993 (Wolszczan & Frail, 1992), mainly due to technical limitations. A specific detection method had already been proposed in 1952 (Struve, 1952). Even though the field of exoplanet observations is relatively young, large-scale observational campaigns carried out in the last three decades have been incredibly productive at detecting exoplanets. As of March 2023, 5076 exoplanets have been confirmed[2].

It is now common practice to classify these exoplanets based on their masses. The upper end of the mass scale is occupied by *giant planets*, with an upper limit at 13 Jupiter masses (beyond this limit, objects are considered *brown dwarfs*). There exist two subtypes of giant planets, which are distinguished based on the composition of their atmospheres. The thick atmospheres of *gas giant planets* consist of hydrogen and helium, similar to the atmospheres of Jupiter and Saturn. On the other hand, the atmospheres of *ice giant planets* are mainly composed of elements heavier than hydrogen and helium, such as oxygen, carbon, nitrogen, and sulfur. In the Solar System, Uranus and Neptune are considered ice giants. An exoplanet with mass below Uranus (0.046 M_J[3], 14.5 $M_\oplus$[4]) and Neptune (0.054 M_J, 17.1 $M_\oplus$), but above Earth is either called a *sub-Neptune* or a *super-Earth*. While the two types are not strictly distinguished by mass, a sub-Neptune is generally larger than a super-Earth, with the border commonly drawn at around 1.75 Earth radii. Correspondingly, *sub-Earths* are exoplanets less massive than Earth. Below that, the lower end of the planetary mass spectrum is not well-defined.

Sometimes, exoplanet nomenclature is additionally based on other characteristics, such as orbital characteristics. For example, a *hot Jupiter* is an exoplanet class with a mass similar to Jupiter, but with a smaller orbital semi-major axis ($\lesssim 0.5$ au, compared to 5.2 au in the case of Jupiter). Hot Jupiters derive their name from their hot atmospheres, which they have obtained as a result of their proximity to the star.

There are too many detection methods to comprehensively review within the framework of this thesis. Some methods are also more theoretical than practical. Below, we review only the basics of the four most productive methods:

- **Radial Velocity.** The radial velocity method is an indirect method that measures the radial velocity variations of a star caused by the gravitational pull of an orbiting planet.

---

[2] According to `exoplanet.eu`

[3] Jupiter mass, 1 $M_J = 1.898 \times 10^{27}$ kg

[4] Earth mass, 1 $M_\oplus = 5.972 \times 10^{24}$ kg

This method favors the detection of massive planets on small orbits. It can constrain both the mass and orbital period of an exoplanet. But, it must be combined with other methods to infer additional planetary properties. Most of the early detections were made using this method, including the detection of the first exoplanet around a solar-type star (Mayor & Queloz, 1995).

- **(Primary) Transit Photometry.** Measures a dip in the brightness of a star when a planet passes in between the star and the observer. The method can directly constrain the orbital period, size, and inclination of an exoplanet. Additional data or models must be used to infer the mass or other characteristics. The transit method allows many stars to be surveyed at once. Notably, the Kepler space telescope has contributed more than 2600 detections using the transit method on its ten-year mission (Narang et al., 2018).
- **Direct Imaging.** As the name suggests, this method detects exoplanets by directly observing their infrared emission (see e.g. Bowler, 2016, for a review). This approach is challenging because of the brightness contrast between the faint planet and its nearby host star. Thus, coronagraphs are often used as a helpful tool to block parts of the radiation of the star. The first directly imaged planets were reported in 2008 (Kalas et al., 2008; Marois et al., 2008). This method is particularly sensitive towards massive ($> 1 M_{\mathrm{Jup}}$) planets at large orbital distances $\gtrsim$ 10 au. It is thus complementary to the previously mentioned methods.
- **Gravitational Microlensing.** This method is another indirect method and uses concepts of general relativity, specifically, the fact that light from a background star gets warped and bent by the mass of a planet passing in front of it. The great strength of this method lies in its ability to detect low-mass planets. Furthermore, it is currently the only method capable of detecting ice giant planets until thirty-meter-class telescopes become available in a few years (Kane, 2011).

It is important to keep in mind that the most productive detection methods (radial velocity and transit) are biased toward detecting large/massive planets at short distances from their star. In Figure 2.7, we plot the mass of 2230 exoplanets as a function of their semi-major axis (only the exoplanets with a known mass and semi-major axis are shown). The exoplanets are color-coded based on their detection method. In Figure 2.7, it is apparent that most planets cluster towards the upper left corner of the plot. Even though this could in fact be a real feature, observational bias must be accounted for when analyzing the data. Furthermore, because every detection method has a distinct operational window within the mass-semi-major-axis space, several methods must be combined to generate a complete picture of the exoplanet population. Figure 2.7 also suggests that gas giants ($\gtrsim 0.1\ M_J$) cluster at two distinct locations. There is a population of hot Jupiters at small orbital distances (< 0.1 au) and a population of cold Jupiters that cluster between ∼ 1 and 5 au. Interestingly, *our* Jupiter lies just at the edge of the latter cluster, while Saturn falls into a relatively empty region of the plot. The ice giants Uranus and Neptune also fall within an empty region of the plot. In principle, this can be interpreted as a result of the uniqueness of the Solar System, but it is more likely that Solar System analogs are outside the detection limits of even the most advanced observational capabilities. This also explains the lack of planets towards the bottom of Figure 2.7. This region is presumably strongly impacted by current detection limits. For example, exoplanet analogs of Mercury and Mars currently lie beyond these limits.

Despite the large number of observed exoplanets, only a handful of young exoplanets (< 10 Myr) have been detected. The prime example of a system containing young exoplanets is the system PDS 70, which is ∼ 5.4 Myr old, with its planets PDS 70 b and c (Müller et al., 2018; Keppler et al., 2018). Such young exoplanets can provide direct observational evidence of the planet formation process and put constraints on the planet formation timescales. Unfortunately, they are extremely difficult to observe.

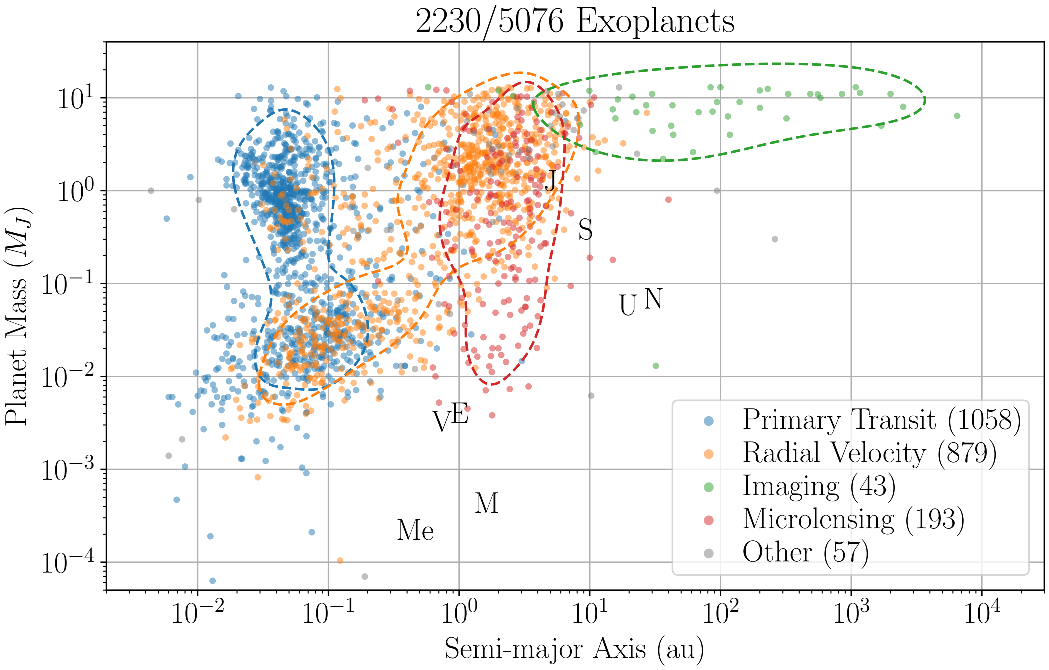

Figure 2.7: Planet mass as a function of the semi-major axis of 2230 exoplanets with known mass and semi-major axis out of 5076 confirmed exoplanets as of March 2023. The different colors indicate different detection methods; transit (blue), radial velocity (orange), direct imaging (green), and microlensing (red). The dashed contours outline the 68 % confidence regions of the corresponding kernel density estimates. The letters indicate the planets of the Solar System. In the legend, the numbers in brackets indicate the number of plotted planets for each detection method. The exoplanets not plotted have a yet unknown mass and/or semi-major axis. Data source: `exoplanet.eu`

2.3.2 Demographics

The large number of detected exoplanets has created the possibility for statistical analysis of the exoplanet population as a whole, which is called *exoplanet demographics*. Ultimately, the goal of exoplanet demographics is to find the distribution function of exoplanets as a function of all the parameters that impact planet formation. These parameters can include but are not limited to, e.g., planet mass, planet radius, orbital properties, properties of the host star (e.g., temperature, luminosity, metallicity), or properties of the galactic environment (see e.g. Gaudi et al., 2021, for a review on the challenges of exoplanet demograpics). The distribution function then serves as the *ground truth* that planet formation theories must reproduce. By comparing the exoplanet distribution to the prediction of current planet formation theory, we can both test and refine the theory (see e.g. the review by Drążkowska et al., 2022). Even though we are still a long way from finding a complete distribution, a few trends have emerged.

Based on statistics gathered from the Kepler data, it was concluded that *on average* every star in the galaxy hosts one or more planets at an orbital distance between 0.5 and 10 au (Cassan et al., 2012). That does not mean that every star has indeed a planet. In fact, only 50-60 % of stars are estimated to host at least one planet (Mulders, 2018; He et al., 2019, 2021), pointing to the conclusion that multi-planet systems are common.

There are a number of peculiarities in the observed exoplanet population. For example, there seems to be a bimodality in the radius distribution between super-Earths and sub-Neptunes (Fulton et al., 2017; Owen & Wu, 2017). The so-called *Fulton gap* is located roughly between 1.5 and 2 Earth radii. Moreover, giant planets are more frequently found around metal-rich and more massive stars, whereas, low-mass planets are more frequent around low-mass stars (Santos et al., 2004; Fischer & Valenti, 2005; Fulton et al., 2021), suggesting that stellar metallicity is a key constraint for the planet formation process.

Among all the types of exoplanets, super-Earths and sub-Neptunes are the most frequent in the galaxy (Fressin et al., 2013; Petigura et al., 2013). Interestingly, these classes do not exist in the Solar System. In this context, it is also important to distinguish between the observational detection frequency, which is intrinsically biased, and the physical *occurrence rate*. The latter denotes the average number of planets per star after bias corrections. Planets smaller than Neptune have an estimated occurrence rate in the range 140-200 % for sun-like stars (Mulders, 2018; Kunimoto & Matthews, 2020). Overall, smaller planets are more common than larger planets, and the occurrence rate falls off rapidly with increasing planetary size beyond about three Earth radii (Youdin, 2011b; Howard et al., 2012; Mulders et al., 2015). Giant planets are found only around about 10-20 % of stars (Cumming et al., 2008; Mayor et al., 2011; Petigura et al., 2018), mostly at orbital distances beyond 1 au (Fulton et al., 2021). Even though hot Jupiters have been detected frequently in transit surveys (in Figure 2.6 they appear roughly as numerous as cold Jupiters), they are expected only to represent 0.5-1 % of the giant planet population (Wright et al., 2012; Howard et al., 2012) and are clearly overrepresented in Figure 2.6. It is estimated that giant planets are most common around 1-10 au (Fulton et al., 2021) and become increasingly rare beyond 10 au (Vigan et al., 2021). Fulton et al. (2021) estimate an occurrence rate of giant planets ($> 0.1\, M_{\mathrm{Jup}}$) at orbital distances between 0.3 and 30 au of 34 %.

After having discussed the exoplanet population as a whole, we consider the Solar System as a specific outcome of planet formation in the next section.

2.4 Solar System Constraints

Compared to the Solar System, our knowledge of individual exoplanetary systems is meager. In many cases, only a few orbital properties of the planets are known, and the power of exoplanet science is more statistical in nature originating from the large number and diversity of known systems as discussed in Sec. 2.3.2. Constraints on the theory of planet formation from the Solar System are much more detailed. Space missions to all the planets of the Solar System have provided detailed information on the surface, and sometimes also on the interior structure, of the planets, satellites, and minor bodies in the Solar System.

In total, the Solar System has eight planets, two gas giants (Jupiter and Saturn), two ice giants (Uranus and Neptune), and four *terrestrial planets* with a rocky surface (Mars, Earth, Venus, and Mercury). Besides, there are a number of dwarf planets like Pluto, Eris, Haumea, and others. The list of dwarf planets will likely grow due to new discoveries in the future. The total mass of the planets is almost negligible compared to the mass of the Sun and only contributes about 0.13 % to the total mass of the Solar System.

2.4.1 Minimum Mass Solar Nebula

Our knowledge about the disk from which the Solar System's planets formed is limited. However, from the mass and composition of the planets, a lower mass limit of the protosolar disk can be derived. This limit is called the *Minimum Mass Solar Nebula* (MMSN) (Weidenschilling, 1977b) and provides an explicit gas surface density profile. The most common profile is provided by

Hayashi (1981):

$$\Sigma_g(r) = 1.7 \times 10^3 \cdot \left(\frac{r}{1\,\mathrm{au}}\right)^{-3/2} \mathrm{g\,cm}^{-2}. \tag{2.6}$$

Integrating the above expression to 30 au, i.e., the orbit of Neptune, gives a total mass of $0.01 M_\odot$. Hayashi (1981) also provides an estimate for the surface density profile of solid material in the protosolar disk:

$$\Sigma_d(r) = \begin{cases} 7.1 \cdot \left(\frac{r}{1\,\mathrm{au}}\right)^{-3/2} \mathrm{g\,cm}^{-2} & \text{for } r < 2.7\,\mathrm{au} \\ 30 \cdot \left(\frac{r}{1\,\mathrm{au}}\right)^{-3/2} \mathrm{g\,cm}^{-2} & \text{for } r > 2.7\,\mathrm{au} \end{cases} \tag{2.7}$$

The discontinuity at 2.7 au is due to the presence of icy material beyond the water snow line (the snow line is the location beyond which water vapor freezes out onto dust grains). Even though the Minimum Mass Solar Nebula has been widely used in modeling the protosolar disk, it should be regarded only as an order of magnitude guide that provides an approximate lower limit for the amount of mass that was available to form the Solar System planets. As we will discuss in chapters 3 and 4, both the gas and solids distribution are likely to have evolved over time.

2.4.2 Minor Bodies in the Solar System

In addition to the planets, the Solar System contains a wealth of minor bodies: asteroids, comets, and Kuiper belt objects. The total mass of these objects is small, e.g., the combined mass of Kuiper belt objects on the order of $0.1\ M_\oplus$ (Chiang et al., 2007). However, their distribution provides important insights into the early history of the Solar System. An interesting property is that the Solar System is, in fact, *dynamically full*, which means that most locations where small bodies could orbit stably for billions of years are populated (Armitage, 2010). Much of what we know about the formation of planets relies on theories aiming to reproduce the distribution of large and small bodies in the Solar System. A review of the dynamical history of the Solar System is beyond the scope of this thesis, and we refer to Chambers (2004) and Raymond et al. (2014) for a review. In chapter 4, we summarize the current understanding of planet formation in general.

Besides physical properties, much of what we know about the early history of the Solar System comes from studying the chemical nature of Solar System objects. We thus focus on chemical and compositional constraints in the remaining sections of this chapter.

2.4.3 Meteorites and Astrochemistry

The Solar System uniquely provides the opportunity for studying relatively primordial material in laboratories in the form of *meteorites*. Meteorites are rocks that have fallen to the surface of Earth from outer space. The most primitive meteorites, called *chondrites*, originate in asteroids or comets that never became hot enough to melt and are thus undifferentiated. They preserve the state they obtained during their formation and allow insights into the earliest history of the Solar System.

Most meteorites contain spherical inclusions, so-called *chondrules* of about 1 mm in size. The composition of chondrules suggests that they are made of primitive dust that was strongly heated above its melting temperature within the protosolar disk, and then rapidly cooled (Scott & Krot, 2014). Some theories predict chondrules to have formed *in situ*, which requires the thermal processing of material over large regions of the protosolar disk. Possible sources of such heating are hydrodynamic shocks or collisions. Alternatively, chondrules might have been heated very close to the young Sun and then transported outward to be incorporated into the parent bodies of meteorites. Additionally, there is evidence of a second origin of chondrules as a result of planetary collisions, i.e., much later in time when the disk has already dissipated (Krot et al., 2005).

Overall, theories on the exact origin of chondrules and the nature of the heating events responsible for their formation are plentiful, but none of them is yet fully satisfying (e.g. Jones et al., 2000; Ciesla, 2005; Scott, 2007).

Meteorites also contain *calcium aluminium rich inclusions* (CAIs) which are very refractory compounds, similar in size to chondrules and with an equally elusive formation history. Interestingly, the ages of CAIs can be calculated from the abundance of lead isotopes formed by the decay of long-lived uranium isotopes. According to these isotopes, CAIs are the oldest Solar System materials we have found, thus, their age is considered synonymous with the age of the Solar System as a whole which is estimated to be 4567.3 ± 0.16 Myr (Connelly et al., 2017). Connelly et al. (2017) predict that chondrules formed simultaneously with CAIs and then continued to form for at least ~ 4 Myr, a time when the first planetesimals and the parent bodies of meteorites are expected to have formed (see Sec. 4.3 for a discussion on the formation of planetesimals). Overall, the timescale constraints for the protosolar disk coming from the analysis of meteorites are in good agreement with the observed lifetimes of protoplanetary disks.

Unlike chondrites, terrestrial planets are differentiated bodies with dense iron-rich cores and low-density silicate-rich mantles. Specifically, Earth's mantle is highly depleted in siderophile (iron-loving) elements compared to silicates. Interestingly, the rocky objects in the Solar System seem to be made up of a different mixture of major rock-forming elements (Drake & Righter, 2002) with a clear correlation to their distance from the Sun (Gradie & Tedesco, 1982), which hints at a heterogeneous presolar disk. We will discuss these findings in more detail for the specific example of carbonaceous material in sections 2.4.4 and 2.4.5. These two sections also serve as the foundation for the study on refractory carbon in the Solar System in Chapter 6.

2.4.4 Case Study 1: Refractory Carbonaceous Material

The rocky bodies in the Solar System, i.e., rocky planets, cores of gas giant planets, and small bodies, have formed from solid material inherited from the interstellar medium (ISM). This material had been delivered to the protosolar disk during the infall process in the early phase of star and disk formation before it was available to be incorporated into the rocky Solar System objects and their parent bodies. Therefore, the composition of rocky bodies in the Solar System today is linked to the composition of the refractory material available during their formation and the physical/chemical alteration processes which have acted on the bodies since their formation. Without any processing, the composition of the rocky bodies in the Solar System should be identical to the composition of the refractory material present in the ISM. Focusing specifically on carbon, we expect about 50 % of the carbon in the ISM to be bound in solid form, i.e., dust, and thus to be potentially refractory (Zubko et al., 2004). Relative to silicon, the solid component of the ISM has a carbon-to-silicon elemental abundance ratio of C/Si ~ 6 (Bergin et al., 2015). However, the primary form and morphology of the solid carbonaceous material remain uncertain. Suggested components include amorphous carbon or hydrocarbon grains and/or aromatic and aliphatic compounds. Gail & Trieloff (2017) summarized the available information on the interstellar carbonaceous material and constructed a representative model which consists of 60 % organic material containing large amounts of H, O, and N atoms, 10 % of pure carbon dust in amorphous form, 20 % of more moderately volatile materials which include aromatic and aliphatic compounds and 10 % other components.

The solid interstellar carbonaceous material which has not been incorporated into Solar System bodies after the infall onto the early solar disk has likely been accreted by the Sun. This is also the case for the volatile components, which have not been accreted by gas-giant planets or have not been lost due to dissipation. The solar photosphere shows a comparable carbon-to-silicon abundance ratio to that of the ISM, with a value of C/Si ~ 8 (Bergin et al., 2015; Grevesse et al., 2010). The similarity to the value in the ISM suggests that the reported C/Si ratio is

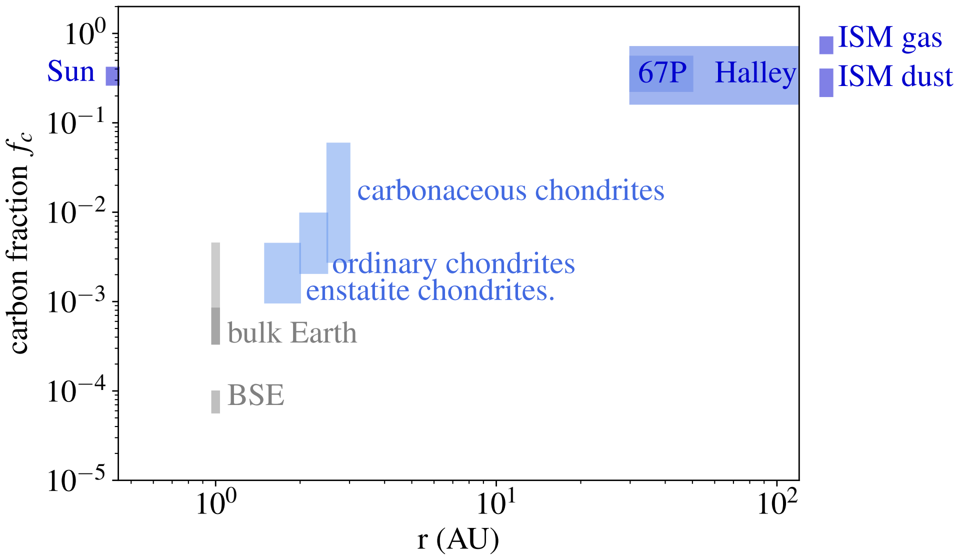

Figure 2.8: Carbon abundance f_c, i.e., the mass fraction of refractory carbon, in some Solar System bodies and their heliocentric distance. In horizontal axes, the width of the boxes represents the expected formation regions of individual objects. For chondrites, the vertical height of the boxes represents the spread in measured values within individual classes. For the other objects, the vertical height represents uncertainties in the expected carbon fraction. For bulk Earth, we show estimates based on detailed geochemical modeling in dark gray and possible upper bounds in light gray. Further, we show estimates for bulk silicate Earth (BSE), i.e., Earth's mantle and crust without the core, and two comets, 67P/Churyumov-Gerasimenko and 1P/Halley. For comparison, values of the Sun and the ISM are added. See section 2.4.5 for further explanations.

somewhat universal in the solar neighborhood, and thus also in the solid material that was available at the beginning of planet/planetesimal formation in the Solar System. Therefore, one would expect to find all the components which are at least moderately refractory in planetesimals and subsequently also in the rocky components of the Solar System, except in regions where high temperatures or radiation lead to the destruction of the refractory compounds. This is typically only the case in the inner disk region ($\lesssim$ 0.5 au Alessio & Woolum, 2005) or in the directly illuminated disk atmosphere. However, measurements of the carbon abundance in rocky Solar System objects reveal a significant depletion in carbon compared to the solid components in the ISM. The carbon content in the bulk silicate Earth (BSE), that is the Earth's mantle and crust without the core, is with a C/Si ratio of $1.1 \cdot 10^{-3}$ more than three orders of magnitude depleted compared to ISM and solar values (Bergin et al., 2015). Even if one considers additional carbon to be incorporated in Earth's core, the entire planet is depleted in carbon by several orders of magnitude (Allegre et al., 2001; Li et al., 2021). There is also evidence that ISM material has survived unprocessed to be incorporated into meteorites originating in the asteroid belt (Alexander et al., 2017). However, the amount of refractory carbon relative to silicon in these meteorites is also decreased by 1–2 orders of magnitude compared to what is available in the ISM. This is the case even in the least processed and most primitive meteorites, the carbonaceous chondrites (Geiss, 1987; Bergin et al., 2015). Beyond the asteroid belt, where comets are expected to have formed, the C/Si ratio is comparable to that in the ISM. There is a clear radial gradient in the Solar System, with the inner Solar System being depleted in refractory carbon relative to silicon (see e.g., Figure 2 in Bergin et al. (2015) or Fig. 2.8 in this work).

This trend does not only exist in the Solar System but is also observed in systems of polluted white dwarfs. Analysis of the spectra of white dwarfs gives insight into elemental abundances of their atmosphere, and due to the strong gravity, heavy elements are not expected to be present there. Therefore, the observed traces of heavy elements in the atmosphere can be explained by tidally disrupted, carbon-depleted rocky objects that are accreted by the star (Jura, 2006). Based on spectral analysis, Xu et al. (2014) report the elemental composition of extrasolar rocky planetesimals, based on traces in the atmospheres of polluted white dwarfs, to resemble, to zeroth order, the composition of bulk Earth (also see section 2.4.5).

In a more extended study, Xu et al. (2019) confirm their previous results and report the detailed elemental composition of 19 polluted white dwarf atmospheres and a carbon mass fraction in the range between $\sim 3 \cdot 10^{-4}$ and $\sim 10^{-1}$ in their samples. Overall, this points to the conclusion that the mechanism, responsible for refractory carbon destruction, might be universal and not unique to the Solar System. Furthermore, the depletion mechanism must be active before planetesimal formation or the formation of the parent bodies of current Solar System objects, to explain the observed carbon depletion. It is likely that this mechanism is either a thermally-induced (e.g., pyrolysis, oxidation, evaporation/sublimation) or a photo-induced (e.g., photochemical) process (or a combination of both). Both options have been studied extensively.

Depletion via pyrolysis (thermal decomposition without oxidation) and oxidation has recently been studied by Gail & Trieloff (2017) who studied refractory carbon destruction by short-period flash heating events. Li et al. (2021) suggest sublimation to be responsible for the observed carbon depletion. As for the photo-induced mechanisms, Lee et al. (2010) studied the erosion of carbon grains via hot oxygen atoms in the UV-illuminated region of the early solar disk. Refractory carbon aggregates are also turned into more volatile compounds if they react with oxygen-bearing species, such as OH or free atomic O (Finocchi et al., 1997; Gail, 2001; Wehrstedt & Gail, 2002). Siebenmorgen & Heymann (2012) and Siebenmorgen & Krügel (2010) studied the destruction of polycyclic aromatic hydrocarbons (PAHs) by X-ray and extreme ultraviolet (EUV) photons. Additionally, refractory carbon grains are directly photochemically destroyed by FUV photons via photolysis (Alata et al., 2014, 2015; Anderson et al., 2017).

While early studies had pointed to the conclusion that photo-induced processes can explain the observed carbon deficiencies in the Solar System, Klarmann et al. (2018) found that radial and vertical transport of carbon grains in the disk constitutes an obstacle to photo-induced refractory carbon depletion when explaining Solar System abundances.

2.4.5 Case Study 2: Carbon on Earth

The carbon content in the bulk silicate Earth (BSE), that is Earth's mantle and crust without the core, is more than three orders of magnitude depleted compared to ISM and solar values (see compilations in e.g. Lee et al., 2010; Bergin et al., 2015). The mass fraction of carbon in the BSE is estimated to be $(1.4 \pm 0.4) \cdot 10^{-4}$ (Hirschmann, 2018), but the carbon content in the core is not known exactly. We summarize estimates for Earth in Table 2.1.

Earth's core is less dense than pure iron, thus, it must contain lighter elements. If the density difference is fully compensated with carbon alone, Li et al. (2021) estimate the carbon mass fraction in the core to be less than 5.0 %. However, this estimate is very generous as the core contains significant amounts of other lighter elements (e.g., sulfur, silicon, oxygen). More realistic estimates yield a carbon mass fraction of $\sim 0.5 - 1$ % (e.g. Allegre et al., 2001; Wood et al., 2013).

For bulk Earth, i.e., including the core, Allegre et al. (2001) arrive at a carbon mass fraction of 0.17 % up to 0.39 %. Li et al. (2021) argue for a more realistic upper bound of (0.4 ± 0.2) % by mass for bulk Earth. The upper bound of Li et al. (2021) is higher than, and thus consistent with, geochemical estimates of 0.053 ± 0.021 % by mass (Marty, 2012) and the results of Fischer et al. (2020) who estimate a range of 0.037-0.074 % by mass for the carbon mass fraction of bulk Earth. On the other hand, the mass fraction of silicon in the BSE is about 21 % (Li et al., 2021). Considering the BSE carbon mass fraction of 0.014 % quoted above, this value is in agreement with Bergin et al. (2015) who estimate a C/Si atomic ratio in the BSE of (0.11 ± 0.04) atomic percent.

Silicon is less abundant in Earth's core than in the mantle and the crust. Wade & Wood (2005) estimate a mass fraction of 5-7 %. Combining the estimates of Li et al. (2021) and Wade & Wood (2005), we estimate the silicon mass fraction of the bulk Earth at $15.9 - 16.5$ %. This result is also in rough agreement with Allegre et al. (2001) who estimate the bulk Earth silicon mass fraction as 17.1 ± 0.1 %. We use the former range and the carbon mass fraction from Li et al. (2021) to calculate an upper bound for the C/Si atomic ratio in the bulk Earth of $5.7 - 5.9$ %. This value is more than 50 times larger compared to the BSE because of the large amounts of carbon which are possibly present in Earth's core. We also calculate the C/Si atomic ratio in the bulk Earth using the lower estimate of the carbon mass fraction of Fischer et al. (2020) which yields a range of $0.53 - 1.1$ atomic percent. This value is only five to ten times larger than in the BSE. These results are summarized in Table 2.1.

Overall, even in the most optimistic case, bulk Earth is depleted in carbon by almost two orders of magnitude with respect to silicates, compared to the ISM. Combined with estimates on chondrites and comets (see Fig. 2.8), there exists a clear trend of decreasing carbon abundance towards the inner region of the Solar System. In Chapter 6, we will provide a possible explanation for this trend.

Table 2.1: Overview of the carbon and silicon abundances on Earth, as described in section 2.4.5. Listed are literature values for the bulk silicate Earth (BSE), Earth's core and bulk Earth. The last column lists the carbon fraction f_c, the fundamental quantity which we evolved in this work.

	C (wt%)	Si (wt%)	C/Si (at.%)	f_c
BSE	0.014 ± 0.004^{a}	21^{b}	0.11 ± 0.04^{c}	$(8 \pm 1) \cdot 10^{-5}$
Earth's core	$\sim 0.5 - 1^{d}$	$5 - 7^{e}$	$16.7 - 23.4$	$(1.1 - 1.6) \cdot 10^{-2}$
Bulk Earth	$< 0.4 \pm 0.2^{b}$	$15.9 - 16.5$	$< (5.7 - 5.9)$	$< (4.0 - 4.1) \cdot 10^{-3}$
	$0.037 - 0.074^{f}$		$0.53 - 1.1$	$(3.7 - 7.7) \cdot 10^{-4}$

Sources: [a]Hirschmann (2018), [b]Li et al. (2021), [c]Bergin et al. (2015), [d]Wade & Wood (2005), [e]Wood et al. (2013), [f]Fischer et al. (2020)

Chapter 3

Protoplanetary Disk Theory

After the previous chapter focused on observational constraints, this chapter summarizes the theoretical concepts and the physics of protoplanetary disks. Classical protoplanetary disk theory, which can be traced back to the early 1970s (e.g. Safronov, 1972), mainly focuses on the description of rotationally supported disks surrounding protostars, which have formed as a result of angular momentum conservation in a collapsing molecular cloud. Many of the concepts summarized here are not only applicable to protoplanetary disks but have been derived to describe accretion disks in general (for a review see e.g. Frank et al., 2002).

It is not a simple task to derive explicit analytical descriptions of protoplanetary disks. General equilibrium solutions require solving for a steady state of the coupled magnetohydrodynamic equations and Poisson's equation. And even if such a solution exists, its dynamical stability is not guaranteed (Papaloizou & Pringle, 1984). However, some explicit analytical descriptions exist for simplified cases of axisymmetric, unmagnetized, inviscid, and low-mass disks, for which the central star dominates the gravitational field everywhere in the disk. These simple disks are well described with the time-dependent Euler equations (see e.g. Shu, 1992), which in Cartesian coordinates take the form

$$\frac{\partial \rho_g}{\partial t} + \frac{\partial}{\partial x_j}\left(\rho_g u_j\right) = 0 \tag{3.1}$$

$$\frac{\partial}{\partial t}(\rho_g u_i) + \frac{\partial}{\partial x_j}\left(\rho_g u_i u_j\right) + \frac{\partial}{\partial x_i} p = \rho_g g_i \tag{3.2}$$

where we have used the Einstein summation convention. Eq. 3.1 is the *continuity equation* that ensures the conservation of mass and describes the time evolution of the gas volume density ρ_g. The quantity u_i is the gas velocity along dimension $i = 1, 2, 3$. Eq. 3.2 describes the dynamics of the gas momentum per unit volume $\rho_g u_i$. While the first and second terms in Eq. 3.2 account for the local change and advection of momentum respectively, the third and fourth terms are contributions by the gradient pressure force and gravitational force respectively. Specifically, p is the gas thermal pressure and g_i is the gravitational acceleration along dimension i. In a low-mass disk, the gravitational acceleration is approximately spherically symmetric and points towards the central star with a magnitude $\mathrm{g} = GM_*/r^2$, where G is the gravitational constant, M_* is the mass of the star, and r is the distance to the star.

The system of two equations (Eqs. 3.1 and 3.2) is not yet closed (there are more unknowns than equations). To close the system, one must define an equation of state and, depending on the functional form of the equation of state, introduce an additional equation that describes the dynamics of the internal energy of the gas. For applications in protoplanetary disks, a simple, locally isothermal equation of state is often assumed, which eliminates the need for an additional internal energy equation. The locally isothermal equation of state reads

$$p = \rho_g c_s^2 \tag{3.3}$$

where c_s is the isothermal speed of sound, which is considered a constant model parameter. The sound speed is related to the gas temperature T as

$$c_s = \sqrt{\frac{k_B T}{m_\mu}} \tag{3.4}$$

where k_B is the Boltzmann constant and m_μ is the mean mass of a gas molecule. Physically, a locally isothermal equation of state assumes the gas temperature is constant at all times, which is equivalent to an infinitely small relaxation time towards the local thermodynamic equilibrium temperature. In many cases, this is a reasonable approximation in protoplanetary disks.

After the pressure term in Eq. 3.2 is replaced with Eq. 3.3, the system of two equations is closed and can be solved.

3.1 Hydrostatic Equilibrium Solution

Equilibrium solutions to the Euler equations (Eqs. 3.1 and 3.2) are found by requiring the time derivatives to vanish. When considering the static vertical equilibrium structure of a protoplanetary disk, one even solves for a static solution which requires the velocities and time derivatives to vanish. A static solution trivially satisfies the continuity equation (Eq. 3.1). Solving for a static solution in the momentum equation (Eq. 3.2), the first two terms on the l.h.s. vanish, and we are left with the terms accounting for the gradient pressure force and the gravitational force. In a vertical static equilibrium, the latter two must balance exactly in the vertical direction (along the z-axis):

$$\frac{\partial p}{\partial z} = \rho_g g_z \tag{3.5}$$

We restrict our analysis to regions close to the disk midplane where the z-component of the stellar gravitational field can be approximated as

$$g_z = -\Omega_K^2 z \tag{3.6}$$

where z is the distance to the disk midplane and Ω_K is the *Keplerian angular velocity* which is defined as $\Omega_K = \sqrt{GM_*/r^3}$.

Assuming the sound speed is vertically constant, Eq. 3.5 simplifies and describes the vertical gas density structure:

$$c_s^2 \frac{\partial \rho_g}{\partial z} = -\Omega_K^2 z \tag{3.7}$$

Integration of Eq. 3.7 leads to the gas volume density as a function of the distance to the disk midplane

$$\rho_g = \rho_{g,0} \exp\left(- \frac{z^2}{2h_g^2} \right) \tag{3.8}$$

where $\rho_{g,0}$ is a constant, and we have defined the vertical *gas pressure scale height* h_g as the ratio between the sound speed and the Keplerian angular velocity

$$h_g \equiv \frac{c_s}{\Omega_K}. \tag{3.9}$$

The *surface density* Σ_g is then defined as the integral of the volume density along the z-axis

$$\Sigma_g = \int_{-\infty}^{+\infty} \rho_g \mathrm{d}z \tag{3.10}$$

and is related to the constant $\rho_{g,0}$ in Eq. 3.8 as

$$\rho_{g,0} = \frac{\Sigma_g}{\sqrt{2\pi} h_g} \tag{3.11}$$

In contrast to the vertical profile, the radial gas density profile can only be derived by first identifying the nature of radial angular momentum transport or from observational constraints. However, given a temperature and density structure, the orbital velocity u_ϕ can be determined. The velocity profile can be derived from the radial component of the gas momentum equation (Eq. 3.2) in cylindrical coordinates:

$$\frac{\partial}{\partial t}(\rho_g u_r) + \nabla \cdot (\rho_g u_r \mathbf{u}) = -\frac{\partial}{\partial r} p + \frac{1}{r} \rho_g u_\phi^2 - \rho_g \Omega_K^2 r \tag{3.12}$$

where $\mathbf{u} = u_r \mathbf{e}_r + u_\phi \mathbf{e}_\phi + u_z \mathbf{e}_z$ is the three-dimensional velocity vector, and we have used the *Del* operator, which in cylindrical coordinates reads

$$\nabla = \mathbf{e}_r \frac{\partial}{\partial r} + \mathbf{e}_\phi \frac{1}{r} \frac{\partial}{\partial \phi} + \mathbf{e}_z \frac{\partial}{\partial z} \tag{3.13}$$

where $\mathbf{e}_i$ are the unit vectors along the coordinate axes.

The l.h.s. of Eq. 3.12 contains the terms that model the temporal change in local radial momentum and advection of radial momentum. The first term on the r.h.s. is a contribution by the pressure gradient force, and the second term is the *centrifugal force* arising from the transformation to cylindrical coordinates. The third term on the r.h.s. is the gravitational force in radial direction.

One typically considers stationary ($\partial \langle \cdot \rangle / \partial t = 0$) and axisymmetric ($\partial \langle \cdot \rangle / \partial \phi = 0$) solutions to Eq. 3.12 in vertical and radial hydrostatic equilibrium ($u_z = u_r = 0$), such that there is no advection in the radial or vertical directions. The only non-zero velocity component in this solution is the orbital velocity u_ϕ. With the aforementioned assumptions, Eq. 3.12 simplifies to

$$u_\phi^2 = \Omega_K^2 r^2 + \frac{r}{\rho_g} \frac{\partial p}{\partial r} \tag{3.14}$$

which implies that the orbital velocity u_ϕ is equal to the Keplerian velocity $u_K = \Omega_K r$ (hence the definition of the Keplerian angular velocity Ω_K) and modified by the radial pressure gradient. Technically speaking, the *static solution* is not fully static but allows for orbital motion along the azimuthal direction.

In smooth disks, the gas pressure typically decreases with increasing radius, such that the pressure gradient term is negative and the gas orbits with a sub-Keplerian velocity ($u_\phi < \Omega_K r$). When considering solely the flow of gas, this difference is mostly negligible and only becomes important when also considering the dynamics of solid bodies within the disk (for more details, see Sec.4.2). The most important insight from this discussion is that a protoplanetary disk in equilibrium shows differential rotation, i.e., the orbital angular velocity $\Omega = u_\phi / r$ changes with orbital distance r to the central star, which contrasts with, for example, the solid body rotation of a rigid object.

It is also worth noting that we find the equation for angular momentum $\rho_g r^2 \Omega$ in conservation form by considering the ϕ-component of the momentum equation (Eq. 3.2) in cylindrical coordinates and multiplying it with radius r:

$$\frac{\partial}{\partial t}(\rho_g r^2 \Omega) + \nabla \cdot (\rho_g r^2 \Omega \mathbf{u}) = 0 \tag{3.15}$$

The above equation implies that angular momentum is conserved globally and, for radially static and azimuthally symmetric disks, also locally. The latter implies that there is no redistribution of angular momentum in addition to no redistribution of mass in the static equilibrium solution. In reality, protoplanetary disks are not static, but because angular momentum transport is a slow process, the equilibrium solution discussed in this section serves as a good approximation in many cases.

3.2 Alpha Disk Theory

Astronomical observations show that protoplanetary disks have a limited lifetime of a few million years, which is in contradiction with the static disk model discussed in the previous section. Thus, more realistic models must take into account the temporal evolution of protoplanetary disks. A popular idea to explain the observed disk lifetimes is to consider the radial accretion of the disk material onto the newly formed central star. Radial accretion can be regarded as an extension to the picture of a static disk, which does not allow for radial transport.

Allowing for accretion, protoplanetary disk theory can borrow concepts from general astrophysical accretion disk theory, with its main ideas originating in the pioneering work of Shakura & Sunyaev (1973). The key concept behind this theory is to have a disk that is somehow turbulent. The turbulence then drives the redistribution of mass and angular momentum within the disk, a concept which is known as *α-disk theory.*

The physical idea behind this is that two neighboring sheets of gas will interact due to the mixing effects of turbulence. The bi-directional exchange of matter (in radial direction) between two neighboring sheets in a differentially rotating disk will accelerate the outer sheet and decelerate the inner sheet, a process that transports angular momentum outwards. At the same time, due to angular momentum conservation, matter must be transported inwards.

Even though the exact origin or even the existence of such turbulence is still a topic of current research (see section 3.5 for a discussion), the turbulent α-disk model developed by Shakura & Sunyaev (1973) has been incredibly successful in advancing protoplanetary disk theory beyond the static model.

In their seminal work, Shakura & Sunyaev (1973) made the physically reasonable assumption that, whatever the source of the underlying turbulence is, the r-ϕ-component of the stress tensor $\sigma_{r,\phi}$ is proportional to the local gas pressure p with a dimensionless proportionality constant denoted α^1 such that $\sigma_{r,\phi} \sim -\alpha p$.

Using Eq. 3.3 and Eq. 3.9, the above expression can be rewritten to read $\sigma_{r,\phi} = -\alpha \rho_g c_s h_g \Omega$. And since in quasi Keplerian rotation the relation $r\partial\Omega/\partial r = -3/2\Omega$ holds, the stress can be written as

$$\sigma_{r,\phi} = \rho_g \nu r \frac{\partial \Omega}{\partial r} \tag{3.16}$$

where a factor 2/3 has been absorbed by the α-parameter, and we have defined an *effective viscosity* ν^2 called the *turbulent viscosity* as

$$\nu \equiv \alpha c_s h_g \tag{3.17}$$

The quantity ν is called the effective viscosity (sometimes also *turbulent viscosity*) because Eq. 3.16 is identical to the r-ϕ-component of the *viscous stress tensor* in cylindrical coordinates. Thus, the main takeaway from α-disk theory is that it predicts the turbulent gas in a protoplanetary disk to behave like a viscous fluid with viscosity parametrized by a dimensionless α

---

[1] Note that the symbol "α" is also used in this thesis to denote the spectral index (see Sec. 2.2.2). However, the corresponding meaning should be evident from the context.

[2] The symbol "ν" is also used in this thesis to denote the frequency (see Sec. 2.2.1). However, the corresponding meaning should be evident from the context.

parameter. In the following section, we will discuss how such a viscous disk evolves.

3.3 Viscous Disk Evolution

The classical mathematical framework that describes the evolution of a viscous accretion disk was first derived by Lynden-Bell & Pringle (1974). In this framework, the viscous stress tensor σ_{ij} is added to Eq. 3.2, such that the new momentum equation reads (e.g. Balbus & Papaloizou, 1999)

$$\frac{\partial}{\partial t}(\rho_g u_i) + \frac{\partial}{\partial x_j}\big(\rho_g u_i u_j - \sigma_{ij}\big) + \frac{\partial}{\partial x_i}p = \rho_g g_i \tag{3.18}$$

In Cartesian coordinates, the full viscous stress tensor reads (e.g. Shu, 1992)

$$\sigma_{ij} = \rho_g \nu \left(\frac{\partial u_i}{\partial x_j} + \frac{\partial u_j}{\partial x_i} - \frac{2}{3}\delta_{ij} \nabla \cdot \mathbf{u} \right) \tag{3.19}$$

where δ_{ij} is the Kronecker delta. The $\partial u_i / \partial x_j$ term of the viscous stress tensor is called *shear tensor* and acts upon velocity gradients.

In an axisymmetric disk, and assuming the orbital velocity is constant in the vertical direction (which is a valid approximation close to the disk midplane), the only non-zero components of the viscous stress tensor in Eq. 3.19 are the r-ϕ and ϕ-r-components which arise due to the velocity shear of the differential rotation in the radial direction of the disk. In cylindrical coordinates, these components indeed take the form of Eq. 3.16, as expected (e.g. Stoll et al., 2017).

It is now advantageous to transform Eq. 3.18 to cylindrical coordinates. The ϕ-component then takes the following form (assuming axisymmetry and vertical hydrostatic equilibrium):

$$\frac{\partial}{\partial t}(\rho u_\phi) + \frac{1}{r}\frac{\partial}{\partial r}\left(r \rho_g u_r u_\phi - \rho_g \nu r \frac{\partial \Omega}{\partial r} \right) = -\rho_g \frac{u_r u_\phi}{r} \tag{3.20}$$

Note, the pressure gradient and gravitational acceleration vanish from the ϕ-momentum equation, but a new geometrical source term appears on the r.h.s due to the transformation to cylindrical coordinates.

When rewriting Eq. 3.20 in terms of angular momentum $\rho_g \Omega r^2$ instead of linear momentum, the geometric source term disappears. We also integrate the entire equation along the z-axis to replace the volume density ρ_g with the surface density Σ_g to find the equation that describes the viscous transport of angular momentum per unit surface area:

$$\frac{\partial}{\partial t}(\Sigma_g r^2 \Omega) + \frac{1}{r}\frac{\partial}{\partial r}\left(\Sigma_g r^3 \Omega u_r - \Sigma_g \nu r^3 \frac{\partial \Omega}{\partial r} \right) = 0 \tag{3.21}$$

The above equation has the form of a conservation law in cylindrical coordinates, indicating that angular momentum $\Sigma_g r^2 \Omega$ in a viscous disk is globally conserved. We now recognize the r-ϕ-component from Eq. 3.16 in the transport term inside the brackets of Eq. 3.21, indicating that this term is indeed responsible for angular momentum transport in the radial direction.

Importantly, in contrast to the static equilibrium solution discussed in Sec. 3.1, a viscous disk, and specifically Eq. 3.21, allow for a stationary solution with non-vanishing radial velocity $u_r \neq 0$, i.e., an accreting disk solution as intended.

3.3.1 Stationary Viscous Disk Solution

We are now interested in stationary solutions to Eq. 3.21. Assuming quasi-Keplerian rotation, the radial profile of the orbital angular velocity Ω is known:

$$\Omega \approx \sqrt{\frac{GM_*}{r^3}} \tag{3.22}$$

Solving for a stationary solution in which the time derivative in Eq. 3.21 vanishes, we find the radial velocity as

$$u_r = -\frac{3}{\Sigma_g r^{1/2}} \frac{\partial}{\partial r}\left(\nu \Sigma_g r^{1/2}\right) \tag{3.23}$$

and the corresponding *mass accretion rate* $\dot{M} \equiv -2\pi r \Sigma_g u_r$ as

$$\dot{M} = 6\pi r^{1/2} \frac{\partial}{\partial r}\left(\nu \Sigma_g r^{1/2}\right). \tag{3.24}$$

Requiring the mass accretion rate to be constant in space and time ($\dot{M}$=constant), it follows from Eq. 3.24 that $\nu\Sigma_g$=constant must hold. Plugging this into Eq. 3.23, the radial velocity of the gas follows:

$$u_r = -\frac{3}{2}\frac{\nu}{r} \tag{3.25}$$

From Eq. 3.24, it also follows that the stationary mass accretion rate

$$\dot{M} = 3\pi \Sigma_g \nu \tag{3.26}$$

is directly proportional to the viscosity ν and is thus ultimately parametrized by the Shakura and Sunyaev α-parameter via Eq. 3.17. Note that in the stationary case, the radial flux of angular momentum is also constant.

Using typical numbers (r = 1 au, T = 300 K, $M_* = M_\odot$, $\alpha = 10^{-2}$), Eq. 3.25 predicts a radial gas velocity of $u_r = -54\,\mathrm{cm/s}$. This is much smaller than the local Keplerian velocity ($u_K = 2.97 \times 10^6\,\mathrm{cm/s}$) or the sound speed ($c_s = 1.04 \times 10^5\,\mathrm{cm/s}$).

Similarly, using a typical value for the gas surface density ($\Sigma_g = 10^3\,\mathrm{g/cm^3}$), a typical value of the gas accretion rate is $\dot{M} = 8 \times 10^{-8}\, M_\odot yr^{-1}$. Typically, protoplanetary disks have accretion rates ranging from 10^{-9} to $10^{-7}\, M_\odot yr^{-1}$ (Alexander et al., 2014).

3.3.2 Surface Density Evolution

A more realistic protoplanetary disk is neither static nor stationary, and its accretion rate will vary. We thus drop the stationary assumption and use the vertically integrated continuity equation in cylindrical coordinates

$$\frac{\partial \Sigma_g}{\partial t} + \frac{1}{r}\frac{\partial}{\partial r}\left(r\Sigma_g u_r\right) = 0 \tag{3.27}$$

to rewrite Eq. 3.21 and obtain a generalized mass accretion formula for viscous disks (Lynden-Bell & Pringle, 1974; Balbus & Papaloizou, 1999):

$$r\Sigma_g u_r = -3r^{1/2}\frac{\partial}{\partial r}(\nu\Sigma_g r^2 \Omega) \tag{3.28}$$

We then plug Eq. 3.28 back into Eq. 3.27 yielding the dynamical equation describing the viscous evolution of the surface density (Lynden-Bell & Pringle, 1974)

$$\frac{\partial \Sigma_g}{\partial t} = \frac{3}{r}\frac{\partial}{\partial r}\left(r^{1/2}\frac{\partial}{\partial r}(\nu r^{1/2}\Sigma_g)\right) \tag{3.29}$$

The above equation is formally a diffusion equation for the surface density Σ_g in which the strength of the diffusion is regulated by the viscosity ν. Eq. 3.29 predicts a viscously spreading disk in which mass is transported inward and angular momentum is transported outward.
For Eq. 3.29 to be applicable, the functional form of the viscosity ν must be defined. Assuming $\nu(r)\propto r^{\gamma}$, there exists an explicit self-similar solution to Eq. 3.29 (Lynden-Bell & Pringle, 1974)

$$\Sigma_g(\tilde{r},\theta) = \frac{C}{3\pi\nu_1\tilde{r}^{\gamma}}\theta^{-(5/2-\gamma)/(2-\gamma)}\exp\left(-\frac{\tilde{r}^{2-\gamma}}{\theta}\right) \tag{3.30}$$

where $\tilde{r} \equiv r/r1$, $\nu_1 \equiv \nu(r_1)$, $\theta \equiv t/t_s + 1$ and $t_s \equiv r_1^2/(3(2-\gamma)^2\nu_1)$. Figure 3.1 shows the solution in Eq. 3.30 for $\theta = 1, 2, 4, 8$. The solution describes a disk with decreasing surface density in the inner disk due to accretion. At the same time, the radial extent of the disk increases due to viscous spreading.

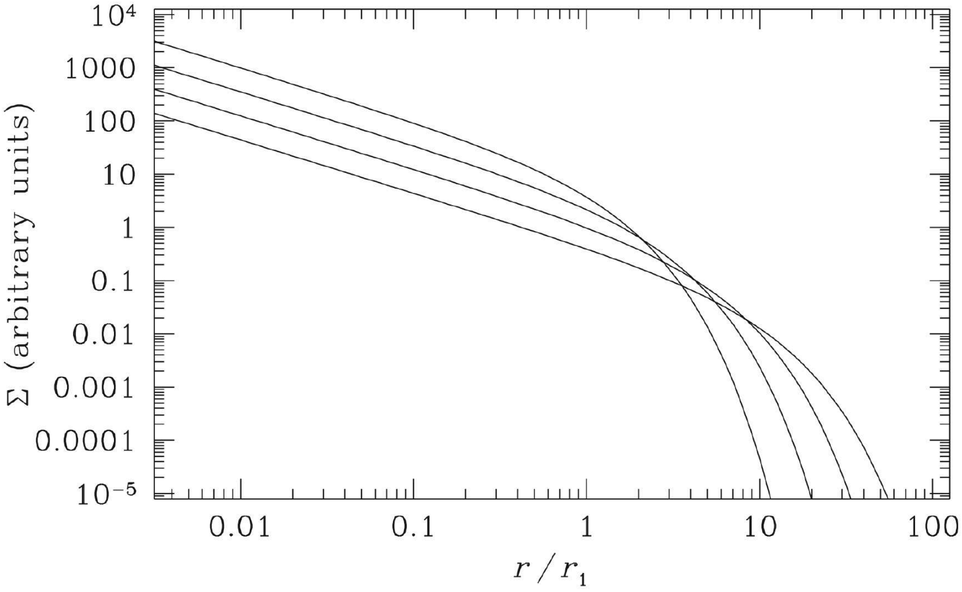

Figure 3.1: Self similar solution to the surface density evolution equation (Eq. 3.29). The initial surface density follows a disk profile $\Sigma_g \propto r^{-1}$ at small radii before cutting off exponentially beyond $r = r_1$. Plotted are the curves described by Eq. 3.30 at times $\theta = 1, 2, 4, 8$. image credit: Armitage (2010).

3.4 Temperature Structure

In this section, we briefly summarize a simple description of the equilibrium temperature structure of a protoplanetary disk. In thermal equilibrium, the disk temperature is set by a balance of cooling and heating processes and determines the vertical hydrostatic density structure that was discussed in Sec. 3.1. There are two main sources of heating in a protoplanetary disk: Irradiation by the central star and accretion heat. In the absence of heat sources, a disk would cool down to the equilibrium temperature of the surrounding interstellar space, which can be as low as 10 K (Schnee et al., 2009).

In this section, we will mainly discuss the temperature of the gas but note that gas opacities in protoplanetary disks are almost entirely dominated by lines that cover only a small fraction of the spectrum. Dust opacities on the other hand cover the entire spectrum and therefore trap radiation much more effectively. Thus, the thermal energy balance is mostly governed by the dust. In principle, gas and dust temperature can decouple, but in this section, we will assume that collisions are frequent enough for heat to be efficiently exchanged between dust and gas such that the gas quickly adjust itself to the dust temperature. Using this assumption, we can limit ourselves to calculating the dust temperature and simply set the gas temperature equal to the dust temperature. This is generally a good approximation for dense regions of protoplanetary disks. In regions where this approximation breaks down, complex radiative transfer models must be used to calculate the gas and dust temperatures individually (see e.g. Woitke et al., 2009), however, this is beyond the scope of this introductory section.

We first consider the process of disk heating by irradiation from the central star. At the relatively short wavelengths where stars emit most of their energy, protoplanetary disks are very optically thick and stellar photons are absorbed in the surface layers. Thus, a volume element in the disk can only be penetrated by stellar photons if it has a clear line of sight to the star. Based on a geometrical argument, it is clear that a disk must be *flared* for its entire surface to have a direct line of sight to the star. A flared disk is a disk for which the surface height increases faster with radius than linear. In other words, h_s/r must be an increasing function of radius, where h_s is the height of the absorbing surface. If at radius r the angle between the disk surface and the path of incoming stellar photons is ϕ, the flux onto the disk surface is approximately

$$F_{\rm irr} \approx \phi \frac{L_*}{4\pi r^2} \tag{3.31}$$

where L_* is the luminosity of the star. The above equation holds because the flaring angle ϕ is generally small $\phi \simeq 0.05$ (Chiang & Goldreich, 1997).

The rate of heating by stellar irradiation is then

$$Q_+^{\rm irr} = \phi \frac{L_*}{2\pi r^2} \tag{3.32}$$

where the factor two comes from the two sides of the disk.

Assuming the rate of cooling is given by blackbody radiation,

$$Q_- = 2\sigma_{\rm SB} T_{\rm disk}^4 \tag{3.33}$$

where $\sigma_{\rm SB}$ is the Stefan-Boltzmann constant, and exactly balances stellar heating, the disk temperature profile becomes

$$T_{\rm disk}^{\rm irr} = \left(\frac{\phi L_*}{4\pi \sigma_{\rm SB}} \right)^{1/4} r^{-1/2} \tag{3.34}$$

assuming the flaring index ϕ is constant.

Via Eq. 3.4., Eq. 3.34 also predicts the radial profile of the sound speed $c_s \propto r^{-1/4}$, and via Eq. 3.9 also the radial profile of the gas scale height $h_g \propto r^{5/4}$ (assuming the disk temperature is vertically constant).

In addition to stellar radiation, friction in the form of viscosity can also lead to the production of heat. In a viscous disk, the total heating rate per unit area is (e.g. Bitsch et al., 2013)

$$Q_{+}^{\text{visc}} = \frac{9}{4}\Sigma_g \nu \Omega_K^2 \tag{3.35}$$

We can rewrite this in terms of the accretion rate

$$Q_{+}^{\text{visc}} = \frac{3}{4\pi}\dot{M}\Omega_K^2 \tag{3.36}$$

This shows that the amount of heat released is proportional to the amount of matter that is accreted. Assuming the disk radiates away all the viscous heat via its surface, the heating in Eq. 3.36 must be balanced by cooling in Eq. 3.33. This gives

$$T_{\text{disk}}^{\text{visc}} = \left(\frac{3}{8\pi\sigma_{\text{SB}}}\dot{M}\Omega_K^2\right)^{1/4} \tag{3.37}$$

In a stationary disk, this profile is with $T \propto r^{-3/4}$ steeper compared to the temperature due to irradiation (Eq. 3.34). Combining the two sources of heating, as $Q_{-} = Q_{+}^{\text{irr}} + Q_{+}^{\text{visc}}$, gives the temperature profile of stationary and irradiated viscous disks:

$$T_{\text{disk}} = \left(\frac{3}{8\pi\sigma_{\text{SB}}}\dot{M}\Omega_K^2 + \frac{\phi L_*}{4\pi\sigma_{\text{SB}} r^2}\right)^{1/4} \tag{3.38}$$

Since for viscous heating, the disk temperature drops more steeply than for irradiation, the disk temperature is dominated by viscous heating at small radii, and by irradiation at large radii.

3.5 Protoplanetary Disk Turbulence

The Shakura and Sunayev α-description provides a useful parametrization for protoplanetary disk viscosity but leaves questions regarding the strength and origin of the underlying turbulence unanswered.

The strength of disk turbulence can be constrained observationally mainly by three distinct methods. The most direct approach is measuring the turbulent broadening of molecular emission lines. Using this method, it was possible for Flaherty et al. (2015, 2017, 2018) and Teague et al. (2016, 2018b) to constrain the strength of turbulence to $\alpha \lesssim 10^{-4} - 10^{-3}$ in the outer regions of the disks of TW Hya, HD 163296, MWC 480 and V4046 Sgr. Only in DM Tau, significantly higher levels of $\alpha \approx 10^{-1}$ were observed (Flaherty et al., 2020).

The second approach to constrain the strength of turbulence is via its effect on the diffusion of dust grains. Measuring the vertical extent of the particle layer in continuum observations, Pinte et al. (2016) found $\alpha \approx 3 \cdot 10^{-4}$ in HL Tau. Focusing instead on diffusion in radial direction in a number of sources, Dullemond et al. (2018) found $\alpha < 5 \cdot 10^{-4}$.

Besides observing turbulent line broadening and grain diffusion, the third approach is to measure disk spreading as a function of disk age as predicted by the viscous disk evolution (see Sec. 3.3). Observing CO emissions in Lupus, Trapman et al. (2020) estimate $\alpha \sim 10^{-4} - 10^{-3}$. Explicit results based on dust continuum disk sizes also exist in the literature, but Rosotti et al. (2019) point out that current dust continuum observations are not sensitive enough to detect viscous disk spreading. They state that the outer disk radius in such studies is influenced by opacity rather than the actual physical disk size.

Altogether, Lesur et al. (2022) interpret the existing measurements of the strength of disk turbulence as being consistent with $\alpha \sim 10^{-4}$. However, they also point out that a certain level of caution is warranted when interpreting the above results. For example, it is inaccurate to strictly equate the values of α measured from turbulence broadening and dust diffusion, to the value of α inferred from angular momentum transport as done in classical alpha disk theory (see Sec. 3.2). The two former methods both assume the turbulent alpha parameter to be proportional to the turbulent velocity dispersion squared $\alpha \propto \delta u^2$. However, classical alpha disk theory defines α as a measure of the efficiency of angular momentum transport and thus should be proportional to the correlation of radial and azimuthal turbulent velocities $\alpha \propto \delta u_r \delta u_\phi$ (e.g. Balbus & Hawley, 1998). Thus, the two definitions are only consistent if the turbulent velocity dispersion squared is equal to the turbulent r-ϕ-velocity correlation, which is not necessarily the case[3]. In principle, a disk can be highly turbulent (i.e., have large δu^2), while either transporting angular momentum outward ($\alpha > 0$), inward ($\alpha < 0$), or not at all ($\alpha = 0$). See, e.g., Lesur et al. (2022) for a more detailed discussion.

More generally, it is worth noting at this point that a viscous theory with a traceless stress tensor, in the form of Eq. 3.19, does not model a turbulent velocity dispersion and only models the off-diagonal velocity correlations of the Reynolds stress responsible for angular momentum transport as a function of the local velocity shear. As a result, depending on the characteristics of the underlying turbulence, a local viscous theory, as discussed in Sec. 3.3, might not be appropriate to describe the turbulent stresses present in a disk (Balbus & Papaloizou, 1999). In Chapter 5, we will continue this discussion and also derive a turbulence model that describes the on-diagonal components of the Reynolds stress.

Further complications arise with the assessment of the strength of disk turbulence when compared to detailed hydrodynamic disk models. Such models do not seem to be consistent with the assumption of a globally constant α-parameter. Most recent models predict the strength of turbulence to change across different vertical layers of a disk (see e.g. the review by Lesur et al., 2022) and potentially vary in radial direction too (e.g. Kretke & Lin, 2007). Depending on the nature of the underlying turbulence, the viscous stress might also be highly anisotropic (Stoll et al., 2017). Hence, these findings point to the conclusion that a single α value is not sufficient to fully describe disk turbulence.

Despite the α-model clearly having limitations, it retains its popularity because it is effective without specifying the nature of the underlying turbulence. This is especially important because possible origins and properties of physical mechanisms leading to disk turbulence are still a topic of current research.

Supported by the increasing computational capabilities, a growing subfield within the protoplanetary disk community is concerned with the nature and origin of disk turbulence. In the remainder of this section, we will summarize a few of the most probable candidates believed to be responsible for disk turbulence.

Several (magneto) hydrodynamical instabilities exist in protoplanetary disks, which can be potential sources of turbulence. A general distinction is made between turbulence of magnetohydrodynamic origin and purely hydrodynamic turbulence. The poster child of the former is the *magnetorotational instability* (MRI) (Balbus & Hawley, 1991) which can become active if partly ionized gas, that is in (quasi) Keplerian rotation, couples to a magnetic field. However, more recent studies show that in large portions of a typical protoplanetary disk, non-ideal MHD effects heavily suppress the MRI (e.g. Bai & Stone, 2013; Lesur et al., 2022). Popular alternatives are purely hydrodynamic instabilities like the *vertical shear instability* (VSI) (Arlt & Urpin, 2004; Nelson et al., 2013), the *convective overstability* (Klahr & Hubbard, 2014; Lyra, 2014) and the *zombie vortex instability* (Barranco & Marcus, 2005; Lesur & Latter, 2016). Which of these mechanisms operate depends on the detailed disk structure.

Interestingly, Barraza-Alfaro et al. (2021) recently argued that a small value of α, as measured by turbulent line broadening, does not necessarily exclude strong turbulence generated by the VSI. Because the molecular emission region of ^{12}CO is relatively thin (Paneque-Carreño et al., 2023),

---

[3] To account for the inconsistency in the definition of α, we will define a parameter δ in Sec. 5.2.2 to parametrize the turbulent velocity dispersion δu^2 and use α strictly to parametrize the effectiveness of turbulent transport as introduced in Sec. 3.2.

observed line broadening is only sensitive to velocity fluctuations on physical scales smaller than the emission layer. Therefore, the large-scale vertical motions caused by the VSI are not detected. In the study of Barraza-Alfaro et al. (2021), the amplitudes of the large-scale motions are about one order of magnitude larger than what is predicted by measurements of line broadening. Lastly, we also want to mention that assuming turbulence is the only mechanism transporting angular momentum, measured values of α (both observationally and in hydrodynamic simulations), are not necessarily consistent with the observed mass accretion rates of YSOs (Mulders et al., 2017; Rafikov, 2017). The values of α predicted for hydrodynamic turbulence are generally too small and consequently not enough angular momentum is transported for turbulent viscosity to be the sole explanation of the observed mass accretion rates in YSOs (Lesur et al., 2022). It is thus suggested that other mechanisms (e.g., disk winds) also contribute to the angular momentum transport in addition to turbulence.

Another argument against the pure viscous disk evolution comes from the observed disk dispersal time. The viscous disk evolution model predicts protoplanetary disks to indefinitely expand and become progressively fainter (Armitage, 2010). However, observations hint at a relatively short dispersal time of only $\sim 10\,\%$ of the total disk lifetime (Andrews, 2020).

Finally, we want to reiterate the cautionary remark by Lesur et al. (2022) who highlight that the viscous disk model should not be regarded as a replacement for the direct numerical modeling of hydrodynamic turbulence and that real protoplanetary disks are essentially inviscid. It is only due to computational limitations that there is currently no better alternative to the viscous disk model for large-scale, long-term global simulations of protoplanetary disks. All the caveats presented in this section must be kept in mind if one is discussing protoplanetary disks within the framework of α disk theory and viscous disk evolution.

Building upon the contents of this chapter, we will focus on the formation of planets from disk material in the next chapter.

Chapter 4

Planet Formation Theory

4.1 Introduction

Planets are made from protoplanetary disk material, and therefore, a newly formed disk with all its physical and chemical properties, as discussed in Chapter 3, can be regarded as the initial condition for planet formation. The understanding of planet formation has improved dramatically in recent years and has evolved significantly from classical theories (e.g. Safronov, 1972; Goldreich & Ward, 1973), also owing to insights gained from observations (see e.g. the review by Drążkowska et al., 2022). As a result, current planet formation theory has become extremely complex and, at the same time, is closely interlinked with the similarly complex protoplanetary disk theory (discussed in Chapter 3). Therefore, in this chapter, we refrain from providing a comprehensive discussion of the problem and only provide a summary of the key aspects of planet formation. Wherever possible, we refer to the literature for a more detailed discussion.

In this chapter, we start by providing the theoretical foundations that describe the dynamics of dust particles in a gaseous environment, in Sec. 4.2. In the subsequent section, we then provide an overview of the evolution of solids from dust to fully formed planets. Because this growth process covers size scales across twelve orders of magnitude, it is conceptually useful to divide it into three main stages: Firstly, in Sec. 4.3 we summarize how dust grains grow to *planetesimals*, which are bodies that are massive enough to be gravitationally bound and are between 100 m and $\sim$ 100 km in size (Armitage, 2010). In Sec. 4.4, we then describe the formation of terrestrial planets from planetesimals, and in Sec. 4.5, we discuss the formation of giant planets. We also want to highlight the caveat that the theory presented in this chapter is not yet complete and that the study of planet formation is an active field of research.

4.2 Dust Dynamics

The dust component in protoplanetary disks is particularly relevant for planet formation because it is the micron-sized grains, inherited from the ISM, that all rocky bodies in planetary systems grow from. Moreover, dust grains provide the bulk of the opacity, which is relevant for astronomical observations (Armitage, 2010), and they host chemical surface reactions that can be important, for example, for the formation of complex molecules (Henning & Semenov, 2013).

Ignoring gravity, dust dynamics is dominated by aerodynamic drag, by which it is coupled to the motion of the gas. This is in contrast to the dynamics of the gas, which is dominated by pressure forces. The degree of aerodynamic coupling between dust and gas in protoplanetary disks is characterized by the *stopping time* t_s, which is the characteristic time in which relative velocities between dust and gas decay due to drag. Assuming spherical dust grains of size a and constant solid density $\rho_\bullet$, the stopping time t_s can be expressed as (Whipple, 1972;

Weidenschilling, 1977a)

$$t_s = \sqrt{\frac{\pi}{8}}\frac{a\rho_\bullet}{c_s\rho_g} \tag{4.1}$$

The strength of the dust-gas coupling increases as the stopping time decreases. Thus, Eq. 4.1 indicates that small dust grains are more tightly coupled than large grains and that the coupling is stronger in a high-gas-density environment compared to a low-density environment. In the theoretical limit where $t_s \rightarrow 0$, dust grains are perfectly coupled to the gas and their motion is identical to that of the gas. Strictly speaking, Eq. 4.1 is only valid as long as dust grains are smaller than the mean free path of individual gas molecules. This is generally the case for dust grains in typical protoplanetary disk environments.

In the protoplanetary disk community, it is customary to define a dimensionless *Stokes number* as the stopping time normalized by the Keplerian angular frequency:

$$St = t_s\Omega_K \tag{4.2}$$

The force per unit volume exerted by aerodynamic drag acting on dust is proportional to the relative velocity between dust and gas $(v_i - u_i)$:

$$f_i^{\mathrm{drag}} = -\frac{\rho_d}{t_s}(v_i - u_i) \tag{4.3}$$

Naturally, the gas experiences an equal force in the opposite direction, the so-called *back reaction.* However, as long as the local dust density ρ_d is small compared to the local gas density ρ_g, the back reaction can in most cases be neglected. However, the local dust density ρ_d can increase with respect to the gas density ρ_g if specific transport mechanisms lead to the local accumulation of dust. We will discuss dust transport mechanisms in the following sections.

4.2.1 Radial Drift

Dust grains do not experience the same pressure force as the gas which has important consequences for their radial transport in a protoplanetary disk (Weidenschilling, 1977a; Nakagawa et al., 1986). In Sec. 3.1 we discussed that due to the radial pressure support, the orbital velocity of the gas is slightly sub-Keplerian. Dust, on the other hand, does not have that pressure support and, in an unperturbed state, does orbit with Keplerian velocity. The resulting difference in azimuthal velocity $(v_\phi - u_\phi)$ results in an exchange of angular momentum between the dust and the gas via the drag force (Eq. 4.3), transporting dust grains in the radial direction. This phenomenon is called *radial drift.* Effects of radial drift can most easily be quantified by rewriting Eq. 3.14 to read

$$u_\phi = v_K(1-\eta)^{1/2} \tag{4.4}$$

where v_K is the Keplerian orbital velocity, and we have defined $\eta = -(r\Omega_K^2\rho_g)^{-1}\partial p/\partial r$ to parametrize the deviation of the gas orbital velocity u_ϕ from Keplerian orbital velocity v_K. The radial velocity of the dust can then be expressed as (see e.g. Takeuchi & Lin, 2002, for a detailed derivation)

$$v_r = \frac{u_r - \eta St v_K}{1 + St^2} \tag{4.5}$$

which for small dust grains $(St \ll 1)$ simplifies to

$$v_r \approx u_r - \eta St v_K \tag{4.6}$$

In smooth protoplanetary disks, the η-parameter is generally positive leading to a radially inward-directed contribution by the second term on the r.h.s. of Eq. 4.6. Also note that this contribution to the radial dust velocity is proportional to the Stokes number, thus, different size dust grains drift at different speeds.

From Eq. 4.5, it follows that radial drift is most efficient for $St = 1$, which is typically the case for mm to cm size pebbles at $r \sim 10 - 100$ au (Takeuchi & Lin, 2002). Depending on the disk properties, the timescale of radial drift can be very short, on the order of 10s of local orbital periods. This fast radial drift poses a fundamental constraint on planet formation theories because growth must occur on timescales faster than particles are lost to the central star via radial drift (Takeuchi & Lin, 2005).

A solution to this problem is relaxing the smooth disk condition. In smooth disks, the gas pressure typically decreases with increasing radius, resulting in sub-Keplerian orbits and inward dust particle drift. In a structured disk, local gas pressure maxima can be present. Such a local pressure maximum has radially increasing pressure on one side, leading to super-Keplerian rotation of the gas in a certain disk region, causing radial outward drift of the dust (Whipple, 1972). As a result, dust particles can accumulate at the location of a gas pressure maximum where drift velocities converge. Besides disarming the radial drift problem, the presence of gas pressure maxima can also explain the substructures observed in mm- continuum observations. But of course, the formation of gas pressure maxima must then be explained too. We will do this in Sec. 4.6.

4.2.2 Vertical Settling

Aerodynamic drag is also important for understanding the vertical dust distribution. We first ignore the effects of potential turbulence (we will discuss this in Chapter 5) and consider the vertical settling of dust grains in a laminar disk. Dust particles suspended in the gaseous environment above the disk midplane experience a vertical gravitational acceleration of the form of Eq. 3.6 and get accelerated towards the midplane. If the aerodynamic coupling is strong, the gravitational force is quickly balanced by the counteracting drag as the particles settle toward the midplane. From an exact balance between the gravity (Eq. 3.6) and drag (Eq. 4.3), and rearranging terms, the vertical dust settling velocity is found (Dubrulle et al., 1995)

$$v_{\mathrm{sett}} = -t_s \Omega_K^2 z \tag{4.7}$$

which is the characteristic velocity of dust grains that settle towards the disk midplane. Like the radial drift velocity, the vertical settling velocity also depends on the size of the dust grains via the stopping time t_s. Furthermore, it is important to note that Eq. 4.7 is only valid if the time it takes a dust particle to reach terminal velocity is small compared to the total time it takes to settle towards the midplane. This is strictly true only for small particles ($St \ll 1$) and is otherwise referred to as the *terminal velocity approximation.*

The combined prediction based on the discussion on radial drift and vertical settling is that smooth disks should exhibit negative particle density gradients both in the radial and vertical direction, such that the largest concentrations are found closest to the central star (Andrews, 2020). However, this picture is not supported by observations. In section 4.6, we discuss appropriate extensions to these fundamental parts of the theory.

Usually at this point, the vertical dust equilibrium distribution is discussed. However, we will postpone this discussion to Chapter 5 where we will establish a more detailed theoretical foundation for doing the discussion justice.

4.3 Dust Growth and Planetesimal Formation

So far in this chapter, we have discussed how dust grains interact with the surrounding gas. But of course, dust grains can also interact with each other, especially when individual particles move relative to each other and collide. In protoplanetary disks, relative velocities and thus collisions are driven by vertical and radial transport, differential coupling to turbulent eddies in the gas, and *Brownian motion* (random motion caused by the thermal motion of the gas). Consequent collision rates can be calculated using the closed-form expressions for the relative velocities of particles, derived by Ormel & Cuzzi (2007). In contrast to dispersed molecular clouds, only in protoplanetary disks is the particle concentration large enough for collisions to become evolutionary relevant. When colliding, small dust grains stick together because of their large surface-to-mass ratio and intermolecular binding forces (e.g., van der Waals forces, hydrogen bonds), forming larger aggregates (Güttler et al., 2010).

The growth from sub-μm sized particles, originally delivered from the ISM to a newly formed protoplanetary disk, to larger aggregates is the first stage of planet formation. Particle-particle collisions and the effective sticking of small dust aggregates lead to fast growth to centimeter size within less than 1000 years in the inner regions of protoplanetary disks (Birnstiel et al., 2011). Early models of planet formation predicted km-sized planetesimals to grow from successive particle-particle sticking collisions (Weidenschilling, 1997). However, these models do not capture the full picture. As particles approach $St = 1$, they quickly drift inward and are lost to the star before they can grow significantly beyond centimeters in size. This phenomenon is called the *drift barrier*. In addition to that, growing dust grains eventually aerodynamically decouple from the gas, which increases their relative velocities, ultimately leading to disruptive collisions and preventing growth beyond a certain size. This growth limit is called the *fragmentation barrier*. In standard protoplanetary disk models, the fragmentation barrier limits the dust grain size to about $\sim 0.1 - 10$ cm (Birnstiel et al., 2012; Blum et al., 2017). In general, growth barriers pose a large obstacle to the formation of gravitationally bound planetesimals solely via sticking collisions.

In classical planet formation theories, a theoretical solution to the growth problem exists. It was proposed that when dust particles efficiently sediment towards the protoplanetary disk midplane, their concentration becomes large enough to become gravitationally unstable, leading to the fragmentation of the disk into gravitationally bound planetesimals (Safronov, 1972; Goldreich & Ward, 1973). However, Weidenschilling (1980) showed the development of the Kelvin-Helmholtz instability introduces self-excited turbulence that prevents the dust layer from sedimenting effectively enough for self-gravity to set in.

A modern alternative is potentially found in the formation of planetesimal via the *streaming instability* (Youdin & Goodman, 2005), which can produce gravitationally bound dust clumps as a result of the complex interaction between gas and dust flows (Johansen et al., 2007). It is found that the streaming instability leads to planetesimals of ~ 100 km in size (Schäfer et al., 2017). However, the streaming instability is not a one-size-fits-all solution as it sensitively depends on local disk parameters and the local dust size distribution. Thus, a comprehensive theory of planetesimal formation remains elusive and is subject to current research. Yet, the existence of numerous minor bodies in the Solar System, e.g., in the Asteroid- and Kuiper Belt, suggests planetesimal formation to be a robust concept even though its details are not yet clear.

4.4 Terrestrial Planet Formation

Once planetesimals have formed, the classical models predict their evolution to be mainly governed by their mutual gravitational interaction, such that their evolution reduces to a “simple” N-body problem that produces planets as a result of planetesimal collisions. The gas, that is still present in the disk at this time, acts to dampen the eccentricity and inclination of the planetesimals. This concept is known as *planetesimal accretion* (see, e.g., the review by Lissauer, 1993).

Planetesimal accretion is dominated by gravitational dynamics. Supported by dynamical friction and gravitational focusing, growth initially proceeds fast (*so-called runaway growth*, Safronov, 1972; Wetherill & Stewart, 1989), until the largest planetary embryos are massive enough to dynamically stir the remaining planetesimals. In this regime, the largest bodies grow faster than the smaller planetesimals (so-called *oligarchic growth*, Kokubo & Ida, 1998). But as they grow, the efficiency of planetesimal accretion quickly drops and the formation of massive planetary cores within a disk lifetime is difficult (Ida & Lin, 2004). Within about 1 Myr, planetesimal accretion can produce a few hundred large bodies with masses on the order of $0.01\,M_\oplus$ to $0.1\,M_\oplus$ which are comparable to the mass of the Moon or Mercury but are not yet comparable to the other terrestrial planets Venus, Earth, and Mars (Armitage, 2010).

A second, but not mutually exclusive paradigm is the *pebble accretion* scenario (Johansen & Lambrechts, 2017; Ormel, 2017). While the planetesimal accretion scenario assumes that all the available solids are present in the form of planetesimals, the pebble accretion scenario assumes that most of the solids remain in the form of much smaller pebbles. Because pebbles are still very much aerodynamically coupled to the gas, accretion is governed by gas drag in addition to gravitational interactions, with drag supporting the dissipation of angular momentum as pebbles spiral toward an accreting planetesimal. However, pebble accretion only becomes efficient for planetesimals above ~ 500 km in size (Drążkowska et al., 2022). As mentioned earlier, planetesimals formed by the streaming instability are generally smaller ($\lesssim 100$ km). Thus, planetesimal accretion is needed to overcome this gap (Liu et al., 2019). In the pebble accretion scenario, mass growth is halted when the accreting protoplanet has become massive enough to open an annular gap in the gas distribution of the protoplanetary disk along its orbit. When such a gap has formed, pebble accretion is halted because pebbles are prevented from reaching the protoplanet by an outward-pointing pressure gradient force at the outer edge of the gap. This mass limit is called the *pebble isolation mass* (Lambrechts & Johansen, 2014; Bitsch et al., 2018; Ataiee et al., 2018). Lambrechts & Johansen (2014) predict a pebble isolation mass, where pebble accretion is halted, for a realistic set of parameters, of 25 $M_\oplus$. This limit is much lower than the mass of, e.g., Saturn (95 $M_\oplus$) or Jupiter (318 $M_\oplus$). Additional processes are necessary to grow such giant planets.

4.5 Giant Planet Formation

So far, we have only discussed the formation of solid bodies, i.e., rocky planets and planetary embryos, but not yet the formation of planets with an extended gaseous envelope like the gas giant planets. When massive enough, rocky planetary embryos, which have formed via e.g., pebble accretion, start to accrete gas from their surrounding disk, forming a gaseous planetary envelope. This concept is often called the *core accretion* scenario (Bodenheimer & Pollack, 1986). For low-mass planetary cores, the accreted gaseous envelope is in hydrostatic equilibrium and grows by contraction via cooling and the release of energy into the surrounding disk environment (Stevenson, 1982; Pollack et al., 1996; Rafikov, 2006). At this point, the gas accretion rate increases with the mass of the planetary embryo but is limited by the amount of cooling of the envelope. Once a critical mass is reached $\sim 10\,M_\oplus$ (Pollack et al., 1996), the hydrostatic forces can no longer support the inward pull of gravity and the planet starts to accrete large amounts of gas in a rapid runaway process limited only by the supply of gas by the surrounding disk (Pollack et al., 1996; Ayliffe et al., 2012). Because the cooling time of a gaseous envelope can be comparable to the disk lifetime itself ($\sim 1\,Myr$), it represents an obstacle to the onset of runaway accretion and the formation of giant planets. However, it seems to be consistent with the formation of less massive gaseous planets like Uranus and Neptune (D'Angelo & Lissauer, 2018).

If a planet reaches the runaway growth phase, the phase typically lasts for only $\sim 10^5$ years before it is terminated when the supply of gas is exhausted as a result of the dissipation of the disk itself, or as a consequence of the planet opening an annular gap along its orbital radius (Armitage, 2010). In Fig. 4.1, we show an illustration by Lin et al. (2018) depicting the possible formation pathway of Jupiter via pebble accretion and subsequent core accretion.

Nowadays, the core accretion scenario is considered the main mode of giant planet formation (D'Angelo & Lissauer, 2018). However, it is worth mentioning that besides core accretion, it is theorized that gravitational instability followed by disk fragmentation, akin to the formation of stellar cores within molecular clouds, also leads to self-gravitating newly formed giant planets in protoplanetary disks (Toomre, 1964). Planet formation via this so-called *disk instability* scenario has the benefit that it avoids the need for a long hierarchical growth chain. However, it has been found that the disk instability scenario is expected to favor massive objects such as brown dwarfs or low-mass stellar companions rather than planetary mass objects (Kratter & Lodato, 2016; D'Angelo & Lissauer, 2018). But, the process has not yet been ruled out as a formation route for gas giant planets far away from their host star (D'Angelo & Lissauer, 2018).
Nonetheless, both scenarios of giant planet formation require further development and refinement, guided by the increasing amount of astronomical data.

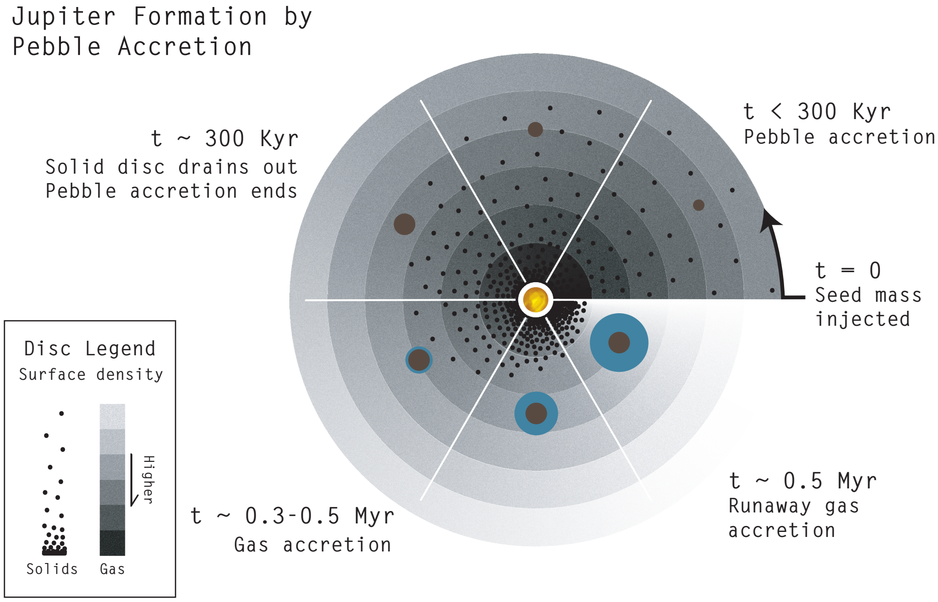

Figure 4.1: Illustrated overview of the gas giant planet formation process via pebble accretion and subsequent runaway gas accretion as a possible formation pathway of Jupiter. The figure is to be read starting from the 3 o'clock position, evolving in a counter-clockwise direction, with each sector representing a different temporal snapshot. In the first panel, a planetesimal (brown), i.e., a gravitationally bound core, has formed, e.g., via the streaming instability, and evolves in a gaseous environment (gray). The planetesimal begins to accrete pebbles (black) as they drift radially inward due to aerodynamic drag, increasing the mass of the accreting body. After $\sim$ 400 kyr, the core starts to accrete a gaseous envelope (blue) which grows by cooling and contracting. Once the envelope mass is roughly comparable to the mass of the core, runaway accretion is triggered, leading to rapid gas accretion and growth to a giant planet. Figure credit: Lin et al. (2018).

4.6 Origins of Disk Substructures

At this point, we have mentioned disk substructures several times. For example, in Chapter 2, we have established that they are regularly observed and in Chapter 3 we have discussed that they are an essential ingredient to resolve the radial drift problem. After having provided a theoretical overview of disk evolution and planet formation, we are now well-equipped to discuss the physical origins of disk substructures, with a special focus on their relation to planet formation.

Since (optically thin) mm-continuum observations trace the dust surface density Σ_d in protoplanetary disks, it is obvious to focus on processes that locally accumulate and/or disperse dust. Promising candidates that have been suggested are condensation fronts, so-called *snowlines*, which are potentially associated with the emergence of substructures in the dust surface density. Snowlines are locations within a disk where potential icy mantles of particles sublimate as particles move across, e.g., as a result of radial drift. Because sublimation causes mass loss in the solids, the dust surface density is depleted just inside the snowline (Stammler et al., 2017). Moreover, gas that has been liberated by sublimation can diffuse outward and re-condense (Stevenson & Lunine, 1988), where it might increase the dust surface density Σ_d just outside the snowline. Thirdly, the presence or absence of ices can affect collision outcomes of particle-particle collisions, changing the particle size distribution which ultimately affects the effective drift speed of the particle population (Pinilla et al., 2017). If particles more easily fragment and thus become smaller after crossing the snowline, their drift speed decreases, leading to a traffic jam-like increase of Σ_d (Birnstiel et al., 2010). However, substructures associated with snowlines are expected to occur at special locations and be axisymmetric. Thus, by themselves, snowlines can not explain the diversity of observed substructures.

Fluid mechanical processes can produce a more diverse set of disk structures. For example, an axisymmetric gas pressure maximum can emerge at the edge of a *dead zone* which is a region where MRI turbulence is suppressed in an otherwise MRI active disk (Regály et al., 2012). Vortices can emerge as a result of hydrodynamic instabilities, attract and concentrate dust particles (Klahr & Bodenheimer, 2006), and also imprint rings and gaps in the dust surface density distribution (Surville et al., 2016).

In sufficiently massive disks, self-gravity can trigger gravitational instability, leading to large-scale spiral patterns (Toomre, 1964; Boss, 1997). The pressure peaks of a spiral can concentrate pebbles and accelerate planetesimal growth (Rice et al., 2004). Other processes are driven by the complex gas-particle coupling and produce substructures via, e.g., a viscous feedback instability (Dullemond & Penzlin, 2018). Overall, there is a wide variety of fluid mechanical processes that can lead to the formation of disk substructures and the local accumulation of solids, ultimately providing the initial conditions for planetesimal formation.

The last and probably most intriguing category of mechanisms to create disk substructure is the tidal interaction with embedded nascent planets. A sufficiently massive planet can generate spiral shocks that transfer angular momentum and repel gas and dust away from its orbit (Lin & Papaloizou, 1979, 1986; Goldreich & Tremaine, 1980; Dipierro et al., 2016). The resulting perturbation clears an annular gap in the gas and dust surface density with a width and depth that depends on the mass of the planet, and the local hydrodynamical structure of the disk (Kley & Nelson, 2012; Crida et al., 2006; Szulágyi, 2017; Zhang & Zhu, 2020; Ziampras et al., 2020). A gas pressure maximum that is created outside this gap can efficiently trap drifting pebbles (Rice et al., 2006; Paardekooper & Mellema, 2006; Zhu et al., 2012). However, except in the case of PDS 70 (Keppler et al., 2018; Isella et al., 2019; Haffert et al., 2019; Christiaens et al., 2019), no substructure has unambiguously been linked to the presence of a planet. The presence of planets can in most cases only be inferred indirectly (e.g. Zhang et al., 2018). Despite a lack of observational confirmation, an explanation by forming planets persists, mainly because planet formation seems to be a very robust process as suggested by the numerous observations of mature exoplanets (see Sec. 2.3).

4.7 Summary

The main takeaway from this chapter is that planet formation is a complicated process and a model that self-consistently explains all aspects of planet formation (dust growth, planetesimal formation, growth of planetary embryos, gas accretion), and convincingly connects dust and gas distributions to fully evolved planetary systems, does not yet exist. The major inconsistency in the present models is likely the lack of a convincing model that bridges the gap between dust and planetesimals (Drążkowska et al., 2022). Fortunately, observations of ubiquitous substructures have somewhat mitigated the problem. Theory predicts that substructure forming processes can halt and/or slow the radial drift of pebbles and thus relax the constraint on the planetesimal formation timescale. Local dust accumulations also provide more favorable conditions for the onset of planetesimal formation, for example, via streaming instability. Currently, significant progress is being made towards a fully self-consistent theory of planet formation, especially thanks to the guidance of increasingly available observational data on protoplanetary disks and mature exoplanets. However, with a few exceptions, direct observational evidence of forming planets is still missing and theorists must rely on indirect evidence.

Chapter 5

Beyond Diffusion: A Generalized Mean-Field Theory of Turbulent Dust Transport in Protoplanetary Disks

The content of this chapter was published in:

Binkert F. (2023), *Beyond diffusion: a generalized mean-field theory of turbulent dust transport in protoplanetary disks, Monthly Notices of the Royal Astronomical Society, Volume 525, Issue 3, November 2023, Pages 4299–4320*

Abstract

Turbulence in protoplanetary disks, when present, plays a critical role in transporting dust particles embedded in the gaseous disk component. When using a field description of dust dynamics, a diffusion approach is traditionally used to model this turbulent dust transport. However, it has been shown that classical turbulent diffusion models are not fully self-consistent. Several shortcomings exist, including the ambiguous nature of the diffused quantity and the nonconservation of angular momentum. Orbital effects are also neglected without an explicit prescription. In response to these inconsistencies, we present a novel Eulerian turbulent dust transport model for isotropic and homogeneous turbulence on the basis of a mean-field theory. Our model is based on density-weighted averaging applied to the pressureless fluid equations and uses appropriate turbulence closures. Our model yields novel dynamic equations for the turbulent dust mass flux and recovers existing turbulent transport models in special limiting cases, thus providing a more general and self-consistent description of turbulent particle transport. Importantly, our model ensures the conservation of global angular and linear momentum unconditionally and implicitly accounts for the effects of orbital dynamics in protoplanetary disks. Furthermore, our model correctly describes the vertical settling-diffusion equilibrium solutions for both small and large particles. Hence, this work presents a generalized Eulerian turbulent dust transport model, establishing a comprehensive framework for more detailed studies of turbulent dust transport in protoplanetary disks.

5.1 Introduction

Protoplanetary disks are believed to exhibit turbulence, driving the redistribution of angular momentum and accretion. Observational constraints on the typical strength of disk turbulence suggest a dimensionless α-parameter (Shakura & Sunyaev, 1973) of 10^{-4}-10^{-3} (Lesur et al., 2022). However, the exact nature and origin of disk turbulence remain unclear. Potential sources include (magneto) hydrodynamic instabilities such as the *magnetorotational instability* (MRI) (Balbus & Hawley, 1991), which can occur if partly ionized gas in quasi-Keplerian rotation couples to a magnetic field. Purely hydrodynamic instabilities include the *vertical shear instability* (VSI) (Arlt & Urpin, 2004; Nelson et al., 2013), the *convective overstability* (Klahr & Hubbard, 2014; Lyra, 2014) and the *zombie vortex instability* (Barranco & Marcus, 2005; Lesur & Latter, 2016). The specific operating mechanism depends on the disk structure.

In addition to driving accretion, turbulence also poses an obstacle to the initial stages of planet formation, specifically dust growth and planetesimal formation. In particular, dust grains within protoplanetary disks are aerodynamically coupled to turbulent gas flows, which influences dust growth (Voelk et al., 1980; Ormel & Cuzzi, 2007; Birnstiel et al., 2010), the dust distribution (Fromang & Papaloizou, 2006), and dust transport (Cuzzi et al., 1993; Youdin & Lithwick, 2007; Carballido et al., 2010; Zhu et al., 2015). Turbulence also prevents dust grains from efficiently clumping together (Umurhan et al., 2020; Chen & Lin, 2020; Gole et al., 2020) to form planetesimals through mechanisms like the *streaming instability* (Johansen et al., 2007) because turbulence acts to diffuse particle concentrations (Goodman & Pindor, 2000; Youdin & Goodman, 2005).

With the Atacama Large Millimeter/submillimeter Array (ALMA) enabling spatially resolved observations of the dust distribution in protoplanetary disks, it has become essential for numerical disk models to incorporate dust physics in addition to gas in order to constrain the physical processes observed in these disks.

While the Navier-Stokes equations effectively describe gas dynamics in such models, no single mathematical tool similarly dominates the description of dust dynamics. Among others, two major approaches to dust modeling in protoplanetary disks are the *Lagrangian* description (Youdin & Johansen, 2007; Charnoz et al., 2011; Yang & Johansen, 2016; Mignone et al., 2019), which describes individual dust particle motion, and the *Eulerian* or *fluid* approach (Johansen & Klahr, 2005; Paardekooper & Mellema, 2006; Meheut et al., 2012; Benítez-Llambay et al., 2019; Huang & Bai, 2022), which describes the collective particle behavior.

Regardless of the approach, solving particle dynamics in protoplanetary disks numerically is especially challenging due to the wide range of spatial and temporal scales involved, particularly in the presence of turbulence. To capture the entire physics of the problem, all relevant length scales must be resolved, which can be computationally demanding and often impossible with current computational capabilities. Further, the detailed nature and origin of turbulence in these disks, if present, is often unknown. Therefore, hydrodynamic dust models are frequently extended with specific phenomenological models that describe the effects of turbulence rather than self-consistently modeling the turbulence itself.

For example, stochastic turbulence models add random fluctuations to the velocities of the gas and dust particles, simulating turbulent mixing and transport. These stochastic models are often used in Lagrangian dust models, allowing accurate modeling of the complex interactions between gas and dust in the presence of turbulence. In contrast, Eulerian turbulence models typically introduce a diffusion term to the dust continuity equation to account for turbulent transport effects (Cuzzi et al., 1993; Goodman & Pindor, 2000; Dullemond & Penzlin, 2018; Weber et al., 2019, and Sec. 5.2.4). However, the classical diffusion approach has a few inconsistencies. Specifically, the approach does not necessarily conserve angular momentum (Tominaga et al., 2019; Weber et al., 2019), and there is no consensus on whether the quantity diffused by turbulence is either the absolute dust density (e.g. Cuzzi et al., 1993) or the dust concentration relative to gas (e.g. Dubrulle et al., 1995). Furthermore, the classical diffusion model must be explicitly adapted for applications in Keplerian disks because orbital effects can reduce the strength of diffusivity (Youdin & Lithwick, 2007), an effect that is not captured by such diffusion models. The aforementioned inconsistencies can be problematic because accurately capturing the physics of turbulent transport is crucial for interpreting observations of protoplanetary disks and their dust distributions, and consequently, for improving our understanding of planet formation.

Recently, two ways have been proposed to resolve the issue concerning the non-conservation of angular momentum. One of which is to introduce correction terms to the dust momentum equation (Tominaga et al., 2019), while making sure not to violate Galilean invariance in the process (Huang & Bai, 2022). A second solution was proposed by Klahr & Schreiber (2021), who modeled turbulent transport with a pressure-like term.

Motivated by the general inconsistencies, we remain agnostic to the specific source of turbulence in this chapter and derive a novel self-consistent Eulerian turbulence model that conserves angular momentum, resolves the question of the fundamental transport quantity, and intrinsically incorporates orbital effects. We recover the previous turbulence models as special limiting cases of our novel turbulent transport model. As such, our approach removes the tension which is currently present in the turbulent transport modeling of particles in protoplanetary disks and provides a novel framework for understanding the complex interplay between turbulence and particle dynamics in protoplanetary disks.

The outline of this chapter is as follows. We first review relevant theoretical background in Sec. 5.2, including a brief review of current Eulerian turbulent diffusion models. On the basis of the introduced theory, we derive a novel turbulent transport model in Sec. 5.3, and then discuss its applications to dust modeling in turbulent protoplanetary disks in Sec. 5.4. In Sec. 5.5, we study the effects of turbulent transport on harmonic perturbations in the absence of external forces and also in the presence of orbital effects. Lastly, in Sec. 5.7, we summarize our findings.

5.2 Theoretical Background

We start this section by comparing models of dust via Lagrangian and Eulerian descriptions in Sec. 5.2.1. Then, Sec. 5.2.2 introduces statistical characteristics of turbulence and defines important turbulent transport quantities, such as the *diffusion coefficient* and the *correlation time*. We review a stochastic Lagrangian turbulent dust transport model and the classical Eulerian gradient diffusion model in Sec. 5.2.3 and Sec. 5.2.4 respectively. Therein, we also discuss the limitations of applying the latter model to turbulent dust transport in protoplanetary disks. In Sec. 5.2.5, we introduce the concept of mean-field theory, and briefly review recent work on turbulent dust transport by Tominaga et al. (2019), Huang & Bai (2022), and Klahr & Schreiber (2021) in Sec. 5.2.6. Finally, Sec. 5.2.7 discusses the turbulent particle dispersion as described by the Hinze-Tchen formalism.

5.2.1 Lagrangian and Eulerian Dust Modeling

This section presents two prevalent mathematical descriptions for modeling dust dynamics in protoplanetary disks, namely the Lagrangian and Eulerian descriptions.

Lagrangian models trace the motion of individual dust particles as they interact with the gas and potentially other dust particles in the disk. The particle trajectories are described by ordinary differential equations, which fully capture the discrete nature of dust particles. Assuming a purely deterministic trajectory, the equations of motion are most effectively described by a Newtonian formalism:

$$\frac{dx_i}{dt} = v_i \tag{5.1}$$

$$\frac{dv_i}{dt} = -\frac{1}{t_s}\big(v_i - u_i\big) + g_i \tag{5.2}$$

The above equations describe the rate of change of the particle position x_i and velocity v_i. The r.h.s. of Eq. 5.2 contains the drag force and the gravitational acceleration g_i. Because the drag force term contains the gas velocity u_i, gas dynamics must be known and solved concurrently with particle dynamics.

A downside to the Lagrangian approach is its computational cost, which scales with the number of particles in the model. Typically, numerical models include a significantly smaller number of particles than the physical particle count in protoplanetary disks, representing these particles as *super particles* (e.g. Youdin & Lithwick, 2007; Zsom & Dullemond, 2008; Wafflard-Fernandez & Baruteau, 2020). An additional challenge is balancing the large computational demands of regions with high particle density against the limited resolution in low-density areas.

Conversely, when individual particle trajectories are irrelevant to a specific problem, and a field description of fundamental flow properties is appropriate (e.g., in terms of mass flux and concentrations), the Eulerian continuum approach can be a suitable alternative. This method constructs *fluid elements* containing a sufficient number of particles to allow volume-averaged quantities like temperature, density, and velocity to statistically describe each fluid element. Nonetheless, the fluid elements must be small relative to the characteristic lengths scale of the system. Usually, a *grid* best represents these fluid elements, subdividing the domain of interest into individual *cells*.

Assuming an appropriate grid exists, the dust phase of a protoplanetary disk can be described by continuum equations analogous to the gas's Navier-Stokes equations. Typically, a set of Euler-like equations in the limit of vanishing particle dispersion describes a pressureless fluid, an appropriate approximation for particles well-coupled to the gas ($St \ll 1$).

For brevity, we will discuss a single-sized particle population, although the approach can be readily generalized (see e.g. Benítez-Llambay et al., 2019). In conservation form, the pressureless fluid equations read:

$$\frac{\partial \rho_d}{\partial t} + \frac{\partial}{\partial x_j}\left(\rho_d v_j\right) = 0 \tag{5.3}$$

$$\frac{\partial}{\partial t}(\rho_d v_i) + \frac{\partial}{\partial x_j}\left(\rho_d v_i v_j\right) = -\frac{\rho_d}{t_s}\left(v_i - u_i\right) + \rho_d g_i \tag{5.4}$$

The pressureless equations are derived from the conservation of mass and momentum, respectively (e.g. Fan & Chao, 1998). The r.h.s. of Eq. 5.4 models the momentum exchange through aerodynamic interactions of the particles with the gas and gravity. Because the particle dispersion vanishes, there is no need for an additional particle energy equation.

In both the Lagrangian and the Eulerian descriptions, particles couple to gas motion via the drag term. If the gas flow is turbulent, the particles couple to the turbulent flow through this term, making additional turbulence models for dust redundant (assuming the turbulent flow in gas is fully characterized). However, the nature of turbulence in protoplanetary disks often remains unknown or requires very large temporal and spatial resolution to fully capture (e.g. Manger et al., 2020). The following sections will discuss the profound impact of turbulence on both gas and dust dynamics.

5.2.2 Statistical Characteristics of Turbulence

There exists no universal turbulence model for protoplanetary disks. Therefore, turbulent fluctuations are typically characterized statistically and compared against specific models, experiments, and observations.

In our statistical analysis, we follow Fan & Chao (1998) and use a Lagrangian tracer that follows the turbulent dynamics of a gas fluid parcel. We simplify by assuming isotropic and homogeneous turbulence, which allows us to describe the turbulent displacement of the fluid parcel along a single dimension. Given the initial position of the fluid parcel $x = 0$ at time $t = 0$ and assuming the turbulent velocity fluctuation u' is known at all times, the position at times $t > 0$

can be evaluated as:

$$x(t) = \int_0^t u'(t')\mathrm{d}t' \tag{5.5}$$

The averaged squared displacement $\overline{x^2}$ of a fluid parcel subject to statistically steady turbulence, is related to the autocorrelation function of the turbulent velocity fluctuations as (Taylor, 1920)

$$\overline{x^2}(t) = 2\int_0^t \mathrm{d}t' \int_0^{t'} \mathrm{d}\tau\, \overline{u'(\tau)u'(0)} \tag{5.6}$$

Here, the overbar signifies a statistical ensemble average. We then define the diffusion coefficient D as the averaged growth rate of the squared displacement over long times (e.g. Fan & Chao, 1998):

$$D \equiv \frac{1}{2}\frac{\mathrm{d}\overline{x^2}}{\mathrm{d}t} \tag{5.7}$$

In a purely diffusive process, Eq. 5.7 approaches a constant value.
According to the *Wiener-Kinchin theorem*, the energy spectrum of turbulent fluctuations in frequency space $\hat{E}_g(\omega)$ is related to the autocorrelation function of the turbulent velocity fluctuations via its Fourier transform:

$$\hat{E}_g(\omega) = \frac{1}{2\pi}\int_{-\infty}^{\infty} \mathrm{d}t'\, \overline{u'(t')u'(0)}e^{i\omega t'} \tag{5.8}$$

The above equation suggests that in statistically steady turbulence, the energy spectrum is an even function of frequency $\hat{E}_g(\omega) = \hat{E}_g(-\omega)$ (e.g. Zhu et al., 2015). The gas diffusion coefficient D_g is then expressed as the integral over the autocorrelation function (e.g. Youdin & Lithwick, 2007):

$$\begin{aligned} D_g &= \int_0^\infty \mathrm{d}t'\, \overline{u'(t')u'(0)} && \text{(5.9a)}\\ &= \int_0^\infty \mathrm{d}t' \int_{-\infty}^{\infty} d\omega\, \hat{E}_g(\omega)e^{-i\omega t'} && \text{(5.9b)}\\ &= \pi\int_{-\infty}^{\infty} \mathrm{d}\omega\, \hat{E}_g(\omega)\delta(\omega) && \text{(5.9c)}\\ &= \pi\hat{E}_g(0) && \text{(5.9d)} \end{aligned}$$

The second line (Eq. 5.9b) follows from Eq. 5.8. The third line, i.e., Eq. 5.9c, introduces the delta distribution as the Fourier transformation of a constant and makes use of the fact that the energy spectrum $\hat{E}_g(\omega)$ is an even function to extend the lower integration boundary to $-\infty$. This shows that the diffusion coefficient D_g is proportional to the energy spectrum at $\omega = 0$.
We introduce the *correlation time* of turbulence t_{corr}:

$$t_{\mathrm{corr}} \equiv \int_0^\infty \mathrm{d}t'\, \frac{\overline{u'(t')u'(0)}}{\overline{u'^2}} \tag{5.10}$$

Here, $\overline{u'^2} = \overline{u'(0)u'(0)}$ is the square of the mean turbulent velocity dispersion.
With the correlation time t_{corr} and the diffusion coefficient D_g as the two important statistical characteristics of turbulence, we use Eq. 5.9a to connect these two quantities with the turbulent velocity dispersion:

$$D_g = \overline{u'^2}\, t_{\mathrm{corr}} \tag{5.11}$$

These definitions apply for any form of the energy spectrum $\hat{E}(\omega)$, provided the turbulence is statistically steady, homogeneous, and isotropic.

We also define a characteristic *eddy length* of the turbulence

$$l_{\rm eddy} \equiv \sqrt{\overline{u'^2}}\, t_{\rm corr} \tag{5.12}$$

and the *diffusion timescale*

$$t_{\rm diff} \sim \frac{l^2}{D_g} \tag{5.13}$$

which describes the time for a fluid parcel to diffuse across a distance l.

In the literature, it is common to relate the gas diffusion coefficient D_g to the particle diffusion coefficient D_d via the dimensionless *Schmidt number* (e.g. Cuzzi et al., 1993):

$$Sc \equiv \frac{D_g}{D_d} \tag{5.14}$$

In the absence of external forces, $Sc = 1$ holds, making the diffusion of dust indistinguishable from that of gas (Youdin & Lithwick, 2007). Hereafter, we will use D to represent both D_g and D_d when a distinction is not required.

Some studies define the Schmidt number differently, as $Sc_{\rm hydro} = \nu/D_g$, the ratio between the kinematic viscosity ν, and D_g (e.g. Johansen & Klahr, 2005; Carballido et al., 2006). Thus, $Sc_{\rm hydro}$ quantifies the relative effectiveness of angular momentum transport (associated with ν) and mixing processes (associated with D_g). The two parameters ν and D_g have the same dimensions and both arise from the same turbulence and are therefore closely related but not necessarily equal (see e.g. Pavlyuchenkov & Dullemond, 2007). Consequently, $Sc_{\rm hydro}$ represents a related, albeit not necessarily equivalent, quantity to our definition. In this chapter, we adopt the definition of the Schmidt number as given in Eq. 5.14, consistent with the convention in Cuzzi et al. (1993) and Youdin & Lithwick (2007).

When studying protoplanetary disks, turbulent diffusion is sometimes parametrized using a dimensionless *diffusivity* parameter δ:

$$\delta = \frac{D}{c_s h_g} \tag{5.15}$$

The definition in Eq. 5.15 is analogous to the dimensionless α-parameter (see Eq. 5.84) introduced by Shakura & Sunyaev (1973). However, while δ parametrizes the level of turbulent diffusion, the α parameter is most commonly used to describe the efficiency of angular momentum transport in a disk. For $Sc_{\rm hydro} = 1$, we find $\delta = \alpha$.

5.2.3 Stochastic Lagrangian Formalism

In the context of turbulent dust dynamics, a Lagrangian description can incorporate a stochastic forcing term into Eq. 5.2, such that the turbulent velocity fluctuation readily fulfills the desired turbulence statistics as discussed in Sec. 5.2.2.

When applying a stochastic Lagrangian turbulence model, the gas velocity u is typically decomposed into a mean-field contribution $\bar{u}$ and a turbulent fluctuation δu such that $u = \bar{u} + \delta u$. The Lagrangian velocity equation for the dust, in one dimension, then becomes:

$$\frac{dv}{dt} = -\frac{1}{t_s}\big(v - \bar{u}\big) + g + \frac{1}{t_s}\delta u \tag{5.16}$$

The r.h.s. of Eq. 5.16 includes terms for drag and gravity, with $\bar{u}$ signifying the laminar gas velocity (e.g. Charnoz et al., 2011). The last term represents the acceleration of dust via the turbulent gas velocity field δu.

As mentioned in Sec. 5.2.2, isotropic and homogeneous turbulence can be statistically characterized using two parameters, namely the diffusion coefficient D and the correlation time t_{corr}. Consequently, a desirable stochastic turbulence model should also be parametrized by these two quantities. We adopt the model from Ormel & Liu (2018) that explicitly defines the stochastic forcing term. Below, we review their formalism in one dimension, but it can readily be extended to higher dimensions. In addition to Eq. 5.1 and Eq. 5.16, the model incorporates an equation for the turbulent velocity field and a stochastic differential equation:

$$\delta u = \sqrt{\frac{D}{t_{\mathrm{corr}}}}\zeta_t \tag{5.17a}$$

$$\mathrm{d}\zeta_t = -\frac{\zeta_t}{t_{\mathrm{corr}}}\mathrm{d}t + \sqrt{\frac{2}{t_{\mathrm{corr}}}}\mathrm{d}W_t \tag{5.17b}$$

Equation 5.17a contains the turbulent velocity dispersion, parametrized by the diffusion coefficient and the correlation time $\sqrt{\delta u^2} = \sqrt{D/t_{\mathrm{corr}}}$, as suggested by Eq. 5.11, and a dimensionless stochastic variable ζ_t. The dynamics of the stochastic variable ζ_t is governed by Eq. 5.17b which formally describes an Ornstein–Uhlenbeck process (Uhlenbeck & Ornstein, 1930), where W_t denotes the Wiener process. The differential of the Wiener process is $\mathrm{d}W_t = \sqrt{\mathrm{d}t}\mathcal{N}(0,1)$, where $\mathcal{N}(0,1)$ is the normal distribution with zero mean and unit variance. Hence, $\overline{\zeta_t} = 0$ and $\overline{\zeta_t^2} = 1$ hold. While ζ_t-values are correlated for timescales shorter than t_{corr}, they become uncorrelated and normally distributed for longer timescales.

In essence, this model incorporates turbulence as an additional stochastic forcing term in the velocity equation. Being a specific turbulence model, it may not necessarily correspond to actual turbulent processes in protoplanetary disks. However, it has proven immensely useful, because the model is parametrized by only two parameters (D, t_{corr}) and has the desired statistical characteristics of turbulence as discussed in Sec. 5.2.2.

In the *strong coupling approximation*, where the stopping time t_s is small, Ormel & Liu (2018) show that the system of equations can be represented by a single stochastic differential equation:

$$\mathrm{d}x = v\mathrm{d}t + \sqrt{2D}\mathrm{d}W_t \tag{5.18}$$

This equation is frequently used to model Lagrangian dust transport in turbulent protoplanetary disks (e.g. Ciesla, 2010; Zsom et al., 2011; Charnoz et al., 2011; Krijt & Ciesla, 2016).

It is crucial to note that the model as presented in this chapter is strictly applicable only in an unstratified gas background. For variations in gas density, additional corrections are necessary, as detailed in Ormel & Liu (2018).

Overall, the stochastic model of Ormel & Liu (2018) provides a versatile Lagrangian turbulence model, enabling the simulation of dust dynamics in turbulent environments. In the following sections, we will turn to the Eulerian description.

5.2.4 Gradient Diffusion and its Limitations

In this section, we review the gradient diffusion model, as an example of an Eulerian turbulent transport model. Gradient diffusion is probably the most popular model employed to describe turbulent dust transport in protoplanetary disks.

We will start by introducing the concept of a gradient diffusion flux in Sec. 5.2.4 and then proceed to highlight several limitations inherent to the gradient diffusion model. Specifically, in Sec. 5.2.4, we will highlight that there appears to be no clear consensus on the functional form of the diffused quantity. In Sec. 5.2.4 we will discuss the predictions and limitations of the gradient diffusion model regarding the vertical settling-diffusion equilibrium solution in protoplanetary disks before we will illustrate issues regarding momentum conservation in Sec. 5.2.4. Lastly, in Sec. 5.2.4, we will review how the model must be explicitly adapted to incorporate the effects of orbital dynamics in disks.

Introducing a Gradient Diffusion Flux

When relying on an Eulerian description, i.e., describing the dust component in a turbulent protoplanetary disk as a continuous fluid, Reynolds averaging techniques are typically employed to incorporate turbulent transport effects into the equations describing dust dynamics (Champney & Cuzzi, 1990; Cuzzi et al., 1993). This approach introduces an additional turbulent transport flux J_i to the dust continuity equation

$$\frac{\partial \rho_d}{\partial t} + \frac{\partial}{\partial x_j}\left(\rho_d v_j\right) = -\frac{\partial}{\partial x_j}\left(J_j\right) \tag{5.19}$$

but does not simultaneously predict its functional form.

As discussed in Sec. 5.2.2, random turbulent displacements in homogeneous and isotropic turbulence behave diffusively. Unsurprisingly, diffusion approaches have been successful in describing the functional form of the turbulent mass flux J_i. The most common approach involves the *gradient diffusion hypothesis*, which assumes the turbulent mass flux J_i to be proportional to the gradient of the particle density, (e.g. Cuzzi et al., 1993; Goodman & Pindor, 2000; Schrapler & Henning, 2004; Shariff & Cuzzi, 2011)

$$J_i = -D \frac{\partial}{\partial x_i} \rho_d \tag{5.20}$$

With this functional form, the continuity equation takes the form of an *advection-diffusion equation.*

In applications involving a nonuniform gaseous background density, the turbulent mass flux from Eq. 5.20 is often modified to account for gradients in the gas density:

$$J_i = -D \rho_g \frac{\partial}{\partial x_i} \frac{\rho_d}{\rho_g} \tag{5.21}$$

This alteration is usually motivated by the heuristic *good mixing condition*, which states that both particle and gas distributions evolve towards a common maximum entropy distribution in which the spatial gradient of the particle concentration vanishes ρ_d/ρ_g = constant (see e.g. Charnoz et al., 2011, for a more detailed discussion).

Consequently, the following advection-diffusion equation is predominantly employed to model the turbulent mass transport of particles in protoplanetary disks (e.g. Dubrulle et al., 1995; Takeuchi & Lin, 2002; Dullemond & Dominik, 2004; Schrapler & Henning, 2004; Fromang & Papaloizou, 2006; Ciesla, 2009; Dullemond & Penzlin, 2018).

$$\frac{\partial \rho_d}{\partial t} + \frac{\partial}{\partial x_j}\left(\rho_d v_j\right) = \frac{\partial}{\partial x_j}\left[D \rho_g \frac{\partial}{\partial x_i}\left(\frac{\rho_d}{\rho_g}\right)\right] \tag{5.22}$$

Despite the success of the gradient diffusion model in modeling turbulent particle transport in protoplanetary disks, it has certain inherent limitations, which we will discuss in the following sections.

The Diffused Quantity

The protoplanetary disk community seems not to have reached a consensus on the functional form of the quantity diffused by turbulence. More rigorous mathematical derivations typically result in a diffusion flux, in which the absolute particle density ρ_d is the diffused quantity (e.g. Cuzzi et al., 1993; Laibe et al., 2020). However, this appears to be inconsistent with the good mixing condition in the small particle limit.

In contrast, heuristic arguments favor the functional form expressed in Eq. 5.21 which assumes the *dust-to-gas ratio* ρ_d/ρ_g to be the diffused quantity, which additionally accounts for gradients in the gas density (e.g. Dubrulle et al., 1995; Charnoz et al., 2011). Although the latter quantity appears to be the more favorable choice, a self-consistent model supporting this choice is yet to be definitively established. To date, we only know of Riols & Lesur (2018) who have proposed a mathematically coherent argument on the basis of Reynolds averages and assuming strongly coupled particles and small dust concentrations.

Vertical Settling-Diffusion Equilibrium

We now explore the use of the gradient diffusion model in the form of Eq. 5.22 to describe the vertical steady-state structure of a protoplanetary disk. For this, we assume a vertically isothermal gaseous background with a vertical hydrostatic equilibrium profile as given by Eq. 3.8. Additionally, we assume the background gas to exhibit isotropic, homogeneous turbulence and a constant diffusion coefficient D. In a steady state, the particle component in this background is in a vertical settling-diffusion equilibrium, typically found by using the terminal velocity approximation (Eq. 4.7).

Substituting Eq. 4.7 into Eq. 5.22, and assuming a steady state such that the time derivative vanishes, we find the following one-dimensional differential equation:

$$\frac{\partial}{\partial z}\left(\ln\frac{\rho_d}{\rho_g}\right) = -\frac{\Omega^2 t_s}{D} z \tag{5.23}$$

Further assuming the vertical gas density profile follows the Gaussian profile of Eq. 3.8 with scale height h_g, integration of Eq. 5.23 yields (Fromang & Nelson, 2009):

$$\rho_d = \rho_{d,0} \exp\left[-\frac{\Omega t_{s,\mathrm{mid}}}{\delta}\left(\exp\left(\frac{z^2}{2h_g^2}\right) - 1\right) - \frac{z^2}{2h_g^2}\right] \tag{5.24}$$

Here, $t_{s,\mathrm{mid}}$ denotes the stopping time evaluated at the disk midplane, and we have used Eq. 5.15 to simplify the expression.

The above solution relies on the terminal velocity approximation, which neglects inertial accelerations, and thus is only applicable for $St \ll 1$, a regime where drag forces are dominant (Youdin & Goodman, 2005). For small particles, with $St \ll 1$ at the disk midplane, this condition is fulfilled everywhere in the disk except the disk atmosphere where even the Stokes number of the smallest particles exceeds unity ($St \gtrsim 1$) due to the exponential stratification of the gas background. For large particles ($St > 1$), this condition is not fulfilled anywhere and Eq. 5.24 technically speaking not applicable.

As Laibe et al. (2020) noted, an analytical model predicting the transition from drag-dominant to gravity-dominant dynamics in turbulent protoplanetary disks does not currently exist.

Momentum Conservation

Incorporating a diffusion flux in the continuity equation as described by Eq. 5.22 may violate the conservation of linear and angular momentum (Goodman & Pindor, 2000; Weber et al., 2019; Tominaga et al., 2019). This non-conservation can be problematic, especially since accurate accounting of angular momentum is key for mass transport in accretion disks. Moreover, Tominaga et al. (2019) showed that the non-conservation non-physically changes the properties of the *secular gravitational instability* (e.g. Youdin, 2011a).

Here, we follow Weber et al. (2019) to illustrate the non-conservation of linear momentum by combining the velocity equation of a particle fluid

$$\frac{\partial v_i}{\partial t} + \frac{\partial}{\partial x_j}(v_i v_j) = \frac{1}{t_s}(u_i - v_i) \tag{5.25}$$

and the continuity equation including the turbulent mass flux (Eq. 5.19) to write the particle momentum equation in conservation form:

$$\frac{\partial}{\partial t}(\rho_d v_i) + \frac{\partial}{\partial x_j}(\rho_d v_i v_j) = \frac{\rho_d}{t_s}(u_i - v_i) - v_i \frac{\partial}{\partial x_j} J_j \tag{5.26}$$

The first term on the r.h.s models the acceleration due to aerodynamic drag and exchanges momentum between the gas and particle fluid. The second term, associated with turbulent mass transport, generally cannot be expressed as a divergence term. As such, it can contribute to the non-conservation of dust momentum $\rho_d v_i$.

We want to stress here that the non-conservation of the dust momentum in Eq. 5.26 by itself is not necessarily a problem. Often, the effect of the last term on the r.h.s. of Eq. 5.26 is regarded as coming from the turbulent gas-particle interaction. The problem only arises if one considers the full system of dust *and* gas. In the full system, momentum is expected to be conserved, but, there is generally no term analogous to the last term in Eq. 5.26, in the gas momentum equations that would model the back reaction of the turbulent gas-particle interaction. Consequently, momentum in the full system is not necessarily conserved.

To prevent this issue, Goodman & Pindor (2000) introduce an artificial term to the particle momentum equation. For demonstrative purposes, we follow their approach here and add a term of the form

$$... - J_j \frac{\partial v_i}{\partial x_j} \tag{5.27}$$

to the r.h.s. of Eq. 5.26 such that the momentum equation can be rewritten as

$$\frac{\partial}{\partial t}(\rho_d v_i) + \frac{\partial}{\partial x_j}\big(\rho_d v_i v_j + v_i J_j\big) = \frac{\rho_d}{t_s}(u_i - v_i) \tag{5.28}$$

Now, the diffusion flux is included in the divergence term on the l.h.s., which means the particle momentum is globally conserved even in the presence of a turbulent mass flux. However, as mentioned before, while it is expected that momentum is conserved in the whole system, there is no clear reason why momentum should be conserved within the dust fluid and cannot be exchanged with the gas. The naive addition of this artificial term (Eq. 5.27) is unproblematic only if the term equals zero. This condition is met if the velocity gradient in the direction of the turbulent mass transport, or equivalently the dot product between the turbulent mass flux J_i and the gradient of the velocity $\partial v_i/\partial x_j$, vanishes.

Conversely, the approach of adding a diffusion flux to the continuity equation, as in Eq. 5.22, can violate momentum conservation if diffusive transport occurs in the direction of a non-zero velocity gradient, specifically wherever $\partial v_i/\partial x_j \neq 0$. This is in agreement with the analysis of Tominaga et al. (2019), who show the non-conservation of angular momentum for diffusive particle transport in the radial direction of a protoplanetary disk, where a radial velocity gradient exists due to the Keplerian shear $\partial v_\phi/\partial r \neq 0$.

Orbital Effects

In their seminal work, Youdin & Lithwick (2007) studied the diffusion of particles in Keplerian gas disks subjected to isotropic and homogeneous turbulence. They showed that orbital effects led to a decline in the strength of particle diffusion for large particles ($St \gtrsim 1$) with increasing Stokes number. Consequently, they revised the Schmidt number (Eq. 5.14) for diffusion in disks as follows:

$$Sc^{\mathrm{YL}} \sim 1 + St^2 \tag{5.29}$$

and also the radial particle diffusion coefficient

$$D_{d,r}^{\mathrm{YL}} \sim \frac{D}{1 + St^2} \tag{5.30}$$

where D is the diffusion coefficient parametrized by the product of turbulent velocity dispersion squared and correlation time (Eq. 5.11).

Such orbital effects are not captured by the gradient diffusion model and must be parametrized explicitly.

We highlight that the presence of, for example, a planet in a protoplanetary disk can introduce complexity to the orbital effects, potentially rendering an explicit parametrization inaccurate.

After illustrating the limitations of the classical gradient diffusion model, we introduce a formalism that enables the derivation of improved turbulent transport models in the following section.

5.2.5 Reynolds-Averaged Mean-Flow Equations

The *Reynolds-averaged Navier-Stokes* (RANS, Reynolds O., 1895) approach is a widely used technique in fluid dynamics to model turbulent gas, focusing on large-scale average behavior of hydrodynamic quantities rather than their instantaneous values on small scales.

Our discussion follows the work of Cuzzi et al. (1993), applying the RANS technique to the mass (Eq. 5.3) and momentum (Eq. 5.4) conservation equations that govern dust particle dynamics in protoplanetary disks. The resulting system of mean-flow equations describes the particle dynamics in a turbulent environment. However, without additional modeling, the system is not closed, meaning that the total number of independent variables exceeds the total number of independent equations, and explicit closure models are required.

We focus on the statistically averaged behavior of the instantaneous particle density $\rho_d(x_j, t)$ and the velocity $v_i(x_j, t)$, which depend on the spatial variables $x_{j=1,2,3}$ and time t. We decompose these variables into averaged and fluctuating components:

$$\rho_d = \bar{\rho}_d + \rho_d' \tag{5.31}$$

$$v_i = \bar{v}_i + v_i' \tag{5.32}$$

Here, the overbar $^{-}$ denotes the Reynolds average and the prime $'$ denotes short-term fluctuations. This decomposition is possible as long as the characteristic length scales and timescales of fluctuations are small compared to those of the mean values.

The averages of the fluctuating components vanish:

$$\overline{\rho_d'} = 0, \quad \overline{v_i'} = 0 \tag{5.33}$$

We interpret the average here primarily as a statistical ensemble average, although it can be equivalent to the time average under the ergodic hypothesis.

Next, we apply the Reynolds decomposition to the instantaneous mass conservation equation

(Eq. 5.3), decomposing both density and velocity into mean and fluctuating components:

$$\frac{\partial \bar{\rho}_d}{\partial t} + \frac{\partial \rho'_d}{\partial t} + \frac{\partial}{\partial x_j}\left(\bar{\rho}_d \bar{v}_j + \bar{\rho}_d v'_j + {\rho'}_d \bar{v}_j + \rho'_d v'_j\right) = 0 \tag{5.34}$$

The averaging operator commutes with time and space derivatives, and already averaged quantities are considered constant. After applying the averaging operator to Eq. 5.34, the equation becomes:

$$\frac{\partial \bar{\rho}_d}{\partial t} + \frac{\partial}{\partial x_j}\left(\bar{\rho}_d \bar{v}_j + \overline{\rho'_d v'_j}\right) = 0 \tag{5.35}$$

This equation describes the dynamics of the mean particle density $\bar{\rho}_d$. Besides a *mean advection flux* $\bar{\rho}_d \bar{v}_j$, the equation contains a new quantity, the *mean turbulent mass flux* $\overline{\rho'_d v'_j}$, which can be interpreted as a mean particle mass flux driven by turbulence. The explicit form of this correlation term is unknown without further modeling, a condition known as the *closure problem* (see e.g. Fox, 2003, for more details on the closure problem).

The two flux components in Eq. 5.35 have independent dynamics, requiring additional equations to describe their evolution. To find these equations, we apply the Reynolds decomposition and averaging procedure to the momentum conservation equation (Eq. 5.4), yet ignoring gravity for simplicity, yielding:

$$\begin{aligned}\frac{\partial}{\partial t}\left(\bar{\rho}_d \bar{v}_i\right) + \frac{\partial}{\partial t}\left(\overline{\rho'_d v'_i}\right) + \frac{\partial}{\partial x_j}\left(\bar{\rho}_d \bar{v}_i \bar{v}_j + \overline{\rho'_d v'_i}\bar{v}_j + \bar{v}_i \overline{\rho'_d v'_j} + \underbrace{\bar{\rho}_d \overline{v'_i v'_j}}_{\text{i}} + \underbrace{\overline{\rho'_d v'_i v'_j}}_{\text{ii}}\right) = \\ \bar{\rho}_d \frac{\bar{u}_i - \bar{v}_i}{t_s} + \underbrace{\frac{\overline{\rho'_d u'_i} - \overline{\rho'_d v'_i}}{t_s}}_{\text{iii}}\end{aligned} \tag{5.36}$$

Besides the mean turbulent mass flux $\overline{\rho'_d v'_i}$, three more terms (i, ii, and iii) contain unknown correlations. In the following section, we illustrate how a gradient diffusion approach can be used to close the system of Reynolds averaged mean flow equations via the approach of Huang & Bai (2022).

5.2.6 Recent Work

The primary issue with the gradient diffusion model, as discussed in Sec. 5.2.4, in the context of disk modeling, is probably its failure to conserve angular momentum (Tominaga et al., 2019). Recently, two solutions to this problem have been proposed. We will briefly summarize these below.

The Approach of Tominaga et al. (2019) and Huang & Bai (2022)

The first approach, proposed by Tominaga et al. (2019) and further refined by Huang & Bai (2022), is based on the Reynolds decomposition formalism by Cuzzi et al. (1993). They argue that the term iii in Eq. 5.36 vanishes for small, well-coupled particles ($St \ll 1$). Similarly, the triple correlation term ii is typically argued to vanish as long as turbulent fluctuations are small (e.g. Blackman & Field, 2003). The term i in Eq. 5.36 represents turbulent particle stresses, analogous to the Reynolds stress in the gas. The on-diagonal elements of the term i represent the effect of a *particle pressure*, similar to a thermal pressure in the gas (Dobrovolskis et al., 1999).

Shariff & Cuzzi (2011) and Tominaga et al. (2019) here use a closure relation of the form

$$\overline{v'_i v'_j} = \delta_{ij} c_d^2 \tag{5.37}$$

to express the turbulent Reynolds stress in terms of a scalar particle velocity dispersion c_d. Here δ_{ij} is the Kronecker delta. For small particles, Huang & Bai (2022) argue the squared dispersion c_d^2 vanishes based on an argument by Garaud et al. (2004), implying that all three terms, i, ii and iii in Eq. 5.36 can be neglected for tightly coupled particles. The mean momentum equation then reads:

$$\frac{\partial}{\partial t}\left(\bar{\rho}_d\bar{v}_i\right) + \underbrace{\frac{\partial}{\partial t}\left(\overline{\rho'_d v'_i}\right)}_{\text{I}} + \frac{\partial}{\partial x_j}\Big(\bar{\rho}_d\bar{v}_i\bar{v}_j + \underbrace{\overline{\rho'_d v'_i}\bar{v}_j + \bar{v}_i\overline{\rho'_d v'_j}}_{\text{II}}\Big) = \frac{\bar{\rho}_d}{t_s}\left(\bar{u}_i - \bar{v}_i\right) \tag{5.38}$$

Except for terms I and II, Eq. 5.38 is equivalent to the instantaneous momentum equation (Eq. 5.4), with instantaneous variables replaced by their averages. Cuzzi et al. (1993) and Tominaga et al. (2019) further neglect the term I assuming it is small compared to the term to its left, yet offer no argument for this assumption. Huang & Bai (2022), however, point out that the removal of term I in Eq. 5.38 would violate Galilean invariance, and therefore the term should be kept. In their work, Huang & Bai (2022) call the combined contribution of terms I and II the *momentum correction* that arises as a result of turbulent particle transport.

The remaining unknown correlation in Eq. 5.38 is $\overline{\rho'_d v'_i}$, generally does not vanish and therefore requires a closure relation. The simplest approach employs a *gradient diffusion hypothesis* (GDH) which assumes turbulent mass flux is proportional to the gradient of the mean particle density (see e.g. Cuzzi et al., 1993; Tominaga et al., 2019; Huang & Bai, 2022):

$$\overline{\rho'_d v'_i} = -D\frac{\partial}{\partial x_i}\bar{\rho}_d \tag{5.39}$$

As a result, the set of Reynolds averaged mean-flow equations is closed. Ignoring the momentum corrections (terms I and II), the equations recover the classical gradient diffusion model (Sec. 5.2.4).

The presented extension to the classical gradient diffusion model, based on robust mathematical foundations like Reynolds averages, indeed conserves total angular momentum (Tominaga et al., 2019; Huang & Bai, 2022). However, it does not resolve the other complications inherent to the gradient diffusion closure in Eq. 5.39.

For illustrative purposes, we employ Eq. 5.39 and Eq. 5.35, rewriting the time derivative in term I of Eq. 5.38 using averaged quantities:

$$\frac{\partial}{\partial t}\left(\overline{\rho'_d v'_i}\right) = D\frac{\partial}{\partial x_j}\frac{\partial}{\partial x_i}\bar{\rho}_d\bar{v}_j - D^2\frac{\partial^2}{\partial x_j^2}\frac{\partial}{\partial x_i}\bar{\rho}_d \tag{5.40}$$

Assuming the diffusion coefficient D to be constant, it can be moved inside the spatial derivatives and the entire r.h.s. of Eq. 5.40 becomes a divergence, confirming the conservation of mean particle momentum in Eq. 5.38. However, the second term on the r.h.s. of Eq. 5.40 may introduce nonphysical accelerations, an issue illustrated via the following one-dimensional example.

Consider a static mean advection flow ($\overline{v} = \bar{u} = 0$) with a small harmonic perturbation atop a constant particle density background $\bar{\rho}_d(x) = \rho_{d,0}(1 + A\sin(kx))$, where $A \ll 1$ and k^{-1} characterizes the perturbation's length scale. Substituting this into Eq. 5.40, and subsequently into Eq. 5.38, the force term acting on the particle fluid is inversely proportional to the lengths scale of the perturbation to the third power:

$$\frac{\partial}{\partial t}\left(\bar{\rho}_d\overline{v}\right) \propto k^3 \tag{5.41}$$

Consequently the diffusion time (Eq. 5.13) scales as $t_{\text{diff}} \propto k^{-2}$, as expected of a diffusive solution. However, for small-scale perturbations ($k \to \infty$), the force acting on the dust fluid becomes arbitrarily large and thus the diffusion timescale t_{diff} arbitrarily small. This is inconsistent with the physical reality that the dust fluid can react to gas turbulence only on timescales similar to or larger than the stopping time t_s. Therefore, the gradient diffusion closure (Eq. 5.39) proves to be non-physical on small scales, smoothing out perturbations too quickly[1].

This consideration can become important, e.g., when studying planetesimal formation via the gravitational collapse of small-scale particle overdensities. For instance, Umurhan et al. (2020) showed that gradient diffusion suppresses the smallest modes of the streaming instability. In Sec. 5.5, we will discuss deviations from the strictly diffusive behavior at small scales that resolve this issue.

The Approach of Klahr & Schreiber (2021)

Klahr & Schreiber (2021) do not employ Reynolds averages or the gradient diffusion hypothesis. Instead, they assume a settling-diffusion equilibrium ansatz, similar to the derivation of Brownian motion by Einstein (1905). Their dynamical equations read:

$$\frac{\partial \rho_d}{\partial t} + \frac{\partial}{\partial x_j}\big(\rho_d v_j\big) = 0 \tag{5.42}$$

$$\frac{\partial}{\partial t}(\rho_d v_i) + \frac{\partial}{\partial x_j}\left(\rho_d v_i v_j + \frac{1}{3}\frac{D}{t_s}\rho_d \delta_{ij}\right) = -\frac{\rho_d}{t_s}\big(v_i - u_i\big) + \rho_d g_i \tag{5.43}$$

In these equations, the dust velocity v_i represents the sum of the advection and diffusion velocities. Interestingly, these equations do not contain an explicit diffusion term, instead turbulent transport is modeled via a pressure-like term in the momentum equation. The equations conserve angular momentum and are significantly simpler than the previous model.

As we will demonstrate in Sec. 5.5, the characteristic turbulent transport timescale in this model is limited from below by the stopping time t_s. However, in the small-particle limit ($t_s \to 0$), the particle pressure diverges and the expression must be modified (see Sec. 5.4.4 and Klahr & Schreiber, 2021, for a more detailed discussion).

5.2.7 The Hinze-Tchen Model

In this section, we briefly review the *Hinze-Tchen model*, which describes the mixing of particles embedded in turbulent gas in the absence of external forces (see e.g., Youdin & Lithwick (2007) or Fan & Chao (1998) for a more detailed review of the Hinze-Tchen model).

The diffusion coefficient D is defined as the time derivative of the mean squared displacement in the limit of $t \to \infty$ (Eq. 5.7). Hinze and Tchen studied the time derivative of the mean squared displacement at arbitrary times t

$$\mathfrak{D}_g(t) = \int_0^t \mathrm{d}t' \, \overline{u'(t')u'(0)} \tag{5.44}$$

where we define $\mathfrak{D}_g$ to be the time-dependent diffusion coefficient.

In homogeneous and steady turbulence, the Hinze-Tchen model predicts the time-dependent diffusion coefficient in gas to read,

$$\mathfrak{D}_g(t) = D_g\big(1 - e^{-t/t_{\mathrm{corr}}}\big) \tag{5.45}$$

---

[1] Further complications arise when solving the mean flow equations numerically. We have found the third-order spatial derivatives of the dust density, in Eq. 5.40, to be challenging to accurately compute when scales in the dust density become comparable to the computational grid.

where D_g is the diffusion coefficient in the limit $t \to \infty$ as defined in Eq. 5.7.

The motion of particles embedded in the turbulent fluctuations of the gas is described by a *Langevin equation*

$$\frac{\mathrm{d}v'}{\mathrm{d}t} = -\frac{v' - u'}{t_s} \tag{5.46}$$

Assuming the particles are small compared to the smallest turbulence wavelength and are always trapped inside the same turbulent eddy, the turbulent particle velocity dispersion is related to the turbulent velocity dispersion of the gas as (Fan & Chao, 1998)

$$\overline{v'^2} = \frac{t_{\mathrm{corr}}}{t_{\mathrm{corr}} + t_s}\,\overline{u'^2} \tag{5.47}$$

For small particles ($t_s \ll t_{\mathrm{corr}}$), the Hinze-Tchen model predicts the turbulent particle velocity dispersion to be equal to the dispersion in the gas $\overline{v'^2} \approx \overline{u'^2}$. For large particles ($t_s \gg t_{\mathrm{corr}}$), the turbulent particle dispersion scales inversely to the stopping time $\propto t_s^{-1}$.

We define the *turbulence time* t_t as

$$t_t \equiv t_{\mathrm{corr}} + t_s \tag{5.48}$$

and combine Eq. 5.47 with Eq. 5.11 to write the squared particle velocity dispersion as

$$\overline{v'^2} = \frac{D_g}{t_t} \tag{5.49}$$

Equivalently to Eq. 5.45, the Hinze-Tchen model also predicts a time dependent diffusion coefficient $\mathfrak{D}_d(t)$ for particles embedded in the turbulent gas:

$$\mathfrak{D}_d(t) = \frac{D_g}{t_s^2 - t_{\mathrm{corr}}^2}\left[t_s^2\left(1 - e^{-t/t_s}\right) - t_{\mathrm{corr}}^2\left(1 - e^{-t/t_{\mathrm{corr}}}\right)\right] \tag{5.50}$$

The time-dependent particle diffusion coefficient approaches D_g on timescales $t \gg \max(t_s, t_{\mathrm{corr}})$ after which it is identical to the diffusion coefficient in the gas.

Interestingly, the Hinze-Tchen model reveals that although the turbulent particle dispersion $\overline{v'^2}$ relies on the particle-gas coupling via the stopping time t_s (Eq. 5.49), the particle diffusion coefficient on long timescales (and in the absence of external forces) remains independent of the stopping time, and consequently, the particle size (Eq. 5.50). The latter is equal to the diffusion coefficient of the gas $\mathfrak{D}_d(t \to \infty) = D_g$. This outcome, albeit somewhat counterintuitive, signifies that large particles weakly coupled to turbulent gas fluctuations do not diffuse less efficiently than the gas.

The physical reasoning for this result is as follows (Youdin & Lithwick, 2007): For small particles well-coupled to the turbulent gas fluctuation, the motion of dust is identical to the motion of the gas and the equality $D_d = D_g$ is straightforward. In contrast, large particles ($t_s \gg t_{\mathrm{corr}}$) show a decrease in their squared turbulent velocity dispersion $\overline{v'^2}$ with an increase in the stopping time $\overline{v'^2} \propto t_s^{-1}$. Simultaneously, the particle mean-free path l_{mfp} increases with the stopping time t_s ($l_{\mathrm{mfp}} = v' t_s$). As such, these effects cancel out, leading to $D_d = D_g$ for large particles as well.

5.3 The Turbulent Particle Pressure Model

After having introduced the necessary theoretical background, we now transition to the main focus of this chapter. In this section, we present the derivation of a novel Eulerian turbulent dust transport model, starting with the introduction of *Favre averaged* mean flow equations of dust dynamics (Sec. 5.3.1) and appropriate turbulence closures (Sec. 5.3.2).

The advantage of Favre averaging over Reynolds averaging is that it removes the turbulent flux term from the continuity equation and reduces the number of terms in the averaged momentum equation by a factor of two[2].

5.3.1 Favre-Averaged Mean-Flow Equations

The Favre average is a density-weighted average (Favre, 1965), and we denote it by a tilde ˜:

$$\tilde{v}_i \equiv \frac{\overline{\rho_d v_i}}{\bar{\rho}_d} \tag{5.51}$$

We define new fluctuations with respect to the Favre average

$$v_i = \tilde{v}_i + v_i'' \tag{5.52}$$

and note that the fluctuations v_i'' do not necessarily vanish when applying the averaging operator:

$$\overline{v''}_i \neq 0 \tag{5.53}$$

in contrast to the fluctuations with respect to the Reynolds average (see Eq. 5.33). Only the density-weighted fluctuations vanish under applying the averaging operator

$$\overline{\rho_d v_i''} = 0 \tag{5.54}$$

as can be seen by replacing v_i'' with Eq. 5.52 and using the definition in Eq. 5.51.
Relating the Reynolds-averaged and Favre-averaged velocities using the aforementioned definitions, we obtain:

$$\tilde{v}_i = \bar{v}_i + v_i^* \tag{5.55}$$

where we have defined the *turbulent transport velocity* as

$$v_i^* = \frac{\overline{\rho_d' v_i'}}{\bar{\rho}_d} \tag{5.56}$$

Next, we decompose the pressureless fluid equations and average them using the Favre decomposition, yielding a Favre-averaged continuity equation:

$$\frac{\partial \bar{\rho}_d}{\partial t} + \frac{\partial}{\partial x_j}\left(\bar{\rho}_d \tilde{v}_j\right) = 0 \tag{5.57}$$

Compared to the Reynolds averaging procedure, Favre averaging indeed eliminates the turbulent flux term from the mass conservation equation above.
In the case of the momentum equation, we only decompose the velocity, not the density. For the interfluid term $\rho_d' u_i'$, we perform a Reynolds decomposition instead of a Favre decomposition, as a Favre average would be ill-defined. Making sure not to mix Favre averaged and Reynolds

---

[2] In their work, Champney & Cuzzi (1990) studied particle turbulent transport using Favre averages, but they considered the elimination of the turbulent flux a major drawback of this method. They argued that the eliminated term is the *key feature of compressible two-phase flows*, further emphasizing that turbulence should cause mixing irrespective of a vanishing mean velocity. The authors abandoned the approach, adopting Reynolds averages instead. As far as we know, Favre averaging has not been used again to study turbulent particle transport in protoplanetary disks. Importantly, the method presented in this chapter allows for turbulent transport and mixing, even in the absence of mean velocity.

averaged quantities, the decomposed momentum equation reads

$$\begin{aligned}\frac{\partial}{\partial t}\left(\rho_d \tilde{v}_i\right) + \frac{\partial}{\partial t}\left(\rho_d v_i''\right) + \frac{\partial}{\partial x_j}\Big(\rho_d \tilde{v}_i \tilde{v}_j + \rho_d \tilde{v}_i v_j'' + \rho_d v_i'' \tilde{v}_j + \rho_d v_i'' v_j''\Big) &= \\ \frac{1}{t_s}\Big(\bar{\rho}_d \bar{u}_i + \bar{\rho}_d u_i' + \rho_d' \bar{u}_i + \rho_d' u_i'\Big) - \frac{1}{t_s}\Big(\rho_d \tilde{v}_i + \rho_d v_i''\Big)\end{aligned} \tag{5.58}$$

to which we then apply the averaging operator:

$$\frac{\partial}{\partial t}\left(\bar{\rho}_d \tilde{v}_i\right) + \frac{\partial}{\partial x_j}\Big(\bar{\rho}_d \tilde{v}_i \tilde{v}_j + \overline{\rho_d v_i'' v_j''}\Big) = \frac{\bar{\rho}_d}{t_s}\left(\bar{u}_i - \tilde{v}_i\right) + \frac{1}{t_s}\overline{\rho_d' u_i'} \tag{5.59}$$

In this equation, there is one unknown correlation containing dust quantities on the l.h.s. and one unknown interfluid correlation on the r.h.s., both requiring explicit modeling. It is now apparent that the Favre-averaged momentum equation (Eq. 5.59) is much simpler than the Reynolds-averaged momentum equation (Eq. 5.36).

5.3.2 Turbulence Closures

A gradient diffusion closure, as discussed in Sec. 5.2.6, cannot be employed for the Favre-averaged equations, because the turbulent mass flux does not appear explicitly in the mean-flow equations(Champney & Cuzzi, 1990). Consequently, the unknown correlations in Eq. 5.59 must be modeled explicitly.

We first consider the *turbulent pressure tensor* $P_{d,ij} \equiv \overline{\rho_d v_i'' v_j''}$, a symmetric rank two tensor, containing correlations of density-weighted velocity fluctuations. Assuming isotropic and homogeneous turbulence, we follow Youdin & Lithwick (2007) and Shariff & Cuzzi (2011), and assume the turbulent pressure tensor to be proportional to the identity matrix $P_{d,ij} = \frac{1}{3}\overline{\rho_d v_i''^2}\delta_{ij}$.

Using the definitions from Eqs. 5.32, 5.52 and 5.56, we rewrite the on-diagonal elements of the turbulent pressure tensor as the sum of three terms

$$\overline{\rho_d v_i''^2} = \bar{\rho}_d \overline{v_i'^2} - \bar{\rho}_d v_i^{*2} + \overline{\rho_d' v_i'^2} \tag{5.60}$$

The third term on the r.h.s. of Eq. 5.60 is a triple correlation term, which, based on prevalent arguments in fluid dynamics, is either small or vanishes entirely (see e.g. Blackman & Field, 2003, for an overview of these arguments). For instance, one could apply Gaussian statistics to show that correlations of odd numbers vanish (as elaborated by Lesieur, 1997).

The second term on the r.h.s. of Eq. 5.60 is generally smaller than the first term because turbulent transport, driven by turbulent velocity dispersion, cannot exceed the velocity dispersion itself, namely $v_i^{*2} \ll \overline{v_i'^2}$. As such, the term is also negligible. Consequently, the on-diagonal elements of the turbulent pressure tensor are well-approximated by the product of mean particle density and the time-averaged velocity fluctuation squared:

$$P_{d,ii} \approx \frac{1}{3}\bar{\rho}_d \overline{v_i'^2} \tag{5.61}$$

We then apply the Hinze-Tchen model (Hinze, 1959; Tchen, 1947), and specifically use Eq. 5.49, to arrive at the explicit closure relation

$$\overline{\rho_d v_i''^2} = \bar{\rho}_d \frac{D}{t_t} \tag{5.62}$$

in which the turbulent pressure tensor is proportional to the ratio of the diffusion coefficient D and the turbulence time t_t.

An important caveat is that the velocity v_i'' in Eq. 5.62 is measured in a fixed Eulerian frame, while the Hinze-Tchen formalism is formulated in terms of Lagrangian velocities. Therefore, the equality in Eq. 5.62 holds strictly only when the distance travelled by a particle during a correlation time t_{corr} is small compared to the scale of the system itself because at this point Eulerian and Lagrangian statistics are equivalent (Biferale et al., 1995). Fortunately, this requirement is already implicitly satisfied by performing the Reynolds/Favre decomposition (see Sec. 5.2.5).
Next, we define the squared turbulent particle velocity dispersion explicitly as

$$c_d^2 \equiv \frac{D}{t_t} \tag{5.63}$$

and focus on the interfluid correlation $\overline{\rho_d' u_i'}$ that appears in the Favre-averaged momentum equation (Eq. 5.59). In the short correlation time limit ($t_{\text{corr}} \ll t_s$), particles are loosely coupled to turbulent fluctuations in the gas, and many turbulent eddies pass over an individual particle within one stopping time t_s. Consequently, in this limit, we expect particle fluid fluctuations to be entirely uncorrelated to turbulent fluctuations in the gas. Thus, the averaging operator in the second-order interfluid correlations acts independently on each quantity, i.e.,

$$\overline{\rho_d' u_i'} = \overline{\rho_d'} \cdot \overline{u_i'} \tag{5.64}$$

where the r.h.s. is by definition zero (Eq. 5.33).
In the short stopping time limit ($t_s \ll t_{\text{corr}}$), the interfluid correlation does not vanish, and we expect particles to perfectly couple to the turbulent fluctuations in the gas. Therefore, in this limit, the relation $v_i' = u_i'$ holds (Cuzzi et al., 1993), yielding $\overline{\rho_d' u_i'} = \bar{\rho}_d v_i^*$.
We propose a simple closure relation, linearly connecting the two asymptotic cases of the interfluid correlation:

$$\overline{\rho_d' u_i'} = \frac{t_{\text{corr}}}{t_t}\, \bar{\rho}_d v_i^* \tag{5.65}$$

The closure relation in Eq. 5.65 has the expected asymptotic properties, namely, $\overline{\rho_d' u_i'} \simeq 0$ for $t_{\text{corr}} \ll t_s$ and $\overline{\rho_d' u_i'} \simeq \bar{\rho}_d v_i^*$ for $t_s \ll t_{\text{corr}}$.
The set of mass and momentum equations using the new closure relations (given by Eq. 5.62 and Eq. 5.65) read:

$$\frac{\partial \bar{\rho}_d}{\partial t} + \frac{\partial}{\partial x_j}\left(\bar{\rho}_d \tilde{v}_i\right) = 0 \tag{5.57}$$

$$\frac{\partial}{\partial t}\left(\bar{\rho}_d \tilde{v}_i\right) + \frac{\partial}{\partial x_j}\left(\bar{\rho}_d \tilde{v}_i \tilde{v}_j + \frac{1}{3}\bar{\rho}_d c_d^2 \delta_{ij}\right) = -\frac{1}{t_s}\bar{\rho}_d\left(\bar{v}_i - \bar{u}_i\right) - \frac{1}{t_t}\bar{\rho}_d v_i^* \tag{5.66}$$

In the system above, Eq. 5.57 represents the mass-conservation equation without source terms, indicating that a local change in mean density $\bar{\rho}_d$ is only governed by the divergence of the total mass flux $\bar{\rho}_d \tilde{v}_i$. The dynamics of the total mass flux are described by Eq. 5.66, containing the turbulent pressure term $\bar{\rho}_d c_d^2$ that drives the dust momentum transport.
The right-hand side of Eq. 5.66 contains two dissipative terms. The first arises from aerodynamic drag between the particles and the gas fluid, acting on a timescale equal to the stopping time t_s. Note how the drag term acts on the mean velocities $\bar{v}_i$ and $\bar{u}_i$, respectively, and not on the Favre-averaged velocities ($\tilde{v}_i$, $\tilde{u}_i$). The second dissipative term dampens the transport effects caused by the turbulent particle velocity dispersion on a timescale t_t, which is generally longer than the stopping time ($t_t \geqslant t_s$). Only when $t_s \gg t_{\text{corr}}$, the timescales are almost identical ($t_t \simeq t_{\text{corr}}$). On timescales significantly shorter than t_t, the turbulent pressure term is the only relevant term for particle dynamics, a regime known as the *ballistic* regime (Taylor, 1920, in contrast to the *diffusive* regime on long timescales).
It is crucial to note that the system of Eq. 5.57 and Eq. 5.66 includes three different mean

particle velocities, the ensemble-averaged velocity $\bar{v}_i$, the turbulent transport velocity v_i^*, and the density-weighted mean velocity $\tilde{v}_i$. While these velocities are related via Eq. 5.55, there are more variables than equations, and the system in its most general form is not yet closed. We will address this issue in the following section.

5.3.3 Three-Equation Formalism

After highlighting that the system in the form of Eq. 5.57 and Eq. 5.66 is not yet closed, we address this issue in this section.

We focus on the momentum equation and use Eq. 5.55 to rewrite the first term of Eq. 5.66

$$\frac{\partial}{\partial t}\big(\bar{\rho}_d \tilde{v}_i\big) = \frac{\partial}{\partial t}\big(\bar{\rho}_d \bar{v}_i\big) + \frac{\partial}{\partial t}\big(\bar{\rho}_d v_i^*\big) \tag{5.67}$$

and recognize that the local rate of change of the total momentum $\bar{\rho}_d\tilde{v}_i$ can be written as the sum of the local rate of change of the mean momentum $\bar{\rho}_d\bar{v}_i$ and the mean turbulent flux $\bar{\rho}_d v_i^*$. Motivated by this insight, we aim to decompose Eq. 5.66 into two separate (but coupled) momentum equations, each describing the dynamics of either the mean momentum $\bar{\rho}_d\bar{v}_i$ or the mean turbulent flux $\bar{\rho}_d v_i^*$. In other words, we aim to find two equations

$$\frac{\partial}{\partial t}\big(\bar{\rho}_d \bar{v}_i\big) = ... \tag{5.68}$$

and

$$\frac{\partial}{\partial t}\big(\bar{\rho}_d v_i^*\big) = ... \tag{5.69}$$

such that the sum of Eq. 5.68 and Eq. 5.69 equals Eq. 5.66.

To find these equations, we consider two special cases. The first case is the limit of vanishing turbulence ($D \to 0$). In this limit, $v_i^* = 0$ holds, thus $\partial\bar{\rho}_d v_i^*/\partial t = 0$, and Eq. 5.66 can be written as

$$\frac{\partial}{\partial t}\big(\bar{\rho}_d \bar{v}_i\big) + \frac{\partial}{\partial x_j}\big(\bar{\rho}_d \bar{v}_i \bar{v}_j\big) = -\frac{1}{t_s}\bar{\rho}_d\big(\bar{v}_i - \bar{u}_i\big) \tag{5.70}$$

Thus, we find an expression for Eq. 5.68 in this special limit.

We compare this to a second case in which turbulence is present ($D \neq 0$) and the mean gas velocity is zero ($\bar{u} = 0$). Additionally, we assume the stopping time to be short ($t_s \ll t$) such that in this case $\bar{v}_i = 0$ holds, thus $\partial\bar{\rho}_d\bar{v}_i/\partial t = 0$, and Eq. 5.66 simplifies to

$$\frac{\partial}{\partial t}\big(\bar{\rho}_d v_i^*\big) + \frac{\partial}{\partial x_j}\left(\bar{\rho}_d v_i^* v_j^* + \delta_{ij}\frac{1}{3}\bar{\rho}_d c_d^2\right) = -\frac{1}{t_t}\bar{\rho}_d v_i^* \tag{5.71}$$

Thus, we have found the functional form of Eq. 5.69 in this special case.

Next, we aim to find the appropriate expressions for a general case. As mentioned above, we also require the sum of Eq. 5.68 and Eq. 5.69 to equal Eq. 5.66 for a general case. We note that the sum of Eq. 5.70 and Eq. 5.71 does not equal Eq. 5.66 but is missing two terms: $\partial/\partial x_j(\bar{\rho}_d\bar{v}_i v_j^*)$ and $\partial/\partial x_j(\bar{\rho}_d v_i^* \bar{v}_j)$. These terms vanish in the two aforementioned special cases, thus, we cannot yet assign them unambiguously to either Eq. 5.70 or Eq. 5.71.

However, we argue that the only possibility to ensure that the sum of Eq. 5.70 and Eq. 5.71 is equal to Eq. 5.66, while at the same time ensuring Galilean invariance and momentum conservation of each equation individually, is to assign the term $\partial/\partial x_j(\bar{\rho}_d\bar{v}_i v_j^*)$ to Eq. 5.70, and to assign term $\partial/\partial x_j(\bar{\rho}_d v_i^* \bar{v}_j)$ to Eq. 5.71.

Consequently, the general form of the two decomposed momentum equations is the following:

$$\frac{\partial}{\partial t}\big(\bar{\rho}_d \bar{v}_i\big) + \frac{\partial}{\partial x_j}\Big(\bar{\rho}_d \bar{v}_i \cdot \big(\bar{v}_j + v_j^*\big)\Big) = -\frac{1}{t_s}\bar{\rho}_d\big(\bar{v}_i - \bar{u}_i\big) \tag{5.72}$$

$$\frac{\partial}{\partial t}\big(\bar{\rho}_d v_i^*\big) + \frac{\partial}{\partial x_j}\left(\bar{\rho}_d v_i^* \cdot \big(\bar{v}_j + v_j^*\big) + \delta_{ij}\frac{1}{3}\bar{\rho}_d c_d^2\right) = -\frac{1}{t_t}\bar{\rho}_d v_i^* \tag{5.73}$$

It is straightforward to show that the sum of Eq. 5.72 and Eq. 5.73 is indeed equal to Eq. 5.66. Moreover, both transport terms can be written as a divergence, and thus do not contribute to the non-conservation of momentum. Note, Eq. 5.72 and Eq. 5.73 both have a dissipative term on their right-hand side. Thus, neither equation by itself is momentum-conserving. When we discuss the turbulent gas equations in Sec. 5.4.1, we will show that both dissipative terms also appear in the gas momentum equations (with opposite sign), thus ensuring momentum conservation in the full system.

Including the continuity equation in the following form

$$\frac{\partial \bar{\rho}_d}{\partial t} + \frac{\partial}{\partial x_j}\Big(\bar{\rho}_d\big(\bar{v}_j + v_j^*\big)\Big) = 0, \tag{5.74}$$

the system of Eq. 5.72, Eq. 5.73 and Eq. 5.74 now represents a closed system.

In this *three-equation formalism*, Eq. 5.72 describes the dynamics of the mean particle momentum $\bar{\rho}_d \bar{v}_i$. It contains the explicit drag term, and in the presence of external forces, would also contain a gravity term. In contrast, Eq. 5.73 describes the dynamics of the turbulent mass flux $\bar{\rho}_d v_i^*$. It includes a turbulent pressure term that drives turbulent transport via a pressure gradient force with the turbulent speed c_d. The dissipative term on the r.h.s. of Eq. 5.73 reestablishes equilibrium flow over a timescale t_t.

It is now apparent that the turbulent particle pressure model, as formulated above, permits non-equilibrium turbulent particle transport via an additional transport equation (Eq. 5.73), in other words, it allows for non-local transport effects.

In the following section, we will discuss the properties of the turbulent particle pressure model and compare it to the classical diffusion approaches.

5.4 Applications

After deriving a novel model for turbulent particle transport, we study its applications. First, to simple illustrative examples in Sec. 5.4.2, and then to protoplanetary disks in Sec. 5.4.3. For this, we first need to explicitly consider the turbulent gas background, which we will discuss in Sec. 5.4.1.

5.4.1 Including Turbulent Gas Dynamics

In this discussion of gas dynamics, we consider a locally isothermal gas fluid in local thermodynamical equilibrium (LTE), modeled by the set of locally isothermal Euler equations, given by (in the absence of external forces)

$$\frac{\partial \rho_g}{\partial t} + \frac{\partial}{\partial x_j}\big(\rho_g u_j\big) = 0 \tag{5.75}$$

$$\frac{\partial}{\partial t}\big(\rho_d u_i\big) + \frac{\partial}{\partial x_j}\big(\rho_g u_i v_j\big) + \frac{\partial}{\partial x_i}\big(\rho_g c_s^2\big) = -\frac{\rho_d}{t_s}\big(u_i - v_i\big) \tag{5.76}$$

These equations are the continuity equation (Eq. 5.75) and the momentum equations (Eq. 5.76). They neglect the effects of molecular viscosity, which is a valid assumption for turbulent protoplanetary disks (Shu, 1992). The locally isothermal equation of state eliminates the need for an energy equation, simplifying the analysis. The term on the r.h.s of Eq. 5.76 describes the exchange of momentum with the dust via aerodynamic drag, i.e., the back reaction.
Analogous to the procedure in Sec. 5.3.1, we formulate a set of mean-flow equations from Eqs. 5.75 and 5.76 using Favre-averages:

$$\frac{\partial \bar{\rho}_g}{\partial t} + \frac{\partial}{\partial x_j}\left(\bar{\rho}_g \tilde{u}_i\right) = 0 \tag{5.77}$$

$$\frac{\partial}{\partial t}\left(\bar{\rho}_g \tilde{u}_i\right) + \frac{\partial}{\partial x_j}\Big(\bar{\rho}_g \tilde{u}_i \tilde{u}_j + \underbrace{\overline{\rho_g u_i'' u_j''}}_{\text{I}}\Big) + \frac{\partial}{\partial x_i}\left(\rho_g c_s^2\right) = -\frac{\bar{\rho}_d}{t_s}\Big(\bar{u}_i - \tilde{v}_i\Big) - \frac{1}{t_s}\underbrace{\overline{\rho_d' u_i'}}_{\text{II}} \tag{5.78}$$

Notably, the averaged continuity equation (Eq. 5.77) is formally equivalent to the instantaneous continuity equation (Eq. 5.75) with the instantaneous variables replaced by the averaged variables ($\rho_g, u_i \rightarrow \bar{\rho}_g, \tilde{u}_i$). The source terms on the r.h.s. of Eq. 5.78 are identical to the source term of Eq. 5.59 (multiplied by -1), indicating that, even though momentum is exchanged between the gas and the dust, momentum is globally conserved.
Adopting the same closure approach as for dust, we use the closure relation of Eq. 5.65 for term II in Eq. 5.78 and recognize the turbulent pressure tensor $P_{g,ij} = \overline{\rho_g u_i'' u_j''}$ in term I. We further decompose the turbulent pressure tensor into a traceless and an isotropic tensor

$$P_{g,ij} = R_{ij} + p_t \delta_{ij} \tag{5.79}$$

Here, the *isotropic turbulent pressure* p_t is defined as

$$p_t = \overline{\rho_g u''^2} \tag{5.80}$$

and the traceless Reynolds tensor as

$$R_{ij} = \overline{\rho_g u_i'' u_j''} - p_t \delta_{ij}. \tag{5.81}$$

Incorporating these definitions, we rewrite the mean-flow gas momentum equation as follows:

$$\frac{\partial}{\partial t}\left(\bar{\rho}_g \tilde{u}_i\right) + \frac{\partial}{\partial x_j}\left(\bar{\rho}_g \tilde{u}_i \tilde{u}_j + R_{ij}\right) + \frac{\partial}{\partial x_i}\left(\bar{\rho}_g c_s^2 + p_t\right) = -\frac{\bar{\rho}_d}{t_s}\left(\bar{u}_i - \bar{v}_i\right) + \frac{1}{t_t}\bar{\rho}_d v_i^* \tag{5.82}$$

Analogous to Sec. 5.3.2, we could now use the Hinze-Tchen formalism and Eq. 5.11 to rewrite the isotropic turbulent pressure p_t in terms of the diffusion coefficient D and the correlation time t_{corr}. However, assuming subsonic turbulence as prevalent in protoplanetary disks (Hughes et al., 2011; Guilloteau et al., 2012; Flaherty et al., 2015, 2018; Teague et al., 2016), the turbulent pressure is vanishingly small compared to the thermal pressure $p_t \ll \bar{\rho}_g c_s^2$. Consequently, we safely neglect the isotropic turbulent pressure in Eq. 5.78 ($\bar{\rho}_g c_s^2 + p_t \approx \bar{\rho}_g c_s^2$).
Next, we need to specify a turbulence model for the Reynolds tensor R_{ij}. Among the numerous models available in fluid dynamics literature, the eddy viscosity model, also known as the *Boussinesq hypothesis* (see e.g. Champney & Cuzzi, 1990), is frequently used in the protoplanetary disk community. This model treats turbulent stresses in gas as an effective turbulent viscosity. The viscous stress tensor in Cartesian coordinates reads (e.g. Shu, 1992)

$$R_{ij} = \rho_g \nu \left(\frac{\partial u_i}{\partial x_j} + \frac{\partial u_j}{\partial x_i} - \frac{2}{3}\delta_{ij} \nabla \cdot \mathbf{u}\right) \tag{5.83}$$

and is parametrized by the turbulent viscosity ν, typically parametrized using the α-description of Shakura & Sunyaev (1973):

$$\nu = \alpha c_s h_g \tag{5.84}$$

We then use the gradient diffusion hypothesis to close the last remaining unknown correlation term. Specifically, we write

$$\overline{\rho_g' u_i'} = -D \frac{\partial}{\partial x_i} \rho_g \tag{5.85}$$

such that we can use Eq. 5.85 and the relation between the turbulent mass flux and the Favre average (analogous to Eq. 5.55 and Eq. 5.56 for dust), to write the mean gas velocity $\bar{u}_i$ as follows:

$$\bar{u}_i = \tilde{u}_i - \frac{D}{\rho_g} \frac{\partial}{\partial x_i} \rho_g . \tag{5.86}$$

Plugging Eq. 5.86 into Eq. 5.82, we rewrite the mean-flow equation of the gas momentum as follows:

$$\frac{\partial}{\partial t}\big(\bar{\rho}_g \tilde{u}_i\big) + \frac{\partial}{\partial x_j}\big(\bar{\rho}_g \tilde{u}_i \tilde{u}_j + \sigma_{ij}\big) + \frac{\partial}{\partial x_i}\big(\bar{\rho}_g c_s^2\big) = -\frac{\bar{\rho}_d}{t_s}\big(\tilde{u}_i - \bar{v}_i\big) + \frac{1}{t_t}\bar{\rho}_d v_i^* - \frac{D}{t_s}\frac{\bar{\rho}_d}{\bar{\rho}_g}\frac{\partial}{\partial x_i}\bar{\rho}_g \tag{5.87}$$

The above equation now only contains one explicit gas velocity variable ($\tilde{u}_i$).
The full two-fluid system of equations (gas+dust) then reads

$$\frac{\partial \bar{\rho}_g}{\partial t} + \frac{\partial}{\partial x_j}\big(\bar{\rho}_g \tilde{u}_i\big) = 0 \tag{5.77}$$

$$\frac{\partial}{\partial t}\big(\bar{\rho}_g \tilde{u}_i\big) + \frac{\partial}{\partial x_j}\big(\bar{\rho}_g \tilde{u}_i \tilde{u}_j + \sigma_{ij}\big) + \frac{\partial}{\partial x_i}\big(\bar{\rho}_g c_s^2\big) = -\frac{\bar{\rho}_d}{t_s}\big(\tilde{u}_i - \bar{v}_i\big) + \frac{1}{t_t}\bar{\rho}_d v_i^* - \frac{D}{t_s}\frac{\bar{\rho}_d}{\bar{\rho}_g}\frac{\partial}{\partial x_i}\bar{\rho}_g \tag{5.87}$$

$$\frac{\partial \bar{\rho}_d}{\partial t} + \frac{\partial}{\partial x_j}\Big(\bar{\rho}_d\big(\bar{v}_j + v_j^*\big)\Big) = 0 \tag{5.74}$$

$$\frac{\partial}{\partial t}\big(\bar{\rho}_d \bar{v}_i\big) + \frac{\partial}{\partial x_j}\Big(\bar{\rho}_d \bar{v}_i \cdot \big(\bar{v}_j + v_j^*\big)\Big) = -\frac{1}{t_s}\bar{\rho}_d\big(\bar{v}_i - \tilde{u}_i\big) + \frac{D}{t_s}\frac{\bar{\rho}_d}{\bar{\rho}_g}\frac{\partial}{\partial x_i}\bar{\rho}_g \tag{5.88a}$$

$$\frac{\partial}{\partial t}\big(\bar{\rho}_d v_i^*\big) + \frac{\partial}{\partial x_j}\left(\bar{\rho}_d v_i^* \cdot \big(\bar{v}_j + v_j^*\big) + \delta_{ij}\frac{1}{3}\bar{\rho}_d c_d^2\right) = -\frac{1}{t_t}\bar{\rho}_d v_i^* \tag{5.88b}$$

and consists of a total of eleven equations describing the dynamics of eleven unknowns ($\bar{\rho}_g, \bar{\rho}_d, \tilde{u}_{i=1,2,3}, \bar{v}_{i=1,2,3}, v^*_{i=1,2,3}$) and, thus, is a closed system of equations.

The equations for gas are the continuity equation (Eq. 5.77) and the momentum equations (Eq. 5.87) which now looks like the Navier-Stokes equation with three additional terms accounting for the interaction with the dust. The dust continuity equation (Eq. 5.74) contains two mass flux, the mean mass flux $\bar{\rho}_d \bar{v}_i$, and the turbulent mass flux $\bar{\rho}_d v_i^*$, that govern the local change of the mean gas density $\bar{\rho}_d$. The equation describing the dynamics of the mean mass flux $\bar{\rho}_d \bar{v}_i$ (Eq. 5.88a) looks like the pressureless momentum equation with which we started in Eq. 5.4, but with the instantaneous velocity v_i replaced by the mean velocity $\bar{v}$. However, it contains a new transport term on the left-hand side and a new term accounting for turbulent flows of the gas on the right-hand side. From the transport term $\bar{\rho}_d \bar{v}_i \cdot \big(\bar{v}_j + v_j^*\big)$ in Eq. 5.88a, it becomes apparent that turbulence can transport mean momentum via the turbulent velocity component v_j^*, which is the key distinction compared to the classical gradient diffusion model. Lastly, Eq. 5.88b is a new additional momentum equation that describes the dynamics of the turbulent mass flux $\bar{\rho}_d v_i^*$. It contains the turbulent pressure term $\bar{\rho}_d c_d^2$ that drives the turbulent transport, and a term $-\bar{\rho}_d v_i^*/t_t$ that acts to dissipate any directed turbulent transport. Note, in Eq. 5.88a, we used Eq. 5.86 to rewrite the gas velocity in the drag term, which is different from Eq. 5.72.

External forces, when present, would appear in Eq. 5.87 and in Eq. 5.88a.
The two-fluid system above is Galilean invariant, and it conserves total momentum (angular and linear) globally.

5.4.2 Turbulent Particle Transport Beyond Diffusion

Before we discuss the system in the presence of gravity, we discuss a simple example in the absence of external forces that illustrates the main difference between the turbulent particle pressure model and gradient diffusion.
We consider a dust distribution in a static gas background ($\tilde{u}_i = 0$) and a small dust-to-gas ratio ($\rho_d/\rho_g \ll 1$) such that the static equilibrium in gas is not affected by the motion of the dust. Further, we consider a quasi-steady state of the dust in force balance, such that the source terms in Eq. 5.88a and in Eq. 5.88b respectively cancel each other.
The conditions for force balance in Eq. 5.88a is

$$\bar{\rho}_d \bar{v}_i = D \frac{\bar{\rho}_d}{\bar{\rho}_g} \frac{\partial}{\partial x_i} \bar{\rho}_g \tag{5.89}$$

This result illustrates that the dust couples to the advection flow of the gas such that we find a mean dust flow against the mean turbulent gas flow $\bar{v}_i = \bar{u}_i = -u_i^*$, where the last equality follows from $\tilde{u}_i = 0$.
The condition for force balance in Eq. 5.88b reads (assuming a constant diffusion coefficient D)

$$\bar{\rho}_d v_i^* = -D \frac{\partial}{\partial x_i} \bar{\rho}_d - D \bar{\rho}_d \frac{\partial}{\partial x_i} \ln t_t^{-1} \tag{5.90}$$

The Eq. 5.90 describes the turbulent dust mass flux. In the first term on the r.h.s, we immediately recognize the gradient diffusion flux from Eq. 5.39. The second term on the r.h.s. is a novel contribution, predicting directed turbulent transport in the direction of increasing values of t_t [3].
We use Eq. 5.55 to combine the equilibrium flux from Eq. 5.89 and that from Eq. 5.90 to arrive at the total dust mass flux:

$$\bar{\rho}_d \tilde{v}_i = -D \rho_g \frac{\partial}{\partial x_i} \frac{\bar{\rho}_d}{\bar{\rho}_g} - D \bar{\rho}_d \frac{\partial}{\partial x_i} \ln t_t^{-1} \tag{5.91}$$

Note, the first term on the r.h.s. now contains the gradient of the *dust-to-gas ratio*.
We conclude that the first term of the turbulent transport flux $\bar{\rho}_d v_i^*$ in Eq. 5.90 is given solely by the absolute gradient of the dust density. Thus, any derivation considering the particle distribution in isolation will arrive at this functional form of the turbulent transport term. However, in this quasi-steady state, the dust couples to the flow of the gas via the explicit drag term, introducing another transport term in the direction of gas density gradients (see Eq. 5.89). The combination of these two effects results in directed transport against gradients of dust-to-gas ratio, as predicted by Eq. 5.91. Note, in a uniform background (ρ_g = const., t_t = const.), Eq. 5.91 simplifies to the classical gradient diffusion flux of Eq. 5.39.
Interestingly, in a non-uniform background, there is a novel transport term arising from gradients of t_t in Eq. 5.91, that is not predicted by any of the gradient diffusion transport models. Therefore, we now aim to confirm this prediction by means of a direct comparison to the Lagrangian turbulence model introduced in Sec. 5.2.3. Specifically, we perform a numerical experiment and study the turbulent spreading of a population of dust grains in a nonuniform, but static ($\bar{u}_i = \bar{v}_i = 0$) gas background.
We set up a numerical experiment such that the gas density in the background is constant, to

---

[3] Defining an entropy in the dust fluid as $s \equiv \ln D t_t^{-1}$, the second term in Eq. 5.90 can also be interpreted transport across an entropy gradient.

eliminate possible contributions from the first term on the r.h.s. of Eq. 5.91. However, we still allow the stopping time t_s to vary in space, e.g., via variations in the speed of sound. Note, we do not discuss the possible physical feasibility of such a setup here since our experiment is purely numerical in nature.

In our first fiducial example, we set the correlation time and the stopping time to constant values ($t_{\mathrm{corr}} = 0.01$ and $t_s = t_{s,0} = 1$ in arbitrary units) such that the stopping time t_s is long compared to the correlation time t_{corr} and consequently $t_t \simeq t_s$, and the background is modeled to be uniform. Further, we set the diffusion coefficient to a constant value of $D = 10^{-3}$ and numerically solve the stochastic equations of motion (Eqs. 5.1, 5.16, 5.17a, and 5.17b) for a number of $N = 2 \cdot 10^3$ particles, initially at rest at $x = 0$, with an explicit Euler scheme and a numerical timestep $\Delta t = 0.01 \cdot t_{\mathrm{corr}}$.

Because the stopping time t_s is constant in this first setup, we do not expect a systematic drift, only symmetric diffusive spreading of the particle population. We confirm this by showing the temporal evolution of the particles in the reference setup in the upper subplot of Fig. 5.1. In the figure, gray background colors show, for each time t, the normalized kernel density estimate of the particle positions in x-t-space. The solid red line shows the mean of the distribution $\langle x \rangle$ at each point in time, and the red-shaded region covers the region within one standard deviation of the mean value. Over time, the distribution diffusively spreads but remains centered around $x = 0$. This is the expected effect of random turbulent motions of particles in a uniform background (Visser, 1997).

In our second example, we allow the stopping time t_s to vary depending on the particle position, to model the motion of particles through a nonuniform gas background. We choose the stopping time to exponentially increase towards increasing values of x as $t_s = t_{s,0} \exp(3x)$, such that if the solution indeed follows Eq. 5.90, the expected systematic drift velocity is independent of x. We show the solution with the varying stopping time in the lower subplot of Fig. 5.1 where we plot the mean particle position with a solid blue line and shade the region within one standard deviation in blue color. We find the width of the particle distribution to spread diffusively, as in the example with a uniform background, but the mean of the distribution $\langle x \rangle$ drift towards increasing values of the turbulent timescale $t_t \simeq t_s$ with a systematic and constant velocity $v = D \nabla \ln t_s$. The mean of the particle distribution coincides with the green dashed line, which represents the prediction of Eq. 5.90.

We conclude that, in a nonuniform gas background with isotropic and homogeneous turbulence ($D =$ const., $t_{\mathrm{corr}} =$ const.), and for large particles such that $t_t \simeq t_s$, there exists systematic transport of particles towards increasing values of the stopping time t_s as described by Eq. 5.90. In other words, in this regime, the turbulent flux is non-Fickian, an effect that is not captured by classical gradient diffusion models.

In the following section, we focus on applications of the model to protoplanetary disks.

5.4.3 The Vertical Steady-State Disk Profile Revisited

In this section, we apply the turbulent particle pressure model to find an analytical solution for the vertical equilibrium profile of a protoplanetary disk. For this, we solve the system of equations along dimension z under the influence of the vertical component of the stellar gravitational field $g_z = -\Omega^2 z$. For the system to be static, the time derivatives and also the velocities vanish $\tilde{v}_z = \tilde{u}_z = 0$. Note that a static solution only requires the Favre-averaged velocities to vanish, such that the net flux is zero ($\bar{\rho}_d \tilde{v}_z = 0$) and the mean and turbulent fluxes cancel each other out ($\bar{\rho}_d \bar{v}_z + \bar{\rho}_d v_z^* = 0$), but it does not necessarily require $\bar{v}_z$ or v_z^* to vanish. The particle mass conservation equation is then fulfilled trivially, and the system of particle equations that we must solve is

$$0 = -\frac{1}{t_s} \bar{\rho}_d \bar{v}_z + \frac{D}{t_s} \frac{\bar{\rho}_d}{\bar{\rho}_g} \frac{\partial}{\partial z} \bar{\rho}_g - \bar{\rho}_d \Omega^2 z \tag{5.92a}$$

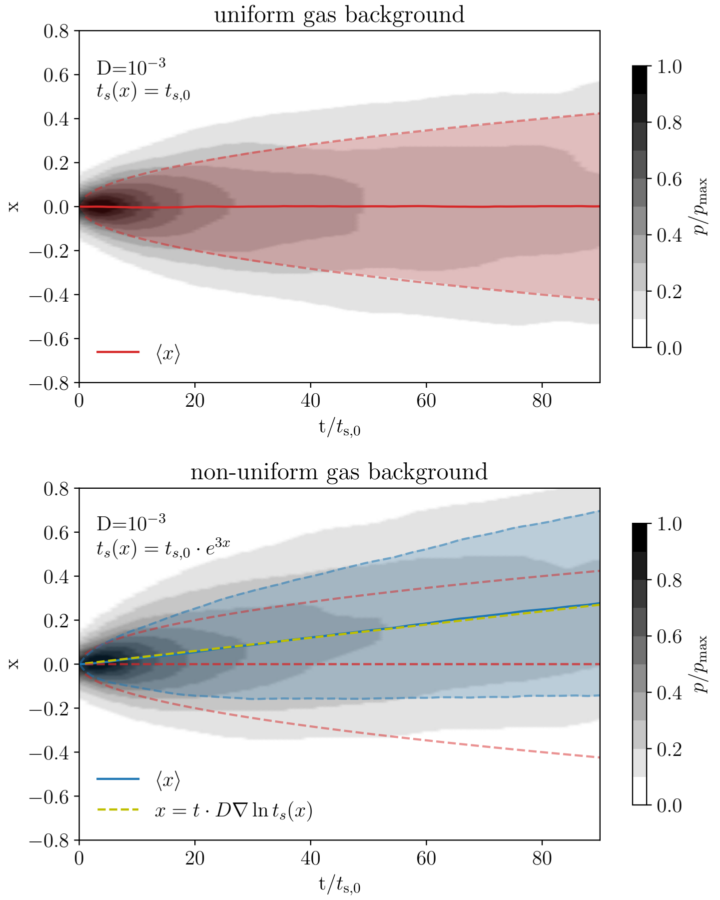

Figure 5.1: Space-time plot of the evolution of $N = 2 \cdot 10^3$ individual (Lagrangian) particles, governed by the stochastic equation of motion (Eqs. 5.16, 5.17a, 5.17b) in the absence of external forces. The gray background colors represent the normalized kernel density estimation of the particle distribution in x-t-space. All the particles are initially at rest at $x = 0$. The solid lines show, for each time t, the mean of the distribution $\langle x \rangle$, the colored shaded region covers a region within one standard deviation of the mean value. The correlation time is kept small compared to the stopping time ($t_{\text{corr}} = 0.01$). *Top:* Particles move through a uniform gas background such that the stopping time of the particles is constant in space $t_{s,0} = 1$ (in arbitrary units). The diffusively spreading distribution remains centered around $x = 0$. *Bottom:* The particles move through a nonuniform gas background in which the stopping time t_s increases exponentially in positive x-direction. As a result, the entire distribution drifts with a systematic and constant velocity $v = D\nabla \ln t_s$ towards increasing values of the stopping time (green dashed line) as predicted by Eq. 5.91. The mean of the distribution $\langle x \rangle$ is shown with a solid blue line and follows the green dashed line. For a visual comparison, the mean and standard deviation of the example in a uniform background is plotted with red dashed lines also in the bottom subplot.

$$\frac{\partial}{\partial z}\left(\frac{D}{t_t}\bar{\rho}_d\right) = -\frac{1}{t_t}\bar{\rho}_d v_z^* \tag{5.92b}$$

From $\tilde{v}_z = 0$ and Eq. 5.55, it follows that $\bar{v}_z = -v_z^*$. Without yet making use of the fact that t_{corr} and D are constant, we reduce the system of Eq. 5.92a and Eq. 5.92b to the following partial differential equation, which describes the vertical dust equilibrium profile of a protoplanetary disk:

$$\frac{\partial}{\partial z}\left[\ln\left(\frac{D}{t_t}\frac{\rho_d}{\rho_g}\right)\right] = -\frac{\Omega^2 t_s}{D} z \tag{5.93}$$

Assuming that the vertical profile of the gas background is Gaussian with scale height h_g, the solution to Eq. 5.93 becomes

$$\rho_d(z) = \rho_{d,0}\left[1 + \frac{t_{s,\mathrm{mid}}}{t_{\mathrm{corr}}}\exp\left(\frac{z^2}{2h_g^2}\right)\right]\cdot\exp\left[-\frac{\Omega t_{s,\mathrm{mid}}}{\delta}\left(\exp\left(\frac{z^2}{2h_g^2}\right)-1\right)-\frac{z^2}{2h_g^2}\right] \tag{5.94}$$

where $t_{s,\mathrm{mid}}$ is the stopping time evaluated at the disk midplane.

For subsonic turbulence ($D/t_{\mathrm{corr}} \ll c_s^2$), we find the difference between Eq. 5.94 and Eq. 5.24 to be vanishingly small. For a turbulent velocity dispersion, which is comparable to the sound speed ($u'^2 = D/t_{\mathrm{corr}} \gtrsim c_s^2$), we find the novel factor $1 + t_s/t_{\mathrm{corr}}$ in Eq. 5.94 to locally increase the dust density in regions where the stopping time is comparable or larger than the correlation time. This increase is due to the transition from drag dominated to inertia-dominated dust dynamics in the disk atmosphere.

In Fig. 5.2, we plot the vertical profile of the dust-to-gas ratio calculated with Eq. 5.94 and a Gaussian gas profile with scale height $h_g^2 = (c_s^2 + D/t_{\mathrm{corr}})/\Omega^2$ in solid lines for different values of the diffusivity δ and $t_{\mathrm{corr}}\Omega = 1$, and $St_{\mathrm{mid}} = 0.1$. For comparison, we also calculate the profile with Eq. 5.24 in dashed lines.

The different values of the diffusivity correspond to a turbulent velocity dispersion $u'^2/c_s^2 = 0.01, 0.1, 1, 10$. The two solutions differ only when the turbulent velocity dispersion approaches the speed of sound $u'^2 \gtrsim c_s^2$, in regions where dust grains decouple from turbulent eddies. For subsonic turbulence $u'^2 \ll c_s^2$, which is expected in protoplanetary disks, the two solutions are indistinguishable.

Focusing on subsonic turbulence, in the limit of small particles ($St \to 0$), the vertical scale height of the dust h_d approaches the scale height of the gas ($h_d \to h_g$) and thus fulfills the good mixing condition.

Close to the disk midplane ($z \ll h_g$), the vertical static equilibrium profile (Eq. 5.94) is approximately Gaussian. We Taylor expand Eq. 5.94 up to the second order in z, and write for small values of z ($z \ll h_g$) the ratio of the scale heights as:

$$\frac{h_d^2}{h_g^2} \approx \frac{\delta}{\delta + St} \tag{5.95}$$

where we have assumed subsonic turbulence $D/t_{\mathrm{corr}} \ll c_s^2$, which is equivalent to the relation $\delta \ll \Omega t_{\mathrm{corr}}$. We highlight that the correlation time t_{corr} does not appear in Eq. 5.95 as a result of assuming subsonic turbulence.

To our knowledge, we present for the first time, a self-consistent derivation of the vertical settling-diffusion equilibrium profile that correctly captures the small and large particle limits, without the use of a heuristic argument.

Next, we derive an effective vertical diffusion coefficient $D_{d,z}^{\mathrm{eff}}$ analogous to Carballido et al. (2011). We assume the dust scale height to be small compared to the gas scale height ($h_d \ll h_g$), such that the dust settles into a thin region close to the midplane in which the gas density is basically constant in the vertical direction. From Eq. 5.86, it then follows that $\bar{u}_z = 0$ and, we can safely neglect the interactions of the dust with the gas via the explicit drag term that would

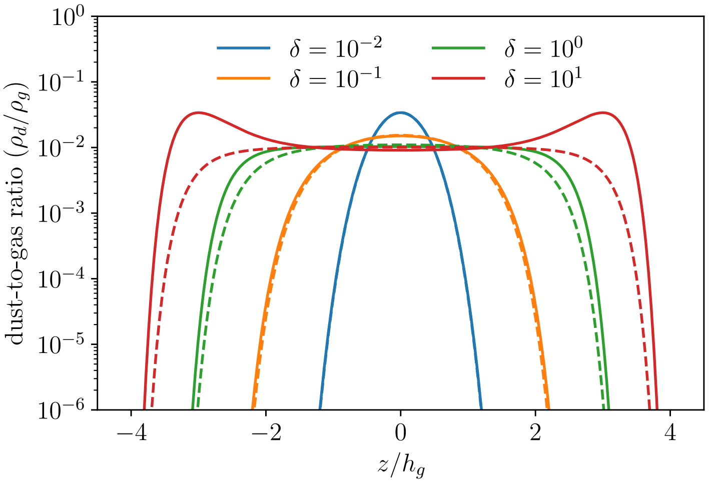

Figure 5.2: Vertical steady-state profile of the dust-to-gas ratio. The solid lines represent Eq. 5.94 for $St_{\mathrm{mid}} = 0.1$ and $t_{\mathrm{corr}}\Omega = 1$, and different values of the diffusivity δ. The vertical gas profile is assumed Gaussian and the surface density ratio is 1:100. The dashed lines follow the gradient diffusion solution of Eq. 5.24. The different values of the diffusivity correspond to $u'^2/c_s^2 = 0.01, 0.1, 1, 10$ where $u'^2 = D/t_{\mathrm{corr}}$ represents the squared turbulent velocity dispersion. The two solutions differ only when the turbulent velocity dispersion approaches the speed of sound $u'^2 \gtrsim c_s^2$, in regions where dust grains decouple from turbulent eddies. For subsonic turbulence $u'^2 \ll c_s^2$, the two solutions are indistinguishable.

be present in a nonuniform gas background. From the condition $h_d \ll h_g$ and Eq. 5.95, it follows that

$$\frac{h_d^2}{h_g^2} = \frac{\delta}{St} \tag{5.96}$$

We then set the diffusion timescale t_{diff} (Eq. 5.13) across the dust scale height, i.e. $t_{\mathrm{diff}} = h_d^2/D_{d,z}^{\mathrm{eff}}$, equal to the vertical settling time t_{sett}. To estimate the settling time, we note that large particles ($St \gg 1$) undergo damped vertical oscillation with a settling time $t_{\mathrm{sett}} = St/\Omega$. Tightly coupled particles ($St \ll 1$) obtain terminal velocity and settle in a time $t_{\mathrm{sett}} = 1/\Omega St$. Combining these two results gives (Youdin & Lithwick, 2007):

$$t_{\mathrm{sett}} \approx \frac{St}{\Omega} + \frac{1}{\Omega St} \tag{5.97}$$

Combining Eq. 5.96 and Eq. 5.97 to calculate an effective diffusion coefficient gives

$$D_{d,z}^{\mathrm{eff}} = \frac{D}{1 + St^2} \tag{5.98}$$

in agreement with Carballido et al. (2011) and Youdin & Lithwick (2007).

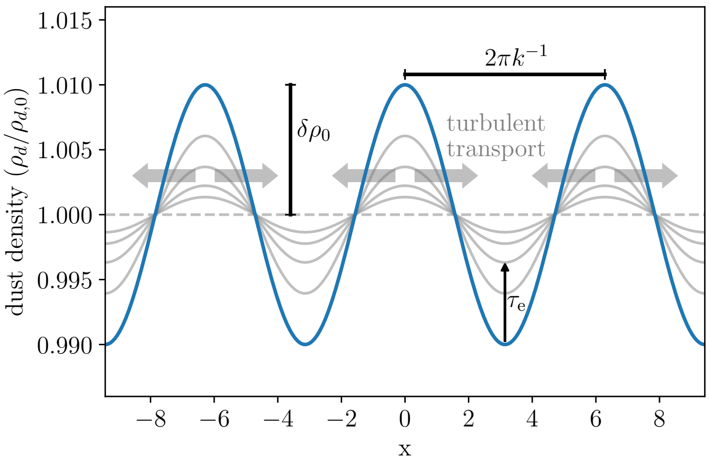

Figure 5.3: This figure illustrates the turbulent decay of a harmonic perturbation to the dust density ρ_d, as analyzed in the linear perturbation analysis in Sec. 5.5, in arbitrary units. The perturbation is characterized by its amplitude $\delta\rho_0$, which is small compared to the background, $\delta\rho_0 \ll \rho_{d,0}$. Its wavenumber k is related to the wavelength of the perturbation as $\lambda = 2\pi k^{-1}$. The blue line represents the initial state of the perturbation, while the gray lines represent the decaying solutions at every half e-folding time, τ_e. An effective diffusion coefficient D^{eff} can be calculated as the inverse of the product of the e-folding time τ_e, and the square of the perturbation's wavenumber, $D^{\text{eff}} = \tau_e^{-1}k^{-2}$. An effective diffusion coefficient can be calculated for any decaying perturbation, but only in a purely diffusive solution D^{eff} is independent of the wavenumber k.

5.4.4 Large Grains Limit

In the limit of large grains ($t_s \gg t_{\text{corr}}$), the two momentum equations, Eq. 5.88a and Eq. 5.88b, can be combined to one equation which reads

$$\frac{\partial}{\partial t}\left(\bar{\rho}_d\tilde{v}_i\right) + \frac{\partial}{\partial x_j}\left(\bar{\rho}_d\tilde{v}_i\tilde{v}_j + \frac{1}{3}\frac{D}{t_s}\bar{\rho}_d\delta_{ij}\right) = -\frac{1}{t_s}\bar{\rho}_d\left(\tilde{v}_i - \bar{u}_i\right) + \frac{D}{t_s}\frac{\bar{\rho}_d}{\bar{\rho}_g}\frac{\partial}{\partial x_i}\bar{\rho}_g. \tag{5.99}$$

In general, Eq. 5.88a and Eq. 5.88b can always be combined to give Eq. 5.66, but only in this limit of large grains, the two velocities $\bar{v}_i$ and v_i^* can be eliminated and Eq. 5.99 can be written in terms of $\tilde{v}_i$ only. Consequently, a second dust momentum equation is not needed anymore for the system of Eq. 5.57 and Eq. 5.99 to be closed, and the system of equations is simplified.
In a uniform gas background ($\rho_g = \text{const.}$), the second term on the r.h.s of Eq. 5.99 vanishes and the equation is formally identical to Eq. 5.43. Therefore, the model of Klahr & Schreiber (2021), can be interpreted as the large-grain limit of our more general model.

5.5 Linear Perturbation Analysis

We perform a linear perturbation analysis to investigate the linear dynamics of our novel turbulent transport model and to identify key characteristics of the turbulent transport model derived in this work. We first study a one-dimensional problem in Sec. 5.5.1, before we focus on a two-dimensional and axisymmetric disk in Sec. 5.5.3.

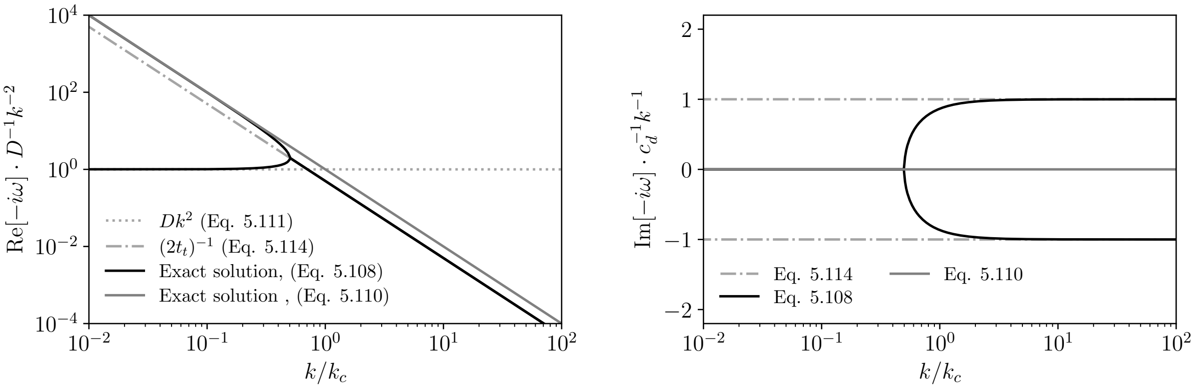

Figure 5.4: Decay rates $-i\omega(k)$ of harmonic perturbations in one dimension in the absence of external forces, i.e., the solution to the dispersion relation in Eq. 5.107. Shown here is a case $t_{\mathrm{corr}} \ll t_s$ such that $t_t \approx t_s$. *Left:* Shows the real part of the decay rates ($\mathrm{Re}[-i\omega(k)]$) normalized by the factor Dk^2, such that diffusive solutions are represented by lines with slope zero. The black solid lines represent the two exact solutions of Eq. 5.108. The gray solid line represents the third exact solution in Eq. 5.110. For $k^2 \gg k_c^2$, there exists no diffusive solution. The gray dotted line traces the diffusive solution (Eq. 5.111) that coincides with the exact solution on small scales ($k^2 \ll k_c^2$). The gray dash-dotted line represents the solution in Eq. 5.114. *Right:* Imaginary part of the decay rate ($\mathrm{Im}[-i\omega]$) normalized by a factor $c_d k$. A non-zero value represents a traveling wave solution, and a zero-slope line represents solutions traveling at the same speed. The black solid lines show the exact solutions to Eq. 5.107. The gray dot-dashed line follows the two analytic solutions of Eq. 5.114, valid for $k^2 \gg k_c^2$. For small wave numbers ($k^2 \ll k_c^2$), these solutions are not travelling ($\mathrm{Im}[i\omega] = 0$), as predicted by the explicit solutions in Eq. 5.112 and Eq. 5.113.

5.5.1 One Dimension Without External Forces

We model dust in a turbulent and uniform gaseous background (with constant $\bar{\rho}_g$) in one dimension along the x-axis. We assume the gas to be static ($\tilde{u} = 0$). From Eq. 5.86, it then follows that $\bar{u} = 0$ and consequently $u^* = 0$. As always in this work, we assume the turbulence to be characterized by a constant diffusion coefficient D and constant correlation time t_{corr}. We describe the dust fluid using the linearized forms of Eq. 5.57 and Eq. 5.66 and assume the dust-to-gas ratio to be small $\bar{\rho}_d/\bar{\rho}_g \ll 1$, such that the dust does not affect the gas. We will introduce small harmonic perturbations to the linearized dust density and velocity equations on top of a static background distribution.

The set of linearized equations is as follows:

$$\frac{\partial \bar{\rho}_d}{\partial t} + \bar{\rho}_d \frac{\partial}{\partial x}(\bar{v} + v^*) = 0 \tag{5.100}$$

$$\frac{\partial \bar{v}}{\partial t} = -\frac{\bar{v}}{t_s} - \frac{D}{t_t \bar{\rho}_d}\frac{\partial \bar{\rho}_d}{\partial x} \tag{5.101}$$

$$\frac{\partial v^*}{\partial t} = -\frac{v^*}{t_t} \tag{5.102}$$

We describe the perturbed dust density as $\bar{\rho}_d = \bar{\rho}_{d,0} + \delta\rho_d$, where the perturbation $\delta\rho_d$ is small compared to the background $\bar{\rho}_{d,0}$. This perturbation to the dust density is illustrated in Fig. 5.3. We also introduce a perturbation to the turbulent transport velocity $v^* = \delta v^*$ and to the mean velocity $\bar{v} = \delta\bar{v}$. The perturbations are harmonic and have the form

$$\delta\rho_d = \delta\rho_0 e^{i(\omega t + kx)} \tag{5.103}$$

$$\delta\bar{v} = \delta\bar{v}_0 e^{i(\omega t + kx)} \tag{5.104}$$

$$\delta v^* = \delta v_0^* e^{i(\omega t + kx)} \tag{5.105}$$

where ω is the frequency and k is the wavenumber of the perturbations.

Plugging in the perturbed quantities into the linearized equations, and considering at most first-order terms, we find the following equations that we represent as a three-dimensional matrix equation as follows:

$$i\omega \begin{pmatrix} \delta\rho_d \\ \delta\bar{v} \\ \delta v^* \end{pmatrix} = \begin{pmatrix} 0 & -ik\bar{\rho}_{d,0} & -ik\bar{\rho}_{d,0} \\ 0 & -t_s^{-1} & 0 \\ -ik\frac{D}{t_t\bar{\rho}_{d,0}} & 0 & -t_t^{-1} \end{pmatrix} \begin{pmatrix} \delta\rho_d \\ \delta\bar{v} \\ \delta v^* \end{pmatrix} \tag{5.106}$$

The dispersion relation of the equation above reads

$$\Big(i\omega\big(i\omega + t_t^{-1}\big) + Dk^2 t_t^{-1}\Big)(i\omega + t_s^{-1}) = 0 \tag{5.107}$$

which has two symmetric solutions

$$i\omega_{1,2} = -\frac{1}{2t_t}\left(1 \pm \sqrt{1 - 4\frac{k^2}{k_c^2}}\right) \tag{5.108}$$

where we have defined the *characteristic wavenumber* k_c as

$$k_c^2 \equiv D^{-1} t_t^{-1} \tag{5.109}$$

and a third solution

$$i\omega_3 = -t_s^{-1} \tag{5.110}$$

A solution to the dispersion relation $i\omega$ is called the *growth rate* of the perturbation. Conversely, $-i\omega$ is called the *decay rate*. In Fig. 5.4, we plot the decay rates $-i\omega(k)$, i.e., the solutions to Eq. 5.107, as solid lines for the special case $t_{\mathrm{corr}} \ll t_s$.

Dynamics on Large Scales (small wave numbers $k^2 \ll k_c^2$)

We analytically study the growth rates on large scales, i.e., small wave numbers $k^2 \ll k_c^2$, where the three solutions to the dispersion relation in Eq. 5.107 are real-valued and negative and can be approximated by

$$i\omega_1 = -Dk^2 \tag{5.111}$$

$$i\omega_2 = -t_t^{-1} \tag{5.112}$$

$$i\omega_3 = -t_s^{-1} \tag{5.113}$$

The three growth rates represent decaying solutions because they are all real-valued and negative. We plot these approximate solutions as gray discontinuous lines as a function of the wave number k in Fig. 5.4 on top of the exact solutions.

Dynamics on Small Scales (large wave numbers $k^2 \gg k_c^2$)

On small spatial scales, i.e., for large wave numbers, the first two solutions to the dispersion relation in Eq. 5.107 can be approximated by

$$i\omega_{1,2} = -\frac{1}{2t_t} \pm ikc_d \tag{5.114}$$

We plot the above growth rate as a gray dot-dashed line as a function of the wave number k in Fig. 5.4. It coincides with the exact solution (black line) for $k^2 \gg k_c^2$. The imaginary part of Eq. 5.114 indicates that the eigensolutions are traveling waves that propagate at speed $c_d = \sqrt{D/t_t}$. The speed of propagation is identical to the value of the turbulent particle dispersion (Eq. 5.63). This traveling wave solution was first discussed in Klahr & Schreiber (2021), but their model predicts a non-physical supersonic wave speed for short stopping times $t_s < D/c_s^2$ and thus must be modified in their model. In this model, the propagation speed c_d does never exceed the turbulent gas velocities, even for short stopping times (see Eq. 5.63).
We write the real parts of the eigensolutions that correspond to the first two eigenvalues in Eq. 5.114 explicitly as

$$\mathrm{Re}(\delta\rho_d) = \pm\delta v_0^* \frac{\bar{\rho}_{d,0}}{D} \cos(kx \pm kc_d t)e^{-t/2t_t} \tag{5.115}$$

$$\mathrm{Re}(\delta v^*) = \delta v_0^* \cos(kx \pm kc_d t)e^{-t/2t_t} \tag{5.116}$$

$$\mathrm{Re}(\delta\bar{v}) = 0 \tag{5.117}$$

These expressions indeed describe waves traveling at speed c_d and decaying on a timescale $\tau = 2t_t$. The third solution to the dispersion relation in Eq. 5.107 has the same form on small scales as on large scales, and decays on a timescale equal to the stopping time without an oscillating imaginary component:

$$i\omega_3 = -t_s^{-1} \tag{5.118}$$

Physical Interpretation of Turbulent Dust Transport in 1D

On large scales ($k^2 \ll k_c^2$), the first eigenvalue in Eq. 5.111 represents a non-oscillating perturbation that decays on an e-folding time $\tau_1 = D^{-1}k^{-2}$, which is equivalent to a diffusive decay characterized by diffusion coefficient D. The corresponding eigensolutions (δv^*, $\delta\rho_\mathrm{d}$) to this eigenvalue fulfill the relation

$$\bar{\rho}_{\mathrm{d},0}\delta v^* = -ikD\delta\rho_\mathrm{d} \tag{5.119}$$

Using Eq. 5.103, this expression can be rewritten as

$$\bar{\rho}_\mathrm{d}\delta v^* = -D\frac{\partial}{\partial x}\bar{\rho}_\mathrm{d} \tag{5.120}$$

It is apparent that Eq. 5.120 represents the gradient diffusion equilibrium flux under force balance (compare to Eq. 5.90) and thus confirms the diffusive nature of this eigensolution.

The second and third eigensolutions corresponding to the eigenvalues in Eq. 5.112 and in Eq. 5.113, do not fulfill the force balance given by Eq. 5.90. Instead, the eigensolutions represent perturbations that evolve towards restoring the force balance on an e-folding time $\tau_2 = t_t$ and $\tau_3 = t_s$, respectively.

To summarize, on large scales ($k^2 \ll k_c^2$), we have found three characteristic solutions. The first solution represents a diffusive decay of a perturbation under force balance on a timescale $\tau_1 = D^{-1}k^{-2}$. The other two solutions represent the decay of an out-of-equilibrium perturbation.

On large scales ($k^2 \ll k_c^2$), the decay of the out-of-equilibrium perturbation is much faster than the diffusive decay of the first solution because, according to Eq. 5.109, on large scales, $t_t \ll D^{-1}k^{-2}$, and also $t_s \ll D^{-1}k^{-2}$, hold. This indicates that the long-time evolution of large-scale perturbations is dominated by diffusive processes.

On small scales ($k^2 \gg k_c^2$), the decay rates either follow the decaying wave solution of Eq. 5.114 or the decaying non-traveling solution of Eq. 5.118, which are both independent of the wavenumber k, indicating that on small scales, there exists no diffusive solution.

This property of our turbulent pressure model is distinctly different from a gradient diffusion model, in which diffusive solutions, per definition, exist on all scales (see Sec. 5.5.2).

From a physics point of view, a diffusive solution does not exist on small scales because momentum cannot be transferred from the turbulent gas to the dust on timescales smaller than t_t (or vice versa). A purely diffusive solution would require perturbation to decay on a timescale $\tau = D^{-1}k^{-2}$ which is per definition smaller than t_t for wave numbers larger than k_c.

We conclude that small-scale perturbations (for wave numbers $k^2 \gg k_c^2$) in this model survive for longer than a purely diffusive evolution would predict, due to the finite coupling of the dust to turbulence.

In Sec. 5.6.3, we will illustrate the difference between the gradient diffusion model and the pressure-driven turbulent transport model (in the case $t_\mathrm{corr} \ll t_s$) in an example of a decaying Gaussian perturbation.

Lastly, we aim to provide an intuitive explanation for the traveling wave solution, which is somewhat unexpected to occur in the originally pressureless dust fluid. This behavior mirrors a sound wave in gas because particles in a high-density region spread out towards an equilibrium distribution, driven by turbulent mixing, similar to how gas molecules in a high-pressure region spread due to thermal pressure. In our model, turbulent dust fluxes carry momentum and thus have inertia. The inertia of the dust particles causes the particles to overshoot their equilibrium distribution, creating another overdensity. This process then restarts and can be described as a wave. Ultimately, the wave solution is a result of turbulence-driven rarefaction and consequent compression from inertia. Further investigations should confirm if these traveling waves are physical or just artifacts of the Reynolds/Favre averaging process.

5.5.2 Gradient Diffusion in One Dimension

For completeness, we also present the linear perturbation analysis and the corresponding decay rates for the gradient diffusion model (see also Weber et al., 2019, for a more extended discussion). Specifically, we analyze the mass equation in Eq. 5.22 and the pressureless momentum equation (Eq. 5.4). The linearized system in its matrix representation reads:

$$i\omega \begin{pmatrix} \delta\rho_d \\ \delta v \end{pmatrix} = \begin{pmatrix} -Dk^2 & -ik\rho_{d,0} \\ 0 & -t_s^{-1} \end{pmatrix} \begin{pmatrix} \delta\rho_d \\ \delta v \end{pmatrix} \tag{5.121}$$

This system has the following dispersion relation:

$$(Dk^2 + i\omega)(t_s^{-1} + i\omega) = 0 \tag{5.122}$$

The dispersion relation has the following two solutions that describe monotonically decaying perturbations:

$$i\omega_1 = -t_s^{-1} \tag{5.123}$$

$$i\omega_2 = -Dk^2 \tag{5.124}$$

The set of eigenstates of the linearized system in Eq. 5.121 that belongs to the growth rate in Eq. 5.123 is:

$$\mathrm{Re}(\delta v_1) = \delta v_0 \cos(kx) e^{-t/t_s} \tag{5.125}$$

$$\mathrm{Re}(\delta\rho_1) = \delta v_0 \frac{k\rho_{d,0}}{Dk^2 - t_s^{-1}} \sin(kx) e^{-t/t_s} \tag{5.126}$$

The above eigenstates represent solutions that exponentially decay on a timescale t_s due to drag. The set of eigenstates that belong to the growth rate in Eq. 5.124 is:

$$\mathrm{Re}(\delta v_2) = 0 \tag{5.127}$$

$$\mathrm{Re}(\delta\rho_2) = \delta\rho_0 \cos(kx) e^{-Dk^2 t} \tag{5.128}$$

The second set of eigenstates represents a diffusive solution that decays on a timescale $D^{-1}k^{-2}$. We plot the decay rates of the solutions in Eq. 5.123 and Eq. 5.124 in Fig. 5.5. Compared to the decay rates of the turbulent pressure model illustrated in Fig. 5.4, the diffusive solution also exists on small spatial scales ($k > k_c$).

5.5.3 Axisymmetric Keplerian Disk

After considering the one-dimensional case in the absence of external forces, we now consider a two-dimensional and axisymmetric Keplerian disk in the presence of gravity. We follow a dust fluid parcel along its orbit and use the linearized local shearing box approximation to describe its dynamics (Goldreich & Lynden-Bell, 1965; Youdin, 2011a). For this, we integrate the dynamical equations, i.e., Eq. 5.74, Eq. 5.88a, and Eq. 5.88b, along the vertical axis and rewrite the dynamical equations in local variables $r = r_0(1 + x)$ such that $x \ll 1$, and in terms of the dust surface density $\bar{\Sigma}_d$ and the two velocity components $\bar{v}_r$, v_r^* and $\bar{v}_\phi$, v_ϕ^*. The five linearized equations of the axisymmetric system are as follows:

$$\frac{\partial \bar{\Sigma}_d}{\partial t} + \bar{\Sigma}_d \frac{\partial}{\partial x}(v_r^* + \bar{v}_r) = 0 \tag{5.129}$$

$$\frac{\partial \bar{v}_r}{\partial t} - 2\Omega(v_\phi^* + \bar{v}_\phi) = -\frac{\bar{v}_r}{t_s} \tag{5.130}$$

$$\frac{\partial \bar{v}_\phi}{\partial t} + \frac{1}{2}\Omega(v_r^* + \bar{v}_r) = -\frac{\bar{v}_\phi}{t_s} \tag{5.131}$$

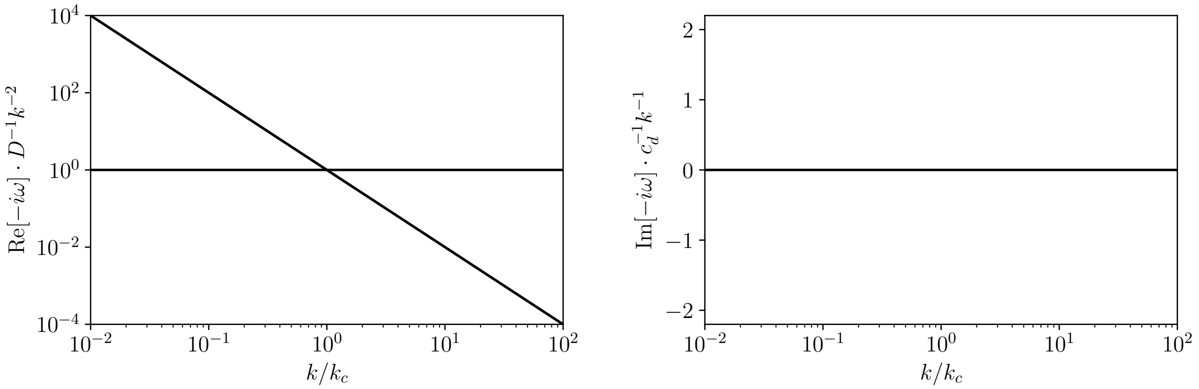

Figure 5.5: The figure illustrates the decay rates $-i\omega$ that characterize the decay of a harmonic perturbation in one dimension in the gradient diffusion model (i.e., solutions to Eq. 5.122). The horizontal line corresponds to Eq. 5.124, and the line with a negative slope corresponds to Eq. 5.123. *Left:* Shows the normalized negative real part ($-\mathrm{Re}[i\omega]$), i.e., the decay rate of harmonic perturbations, as a function of the wavenumber k. The solutions are normalized by the factor Dk^2, such that a line with zero slope represents a diffusive solution. *Right:* This shows the imaginary part of the solution ($\mathrm{Im}[i\omega]$) to the dispersion relation, as given by Eq. 5.122. Both solutions of the gradient diffusion model have a vanishing imaginary part.

$$\frac{\partial v_r^*}{\partial t} = -\frac{v_r^*}{t_t} - \frac{D}{t_t \bar{\Sigma}_d} \frac{\partial}{\partial x} \bar{\Sigma}_d \tag{5.132}$$

$$\frac{\partial v_\phi^*}{\partial t} = -\frac{v_\phi^*}{t_t} \tag{5.133}$$

We introduce small perturbations, analogous to Eqs. 5.103-5.105, in the radial direction to the dust surface density $\bar{\Sigma}_d = \bar{\Sigma}_{d,o} + \delta\Sigma_d$ and the radial and azimuthal components of the velocities ($\bar{v}_r = \delta\bar{v}_r$, $v_r^* = \delta v_r^*$, $\bar{v}_\phi = \bar{v}_{\phi,0} + \delta v_\phi$, $v_\phi^* = \delta v_\phi$). The azimuthal component of the mean velocity describes the Keplerian shear $\bar{v}_{\phi,0} = \Omega r_0(1 - \frac{3}{2}x)$.

We plug in the harmonic perturbations to the linearized equations and consider only first-order terms. The system in matrix notation reads

$$i\omega \begin{pmatrix} \delta\bar{\Sigma}_d \\ \delta\bar{v}_r \\ \delta\bar{v}_\phi \\ \delta v_r^* \\ \delta v_\phi^* \end{pmatrix} = \begin{pmatrix} 0 & -ik\bar{\Sigma}_{d,0} & 0 & -ik\bar{\Sigma}_{d,0} & 0 \\ 0 & -t_s^{-1} & 2\Omega & 0 & 2\Omega \\ 0 & -\Omega/2 & -t_s^{-1} & -\Omega/2 & 0 \\ -\frac{ikD}{t_t\bar{\Sigma}_d} & 0 & 0 & -t_t^{-1} & 0 \\ 0 & 0 & 0 & 0 & -t_t^{-1} \end{pmatrix} \begin{pmatrix} \delta\bar{\Sigma}_d \\ \delta\bar{v}_r \\ \delta\bar{v}_\phi \\ \delta v_r^* \\ \delta v_\phi^* \end{pmatrix} \tag{5.134}$$

The fifth-order dispersion relation in Eq. 5.134 is too complex to study analytically. Therefore, we determine its solutions numerically. In Fig. 5.6, we plot the decay rates of the eigensolutions to the system in Eq. 5.134 as black solid lines for values of $St = 10$ and $t_{\mathrm{corr}}\Omega = 1$.

Next, we study the dispersion relation in two limiting cases: large scales (in Sec. 5.5.3) and small scales (in Sec. 5.5.3).

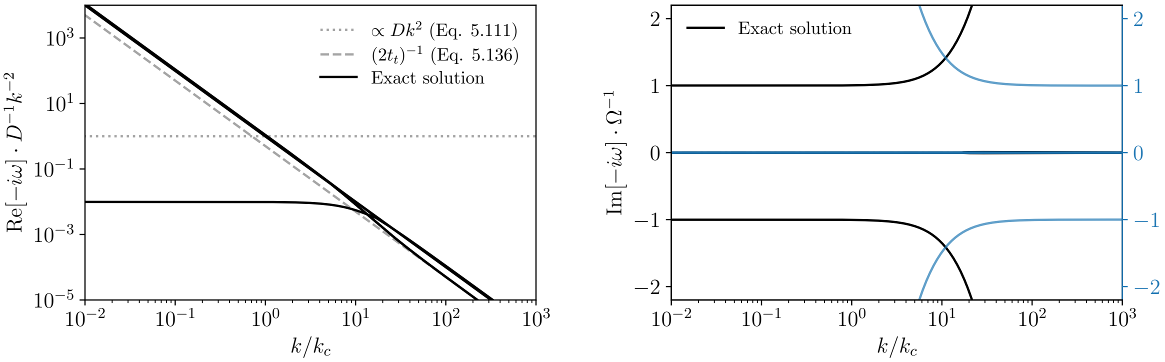

Figure 5.6: We illustrate the decay rates $-i\omega(k)$ of harmonic perturbation to the dust density in a two-dimensional, axisymmetric Keplerian disk. Shown is the numerical solution to the dispersion relation of Eq. 5.134 for $\Omega t_{\mathrm{corr}} = 1$ and $St = 10$. *Left:* Shows the real part of the decay rates ($\mathrm{Re}[-i\omega]$), normalized by the factor Dk^2, such that diffusive solutions are represented by lines with slope zero. The black solid lines represent the exact solutions. The gray dashed lines represent the solution given by $-i\omega = (2t_t)^{-1}$ as in Eq. 5.136. The gray dotted line represents a diffusive solution $-i\omega = Dk^2$. Note, how the actual diffusive solution (horizontal black line) decays a factor 100 slower than expected due to the effects of epicyclic oscillations and the factor $1/(1 + t_t^2\Omega^2)$ reducing the effective diffusivity in radial direction (Eq. 5.140). *Right:* Imaginary part of the normalized decay rate ($\mathrm{Im}[-i\omega]$). The black solid lines represent the exact solutions and are normalized by a factor Ω^{-1} such that the epicyclic frequency represents a horizontal line at $\mathrm{Im}[-i\omega]\Omega^{-1} = \pm 1$. The blue solid line represents the same solution but is normalized by a factor $c_d k$ such that a horizontal line represents wave solutions traveling at speed c_d.

Dynamics on Small Scales (large wave numbers)

On small scales, i.e., for large wave numbers $k^2 \gg k_c^2(1+St^2)$, we identify four traveling solutions with a constant decay rate (see Sec. 5.5.3 for an explanation of why there is an additional factor $1+St^2$). The first two solutions decay on a timescale equal to the stopping time t_s:

$$\mathrm{Re}[i\omega_{1,2}] = -t_s^{-1} \tag{5.135}$$

The third and the fourth solutions decay on a timescale equal to $2t_t$:

$$\mathrm{Re}[i\omega_{3,4}] = -(2t_t)^{-1} \tag{5.136}$$

The fifth and final solution is a non-traveling solution and decays on a timescale equal to t_t:

$$i\omega_5 = -t_t^{-1} \tag{5.137}$$

For comparison with the exact solution across all scales, we illustrate the decay rates of the limiting solutions, as discussed here, on the l.h.s of Fig. 5.6. For $t_s \gg t_{\mathrm{corr}}$, Eq. 5.135 and Eq. 5.136 are indistinguishable. Therefore, only two parallel lines appear in the lower right corner of the left subplot in Fig. 5.6.

Notably, there exists no diffusive solution on small scales ($k^2 \gg k_c^2(1+St^2)$) akin to the behavior in one dimension as discussed in Sec. 5.5.1. Assuming $t_t = \Omega^{-1}$, a disk aspect ratio of $h_g/r = 0.05$ and a diffusivity $\delta = 10^{-3}$, as appropriate for turbulent protoplanetary disks, the wave number k_c corresponds to a length scale $2\pi k_c^{-1} \sim 0.2h_g$, i.e., 20 percent of the gas scale height. This is comparable to the vertical scale height of a dust disk with $St_{\mathrm{mid}} = 0.025$ ($h_d/h_g \sim \sqrt{\delta/St} \sim 0.2$).

Dynamics on Large Scales (small wave numbers)

On large scales, i.e., for small wave numbers ($k^2 \ll k_c^2(1+St^2)$), we find not five, but four decay rates that are independent of the wavenumber k. Two of them decay again on a timescale equal to the stopping time:

$$\mathrm{Re}[i\omega_{1,2}] = -t_s^{-1} \tag{5.138}$$

Another pair decays on a constant timescale equal to t_t:

$$\mathrm{Re}[i\omega_{3,4}] = -t_t^{-1} \tag{5.139}$$

For $t_s \gg t_{\mathrm{corr}}$, the solution in Eq. 5.138 is indistinguishable from the solution in Eq. 5.139. Therefore, the four solutions are represented by only a single sloped line in the upper left corner of the left subplot of Fig. 5.6.

The fifth solution that we find on large scales is a diffusive solution akin to Eq. 5.111 in one dimension and is therefore distinctly different from the other four:

$$i\omega_5 = -\frac{Dk^2}{1+St^2} \tag{5.140}$$

The decay rate in Eq. 5.140 is proportional to $\propto k^2$ and thus has the properties of a diffusive solution. Notably, compared to the diffusive solution in one dimension, the decay rate is modified by an additional factor $1/(1+St^2)$, i.e., the solution decays more slowly for Stokes numbers above unity, where it scales as St^{-2}. This is also the reason the transition from small-scale behavior to large-scale behavior occurs at a wavenumber $k = k_c\sqrt{1+St^2}$, which is a factor of $\sqrt{1+St^2}$ above the characteristic wavenumber k_c (i.e., at smaller scales for $St > 1$).

Based on the result in Eq. 5.140, we define the effective radial dust diffusion coefficient as

$$D_{d,r}^{\mathrm{eff}} = \frac{D}{1+St^2} \tag{5.141}$$

where D is the diffusion coefficient, calculated using the values of the correlation time t_{corr} and the squared turbulent velocity dispersion u'^2, as in Eq. 5.11. Here, the effective radial dust diffusion coefficient $D_{d,r}^{\mathrm{eff}}$ is the actual measure of the strength of turbulent dust diffusion in radial direction. Interestingly, the strength of turbulent diffusion is independent of the correlation time t_{corr}. As such, this result is in agreement with Eq. 5.30 and confirms the findings of Youdin & Lithwick (2007).

In Fig. 5.7, we plot the numerically determined diffusive solution of the dispersion relation of Eq. 5.134 as a function of the Stokes number (black line). In Fig. 5.7, we also plot the exact result of Youdin & Lithwick (2007) regarding radial turbulent transport in an axisymmetric disk (their Eq. 37). For small Stokes numbers ($St \ll 1$), our solution is identical to that of Youdin & Lithwick (2007). For large Stokes numbers ($St \gg 1$), our solution and the detailed formula of Youdin & Lithwick (2007) have the same scaling ($\propto St^{-2}$) but deviate by a constant factor of an order of unity.

Physical Interpretation

We provide a physical explanation for the reduced strength of radial diffusion in a two-dimensional disk by reiterating the explanation by Youdin & Lithwick (2007).

We consider the case $t_s \gg t_{\mathrm{corr}}$ and $St \gg 1$ so that particles decouple from the turbulent motion and also the orbital motion of gas. In a Keplerian disk, these loosely coupled particles undergo epicyclic oscillations with frequency Ω and length scale $l_{\mathrm{epi}} = \sqrt{u'^2}/\Omega$. As the particles undergo epicyclic oscillations, they receive short uncorrelated kicks of duration t_{corr}. An individual particle receives a number of $N = 1/(t_{\mathrm{corr}}\Omega)$ velocity kicks of magnitude $v_{\mathrm{kick}} \sim \sqrt{u'^2}/(t_s\Omega)$ during an orbital oscillation. Interpreting this as a random walk, the total change in the velocity of a particle during an orbital time is $\delta v \sim v_{\mathrm{kick}}\sqrt{N} \sim \sqrt{u'^2 t_{\mathrm{corr}}}/t_s$, which moves the particle a distance of $\delta r \sim \delta v \Omega^{-1}$ every orbital period. A random walk with step size δr every orbital period gives a diffusion coefficient $D_{d,r}^{\mathrm{eff}} \sim \delta r^2 \Omega \sim D/St^2$ as in Eq. 5.141. For the last equality, we have taken $D = u'^2 t_{\mathrm{corr}}$ as in Eq. 5.11.

5.6 Numerical Tests

In this section, we will summarize the numerical tests that we conducted. These tests support the findings we made from the linear perturbation analysis presented in Sec. 5.5.

5.6.1 Eigenstates in One Dimension

We first compare the decaying eigensolutions in one dimension between the gradient diffusion model and the turbulent pressure model. For the gradient diffusion model, we found two sets of eigenstates. The first set consists of Eq. 5.125 and Eq. 5.126. The second set consists of Eq. 5.127 and Eq. 5.128. For the turbulent pressure model, the eigenstates are identical on large scales. However, on small scales ($k \gg k_c$), traveling wave solutions exist, described by Eq. 5.115 and Eq. 5.116.

We plot these eigenstates as a function of time in Fig. 5.8 in black solid lines. In the first two columns, we show each set of eigenstates on large spatial scales ($k = 0.1k_c$). In the third column, we show the eigenstates on small spatial scales ($k = 10k_c$). The upper sub-plots show the normalized density perturbation and the lower sub-plots show the normalized velocity perturbation.

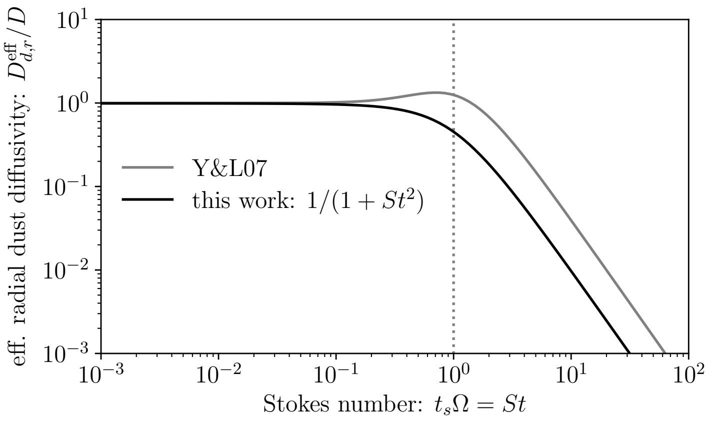

Figure 5.7: Effective radial diffusion coefficient $D^{\mathrm{eff}}_{d,r}$ as a function of Stokes number in a two-dimensional Keplerian disk (as described by Eq. 5.141). We set $k^2/k_c^2 = 0.01$. The vertical dotted gray line represents the transition at $St \sim 1$ below which the effective diffusion is constant. The solid gray line represents the solution of Youdin & Lithwick (2007) (their Eq. 37). Ignoring corrections of order unity, our results describing turbulent transport in radial direction are consistent with the results of Youdin & Lithwick (2007).

We use the JUPITER code to numerically confirm the analytic solutions. For this, we assume $t_{\mathrm{corr}} \ll t_s$ such that $t_t \approx t_s$. We set the parameters to $t_s = \rho_{d,0} = 1$, $D = 4$ and $\delta\rho_0 = \delta\tilde{v}_0 = 10^{-3}$ (in code units) and show the solutions in Fig. 5.8 at a fixed location $x = \pi/4k$. In Fig. 5.8, the blue circles represent the numerical solution of the gradient diffusion model, whereas the red circles represent the turbulent pressure model. At large scales ($k = 0.1k_c$), the two models are identical and both show an exponential decay. On small scales ($k = 10k_c$), their behavior is distinctly different. Note that we do not show the diffusion solution of the gradient diffusion model on small scales. This solution decays 800 times faster than the eigenstates of the turbulent pressure model shown in the third column of Fig. 5.8.

5.6.2 Decaying Gaussian Perturbation in One Dimension

After considering harmonic perturbations, we further illustrate the decay of a one-dimensional Gaussian perturbation similar to the one presented in Huang & Bai (2022) and illustrate the difference between the gradient diffusion model and the turbulent pressure model. We use the JUPITER code to calculate the solution numerically.

We set up a static one-dimensional isothermal viscous gas background with a constant density in the absence of external forces ($g = 0$). We describe the dust density by a Gaussian centered around $x = 0$, scaled such that the dust-to-gas ratio is 0.01 at $x = 0$.

In the first example, the Gaussian has a standard deviation $\sigma = 0.5k_c^{-1}$ at $t = 0$ and amplitude 0.9, and we allow it to diffusively spread over time. We keep all other relevant parameters constant (stopping time $t_s = 0.2$, sound speed $c_s = 2$, gas viscosity $\nu = 0.2$, dust diffusion coefficient $D = 0.2$). We set $N_x = 1000$ and $x = [-2, 2]$. We also assume the correlation time to be small, such that $t_t = t_s$ and the turbulent pressure model is described by Eq. 5.57 and Eq. 5.99. We do not include a turbulent pressure in the gas. The gradient diffusion model is described by Eq. 5.22 and Eq. 5.4.

The characteristic property of this example is that the standard deviation of the Gaussian is smaller than the inverse of the characteristic wavenumber ($\sigma k_c = 0.5$). We plot the solution to this setup in the first row of Fig. 5.9. The gradient diffusion model is plotted in gray dashed lines, the turbulent pressure model is either in red or blue solid lines. We show the solution at

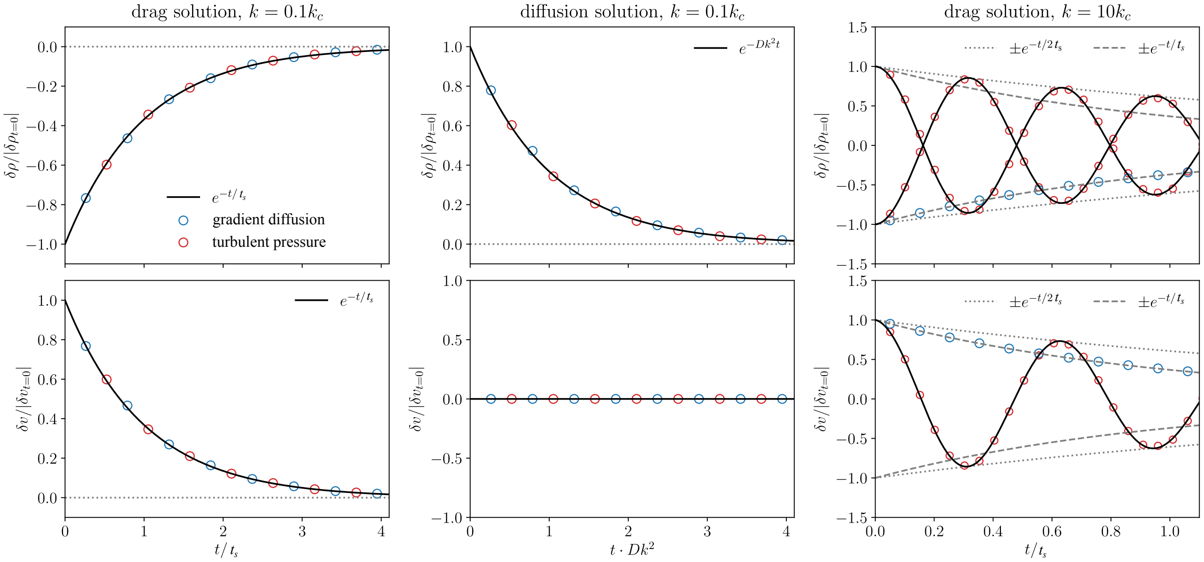

Figure 5.8: Density (*upper row*) and velocity (*lower row*) eigenstates versus time of the one-dimensional perturbation analysis. Plotted are analytical results (black lines) and numerical results of the gradient diffusion model (blue circles) and the turbulent pressure model (red circles) at $x = \pi/4k$ (*first, second column*) and $x = 0$ (*third column*) with $t_s = \rho_{d,0} = 1$, $D = 4$ and $\delta\rho_0 = \delta v_0 = 10^{-3}$ (in code units). The left column shows the exponential decay of the solution on a timescale t_s. The middle column shows the diffusive solution, i.e., the exponential decay on a timescale $D^{-1}k^{-2}$ on a large spatial scale ($k = 0.1k_c$). Both models are identical on this scale. The right column visualizes the difference between the two diffusion models on a small spatial scale ($k = 10k_c$). While the gradient diffusion model is static and decays monotonically and exponentially on a timescale t_s, the turbulent pressure model propagates wave-like with speed c_d and decays on a timescale $2t_s$. Note, for readability, the diffusion solution of the gradient diffusion model is not plotted in the right column. It decays on a timescale 800 times shorter on this small spatial scale compared to the turbulent pressure model.

four different points in time ($t/t_s = 0,\ 0.2,\ 0.6,\ 1.0$).
In the second example, we increase the standard deviation of the Gaussian to $\sigma = 10k_c^{-1}$, and set the stopping time to $t_s = 0.1$, the dust diffusion coefficient to $D = 0.1$, the gas viscosity to $\nu = 0.2$, and the sound speed to $c_s = 2$. We set $N_x = 1000$ and $x = [-20, 20]$. The characteristic property of this example is that the standard deviation is larger than the inverse of the characteristic wavenumber ($\sigma k_c = 10$). We plot the solution to this setup in the second row of Fig. 5.9. We show the solution at four different points in time ($t/t_s = 0,\ 5,\ 15,\ 25$).
In both examples, the gradient diffusion model leaves the dust velocity (second column), the gas density (third column), and the gas velocity (fourth column) at their initial value of zero. That is because the gradient diffusion model describes turbulent transport as pure mass diffusion and thus is not associated with an explicit velocity. On the other hand, the turbulent pressure model disturbs the dust velocity as well as the gas density and velocity. This is because turbulent transport in the dust is associated with a dust momentum, thus changing the dust velocity. Due to the conservation of momentum, the gas reacts to the turbulent redistribution of the dust.
In the top left subplot showing the dust density evolution of the first example, there is also a distinct difference between the gradient diffusion model (gray) and the turbulent pressure model (red). This is because, in this example, the scale of the Gaussian perturbation is smaller than the inverse of the characteristic wave number ($\sigma k_c = 0.5$). At these small scales, the perturbation in the turbulent pressure model decays slower than in the gradient diffusion model, as discussed in Sec. 5.5.1.
In the bottom left subplot showing the dust density evolution of the second example, the difference between the two models is small. For a vanishing dust-to-gas ratio, the two models would be indistinguishable. However, due to the conservation of momentum in the turbulent pressure model, the gas reacts to the spreading of the dust (as seen in the third column of Fig. 5.9). Consequently, the changing gas density and velocity field influence the dust distribution via the drag interaction. Such an interaction is absent in the gradient diffusion model. Because the dust-to-gas ratio is small (0.01), the difference in the dust density distribution between the models is small.

5.6.3 Radial Dust Spreading in a Two-Dimensional Axisymmetric Disk

We aim to numerically confirm the result of the two-dimensional linear perturbation analysis in Sec. 5.5.3 using the Jupiter code. Specifically, the decrease in the effective strength of diffusion for $St > 1$, as predicted by Eq. 5.141. For this purpose, we study the diffusive spreading of an (initially infinitesimally thin) axisymmetric ring in a two-dimensional Keplerian disk in cylindrical coordinates. We compare the gradient diffusion model with the turbulent pressure model derived in this work.
Weber et al. (2019) derived an analytic solution of the diffusive spreading of a δ-distribution, which is given by the following equation:

$$\rho_d(r,t) = \frac{mr_0}{2Dt}\exp\left(-\frac{r^2+r_0^2}{4Dt}\right)I_0\left(\frac{rr_0}{2Dt}\right) \tag{5.142}$$

Here, I_0 is the modified Bessel function of the first kind of order 0.
In our test setup, we assume the dust density to be small compared to the gas density ($\rho_d \ll \rho_g$) and the gas density to be constant in time and space. We set up the gas background to orbit with Keplerian velocity, such that there is no radial drift of the dust. When we set up the gradient diffusion model, we also set the radial dust velocity to zero. For the turbulent pressure model, the initial radial dust velocity depends on the local dust density profile and follows Eq. 5.91. For both models, we set $D = 10^{-4}$, $m = 2 \cdot 10^{-3}$, $r_0 = 1$, $N_r = 1000$, and $r = [0.1, 2.5]$. For the turbulent pressure model, we assume $t_{\mathrm{corr}} \ll t_s$ for simplicity, such that dust dynamics according

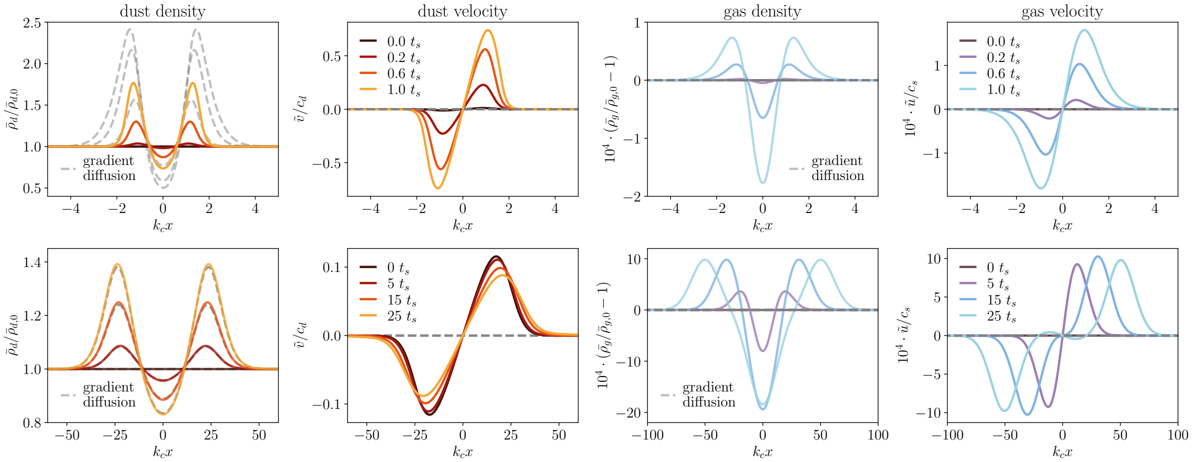

Figure 5.9: Illustrative comparison between the gradient diffusion model (*gray dashed lines*) and the turbulent pressure model (*red/blue solid lines*). We apply the models to describe the one-dimensional diffusive spreading of an initially Gaussian dust distribution with an initially constant gas background. The top row shows the decay of a small-scale Gaussian with standard deviation $\sigma = 0.5k_c^{-1}$, and the bottom row shows the decay of a large-scale Gaussian with standard deviation $\sigma = 10k_c^{-1}$ (see Sec. 5.6.2 for more details). The main difference between the two models is that, in the turbulent pressure model, turbulent dust transport is associated with momentum and thus velocity (see second column). In the gradient diffusion model, diffusion does not affect the dust velocity. Moreover, due to momentum conservation in the turbulent pressure model, the gas reacts to the turbulent transport of the dust. In the first column, the turbulent spreading of the dust density is significantly slower for the turbulent pressure model at small scales (upper row) compared to the gradient diffusion model, as expected based on the discussion in Sec. 5.5.1. On the other hand, at large scales (bottom row), the dust density distribution between the two models is almost identical. The small difference that is present arises from the fact that momentum conservation in the turbulent pressure model redistributes the gas (as illustrated in the third column), which again has an influence on the dust via the drag interaction. Such an interaction is absent in the gradient diffusion model. Note, for a vanishing dust-to-gas ratio, the two models would be indistinguishable at large scales and over long times.

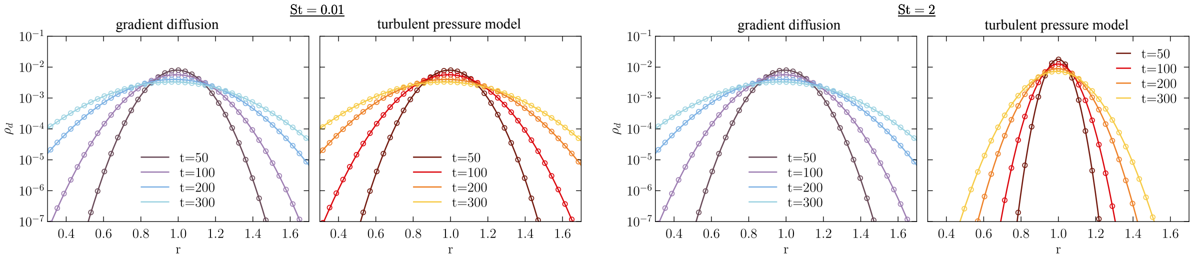

Figure 5.10: Comparison of the radial spreading of an axisymmetric dust ring in cylindrical coordinates between two different diffusion models and at two different Stokes numbers. We set $m = 2 \cdot 10^{-3}$, $r_0 = 1$ and $D = 10^{-4}$ in code units. In blue color, we show the gradient diffusion model. In red color, we show the turbulent pressure model. The solid lines represent the analytic prediction of Eq. 5.142, and the circles represent the numerical solution. The two sub-panels on the l.h.s. show the two models for well-coupled dust ($St = 0.01$) for which the two solutions agree. The two sub-panels on the r.h.s. show the two models for moderately coupled dust ($St = 2$). Orbital effects reduce the effective diffusivity by a factor $1/(1 + St^2) = 5$ in the turbulent pressure model, and the spreading proceeds slower.

to the turbulent pressure model is described by Eq. 5.57 and Eq. 5.99. The gradient diffusion model is described by Eq. 5.22 and Eq. 5.4.

In Fig. 5.10, we illustrate the diffusive spreading of the two models for well-coupled dust grains with $St = 0.01$ (left) and moderately coupled dust grains $St = 2$ (right). The analytical solution of Eq. 5.142 is drawn as solid lines and the numerical solution as circles. For the analytical solution in the case of the turbulent pressure model, we scale the diffusion coefficient with a factor $(1 + St^2)^{-1}$, to match the expected behavior predicted in Sec. 5.5.3. We initialize all the distributions at $t = 50$.

For well-coupled grains, the solution predicted by the turbulent pressure model is identical to the solution predicted by gradient diffusion. For moderately coupled grains ($St = 2$), the radial diffusive spreading proceeds slower compared to the gradient diffusion model. The effective diffusivity is reduced by a factor of 5 as expected from the predicted $1/(1 + St^2)$ behavior.

5.7 Discussion and Summary

In this work, we derive a novel dust turbulent transport model based on a density-weighted mean-field theory and appropriate turbulence closures. The main contribution of this work is a set of mean-field equations that describe the dynamics of dust in protoplanetary disks exhibiting homogeneous and isotropic turbulence. The model is characterized by two parameters, namely the diffusion coefficient D and the correlation time t_{corr}.

In this chapter, we review the popular gradient diffusion approach, for describing the turbulent transport of dust in protoplanetary disks, in Sec. 5.2.4, and highlight the fact that classical gradient diffusion does not guarantee angular momentum conservation in disks. Further, there seems to be no clear consensus on whether the diffused quantity is the absolute dust density ρ_d or the dust concentration relative to gas ρ_d/ρ_g. Moreover, orbital effects, that have the potential to reduce the effective strength of diffusion, are not self-consistently captured. Given these limitations, we argue that there is a need for improved transport models that accurately capture the physics of turbulent dust transport in protoplanetary disks.

The model in its most general form describes the averaged dust dynamics with a set of 1+3+3 = 7 partial differential equations (Eqs. 5.72, 5.73 and 5.74). Applying the same averaging approach to the locally isothermal gas equations, we combine them with another set of $1+3 = 4$ equations

(Eqs. 5.77 and 5.87) to describe the full two-fluid system (gas+dust) in three dimensions with a set of eleven coupled partial differential equations. With Eqs. 5.10 and 5.11, our mean-field approach provides a method for calibrating the two model parameters for a specific example of turbulence.

Compared to previous models, our model introduces a novel momentum conservation equation that describes the dynamics of the turbulent dust mass flux $\bar{\rho}_d v_i^*$, and is thus capable of capturing non-local turbulent transport effects. In essence, the turbulent dust transport is driven by a turbulent pressure and dissipated by a drag-like term, and as such, the model fully conserves global angular and linear momentum. In the dynamic equilibrium between the driving and dissipating forces, we recover the gradient diffusion model of Huang & Bai (2022). In the limit of large particles $t_s \gg t_{\mathrm{corr}}$ (or equivalently short correlation times) and a uniform gas background ($\rho_g = \mathrm{const.}$, $c_s = \mathrm{const.}$), our dynamical equations are identical to the momentum-conserving model of Klahr & Schreiber (2021).

We show in Sec. 5.4.2 that in a balance between the driving and dissipative terms, we recover the classical gradient diffusion solution, with the diffused quantity being the absolute dust density ρ_d. However, we further argue that turbulent dust transport should not be considered in isolation. We find that in a nonuniform and static gas background ($\nabla\rho_g \neq 0$ and $\tilde{u} = 0$), dust to couple to a mean flow in the gas via the explicit drag term, introducing an additional transport flux to the dust. Consequently, our formalism shows self-consistently that the turbulent dust mass flux in a static gas background ($\tilde{u} = 0$) is ultimately governed by the gradient of the dust concentration ρ_d/ρ_g.

Furthermore, for large dust particles ($t_s \gg t_{\mathrm{corr}}$), we find novel turbulent transport flux towards gradients of the stopping time which have not been predicted by previous Eulerian gradient diffusion models. We confirm this by means of a numerical experiment, comparing to the stochastic Lagrangian turbulence model of Ormel & Cuzzi (2007).

In the absence of orbital effects and in a steady-state gas background, the total turbulent equilibrium dust flux reads

$$\bar{\rho}_d \tilde{v}_i = -D\rho_g \frac{\partial}{\partial x_i}\frac{\bar{\rho}_d}{\bar{\rho}_g} - D\bar{\rho}_d \frac{\partial}{\partial x_i} \ln t_t^{-1} \tag{5.91}$$

which contains both the gradient diffusion flux and the novel flux contribution. We stress that Eq. 5.91 is only valid in equilibrium, i.e., under force balance.

Applying our novel turbulent transport model to study the dust distribution in protoplanetary disks in Sec. 5.4.3, we recover the vertical steady-state profile of Fromang & Nelson (2009) in the limit of subsonic turbulence $u'^2 \ll c_s^2$. Formally, we extend the validity of the solution to large grains ($St \gtrsim 1$) because in our derivation, we do not invoke the terminal velocity approximation, which in the aforementioned work limited the validity of the solution to small particles ($St \ll 1$). Consequently, we self-consistently reproduce the small particle scaling ($h_d^2/h_g^2 = 1$ for $St \ll 1$) *and* the large particle scaling ($h_d^2/h_g^2 = \delta/St$ for $St \gg 1$) of the vertical dust scale height without the need for heuristic arguments.

In Sec. 5.5, we study the decay of small perturbations to the dust density due to turbulent mixing. We find the turbulent time $t_t = t_s + t_{\mathrm{corr}}$, to set a lower limit on the decay timescale. For small dust grains ($t_s \ll t_{\mathrm{corr}}$) this lower limit is equal to the correlation time $t_t \approx t_{\mathrm{corr}}$, which can, depending on the nature of the underlying turbulence, be comparable to the orbital time. For large grains ($t_s \gg t_{\mathrm{corr}}$), the lower limit to the decay time is equal to the stopping time t_s, which can be larger than the orbital timescales for $St > 1$.

Small-scale perturbations, with a wave number k larger than the characteristic wavenumber $k_c = 1/\sqrt{Dt_t}$ decay slower (by a factor k^2/k_c^2) than a diffusive solution would predict. For values appropriate for protoplanetary disks ($St = 0.025$, $\delta = 10^{-3}$), the characteristic wave number k_c, that is the threshold above which (meaning on larger wavenumbers and smaller physical scales) diffusion is quenched, corresponds to a spatial length scale of 20 percent of the gas scale height h_g. At these small scales, perturbations still decay due to drag, but by a factor $Dk^2 t_t$ slower compared to gradient diffusion.

Umurhan et al. (2020) showed that gradient diffusion suppresses the smallest modes of the streaming instability. Future work should explore, how the reduction of the strength of diffusion at small scales that we predict affects this result.

In a protoplanetary disk, we find that orbital effects reduce the effective diffusivity of large grains ($St \gtrsim 1$). Specifically, we find the strength of diffusion in both radial and vertical directions to scale as $1/(1 + St^2)$ in agreement with the detailed analysis of Youdin & Lithwick (2007) (up to order unity corrections). We emphasize that the effects of orbital dynamics are implicitly captured by our model. We thus expect our model to appropriately capture orbital effects in disk regions where the flow deviates from being purely Keplerian, such as in the vicinity of orbiting planets.

Lastly, our model also offers advantages over classical gradient diffusion models in terms of numerical implementation. Turbulent transport in our model is pressure-driven, allowing the use of standard, locally isothermal fluid solvers to solve the hydrodynamic dust equations. This removes the need to calculate second-order spatial derivatives of the dust density in the gradient diffusion approach, which can be challenging numerically.

In conclusion, we present an improved general Eulerian model of turbulent dust transport in protoplanetary disks. Our model improves upon several limitations of gradient diffusion models, including the conservation of angular momentum, orbital effects, and the functional form of the diffused quantity. By recovering earlier models in special limiting cases, we improve upon the understanding of turbulent dust transport in protoplanetary disks. Future work should extend this model to more complex scenarios like non-homogeneous or anisotropic turbulence and explore their impact on dust transport in protoplanetary disks.

Table 5.1: List of notations of Chapter 5.

Symbol	Definition/ First use	Description
Ω	v_ϕ/r	Orbital angular velocity
Ω_K	$\sqrt{GM_*/r^3}$	Keplerian angular velocity
Σ_d, Σ_g	Sec. 5.5.3	Dust, gas surface density
α	Eq. 5.84	Shakura-Sunyaev parameter
δ	Eq. 5.15	Dimensionless diffusivity
δ_{ij}	Eq. 5.37	Kronecker delta
ν	Sec. 5.2.2	Viscosity
ζ_t	Eq. 5.17b	Stochastic variable
τ	Eq. 5.6	Time-like integration variable
τ_e	Fig. 5.3	E-folding time
ω	Sec. 5.2.2	Angular frequency
$i\omega$	Sec. 5.5.1	Growth rate
$-i\omega$	Sec. 5.5.1	Decay rate
D	Eq. 5.7	Diffusion coefficient
D_d^{eff}	Eq. 5.98	Effective dust diffusion coefficient
$\mathfrak{D}(t)$	Eq. 5.44	Time-dependent diffusion coefficient
$\hat{E}_g(\omega)$	Eq. 5.8	Energy spectrum
J_i	Eq. 5.20	Turbulent mass flux
P_{ij}	Eq. 5.79	Turbulent pressure tensor
R_{ij}	Eq. 5.81	Reynolds tensor
Sc	D_d/D_g, Eq. 5.14	Schmidt number
Sc_{hydro}	ν/D_g, Sec. 5.2.2	Hydro Schmidt number
St	$t_s\Omega$, Eq. 4.2	Stokes number
W_t	Eq. 5.17b	Wiener process
c_d	Eq. 5.63	Turbulent particle velocity dispersion
c_s	Eq. 3.4	Gas sound speed
g_i	Eq. 5.2	Gravitational acceleration
h_g	Eq. 3.9	Gas pressure scale height
h_d	Eq. 5.95	Dust scale height
k	Eq. 5.103	Wave number
k_c	Eq. 5.109	Characteristic wave number
l_{eddy}	Eq. 5.12	Eddy length
p	Eq. 3.3	Thermal pressure
p_t	Eq. 5.80	Isotropic turbulent pressure
t_s	Eq. 4.1	Stopping time
t_{corr}	Eq. 5.10	Correlation time of turbulence
t_{diff}	Eq. 5.13	Diffusion timescale
t_t	$t_s + t_{\mathrm{corr}}$, Eq. 5.48	Characteristic time of turbulence
u_i	Eq. 3.1	Instantaneous gas velocity
δu	Eq. 5.17a	Stochastic turbulent fluctuation
v_i	Eq. 5.1	Instantaneous dust velocity
$\bar{v}_i$	Eq. 5.32	Reynolds-averaged dust velocity
$\tilde{v}_i$	Eq. 5.51	Favre-averaged dust velocity
v_i^*	Eq. 5.56	Turbulent dust transport velocity
v_i'	Eq. 5.32	Fluctuation w.r.t. to $\bar{v}$
v_i''	Eq. 5.52	Fluctuation w.r.t. to $\tilde{v}$

Table 5.1 – continued from previous page

Symbol	Definition/ First use	Description
v_{sett}	Eq. 4.7	Vertical settling velocity

Chapter 6

Carbon Depletion in the Early Solar System

The content of this chapter was published in:

Binkert F., Birnstiel, T. (2023), *Carbon depletion in the early Solar system, Monthly Notices of the Royal Astronomical Society, Volume 520, Issue 2, April 2023, Pages 2055–2080*

Abstract

Earth and other rocky objects in the inner Solar System are depleted in carbon compared to objects in the outer Solar System, the Sun, or the ISM. It is believed that this is a result of the selective removal of refractory carbon from primordial circumstellar material. In this work, we study the irreversible release of carbon into the gaseous environment via photolysis and pyrolysis of refractory carbonaceous material during the disk phase of the early Solar System. We analytically solve the one-dimensional advection equation and derive an explicit expression that describes the depletion of carbonaceous material in solids under the influence of radial and vertical transport. We find both depletion mechanisms individually fail to reproduce Solar System abundances under typical conditions. While radial transport only marginally restricts photodecomposition, it is the inefficient vertical transport that limits carbon depletion under these conditions. We show explicitly that an increase in the vertical mixing efficiency, and/or an increase in the directly irradiated disk volume, favors carbon depletion. Thermal decomposition requires a hot inner disk (> 500 K) beyond 3 au to deplete the formation region of Earth and chondrites. We find FU Ori-type outbursts can produce these conditions such that moderately refractory compounds are depleted. However, such outbursts likely do not deplete the most refractory carbonaceous compounds beyond the innermost disk region. Hence, the refractory carbon abundance at 1 au typically does not reach terrestrial levels. Nevertheless, under specific conditions, we find photolysis and pyrolysis combined can reproduce Solar System abundances.

6.1 Introduction

The background of this chapter was established in Sec. 2.4.5 and Sec. 2.4.4 in the context of observational constraints of the Solar system. In this study, we build upon the work of Klarmann et al. (2018) by developing an analytical model of refractory carbon depletion via photolysis to show that the barriers imposed by grain transport are not insurmountable if the total dust mass (or the global dust-to-gas ratio) is low enough. Further, we extend our analytical model to include the refractory carbon depletion via sublimation during FU Ori-type stellar luminosity outbursts.

6.2 Model and dust transport

In this section, we present the details of our dust model, describe the stationary disk model and introduce the equations that describe the transport of the dust components within the disk. Further, we introduce the local carbon depletion timescale τ_c, which is used to describe the timescale over which a given process depletes the disk of refractory carbon.

6.2.1 Dust Model

In Sec. 2.4.5 and Sec. 2.4.4, we have summarized the detailed accounting of the C/Si atomic ratio and/or the individual elemental mass fractions of carbon and silicon obtained in remote observations and/or direct measurements of objects in the Solar System. In the Solar System, it is expected that all the solid bodies that are currently observed (i.e., planets, asteroids, comets, etc.), have formed from solid refractory components that already existed in the early Solar nebula. In the remainder of this study, we model the evolution of the early solid refractory compounds (carbonaceous and non-carbonaceous) in a young prestellar disk, in conditions similar to the early Solar System. Particularly, we model the refractory compounds as two distinct dust grain populations, a non-carbonaceous component, and a carbonaceous component, of which we further divide the latter into five individual carbonaceous compounds which all are subject to photo- and thermal decomposition processes. We model the non-carbonaceous dust component as silicate and assume, for simplicity, that every silicon atom in this component is locked up in bare silicate $\left((\mathrm{Mg,Fe})_2\mathrm{SiO}_4\right)$, similar to the dust model in Zubko et al. (2004). Meaning, for every silicon atom, we add another six atoms, which together form the atomic composition of the non-carbonaceous bare silicate dust compound. With this approach, the relative abundance of atoms in $(\mathrm{Mg,Fe})_2\mathrm{SiO}_4$ roughly agrees with relative abundances in the ISM (Zubko et al., 2004).

In order to track the abundance of refractory carbon in dust conglomerates consisting of carbonaceous and non-carbonaceous components, we track the individual mass of each component, i.e., M_c is the total mass of carbonaceous material and M_s is the total silicate mass in a conglomerate. We define the *carbon fraction* $f_c = M_c/(M_c + M_s)$ to trace the carbon mass fraction relative to the total refractory dust mass. In order to connect the carbon fraction f_c to observational data, we convert the C/Si atomic ratios reported in Sec. 2.4.4 and Sec. 2.4.5, to carbon fractions f_c, assuming every silicon atom is locked up in bare silicate. The obtained carbon fractions for Earth are listed in the last column of Table 2.1. In Fig. 2.8, we visualize the carbon fractions of some Solar System bodies and the ISM. The data is based on the review of Bergin et al. (2015) to which we have added the estimate for bulk Earth as discussed in Sec. 2.4.5. In Fig. 2.8, the horizontal extent of the boxes corresponds to the heliocentric distances of the expected formation region of individual objects. We place the formation location of carbonaceous chondrites at $1.5 - 2$ au, the location of ordinary chondrites at $2.0 - 2.5$ au and the location of enstatite chondrites at $2.5 - 3.0$ au (Morbidelli et al., 2012). The range of carbon fractions in chondrites is based on the C/Si ratios from Bergin et al. (2015). For chondrites, the vertical extent of the boxes in Fig. 2.8 represents the ranges of measurements of different samples and not uncertainties. Unlike all the other boxes, which represent model and/or measurement uncertainties. We place the origin of comet 67P/Churyumov-Gerasimenko (67P) in the Kuiper belt $(30 - 50$ au) where, according to a long-standing hypothesis, Jupiter-family comets originate (Duncan & Levison, 1997). We highlight that this hypothesis has somewhat weakened in recent years, and today it is also thought possible that Jupiter-family comets formed over

a wider range of distances from the Sun (Altwegg et al., 2015). It is also possible that comet 1P/Halley (Halley) originates from regions beyond the Kuiper belt (Jewitt, 2002). Further, we arrive at a carbon fraction $f_c = 0.29$ for the dust component of the ISM. This is close to the carbon fraction $f_c = 0.25$ assumed in Klarmann et al. (2018), who use an identical definition of the carbon fraction. The upper bound for Bulk Earth is $f_c = 4.1 \cdot 10^{-3}$, less than two orders of magnitude below ISM values. The estimated range based on geochemical modelling is in the range $f_c = 3.7 - 7.7 \cdot 10^{-4}$, roughly another order of magnitude lower.
After detailing the total amount of refractory carbonaceous material expected to be found in presolar material, we now specify its composition. We divide the refractory carbonaceous component into five distinct carbonaceous compounds with different decomposition properties. For this, we follow the model of Gail & Trieloff (2017) and divide the carbonaceous components into the moderately volatile aliphatic (3.0 % by mass) and aromatic compounds (3.0 % by mass), the refractory hydrocarbon compounds Kerogen I (10.0 % by mass) and kerogen II (10.0 % by mass) and a fifth component, amorphous carbon (3.0 % by mass). The mass fractions in brackets are given relative to the total refractory dust mass and add up to 29 % by mass of carbonaceous material. The relative abundances are thought to reflect our (limited) knowledge of the composition of cometary material and interplanetary dust particles (IDPs). In Fig. 6.2.1, we illustrate the composition and relative abundance of the refractory dust components considered in our model.

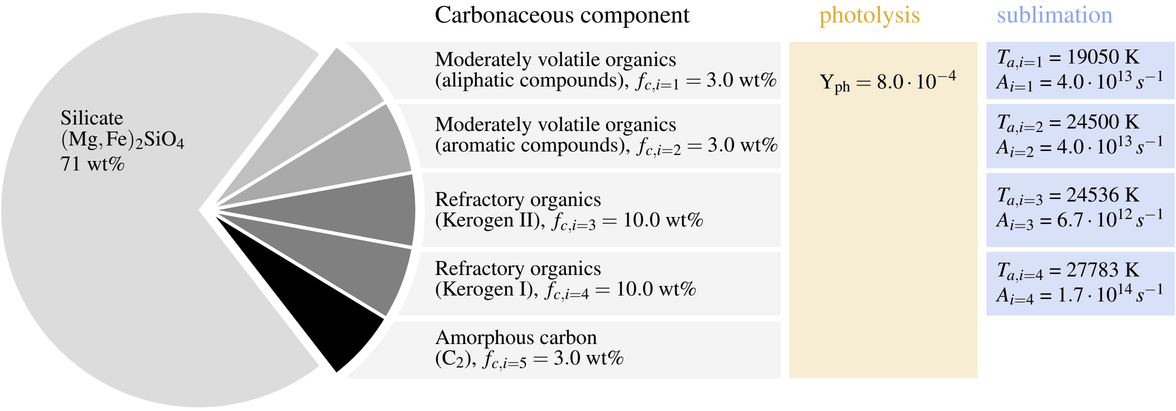

Figure 6.1: Refractory dust composition model (Note, for better visualization, the size of the individual wedges of the carbonaceous components are all equal in size and not proportional to their respective fractional abundance. Only their combined size accurately represents the total initial fractional abundance of carbonaceous material (29 %). The yellow and blue boxes contain the model parameters for photolysis and irreversible sublimation. Note that we do not consider the sublimation of the amorphous carbon compound in this study.

6.2.2 Disk Model

With the goal of modeling the conditions in the early Solar System in mind, we assume a pre-main-sequence star located at the center of a circumstellar disk. We adopt stellar parameters for a Solar-mass pre-main-sequence star ($M_\star = 1 M_\odot$) from Siess et al. (2000) at 1 Myr with a total luminosity of $L_\star = 2.39 L_\odot$. We assume the FUV-luminosity to be $L_{UV} = 0.01 L_*$, as proposed by, e.g., Siebenmorgen & Krügel (2010). We describe the disk around the central star using radial power-law dependencies for surface densities and temperature. The gas surface density follows a power law of the form

$$\Sigma_g = \Sigma_{g,0} \cdot \left(\frac{r}{r_0}\right)^{-p_g} \tag{6.1}$$

where $r_0 = 1$ au and $p_g = 1$. We assume a total (gas) disk mass of $M_{g,\mathrm{tot}} = 0.04 M_\odot$ up to $r_\mathrm{out} = 200$ au. This results in a gas surface density of $\Sigma_g = 283\,\mathrm{g\,cm^{-2}}$ at 1 au.

We assume the disk temperature to be set by external heating at all the heliocentric distances which are relevant for this study ($r \gtrsim 1$ au), and to be vertically isothermal. The disk temperature is then proportional to the fourth root of the stellar luminosity L_* (Eq. 3.34). We take the flaring angle to be $\Phi = 0.05$. Thus, the disk temperature profile takes a power law form

$$T = T_0 \cdot \left(\frac{r}{r_0}\right)^{-q} \tag{6.2}$$

with $T_0 = 231$ K and $q = 1/2$. Consequently, the vertical gas volume density follows the Gaussian distribution in Eq. 3.8.

For the initial dust surface density, we also assume a power law profile,

$$\Sigma_d = \Sigma_{d,0} \cdot \left(\frac{r}{r_0}\right)^{-p_d}. \tag{6.3}$$

where we set the power law index p_d equal to 1.5 and $\Sigma_{d,0} = 19.7\,\mathrm{g\,cm^{-2}}$. This slope corresponds to the equilibrium dust surface density in the fragmentation limit (Birnstiel et al., 2012) and the prefactor to a dust mass accretion rate (in the fragmentation limit) of $10^{-5}\,\mathrm{M_\oplus/yr}$. With this profile, the dust-to-gas mass ratio is globally at 0.01, i.e., the canonical value expected in the ISM. With the term *dust* we refer to any solid refractory disk component, which includes carbonaceous components and non-carbonaceous components (e.g., silicates). In Table 6.1, we summarize the fiducial disk parameters.

We divide the total dust population into six distinct refractory populations ($i = 0...5$), according to the dust model described in Sec. 6.2.1, with each population contributing with a mass-fraction $f_{c,i}$ to the total dust surface density Σ_d such that

$$\Sigma_d = \sum_{i=0}^{5} \Sigma_{d,i} \tag{6.4}$$

and

$$\Sigma_{d,i} = f_{c,i} \Sigma_d \tag{6.5}$$

are fulfilled. We consider the zeroth component ($i = 0$) to be the silicate component and components $i = 1...5$ to be the carbonaceous compounds (see Fig. 6.2.1). From this, it follows directly that the total carbon fraction f_c, as introduced in Sec. 6.2.1, is the sum of the individual mass fractions of components one to five

$$f_c = \sum_{i=1}^{5} f_{c,i} \tag{6.6}$$

and the mass fraction of silicates is

$$f_s = f_{c,0} \tag{6.7}$$

Likewise, we denote the surface density of silicate grains with Σ_s.

Table 6.1: Fiducial model parameters. Here, *p.l.i.* stands for *power law index.*

Quantity	symbol	value
Stellar luminosity	L_*	2.39 $L_\odot$
Stellar UV luminosity	L_{UV}	0.01 $L_\odot$
Total (gas) disk mass	$M_{\mathrm{g,tot}}$	0.04 $M_\odot$
Gas surface density p.l.i.	p_g	1
Initial dust accretion rate	$\dot{M}_d$	$1 \times 10^{-5}\ M_\oplus$/yr
Dust surface density p.l.i.	p_d	1.5
Disk temperature at 1 au	T_0	231 K
Flaring angle	Φ	0.05
Turbulence strength	α	10^{-2}
Fragmentation velocity	v_{frag}	300 cm/s

6.2.3 Radial Dust Transport

In this section, we describe the radial transport of dust, which happens as a result of the loss of angular momentum caused by the drag interaction with the gas. When considering dust transport, we do not differentiate between the different dust compounds and assume all the compounds to have the same size distribution and the same average solid density $\rho_\bullet = 3.0$ g cm^{-3}. This allows us to transport the dust distribution as a whole, and is also closer to reality, in which compounds are mixed within individual grains and do not exist as distinct populations. Similar to Birnstiel et al. (2012), we assign the total dust mass to two grain sizes, small and large grains, as a representation of a grain size distribution in coagulation-fragmentation equilibrium. The small dust grains are well coupled to the gas, and we assume their radius to be $a_s = 0.1\mu m$. The large grains of radius a are generally only moderately coupled to the gas and thus subject to radial drift. In our model, we assume that collisions between dust grains are frequent enough that any radial transport happens at the drift speed of the large grains. We express the degree of coupling via the dimensionless Stokes number St which we parametrize with a power law as:

$$St = St_0 \cdot \left(\frac{r}{r_0}\right)^s. \tag{6.8}$$

We find for grains in the fragmentation limit

$$St_0 = f_{\mathrm{f}} \frac{m_g}{3\alpha k_B} \frac{v_f^2}{T_0}, \quad s = q \tag{6.9}$$

where f_{f} is a calibration factor of order unity (Birnstiel et al., 2012) and α is the dimensionless turbulence parameter (Shakura & Sunyaev, 1973). With the parametrization of the Stokes number as in Eq. 6.8, we write the radial drift velocity of the dust grains with Stokes number St≪1 as:

$$v_r = -\gamma St \frac{c_s^2}{v_k} \tag{6.10}$$

With $\gamma = q/2 + p_g + 3/2$ being the modulus of the power-law exponent of the gas pressure $P_g = \rho_g c_s^2$. We also express the radial drift velocity in power-law form. Thus, we rewrite Eq. 6.10 as

$$v_r = v_0 \cdot \left(\frac{r}{r_0}\right)^l \tag{6.11}$$

with $v_0 = -\gamma St_0 c_{s,0}^2 / v_{k,0}$ and $l = s - q + 1/2$

Transport equations

Ultimately, we aim to find the radial distribution of the dust surface density (of carbonaceous and non-carbonaceous grains). We describe its evolution with a one-dimensional radial advection equation without diffusion and a source term that models the depletion of refractory carbon compounds

$$\frac{\partial \Sigma_d}{\partial t} + \frac{1}{r}\frac{\partial}{\partial r}(r\Sigma_d v_r) = -\dot{\Sigma}_d \tag{6.12}$$

Using Eq. 6.4, we rewrite Eq. 6.12 as the sum of six individual equations

$$\frac{\partial \Sigma_d}{\partial t} = \sum_{i=0}^{5} \frac{\partial \Sigma_{d,i}}{\partial t} \tag{6.13}$$

of which each summand has the general form

$$\frac{\partial \Sigma_{d,i}}{\partial t} + \frac{1}{r}\frac{\partial}{\partial r}(r\Sigma_{d,i} v_r) = -\dot{\Sigma}_{d,i} \tag{6.14}$$

In our models, we assume that silicate grains do not decompose and that their surface density is conserved. Thus, we write $\dot{\Sigma}_{d,i=0} = 0$. For all the carbonaceous components ($i = 1..5$) we will discuss the explicit form of the source terms $\dot{\Sigma}_{d,i}$ in the following sections. Throughout this work, we use the subscript c to refer to the sum of all the carbonaceous components ($i > 0$) and the subscript s to refer to the silicate component ($i = 0$). Note that because we model the radial transport of the dust as one population, the radial drift velocity v_r is identical for each component.

6.2.4 Carbon Depletion Timescale

We assume that a carbonaceous compound, as introduced in Sec. 6.2.1, can be gradually decomposed by a yet unspecified carbon-depletion mechanism. We define the time t_d to be the time it takes for a carbonaceous grain of radius a to be completely decomposed by this mechanism. The efficiency of the mechanism can have a radial power-law dependence, thus, we define

$$t_d = t_{d,0} \cdot \left(\frac{r}{r_0}\right)^b \tag{6.15}$$

where $t_{d,0}$ is the time it takes to decompose a carbon grain of size a at radius r_0 in the disk. Further, we define the *carbon depletion timescale*,

$$\tau_c = \frac{\Sigma_c}{\dot{\Sigma}_c} \tag{6.16}$$

which describes the characteristic carbon depletion time of the disk and is the ratio between the surface density of all the carbonaceous compounds Σ_c and its depletion rate $\dot{\Sigma}_c$. Assuming the entire dust disk consists only of grains of size a, and the arbitrary carbon depletion mechanism is active throughout the entire disk, all the carbonaceous material will be destroyed within time t_d and we find $\dot{\Sigma}_c = \Sigma_c / t_d$. Thus, in this simple case, the carbon depletion timescale is equal to the destruction time of a single grain $\tau_c = t_d$. However, it is possible that a given depletion mechanism is only active in certain layers of the disk, or the mechanism is only efficient in a certain fraction of the grain size distribution (or both). Therefore, we assume a given depletion mechanism is active only in a fraction Σ_c^* of the total surface density Σ_c. This increases the carbon depletion timescale τ_c, which is now generally larger than the time it takes to decompose a single grain t_d because $\Sigma_c^* \leqslant \Sigma_c$. Thus, we write the carbon depletion timescale as

$$\tau_c = \frac{\Sigma_c}{\Sigma_c^*} t_d \tag{6.17}$$

where Σ_c^* is the carbon surface density in which depletion is active. From the definition of the carbon fraction, we find $\Sigma_c = f_c \Sigma_d$, and if we assume for now that the vertical mixing timescale ($t_{\text{mix}} = 1/\alpha\Omega$) is small compared to the destruction time $t_{\text{mix}} \ll t_d$, the carbon fraction f_c is vertically uniform and $\Sigma_c^* = f_c \Sigma_d^*$ holds (compare to Sec. 6.3.3 where this assumption is lifted). Thus, we write the carbon depletion timescale as

$$\tau_c = \frac{\Sigma_d}{\Sigma_d^*} t_d \tag{6.18}$$

Depending on the detailed physics of the depletion mechanism, it is possible that the destruction time is better described by an exponential law, rather than a power-law

$$t_d' = t_{d,0}' \exp(-t_d) \tag{6.19}$$

where t_d is the generic power law as defined in Eq. 6.15. Irrespective of the detailed functional dependence of t_d, the considerations in this section still hold.

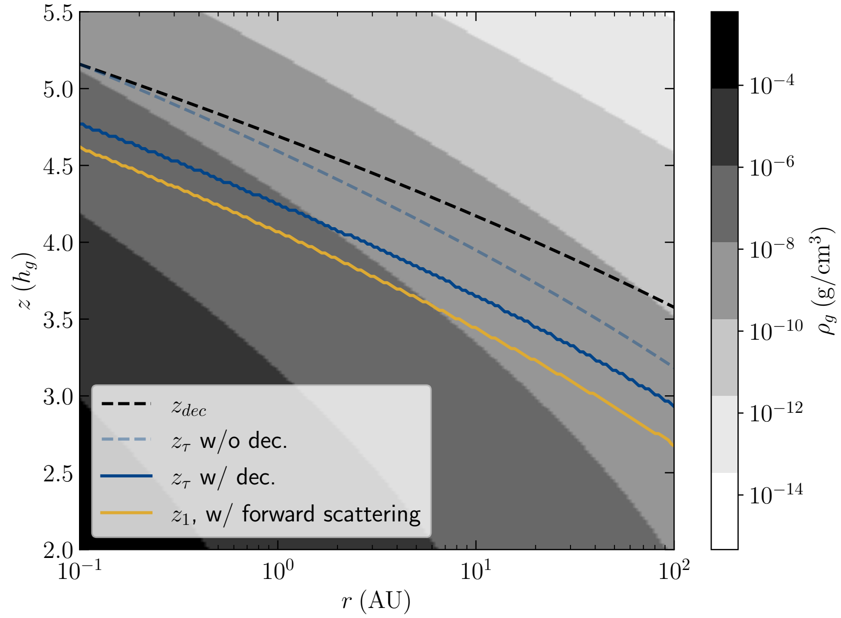

Figure 6.2: The black dashed line plots the height at which 0.1 μm sized grains decouple (z_{dec}) as calculated with Eq. 6.22. The blue lines represent the τ = 1-surface at z_τ. The dashed blue line is calculated using the analytical approximation, i.e., Eq. 6.21, that does not consider the decoupling of grains at large z. The solid blue line does include the effects of grains decoupling and is the numerical solution to Eq. 6.67. The yellow line represents the solution to Eq. 6.31 which includes the effects of photon forward scattering. Thus, FUV photons penetrate deeper than the τ = 1-surface. The background colors illustrate the gas volume density ρ_g, as in Eq. 3.8.

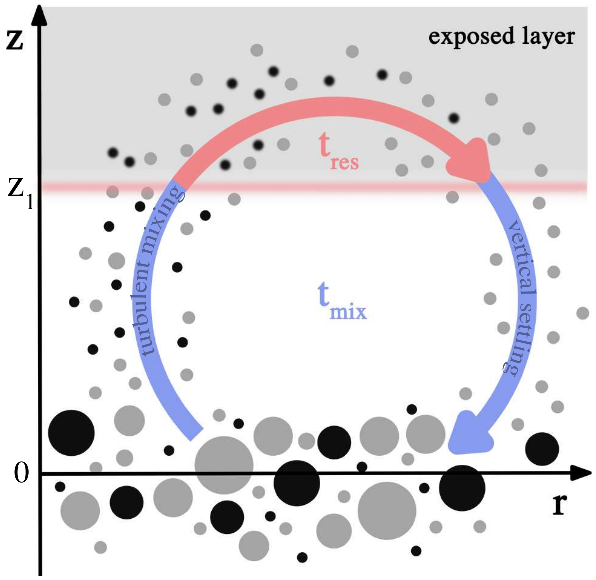

Figure 6.3: Vertical profile of the disk above the midplane. Silicate grains are plotted in gray color, and carbon grains in black. Large grains are confined to the midplane region. Small grains which are produced in collisions in the high-density region around the midplane are lifted to higher disk layers by turbulence. Above z_1, the grains reach the UV-irradiated exposed layer where carbon grains are destroyed by photolysis while silicate grains are unaffected. The longer the carbon grains spend in the exposed layer, the more carbon grains are destroyed and the carbon fraction drops. The residence time t_{res} is the total time the small grains spend in the exposed layer before settling toward the midplane where they collide and coagulate with other grains. During one of these mixing cycles, carbon depletion can become inefficient if the local carbon fraction in the exposed layer drops due to efficient carbon grain destruction. This is indicated by a gradient in the number of carbon grains which, in the sketch, move in the exposed layer from left to right. If z_1 moves closer to the midplane t_{res} takes up a larger fraction of the total mixing time t_{mix}. At the same time, the surface density contained in the exposed layer Σ^* takes up a larger fraction of the total dust surface density Σ_d.

6.3 Photodecomposition

In this section, we consider the photodecomposition of refractory carbon. Specifically, we study the effects of photolysis via stellar UV radiation.

6.3.1 The Exposed Layer

The far ultraviolet-flux (FUV) coming from the central disk region is largely unaffected by gas in the disk, but is mainly attenuated by small dust grains. Thus, the disk layers containing dust are generally very optically thick at FUV-wavelengths. Thus, potential photo-induced carbon depletion by FUV-photons can only be active in the layers of the disk in which stellar FUV-photons penetrate. Following Klarmann et al. (2018), we call this the *exposed layer* (Siebenmorgen & Krügel (2010) call this layer the *extinction layer*). The exposed layer extends vertically from height $z = z_1$ to $z = \infty$ and contains the dust surface density Σ_d^*. Our goal in this section is to quantify Σ_d^* and z_1. In a first approach, we assume all the stellar FUV photons to be absorbed in the region where the optical depth is smaller than unity, i.e., we ignore the effects of scattering. Further, we assume that the FUV flux has the form of a step function, where it is not attenuated above z_1 and zero below. This is a reasonable approximation because the bulk of the photons is absorbed close to z_1 due to the steep exponential increase of the dust density $\rho_d(z)$. Then, the height z_1 is equal to the height at which the (radial) optical path has optical depth $\tau = 1$. Due to the flaring of the disk, a radial optical depth $\tau = 1$ corresponds to a vertical optical depth of $\tau_z = \Phi$, where Φ is the flaring angle of the disk. This is nicely illustrated in Fig. 5 of Siebenmorgen & Krügel (2010).

For the sake of simplicity, we assume a single dust grain size a_s to be the dominant contributor to the opacity at FUV-wavelengths. This assumption is reasonable because for a given wavelength λ, grains smaller than $a = \lambda/2\pi$ are in the Rayleigh regime of scattering where the absorption of photons is a by-mass effect, meaning the grain size dominating the mass budget also dominates the opacity. In a coagulation-fragmentation equilibrium, larger grains generally contribute more to the total dust mass. Hence, in the Rayleigh regime, larger grains contribute most to the opacity. On the other hand, the opacity for grains larger than $a = \lambda/2\pi$, in the geometrical optics limit, is calculated as the ratio between the geometrical cross-section σ and the mass of a grain m as $\kappa = \sigma/m = 3/(4\rho_\bullet a)$. Here, $\rho_\bullet$ is the solid density of a dust grain. Hence, in the geometrical optics limit, small grains contribute more to the opacity. To conclude, in this simple argument, the grain size that dominates the opacity is the size in between the two scattering regimes with an optical size of unity, i.e., the grains with size $a_s = \lambda/2\pi$ and opacity $\kappa_0 = 3/(4\rho_\bullet a_s)$. For $\lambda = 0.6\mu m$ and $\rho_\bullet = 3gcm^{-3}$, we find $a_s \sim 0.1\mu m$ and $\kappa_0 \sim 2.5 \cdot 10^4 cm^2 g^{-1}$ for the opacity. The surface density contained in the exposed layer in the disk is

$$\Sigma_{\mathrm{d}}^* = 2\Phi/\kappa_0 \tag{6.20}$$

or equivalently $\Sigma_{\mathrm{d}}^* = 8\Phi/3\rho_\bullet a_s$. The factor two in Eq. 6.20 comes from the two sides of the disk. As for z_1, i.e., the lower edge of the exposed layer, an exact explicit expression cannot be found. But because we define the lower boundary of the exposed layer to be the location at which the radial optical depth equals unity $z_1 = z_\tau$. In Appendix 6.A, we derive the implicit Eq. 6.67 that we solve numerically to find z_1 in all our quantitative analyses. In addition to that, in Appendix 6.A, we derive an explicit, but approximate, expression for z_τ under the assumption that the opacity dominating dust grains are perfectly coupled to the gas:

$$\frac{z_\tau}{h_g} \simeq \sqrt{2 \ln \frac{f_{\leqslant a_s} \Sigma_d \kappa_0}{2\sqrt{\pi}\Phi}} - \frac{1}{5} \tag{6.21}$$

It is straightforward to see that z_τ, in units of the gas scale height h_g, is farther away from the midplane if the flaring angle Φ is small because a larger fraction of the photon path lies inside the disk atmosphere. In addition to that, z_τ lies farther away from the midplane if the surface density of small dust grains ($f_{\leqslant a_s}\Sigma_d$) is large and if the opacity κ_0 is large. For the fiducial parameters, we obtain $z_{\tau,0} = 4.6\, h_{g,0}$. Interestingly, z_τ is quite insensitive to changes of parameters because the density $\rho_d(z)$ changes rapidly with z. Decreasing the argument in the natural logarithm in Eq. 6.21 by a factor of 10, e.g., by decreasing the total dust surface density Σ_d, results in $z_{\tau,0} = 4.1\, h_{g,0}$, which is a decrease of only eleven percent. In the top panel of Fig. 6.2, we show the radial dependence of the solution to Eq. 6.21 using our fiducial model parameters (dashed blue line). We want to highlight that Eq. 6.21 is only accurate to first-order, if $z_\tau > h_g$, and assumes small grains are perfectly coupled to the gas. For more accurate results, one should use higher-order terms, as in Eq. 6.62, or use a numerical approach. For our fiducial set of parameters, the solution lies well above the gas scale height h_g. To evaluate whether the well-coupling condition is fulfilled, we also plot the location at which the opacity-dominating dust grains decouple from the gas

$$\frac{z_{\mathrm{dec}}}{h_g} = \sqrt{2 \ln \frac{2\alpha\Sigma_g}{\pi \rho_\bullet a}} \tag{6.22}$$

We derive the above equation in Appendix 6.A by finding the height at which the local Stokes number is equal to the turbulent alpha-parameter α. In Fig. 6.2, we plot z_{dec} calculated with Eq. 6.22 in black color with a dashed line. The solution to Eq. 6.21 crosses z_{dec}, i.e., the height at which we find the opacity dominating dust grains to decouple. Therefore, we expect the solution of Eq. 6.21 to deviate slightly from the exact result for our fiducial choice of parameters. This difference becomes apparent when comparing the dashed and solid blue lines in Fig. 6.2. If the decoupling of small grains were negligible, the two solutions would be identical. Nonetheless, Eq. 6.21 serves as a valuable tool in the qualitative analysis of our results. For all the quantitative results, we use the exact numerical solution for z_τ, as found by solving Eq. 6.65. We show this solution in Fig. 6.2 with a solid blue line. Indeed, we find the approximate solution to be about ten percent above the exact solution because it does not account for grain decoupling. Further, we stress here that setting $z_1 = z_\tau$ is not always a good approximation, as photons can reach deeper layers when scattering such that $z_1 < z_\tau$. We briefly investigate the effects of forward scattering in Sec. 6.3.4.

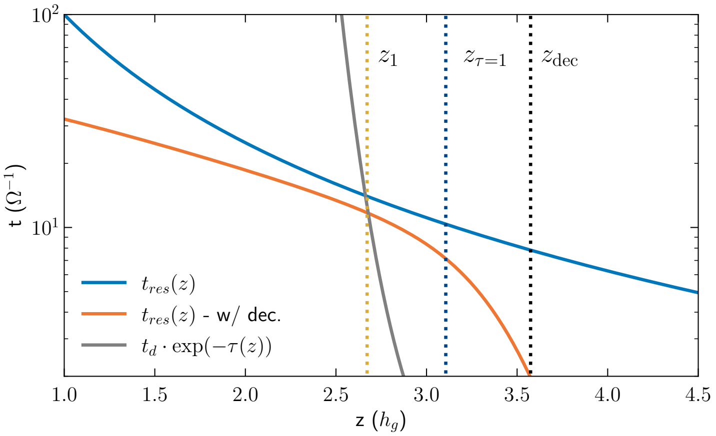

Figure 6.4: Residence times t_{res} of 0.1 μm sized dust grains at different heights z above the midplane are calculated at 100 au in units of the inverse of the Keplerian frequency Ω^{-1}. The orange line shows the residence time calculated with Eq. 6.27. Due to grains decoupling, the residence time sharply decreases above about three gas scale heights. We indicate the height at which grains decouple z_{dec}, as calculated with Eq. 6.22, with the black vertical dotted line. The blue line shows the approximate $(h_g/z)^{-2}$ dependency of the residence time, as introduced in Eq. 6.80. The solid gray line represents the grain destruction time t_d multiplied by an exponential factor that accounts for the attenuation of the FUV field in the optically thick region of the disk. The blue vertical dotted line indicates the height of the $\tau = 1$ surface as determined by solving Eq. 6.67. The yellow dotted lines indicate the location of the solution to Eq. 6.31, i.e., the location where the gray and orange lines intersect.

6.3.2 Photolysis

In this section, we discuss *photolysis* as a specific example of a carbon depletion mechanism, which was also discussed in previous studies (e.g. Klarmann et al., 2018; Anderson et al., 2017). Similarly, we use the term photolysis to refer to the photon-induced release of small hydrocarbons from the surface of a carbonaceous grain (as opposed to the photodissociation of a single molecule). When considering photolysis, Alata et al. (2014, 2015) found methane to be the C-bearing product of the highest yield. Therefore, we will only focus on this product here. The photolysis rate of C-bearing grains in a FUV field is $R_{\mathrm{UV}} = \sigma Y_{\mathrm{ph}} F_{\mathrm{UV}}$. Here, R_{UV} describes the

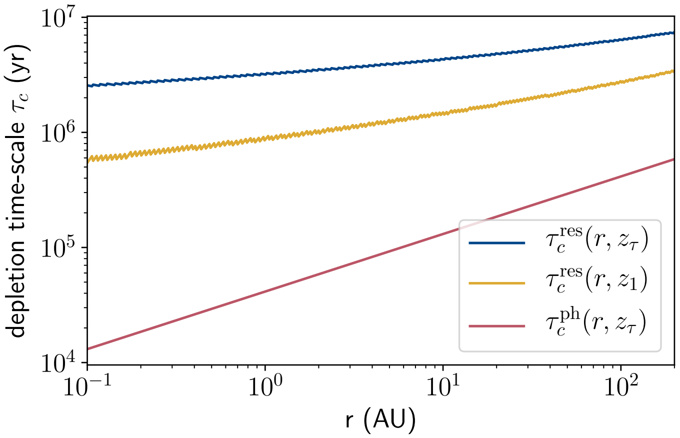

Figure 6.5: Photolysis depletion timescale as a function of radius. The red line shows the unrestricted depletion timescale τ_c^{ph} as defined in Eq. 6.24. At 1 au, it has a value of 40 kyr. The blue line shows the depletion timescale limited by vertical transport at the optical surface of FUV-photons as calculated with Eq. 6.26. It is significantly larger, with a value of 2.6 Myr at 1 au. The yellow line shows the resulting depletion timescale when FUV photons are allowed to penetrate the disk beyond the $\tau = 1$-surface due to forward scattering. It has a value of 695 kyr at 1 au.

number of C-atoms with mass m_c released per unit time from a single grain where $\sigma = a^2\pi$ is the geometric cross-section of the carbon grain, Y_{ph} is the yield of the photolysis reaction per incoming photon ($\sim 8 \times 10^{-4}$) and F_{UV} is the *local* FUV flux ($[F_{\mathrm{UV}}] = cm^{-2}s^{-1}$). The time it takes to destroy a single carbon grain of radius a and mass m via photolysis is

$$t_{\mathrm{ph}} = \frac{m}{m_c R_{\mathrm{UV}}} = \frac{4}{3}\frac{a\rho_c}{m_c Y_{\mathrm{ph}} F_{\mathrm{UV}}} \tag{6.23}$$

and the depletion timescale, as introduced in Eq. 6.17, for unrestricted photolysis is

$$\tau_c^{\mathrm{ph}} = \frac{\Sigma_d}{\Sigma_d^*} t_{\mathrm{ph}} \tag{6.24}$$

By *unrestricted*, we refer to the simplified assumption that the carbon fraction is vertically constant. This assumption only holds if carbon in the exposed layer is depleted on a much shorter timescale than the vertical mixing timescale of the disk. In reality, carbon depletion can be restricted by inefficient vertical mixing when the carbon fraction is significantly lower in the exposed layer compared to the rest of the disk. Therefore, the unrestricted carbon depletion timescale in Eq. 6.24 does only represent a lower limit.
Combining Eq. 6.20, Eq. 6.23 with Eq. 6.24, we find

$$\tau_c^{\mathrm{ph}} = \frac{\Sigma_d}{2 m_c Y_{\mathrm{ph}} \Phi F_{\mathrm{UV}}} \tag{6.25}$$

where we have used $\kappa_0 = 3/(4\rho_\bullet a)$. Thus, photolysis, when not limited by other mechanisms such as transport, is more efficient in disks with a large flaring angle Φ and regions with a large UV flux F_{UV}. It is also more efficient where the dust surface density Σ_d is small. Interestingly, in Eq. 6.25 the opacity cancels out and Eq. 6.25 is independent of the amount of surface density contained in the exposed layer. In our fiducial model, the unrestricted depletion timescale at 1 au is $\tau_{c,0} = 40\,\mathrm{kyr}$ which is short compared to the typical disk lifetimes (∼Myr).

6.3.3 Vertical Transport

The carbon-depletion efficiency can be limited by vertical transport when the stellar FUV photons do not penetrate the entire disk because the carbon grains must be vertically transported from the disk midplane to the exposed layer. To be specific, the carbon depletion process becomes inefficient if the local carbon fraction f_c in the irradiated exposed layer becomes significantly smaller than the average carbon fraction below the exposed layer. This is the case whenever carbon grains in the exposed layer are destroyed faster than they are recycled through collisions and vertical transport with the rest of the grains in the lower dense disk layers. In this situation, the carbon grain destruction time t_d is not a limiting factor to the depletion timescale anymore, as suggested by Eq. 6.18. In such a situation, decreasing the carbon grain destruction time t_d does not decrease the depletion timescale τ_c because any carbon that reaches the exposed layer is destroyed anyway. In other words, there is a lower limit to the carbon depletion timescale τ_c, below which Eq. 6.18 is not valid anymore. This limit is reached if the grain destruction time t_d becomes equal to the typical time a grain spends in the exposed layer before it gets recycled through vertical transport and collisions in the lower disk layers. We call this time the *residence time* t_{res}. Hence, if $t_{\mathrm{res}} > t_d$, carbon depletion is *residence-time-limited* and the smallest possible depletion timescale is

$$\tau_c^{\mathrm{res}} = \frac{\Sigma_d}{\Sigma_d^*} t_{\mathrm{res}}. \tag{6.26}$$

In Fig. 6.3, we present a sketch of a mixing cycle of small dust grains between the disk midplane and the exposed layer where we illustrate the residence time as a fraction of the full mixing cycle. In Appendix 6.B, we derive an expression for the residence time t_{res} taking into account the random turbulent motions of a grain in the disk, which we model as a stochastic Ornstein-Uhlenbeck process (Uhlenbeck & Ornstein, 1930). For readability, we only report the results in this section and refer the reader to Appendix 6.B for the full derivation. We find the residence time of a particle at height z can be calculated with an integral over the complementary error function and a dimensionless variable χ as

$$t_{\mathrm{res}}(z) = \frac{1}{2} \int_0^{t_{\mathrm{mix}}} \mathrm{erfc}\big(\chi(z,t)\big)\mathrm{d}t \tag{6.27}$$

The dimensionless variable χ is time-dependent and defined as

$$\chi(z,t) = \frac{z - \bar{z}(t)}{\sqrt{2}v(t)} \tag{6.28}$$

where we integrate up to the mixing time $t_{\mathrm{mix}} = 1/\alpha\Omega$ and define a time-dependent mean $\bar{z}(t) = ze^{-\eta t}$. Further, we define the time-dependent variance of the stochastic Ornstein-Uhlenbeck process $v^2(t) = \frac{D_d}{\eta}\left(1 - e^{-2\eta t}\right)$ and the rate η as

$$\eta = St(z)\Omega + \frac{D_d}{h_g^2} \tag{6.29}$$

In Fig. 6.4, we plot the z-dependence of Eq. 6.27 in orange color. The residence time t_{res} has a shallow negative slope above the midplane up to the point at which dust grains decouple from the gas (z_{dec}). Beyond this point, the residence time drops off sharply. When approaching the midplane, the residence time approaches half the mixing time and at for $z = 0$ we find

$t_{\mathrm{res}} = t_{\mathrm{mix}}/2$. This makes sense if one considers the mixing time to be the time a grain performs a full mixing cycle. Since the residence time only considers one side of the disk ($z > 0$), at $z = 0$ it must be equal to half a mixing time.

6.3.4 Photon Scattering

In this section, we further investigate residence-time-limited carbon depletion, i.e., $t_{\mathrm{res}} > t_{\mathrm{ph}}$ at the $\tau = 1$-surface, and study what happens when we include the effects of photon scattering (see also Klarmann et al., 2018). FUV-photons do not only penetrate the disk down to the $\tau = 1$-surface, but penetrate optically thicker regions due to forward scattering (Van Zadelhoff et al., 2003). Consequently, the lower edge of the exposed layer z_1 is lower than the $\tau = 1$-surface and the FUV field extends deeper into the disk. Below the $\tau = 1$-surface, with increasing optical depth, the UV-field is exponentially attenuated $F_{\mathrm{UV}}(z) \propto \exp\big(-\tau(z)\big)$. Hence, at a given radius, the lifetime of a carbon grain t_{ph} that is exposed to UV radiation, increases by a factor $\exp\big(-\tau(z)\big)$. In Fig. 6.4, we plot the vertical dependence, i.e., the exponential increase towards the midplane, of the lifetime of a grain t_d in gray color. At the same time, the surface density that is exposed to UV photons is larger by a factor $\tau(z)$, and we adapt the definition in Eq. 6.20 when considering forward scattering to read

$$\Sigma_d^* = \tau(z) 2\Phi/\kappa_0. \tag{6.30}$$

Thus, below the $\tau = 1$-surface, the unrestricted depletion timescale $\tau_c^{\mathrm{ph}}(z)$ increases with decreasing distance to the midplane. In fact, it increases faster with decreasing distance than the residence-time-limited depletion timescale $\tau_c^{\mathrm{res}}(z)$. Thus, we find the effective depletion timescale by solving

$$\tau_c^{\mathrm{res}}(z_1) = \tau_c^{\mathrm{ph}}(z_1) \tag{6.31}$$

for z_1 where now, $z_1 < z_\tau$ holds. Then, all the grains above z_1 are destroyed faster than their residence time at z_1. Hence, when considering forward scattering in the residence-time-limited case, we consider z_1, to be the lower boundary of the exposed layer. In Fig. 6.2, we visualize the location of z_1 as a function of radius in our fiducial model (in yellow color). Throughout the entire disk, it lies less than half a gas scale height ($0.5h_g$) lower than the $\tau = 1$-surface without forward scattering.

In Fig. 6.5 we visualize the depletion timescales (as a function of radius) for three different models with increasing levels of sophistication. First, the red line shows the unrestricted carbon depletion timescale at the $\tau = 1$-surface, calculated with Eq. 6.24. It is 41 kyr at 1 au. The blue line shows the depletion timescale limited by vertical transport, i.e., the residence time limit, as calculated with Eq. 6.26. It is 2.6 Myr at 1 au. The yellow line shows the depletion timescale under the consideration of forward scattering, as calculated with Eq. 6.31. It has a value of 695 kyr at 1 au.

6.3.5 Analytical Solution of the Carbon Fraction

In Appendix 6.C, we derive an analytical solution describing the carbon fraction as a function of radius and time $f_c(r, t)$, as described by the transport equations in Sec. 6.2.3. In this section, we only summarize the most important results. In the derivation, we study the movement of individual grains subject to radial drift at radial velocity v_r. Assuming we find grains at radius r in the disk at a time $t > 0$, and knowing the radial dependence of v_r from Eq. 6.11, we infer

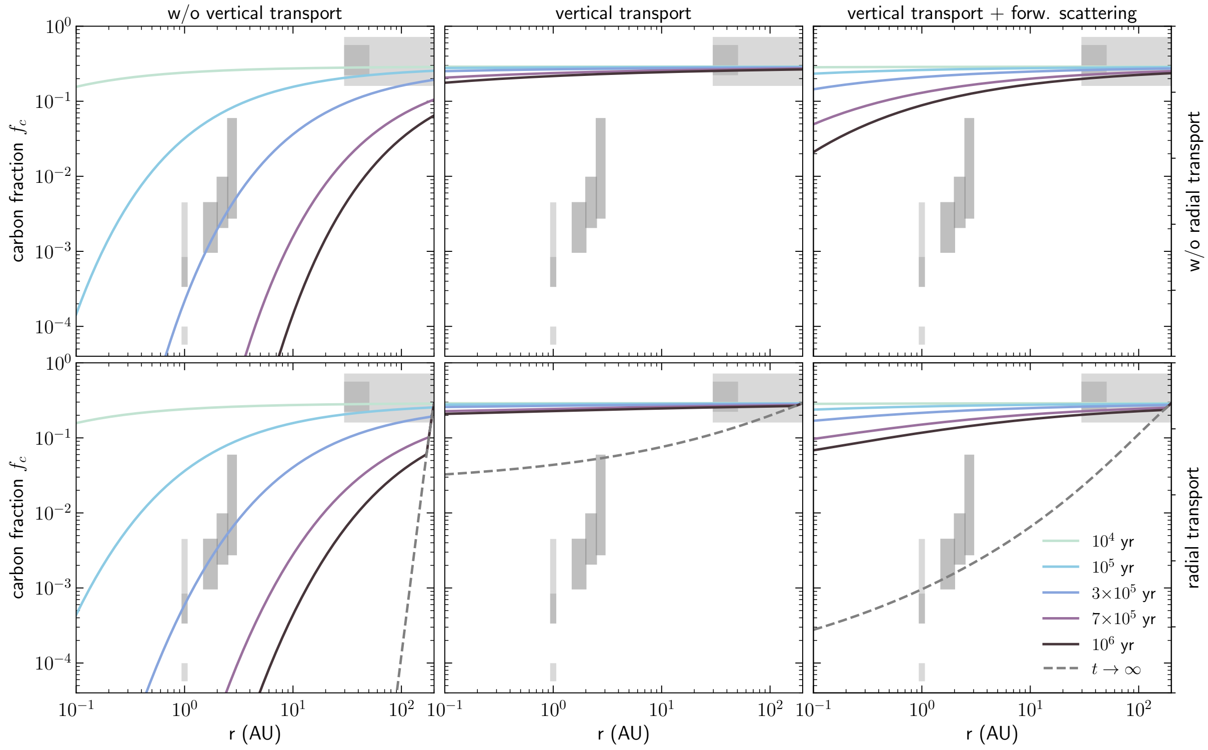

Figure 6.6: Carbon fraction f_c as a function of radius at different times over 10^6 years is depicted, using the fiducial model parameters. The gray boxes represent the estimated carbon fraction on Earth, meteorites and comets and are the same as in Fig. 2.8. *Upper row:* Carbon fraction without radial transport using Eq. 6.84 and Eq. 6.36. *Lower row:* Full model including radial transport using Eq. 6.36 and Eq. 6.33. The gray dashed line represents the carbon fraction at $t \rightarrow \infty$. *Left:* Photolysis without constraints by vertical transport, for which the depletion timescale is calculated using Eq. 6.25. At 1 au we find $\tau_c^{\mathrm{ph}}(z_\tau) = 40$ kyr. *Middle:* Smallest possible carbon fraction if vertical transport is considered and the depletion is only active above the $\tau = 1$-surface. The depletion timescale is calculated using Eq. 6.26 which results in a value of $\tau_c^{\mathrm{res}}(z_\tau) = 2.6$ Myr at 1 au. *Right:* Same as the middle panels, but including forward scattering. The depletion timescale is calculated using Eq. 6.31 which results in a value of $\tau_c^{\mathrm{eff}}(z_1) = 695$ kyr at 1 au.

the initial radial position r' of the grains at time $t = 0$

$$r'(r,t) = \begin{cases} r \cdot \exp\left(-\frac{v_0}{r_0}t\right) & \text{if } l = 1 \\ \left(r^{1-l} + (l-1)r_0^{-l}v_0 t\right)^{1/(1-l)} & \text{else} \end{cases} \tag{6.32}$$

where time t is the time when the grains are at radius r. Knowing the initial radius $r'(r,t)$ of grains at radius r at time t, we calculate the surface density ratio $f_\Sigma = \Sigma_c/\Sigma_s$ at radius r at time t as

$$f_\Sigma(r,t) = \begin{cases} f_\Sigma(r',0) \cdot \left(\frac{r'}{r}\right)^{\frac{r_0}{\tau_{c,0}v_0}} & \text{if } \beta = 0 \\ f_\Sigma(r',0) \cdot \exp\left(\frac{r_0}{\tau_{c,0}v_0\beta}\left[\left(\frac{r'}{r_0}\right)^\beta - \left(\frac{r}{r_0}\right)^\beta\right]\right) & \text{else} \end{cases} \tag{6.33}$$

where

$$\tau_{c,0} = \frac{\Sigma_{c,0}}{\dot{\Sigma}_{c,0}} \tag{6.34}$$

is the carbon depletion timescale at $r = r_0$ and the power-law index β is defined as $\beta = p_d - b - l + 1$. Here, we require $p_d = l + 1$ because only then $\Sigma_d(r)$ is time independent (assuming $\Sigma_d \gg \Sigma_c$) and retains a power-law form, which is a requirement for our analytical analysis. Consequently, the carbon depletion timescale $\tau_{c,0}$ is also time-independent. This becomes clear if we rewrite Eq. 6.34 using Eq. 6.18. The carbon depletion timescale then becomes

$$\tau_{c,0} = \frac{\Sigma_{d,0}}{\Sigma_d^*} t_{d,0} \tag{6.35}$$

and is a function of time-independent quantities only. From the equation above, one finds the carbon depletion timescale to be inversely proportional to the fraction of surface density in which the depletion mechanism is active $\Sigma_{d,0}/\Sigma_d^*$ and directly proportional to the carbon grain destruction time t_d. Ultimately, the carbon fraction f_c as a function of radius and time is

$$f_c(r,t) = \left(1 + \left(f_\Sigma(r,t)\right)^{-1}\right)^{-1} \tag{6.36}$$

or whenever $\Sigma_s \gg \Sigma_c$ holds, the carbon fraction is

$$f_c(r,t) \approx f_\Sigma(r,t) \tag{6.37}$$

From our set of governing equations (Eq. 6.32, Eq. 6.33, and Eq. 6.36), it becomes clear that the evolution of the carbon fraction f_c at a given radius r is mainly driven by the dimensionless quantity $\tau_c v_r/r$ which is the product of the carbon depletion timescale and the radial drift velocity normalized by the radius. Carbon depletion at a given radius will be more efficient the smaller this quantity is. The quantity $\tau_c v_r/r$ is small if the destruction mechanism is active in a large fraction of the disk surface density, i.e., Σ_d^*/Σ_d is large, if the carbon grain destruction time t_d is small or if the radial drift velocity v_r is small. In order to apply the analytical model, we must define Σ_d^* and t_d, which we will do in the following sections.

6.3.6 Connection to the Analytical Solution

Up to this point, we have introduced all the necessary ingredients to evaluate the time evolution of the carbon fraction f_c. We plug in the relevant depletion timescale $\tau_{c,0}$ and the power law index b. For photolysis, unrestricted by vertical transport and without considering forward scattering, we use Eq. 6.25 and evaluate it at r_0=1 au to find $\tau_{\mathrm{c},0}^{\mathrm{ph}}$. Because $F_{UV} \propto r^{-2}$ we immediately find the power-law index $b = 2$. On the other hand, if depletion is limited by vertical transport, we generally do not find an explicit expression for $\tau_{c,0}^{\mathrm{res}}$ and b. Moreover, the carbon depletion timescale τ_c^{res} does not necessarily have power-law dependence in r. Therefore, we approximate it with a power law as

$$\tau_c^{\mathrm{res}}(r,z) \approx \tau_{c,0}^{\mathrm{res}}(z) \cdot \left(\frac{r}{r_0}\right)^{b-3/2} \tag{6.38}$$

and find the corresponding values at a given height z for $\tau_{c,0}^{\mathrm{res}}$ and b in a least-square fit. When combining photolysis and vertical transport in the disk, we calculate an *effective* depletion timescale at every radius r. In cases when we do not consider forward scattering, we calculate the effective depletion timescale at the $\tau = 1$-surface

$$\tau_c^{\mathrm{eff}}(r,z_\tau) = \max\left[\tau_c^{\mathrm{res}}(r,z_\tau), \tau_c^{\mathrm{ph}}(r,z_\tau)\right]. \tag{6.39}$$

When we consider forward scattering, and we find z_1 with Eq. 6.31, the effective depletion timescale is

$$\tau_c^{\mathrm{eff}}(r,z_1) = \tau_c^{\mathrm{res}}(r,z_1) = \tau_c^{\mathrm{ph}}(r,z_1). \tag{6.40}$$

6.4 Thermal Decomposition (Pyrolysis / Irreversible Sublimation)

The second carbon depletion mechanism we study, in addition to photolysis, is the process of *pyrolysis* (this process is sometimes also referred to as the *irreversible sublimation* of the carbonaceous material) which is one of the prime suspects for depleting the inner protosolar disk of its refractory carbon (Li et al., 2021; Van 't Hoff et al., 2020; Gail & Trieloff, 2017; Nakano et al., 2003). While sublimation is a physical change of state that does not involve chemical alterations, pyrolysis is a thermal decomposition process that transforms a solid into a gas via the decomposition of larger organic molecules into smaller molecules (e.g., CO, CO_2, CH_4 or hexane, toluene, phenol, heptane) and as such is generally irreversible. The pyrolysis temperatures of large organic molecules are typically much higher than the sublimation temperatures of the volatile, newly produced molecules. Thus, the products directly enter the gas phase. In this section, we consider the *soot line* (Kress et al., 2010) to be the outer edge of a region within which thermally driven irreversible sublimation, i.e., the combined effect of breaking down molecular bonds within large organic molecules and the consequent release of small molecules into the gas phase, irreversibly destroys carbonaceous material.

6.4.1 Depletion Timescales

Similarly to Sec. 6.3.2, in this section, we define a depletion time t_d' for irreversible sublimation by describing the sublimation process as a first-order reaction process, i.e., the reaction rate is proportional to the local volume density of carbonaceous material in the disk, using kinetic theory. Thermogravimetric laboratory experiments on kerogen, a terrestrial analog to interstellar carbonaceous material, show that the rate coefficient k_i of irreversible sublimation is best described by an Arrhenius-law equation (Chyba et al., 1990)

$$k_i = A_i e^{-E_{i,a}/RT} \tag{6.41}$$

where k_i is the rate, A_i is the exponential prefactor, $E_{i,a}$ is the activation energy and T is the temperature of the carbonaceous material. Due to the expected chemical analogy of the carbonaceous material and the terrestrial kerogen, we also adopt this theory to describe the sublimation of carbonaceous material in our dust compounds in the presolar disk. During the heating of kerogen, various volatile organic compounds are released, for which Oba et al. (2002)

measured activation energies E_a and prefactors A. For photolysis, limited laboratory data do not allow us to differentiate between different carbonaceous compounds. For pyrolysis, more laboratory data exists. However, for simplicity, we describe the sublimation process of each of our five carbonaceous compounds with only a single rate law, as in Eq. 6.41. A more detailed analysis would not be justified given the uncertainty in the exact composition of the presolar material. In Fig. 6.2.1, we list the prefactors A_i and activation energies $E_{a,i}$ for four carbonaceous components (i=1...4, see Sec. 6.4.1 for $i = 5$). Further, we assume that the internal temperature of a dust grain is uniform, and the decomposition process follows Eq. 6.41 uniformly inside the grain volume (as opposed to e.g., evaporation which is a surface process). Patisson et al. (2000) confirm this uniformity, and as such the validity of our first-order approach, for carbonaceous grains which are comparable in size and on temperature variation timescales that are much shorter than what we consider in this work. Moreover, we assume the dust grains to be in thermal equilibrium with their gaseous environment at all times. Assuming a vertically isothermal disk, dust grains only encounter different thermal environments via radial movements, and Stammler et al. (2017) argue that the radial motion of dust grains is slow enough that the instantaneous adaption of the grain temperature to the ambient temperature is well justified. Therefore, we write the destruction time of an individual grain of compound i at disk temperature T as

$$t_{d,i}^{\mathrm{sub}} = A_i^{-1} e^{E_{i,a}/RT} \tag{6.42}$$

Because in our model, the disk is vertically isothermal, at every radius, sublimation is active throughout the entire vertical column of the disk. Thus, the depletion timescale is equal to the time it takes to deplete an individual grain, i.e.

$$\tau_{c,i}^{\mathrm{sub}} = t_{d,i}^{\mathrm{sub}} \tag{6.43}$$

The Case of Amorphous Carbon

Compared to the other carbonaceous compounds considered in our model, amorphous carbon is more refractory. Also, it mainly consists of atomic carbon, without additional O, N, or S, which prevents it from being thermally decomposed into small hydrocarbons like the more volatile kerogen compounds at low temperatures. Instead, only at temperatures above $\sim$ 1500 K, it vaporizes via the release of chain molecules (mainly $C_1 ... C_5$) where the molecules readily react with oxygen (Duschl et al., 1996). However, in protoplanetary disk environments, the amorphous carbon is eroded by chemical reaction with OH molecules, at temperatures below its sublimation temperature ($\sim$ 1200 K). Thus, amorphous carbon can be destroyed by a combustion process before it sublimates (Duschl et al., 1996; Gail, 2001; Gail & Trieloff, 2017). To model this thermochemical decomposition, a complex chemical model of the gas phase is required and is beyond the scope of this work. In a steady state, the temperature required for the oxidation of amorphous carbon via OH is only reached well at the midplane within Earth's orbit, a region that is not relevant to this chapter. Alternatively, Anderson et al. (2017) and Klarmann et al. (2018) studied the effects of carbon depletion via oxidation in the hot disk atmosphere, but it was found to not significantly contribute to the carbon depletion in the inner Solar System.

6.4.2 Analytical solution of the carbon fraction

Based on the consideration in the previous section, and considering only the irreversible sublimation to affect the abundance of refractory carbonaceous material in the disk, we find the source term for the i^{th} carbonaceous compound ($i = 1..4$) in Eq. 6.14 to read

$$\dot{\Sigma}_{d,i} = \Sigma_{d,i} A_i \exp\left(- \frac{E_{i,a}}{RT(r)} \right) \tag{6.44}$$

In Appendix 6.D, we derive the solution to Eq. 6.14 with the source term of the form (6.44) to model effects of irreversible sublimation. The solution to Eq. 6.14 for $i = 1...4$ reads

$$\begin{aligned} &\Sigma_{d,i}(r,t) = \Sigma_{d,i}(r',t')\Big(\frac{r}{r'}\Big)^{-(l+1)} \cdot \\ &\exp\left\{\frac{r_0}{v_0}\frac{A_i R T_0}{q E_{i,a}}\left[\exp\Big(-\frac{E_{i,a}}{RT_0}\Big(\frac{r}{r_0}\Big)^q\Big) - \exp\Big(-\frac{E_{i,a}}{RT_0}\Big(\frac{r'}{r_0}\Big)^q\Big)\right]\right\} \end{aligned} \tag{6.45}$$

By plugging the solution of Eq. 6.45 into Eq. 6.4), we find the solution to the total dust surface density $\Sigma_d(r,t)$. By using Eq. 6.5 and Eq. 6.6, we find the carbon fraction as a function of radius and time $f_c(r,t)$. We discuss these results in Sec. 6.5.2. In Sec. 6.5.4, we combine the results of irreversible sublimation with photolysis to study the combined effects of the carbon depletion mechanisms.

6.5 Results

Here we present the results of our analysis. In Sec. 6.5.1, we first present the effect of photolysis on the abundance of carbonaceous material in our disk model and discuss the influence of model parameters on the results. In Sec. 6.5.2, we report the results when considering the effects of sublimation. In Sec. 6.5.4, we combine photolysis and sublimation.

6.5.1 Photolysis

Depletion Timescales

In our fiducial model, the depletion timescale of unrestricted photolysis in the exposed layer above $z = z_\tau$, i.e., without including restrictions by vertical transport, as calculated with Eq. 6.25, has a value of $\tau_c^{\mathrm{ph}} = 40$ kyr at 1 au and is proportional to $r^{0.5}$. The radial profile of the unrestricted depletion timescale is plotted in Fig. 6.5 in yellow color. When vertical transport is included, i.e., the depletion timescale is calculated with Eq. 6.26 at $z = z_\tau$, the depletion timescale follows the blue line in Fig. 6.5. This profile is not strictly a power law, thus, as described in Sec. 6.3.6, we approximate it with a power law of the form of Eq. 6.38. We find the proportionality factor of the depletion timescale to be equal to $\tau_{c,0}^{\mathrm{res}} = 2.57$ Myr and the power-law exponent to have a value of 0.22. When considering the limiting effects of vertical transport, the depletion timescale is almost two orders of magnitude larger compared to the unrestricted case. This is because, even though the exposed layer gets depleted in carbon quite quickly, it cannot be replenished efficiently with undepleted material from the midplane by vertical mixing. This supports the findings of Klarmann et al. (2018) who found that vertical dust transport reduces the efficacy of carbon depletion. We also find the slope of $\tau_c^{\mathrm{res}}(z_\tau)$ to be shallower than the slope of $\tau_c^{\mathrm{ph}}(z_\tau)$, meaning the carbon depletion efficacy does not drop as much at larger distances from the star as compared to the unrestricted model. In a third model, we also include the effects of photon forward scattering. When considering forward scattering, UV photons penetrate deeper into the disk than the $\tau = 1$-surface, and we calculate the depletion timescale at height z_1 with Eq. 6.40. Because z_1 lies below the $\tau = 1$-surface, the relevant residence time is larger than without scattering $t_{\mathrm{res}}(z_1) > t_{\mathrm{res}}(z_\tau)$ and grains spend more time in the exposed layer before being mixed back into the deeper layers of the disk. An increased residence time alone would result in less efficient carbon depletion. But as a result of forward scattering, a larger fraction of the surface density is exposed to stellar radiation. With decreasing height z, the inverse of the exposed surface density fraction (Σ_d/Σ_d^*) in Eq. 6.26 decreases faster than the residence time (t_{res}) increases. Therefore, the carbon depletion timescale with scattering (yellow line in Fig. 6.5) is overall smaller than the depletion timescale without scattering (blue line in Fig. 6.5). We find the power-law approximation to have a value of $\tau_{c,0}^{\mathrm{res}}(z_1) = 695\,\mathrm{kyr}$, almost four times smaller than without scattering, but still more than an order of magnitude larger than for unrestricted photolysis. Its dependence on r is steeper than without scattering, $\propto r^{0.31}$.

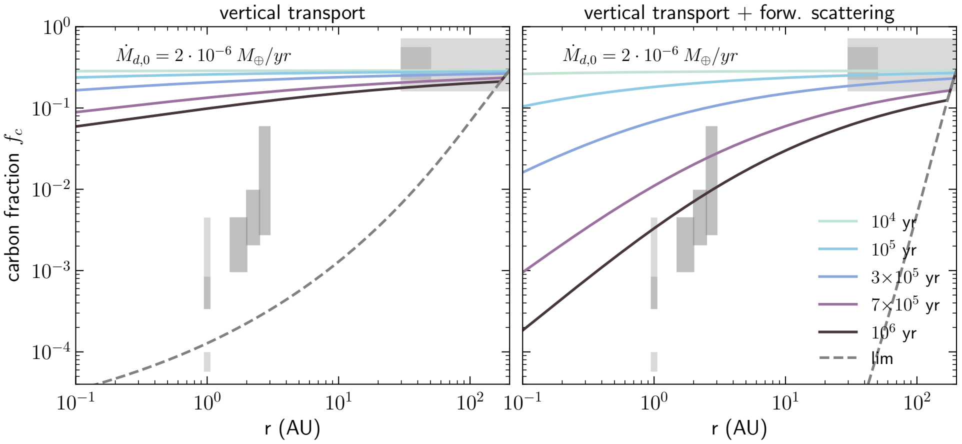

Figure 6.7: Carbon fraction f_c as a function of radius at different times over 10^6 years, with dust surface density Σ_d reduced by a factor of five compared to the fiducial model (including radial and vertical transport). *left:* Carbon fraction as a function of radius and time for residence-time-limited depletion without forward scattering, i.e., the depletion timescale is calculated using Eq. 6.26 which results in a value of $\tau_c^{\mathrm{res}}(z_\tau) = 617$ kyr at 1 au. *right:* Same as the left panel but including forward scattering. The depletion timescale is calculated using Eq. 6.31 which results in a value of $\tau_c^{\mathrm{eff}}(z_1) = 158$ kyr at 1 au.

Photolysis without Radial Transport

We plug the three different depletion timescales, as reported in the previous Sec. 6.5.1, into the analytical evolution equations of the carbon fraction f_c in Eq. 6.36. We first consider cases without radial transport, i.e., we use Eq. 6.84 to calculate the surface density ratio f_Σ in Eq. 6.36. In the upper row of Fig. 6.6, we plot, in the first panel, the carbon fraction f_c as a function of disk radius at different times for photolysis without restrictions by vertical transport using $\tau_{c,0}^{\mathrm{ph}} = 40$ kyr. In the second panel, we show the case in which the depletion is limited by vertical transport and $\tau_{c,0}^{\mathrm{res}} = 2.6$ Myr, i.e., without scattering. In the third panel, we show the case with scattering and $\tau_{c,0}^{\mathrm{res}} = 695$ kyr. The gray boxes in the background of each sub-panel in Fig. 6.6 represent the estimated carbon fractions of Solar System objects, as discussed in Sec. 6.2.1. We confirm the results of Klarmann et al. (2018) by showing that unrestricted photolysis (without restrictions by radial or vertical transport) depletes the inner disk of carbon to values of almost 10^{-4} at 1 au within < 300 kyr. The outer disk shows carbon depletion by more than a factor of ten within the same time, such that Solar System values can be reproduced within a few hundred thousand years. We also find that vertical transport significantly reduces the carbon depletion efficacy because the carbon fraction in the exposed layer drops and vertical transport cannot efficiently replenish these layers with undepleted material from lower disk layers. As a result, the carbon fraction, in the second panel of Fig. 6.6, is barely reduced. Within 1 Myr, values below 10^{-1} are not reached anywhere in the disk. This result represents a lower limit not only for photolysis with vertical transport included but more generally for any photo-induced carbon depletion mechanism that is active in the FUV-irradiated layer of the disk.

Further, we find that including forward scattering improves the carbon depletion efficacy, but it does not sufficiently decrease the depletion timescale such that levels required to reproduce Solar System abundances are not reached. After 1 Myr, the carbon fraction at 1 au is just slightly below $f_c = 10^{-1}$.

Photolysis with Vertical and Radial Transport

Next, we also include the effects of radial transport. Including radial transport does not change the depletion timescale τ_c in our models, but exposes grains to different environments with different depletion timescales as they radially drift inward. Because the depletion timescales in all the three cases presented in Fig. 6.5 have a positive radial gradient, including radial transport decreases the overall carbon depletion efficacy. This is because, at early times, grains experience environments with a lower depletion timescale at larger radial distances. This is not the case if radial transport is ignored and grains are exposed to the same depletion environment at all times. In the lower row of Fig. 6.6, we show the results of the full model, i.e., calculating the carbon fraction using Eqs. 6.32, 6.33, and 6.36. When radial transport is included, the carbon fraction f_c does not decrease indefinitely but eventually reaches a steady state. We indicate the steady-state solution with the gray dashed line in every sub-panel in the lower row of Fig. 6.6. The steady-state solution is the minimal possible carbon fraction when the dust disk is continuously replenished by undepleted material via the outer disk boundary. In all three solutions presented in the lower row of Fig. 6.6, the carbon fraction at 1 Myr is still far away from the steady-state solution throughout most of the disk because radial drift is relatively slow compared to the depletion timescale. At 200 au the radial drift timescale (r/v_r) is $\sim$ 6.5 Myr. Overall, in our models, the influence of radial drift is significantly smaller than the restrictions by vertical transport. However, this is only true as long as the steady-state solution is not reached. At later times, the solutions with and without radial transport will diverge significantly. This divergence will only become relevant once the system approaches the drift timescale (r/v_r) of the grains at the outer disk boundary. In our models, this timescale is much larger than the timescale on which we expect planetesimal formation to occur. However, when radial transport is included in our fiducial model with scattering, the carbon fraction must come very close to the steady-state solution to successfully reproduce Solar System abundances. This happens on a timescale of a few Myr.

Overcoming Dust Transport

In the previous section, we have shown that inefficient vertical transport is the main limiting factor in photo-induced carbon depletion via photolysis because the typical time a grain spends in the exposed layer, per mixing cycle (its residence time), is long compared to the time it takes to destroy an individual grain. In this section, we will study the properties of our analytical model to understand under which circumstances the carbon depletion timescale can be decreased sufficiently to reproduce carbon fractions f_c as measured in the Solar System. It is not straightforward to understand how model parameters influence the carbon depletion timescale τ_c^{res} as presented in Eq. 6.31, due to its implicit form. Therefore, we derive an explicit (but only approximate) expression of the depletion timescale. This allows us to understand the influence of individual parameters on our results. Later, we will confirm our findings by comparing them with the exact result. We plug the explicit approximation of the residence time as derived in Eq. 6.81 into the definition of the depletion timescale in Eq. 6.26, and obtain an explicit expression of the carbon depletion timescale in the residence time limit, i.e., with vertical transport:

$$\tau_c^{\mathrm{res}} \simeq \frac{\Sigma_d \kappa_0}{2\Phi\alpha\Omega} \cdot \left(\sqrt{2 \ln \frac{f_{\leqslant a_s} \Sigma_d \kappa_0}{2\sqrt{\pi}\Phi}} - \frac{1}{5} \right)^{-2} \tag{6.46}$$

In the above expression, $f_{\leqslant a_s} \approx (a_{\max}/a_s)^{-0.5}$ is the mass fraction of grains below or equal to size a_s which we derive in Appendix 6.A. The quantity $a_{\max}$ is the upper limit of the grain size distribution and, in the fragmentation limit, is estimated using Eq. 6.8 and Eq. 6.9. In the fragmentation limit, $a_{\max}$ is inversely proportional to the turbulent alpha parameter $a_{\max} \propto \alpha^{-1}$. Equation 6.46 approximates the depletion timescale when limited by vertical transport, but without taking into account the effects of forward scattering. However, the results in Eq. 6.46 do serve as a good estimate of an upper limit for the solution which includes scattering. In our fiducial model, using Eq. 6.46, we find $\tau_c^{\mathrm{res}}(z_\tau) = 3.6$ Myr at 1 au without decoupling of dust grains. For comparison, we calculated a value of 2.6 Myr with grain decoupling in 6.3.4. The lower value arises from the fact that more weakly coupled grains have a smaller residence t_{res} (see Fig. 6.4).

Due to the explicit nature of Eq. 6.46, we understand its dependence on model parameters. From the first factor in Eq. 6.46, we find that four parameters influence the depletion timescale $(\Sigma_d, \kappa_0, \Phi, \alpha)$, plus the Keplerian frequency Ω, but the latter is not influenced by the choice of model parameters. In Eq. 6.46, the dust surface density (Σ_d) also appears in the argument of the natural logarithm (ln) in addition to the linear dependence of the first factor. Overall, both contributions counterbalance each other due to the negative exponent in the second factor. However, the argument of the natural logarithm is generally much larger than unity, and, thus, its argument contributes less than linear to the overall depletion timescale. Therefore, a decrease in the dust surface density also decreases the depletion timescale because a lower dust surface density decreases the optical depth of the disk, which increases the surface density fraction contained in the exposed layer. The same scaling argument holds for changes in the opacity κ_0 or the flaring angle Φ. A smaller opacity similarly decreases the optical depth of the disk and thus increases the carbon depletion efficacy. A larger flaring angle allows stellar photons to arrive at a steeper angle and thus penetrate deeper into the disk. On the other hand, the turbulence parameter (α) does only appear in the first factor, but not explicitly in the argument of the natural logarithm. However, it implicitly acts on $f_{\leqslant a_1}$ via the maximum grain size in the fragmentation limit $a_{\max}$. The maximum grain size is proportional to α^{-1}. Thus, $f_{\leqslant a_1} \propto \alpha^{0.5}$ and consequently, the turbulence parameter contributes slightly more than linear to the depletion timescale because more turbulence increases the efficiency of vertical transport and, at the same time, increases the number of small grains in the disk because large grains fragment more frequently. To conclude, we find carbon depletion to be favored by a low dust surface density, low opacity, high flaring angles, and high turbulence. Moreover, it is favored by a large mass fraction in small grains, but to a lesser degree than the other factors because $f_{\leqslant a_1}$ only appears in the argument of the natural logarithm.

In our fiducial model, the turbulence parameter is already large, and the constraints on the flaring angle and the opacity are relatively tight in our model. The dust surface density Σ_d, on the other hand, is not well constrained. Decreasing the dust surface density by a factor of five compared to the fiducial model reduces the approximate depletion timescale at 1 au, as calculated with Eq. 6.46, from 3.6 Myr to 860 kyr. The exact result that also considers grain decoupling decreases from 2.6 Myr to 617 kyr. In both cases, the decrease is a factor of 4.2, while the latter values are lower because the residence times of more weakly coupled grains are generally smaller (see Fig. 6.4). We plot the evolution of the carbon fraction in the disk with the decreased depletion timescale (without forward scattering) in the left panel of Fig. 6.7. With a decreased dust surface density, the carbon fraction reaches levels of 10^{-2} at 1 au within 1 Myr which is a depletion by almost a factor of 30. To compare, in the fiducial model, the carbon fraction was only decreased by a factor of 1.5.

When including forward scattering, and solving Eq. 6.31, we do not provide an explicit expression. However, the functional dependence of the depletion timescale will be expanded to include the stellar UV-flux. Forward scattering further decreases the depletion timescale at 1 au to 87 kyr. We show the evolution of the carbon fraction with scattering in the right panel of Fig. 6.7. For comparison, the depletion timescale for photolysis unrestricted by vertical transport is also smaller with lower dust surface density, with a value of 13 kyr at 1 au. The lower dust surface density allows the carbon fractions in our model to reach levels comparable to Solar

System abundances within a time of $\sim 7 \times 10^5$ years, even when radial and vertical transport is included. The same is true for a decrease in the opacity or an increase in the turbulence or flaring angle. Or a change in all parameters which results in a combined decrease in the depletion timescale by a factor of eight compared to the fiducial model.

6.5.2 Irreversible Sublimation

In this section, we study the effects of irreversible sublimation on the carbon fraction f_c, as introduced in Sec. 6.4. We first ignore contributions from photodecomposition processes. In Fig. 6.8, we display the carbon fraction f_c as a function of radius at various times, assuming that the refractory carbonaceous material is continuously decomposed by irreversible sublimation according to Eq. 6.44. Note, Fig. 6.8 only shows the radial range between 0.1 and 5 au, and plots the carbon fraction f_c at earlier times compared to the previous figures in which we showed the results of photolysis. This is because the inner disk is depleted significantly faster due to the exponential dependence on temperature. The upper row of Fig. 6.8 shows the evolution of the carbon fraction in the absence of radial drift. At each point in time, one can identify multiple distinct steps in the radial profile of the carbon fraction f_c. These steps correspond to the soot lines of the individual carbonaceous compounds in our model (see Fig. 6.2.1). The carbon fraction reaches a floor value at $f_c = 0.03$ when only the amorphous carbon compound is left. In the absence of radial drift, these soot lines continuously move outward because the depletion timescale is finite everywhere in the disk. At 1 Myr, all the carbonaceous compounds, except the amorphous carbon, have completely sublimated in the disk region within 0.3 au from the star.

In the bottom row of Fig. 6.8, we include the effects of radial drift. The main difference compared to the no-drift situation is the fact that a steady-state distribution exists, which in our model is reached between 10 kyr and 100 kyr. After that, the carbon fraction profile does not change anymore and the individual soot lines are stationary because the inward drift of the dust exactly cancels the outward motion of the soot line. Due to the exponential dependence of the depletion timescale on temperature, the transition region in which an individual compound is only partially sublimated is very narrow (fractions of an au). Thus, the radial gradient in the disk is more the result of the different sublimation temperatures of the individual compounds, rather than a product of the radial variation in the depletion timescale of an individual compound. This property is distinctly different from photolysis, where the shallow radial slope of the depletion timescale is responsible for the global radial carbon fraction gradient in the disk. Overall, we find irreversible sublimation in our passively heated steady-state disk model to only deplete the innermost disk region. Furthermore, it decreases the carbon fraction by at most a factor of ten due to the presence of a highly refractory amorphous carbon compound, which only decomposes at temperatures > 1000 K. The carbon fraction in the colder disk regions, where Earth or the chondrites are found, is not depleted. The lowest level that the inner disk can be depleted to by irreversible sublimation is strictly set by the abundance of amorphous carbon ($f_5 = 0.03$). The detailed composition of the carbonaceous material in the ISM is highly uncertain. However, the adopted value of 3 % is close to the value of 4.2 % reported in Fomenkova et al. (1994) for in situ measurements in the coma of comet Halley (however, the latter value is reported as a number fraction of measured dust grains rather than a mass fraction). In order to reach values relevant for bulk Earth with irreversible sublimation alone, the abundance of amorphous carbon must be a factor ten lower, i.e., as low as $f_4 \lesssim 0.4\,\%$.

In our model, the steady state soot line is located at a heliocentric distance of about $r \sim 0.25$ au, which corresponds to a temperature of about ~ 450 K in our passively heated, thermal equilibrium disk (see lower panel of Fig. 6.8). The inclusion of viscous disk heating in our model could move the soot line radially outward as a result of the increased disk temperature. However, at 1 au, we find the disk surface temperature to be dominated by viscous heating only if the mass accretion rate is larger than $\sim 2.7 \cdot 10^{-7} \mathrm{M}_{\odot}/\mathrm{yr}$. In our disk model with $\alpha = 10^{-2}$, the accretion

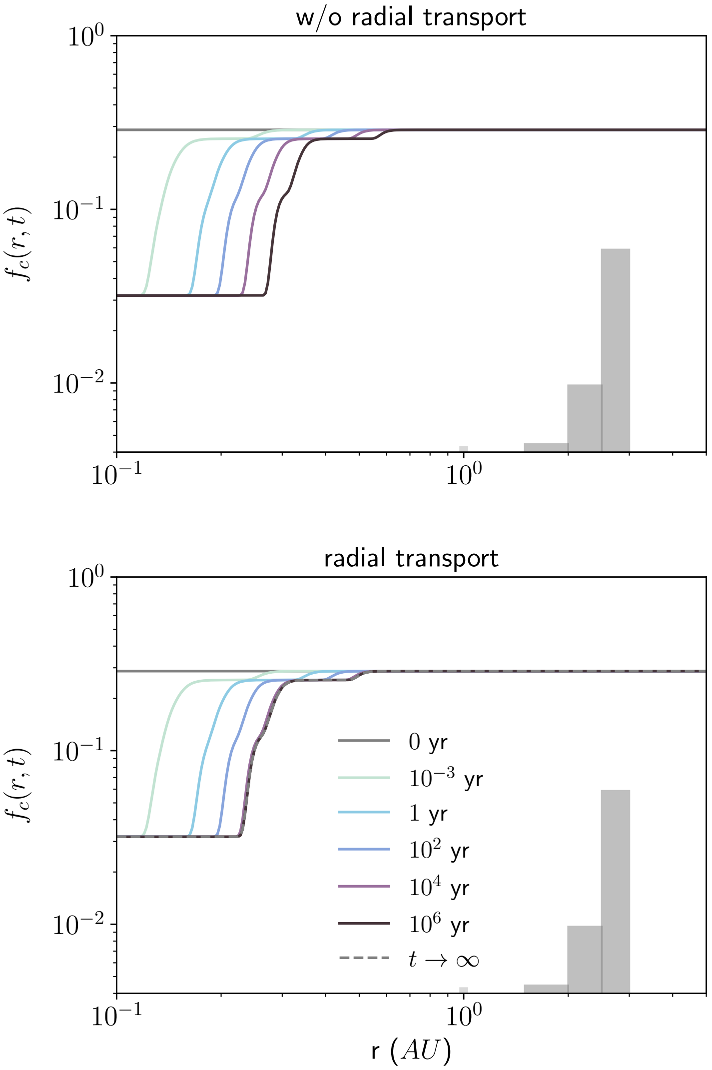

Figure 6.8: Carbon fraction f_c as a function of radius at different times under the assumption that irreversible sublimation is the sole contributor to the decomposition of refractory carbon. The upper panel shows the carbon fraction profile in the absence of radial drift. The individual soot lines continuously move outward, such that the region within about 0.3 au only consists of amorphous carbon after about 1 Myr. The bottom panel shows the same situation but including radial drift. At a time between 10 kyr and 100 kyr the outward motion of the soot lines is counterbalanced by the inward drift of the dust and a steady state forms. The gray boxes indicate the carbon fraction as found in chondrites.

rate at 1 au is lower, with a value of $\sim 3.5 \cdot 10^{-8} \mathrm{M}_{\odot}/\mathrm{yr}$. Hence, the soot line does stay within Earth's orbit even with the contribution of viscous heating. For comparison, Li et al. (2021) show that the soot line in their model moves outward to about 1 au with $\alpha = 10^{-3}$ when viscous dissipation does contribute to the local heating of the disk. Thus, in a steady-state disk model with viscous heating, the disk region out to Earth's orbit might get depleted. But only by a factor of ten because the remaining amorphous carbon compounds survive up to temperatures of over 1200 K before the OH abundance level in the disk rises to levels sufficient for the amorphous carbon to oxidize (Gail & Trieloff, 2017; Gail, 2001; Finocchi et al., 1997). Such temperatures are only reached well within Earth's orbit. Thus, with an amorphous carbon abundance above 0.4 %, we fail to explain the two to three orders of magnitude depletion required to reproduce the carbon fraction of bulk Earth. Analogous arguments hold for the depletion of parent bodies of chondrites.

6.5.3 FU Ori-type Outbursts

In the previous section, we have shown that it is difficult to explain the carbon depletion of Earth and chondrites via irreversible sublimation in a steady-state disk. In this section, we briefly study the effects of transient luminosity outbursts and irreversible sublimation on the carbon fraction. In the Solar System, there is considerable evidence that short-lasting and frequent temperature increases happened during the formation of chondrules (see e.g. Ciesla, 2005, for a review). Additional evidence against a steady state scenario during the early phases of planet formation comes from FU Orionis-type objects, which are a class of objects containing a pre-main sequence star and show sudden increases in luminosity over a short period of time (Herbig, 1966; Hartmann & Kenyon, 1996). We do not aim to imply a connection between the formation of chondrules and FU Ori-type outbursts here, but both phenomena suggest a highly variable disk environment in the early formation phase of solids. Even though it is not clear if the early Solar System has undergone any FU Ori-type outbursts, there are reasons to believe that frequent outbursts are common in the early phase of stellar evolution (Hartmann & Kenyon, 1996). Thus, in this section, we study the particular effects FU Ori-type outbursts on the destruction of carbonaceous material. While the underlying triggering mechanism of FU Ori-type outbursts is not well understood, the typical luminosity increase by a factor of $10^2 - 10^3$ within a timescale of a year to a decade that lasts about a century (Hartmann & Kenyon, 1996) is thought to be the result of a burst of the accretion rate in the inner disk region ($r < 1$ au, Zhu et al., 2007). Even though no object has been observed to have undergone multiple such outbursts, statistical arguments lead to the conclusion that they are repetitive, and an object undergoes at least ten outbursts, assuming that all (low-mass) young stars have FU Ori-type outbursts (Hartmann & Kenyon, 1996), i.e., one every $\sim 10^5$ years (Peña et al., 2019).

In our model, we assume the disk to undergo episodic accretion events which last for 100 years and recur with a period of 100 kyr. We also assume that the region of increased accretion during an outburst is confined to the innermost disk region ($r \ll 1$ au) which we do not explicitly model. We only model the disk outside the region of increased accretion, where we take into account passive heating via the increased accretion luminosity of the innermost disk. In FU Ori-type objects, the transition between the active and passive region is derived to lie anywhere between 5 $R_{\odot}$ and $\sim 0.5 - 1$ au (Audard et al., 2014) which is consistent with our model assumption. Further, we assume the passive portion of the disk to be heated instantly during outbursts and follows the temperature profile as in Eq. 3.34 where the stellar luminosity L_* is replaced by the accretion luminosity L_{acc} of the inner disk. We set $L_{\mathrm{acc}} = 500 L_*$. Consequently, the resulting disk temperature during an outburst increases by a factor $T_{\mathrm{burst}} \approx 4.7 \cdot T$. Alternatively, we find the disk temperature during the outbursts to shift radially by a factor ~ 22.4 like $T_{\mathrm{burst}}(r) \approx T(r/22.4)$, i.e., the steady-state soot line moves from ~ 0.25 au to ~ 5.6 au during an outburst. Naturally, any other sublimation line does moves by the same factor. This is also roughly consistent when comparing the results of Cieza et al. (2016), who observed the

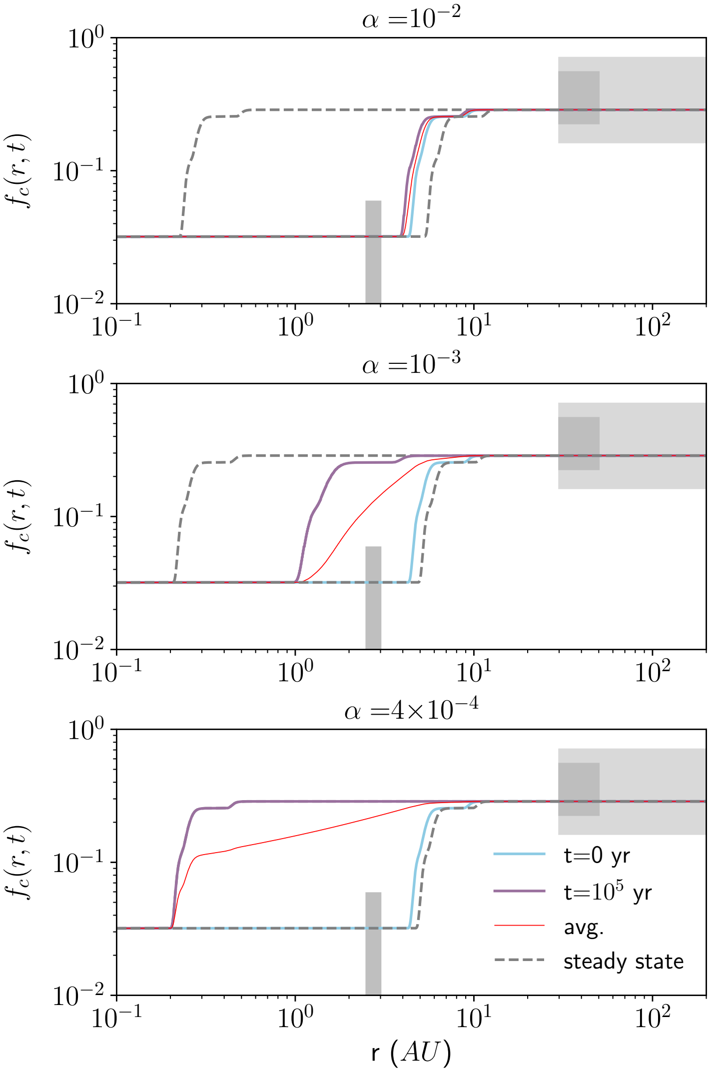

Figure 6.9: Radial shift of the soot line as a result of an FU Ori-type outburst. Plotted is the carbon fraction f_c as a function of radius for three different turbulent alphas. The dashed lines show the steady states in cases without outbursts and a state in which the luminosity is continuously increased by a factor 100. The light blue line shows the carbon fraction after a 100-year-long outburst. The purple line shows the carbon fraction 100 kyr after an outburst when the dust had time to radially drift inward. The red line shows the time-averaged carbon fraction at every radius, assuming the outburst happens every 100 kyr.

water-snow line in the outbursting system V883 Ori at a distance of 42 au, to the location of the steady state snow line in the early Solar System, which is expected around ~ 3 au (Martin & Livio, 2012).

In Fig. 6.9, we show the radial shift of the soot line during one of our model outbursts in disks with a different turbulent alpha. The two dashed lines in each subplot indicate the steady-state carbon fraction f_c. The inner profile corresponds to the steady-state in the absence of any outburst, while the outer line corresponds to a steady state in a disk with 500 times increased luminosity. As mentioned above, the profile shifts to the outer disk by a factor of about 22.4. The light-blue solid line shows the carbon fraction at the end of an outburst episode of 100 years, i.e., the expected duration of an FU Ori-type outburst. We label this with $t = 0$. The purple line shows the carbon fraction at 100 kyr after the end of an outburst when the dust had time to radially drift inward. The drift speed follows Eq. 6.11 and is inversely proportional to the alpha parameter. During the relatively short outburst duration of 100 years, the soot-line moves outward by a considerable distance due to the short sublimation timescales (see Eq. 6.41). From the steady-state location at ~ 0.25 au, it moves out to ~ 5.6 au. For $\alpha = 10^{-2}$, the dust grains are so small that they barely drift inward in the 100 kyr time period between outbursts, i.e., one outburst every 100 kyr is enough to permanently shift the soot line from ~ 0.25 au to ~ 5 au and the region within 5 au remains permanently depleted. For $\alpha = 10^{-3}$, the grains drift fast enough to just reach 1 au, while for $\alpha = 4 \cdot 10^{-4}$ they reach the inner steady state radius slightly before the next outburst.

Assuming a mechanism would continuously produce planetesimals at a given radius r, the produced planetesimals would show a different carbon fraction f_c depending on whether the soot line was inside or outside their formation radius. We further assume the planetesimals are produced over an extended period of time and calculate the average carbon fraction of the entire population of planetesimals that has formed at a given radius and plot their average carbon fraction in red color in Fig. 6.9. Interestingly, for $\alpha \sim 10^{-3}$, the time-averaged carbon fraction (red line) distributes the carbon more evenly in the system and does not show its step-like character.

Note that, as a result of the different drift velocities, the location of the steady-state soot lines also changes for different values of α. However, as a result of the exponential dependence on temperature in Eq. 6.41, the radial change is small.

6.5.4 Photolysis, Sublimation, and Outbursts Combined

In Sec. 6.5.1, we showed that photolysis is residence-time-limited in our models. And in Sec. 6.5.1, we showed with Eq. 6.46 that, in the residence time limit, the carbon depletion timescale τ_c^{res} is independent of the incident radiation flux and consequently also of the underlying stellar luminosity. Therefore, we conclude that at least to first order, carbon depletion via photolysis is not altered by an increase in luminosity during FU Ori-type outburst. The same is true for any photo-induced process that is active in the UV-irradiated layers of the disk (e.g., oxidation). Nonetheless, we combine the results on stellar outbursts with the results of photolysis in Sec. 6.5.1 and study the combined effects of two depletion mechanisms of irreversible sublimation and photolysis. In Fig. 6.10, we show the combined effects of photolysis and time-averaged irreversible sublimation with the fiducial dust-to-gas ratio (*left subplot*) and reduced by a factor of five (*right subplot*). We find the characteristic step-like shape at the soot lines beyond 4 au as a result of FU Ori-type outbursts. Thus, at every time, there is a decrease by a factor of ten in the inner disk compared to the outer disk. In the inner disk, photolysis further decomposes the refractory amorphous compounds. In the fiducial model, the carbon fraction reaches levels of carbonaceous chondrites within 1 Myr, but not the levels of the more depleted chondrites or of Earth. On the r.h.s. of Fig. 6.10, the initial dust surface density Σ_d is reduced by a factor of five, which decreases the photolysis depletion timescale by a factor of 4.2

(as described in Sec. 6.5.1). As a result, photolysis depletes the inner disk more efficiently and the carbon fraction f_c reproduces Solar System values of chondrites and bulk Earth within 700 kyr.

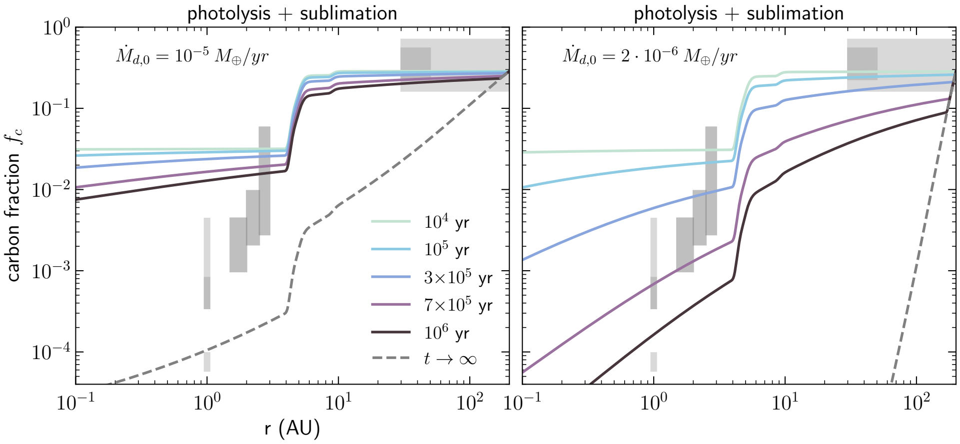

Figure 6.10: Evolution of the carbon fraction f_c under the influence of the combined effects of photolysis and time-averaged irreversible sublimation including FU Ori-type outbursts, with the fiducial dust surface density (left) and reduced by a factor of five (right). In the fiducial case, the carbon fraction does not reproduce the observed values for the inner Solar System within 1 Myr. On the other hand, when the dust-to-gas ratio is reduced by a factor of five, the observed Solar System values are reached within about $7 \cdot 10^5$ years.

6.6 Discussion

6.6.1 Bouncing Collisions and Photolysis

In this section, we consider the effect of bouncing collisions, which can alter the size distribution of the solid disk material(Blum, 2010), on the depletion timescale in the case of photolysis. Throughout this work, we have assumed the dust size distribution to be in a coagulation-fragmentation equilibrium in which the surface area of solids is dominated by the smallest grains. Bouncing collisions, rather than fragmenting collisions, reduce the number of small grains in the size distribution. We first assume bouncing and fragmenting collisions to coexist in a way that the net effect of bouncing is a reduction in the number of small grains, but fragmentation still replenishes small grains efficiently enough so that they are still the dominant contributor to the UV-opacity at the $\tau = 1$-surface. The removal of small grains moves the $\tau = 1$-surface closer to the midplane. If photolysis is still residence-time-limited, bouncing increases the carbon depletion timescale, i.e., photolysis becomes less efficient because the residence time $t_{\rm res}$ increases with a shift of the $\tau = 1$-surface towards the midplane (see Eq. 6.26 and Fig. 6.4). Photolysis becoming less efficient when bouncing is considered is also apparent when considering Eq. 6.46. As long as the smallest grains dominate the opacity at the $\tau = 1$-surface, the inclusion of bouncing decreases the mass fraction $f_{\leqslant a_1}$ in Eq. 6.46, and the remaining parameters remain unchanged. Because the depletion time $\tau_c^{\rm res}$ scales with the logarithm of the mass fraction $f_{\leqslant a_1}$, a change in the mass fraction $f_{\leqslant a_1}$, typically only has a small effect on the depletion time of photolysis.

We further consider a more extreme example in which fragmentation does not replenish small grains efficiently, such that the smallest grains are no longer the main contributor to the UV-opacity at the optical surface and instead, the surface area is dominated by the largest particles at the bouncing barrier. As a result, the residence time $t_{\rm res}$ increases, but as we show in Sec. 6.3.3, it always stays smaller than half the mixing time $t_{\rm mix}$, i.e., it increases by at most a factor five. The destruction time $t_{\rm ph}$, on the other hand, scales with the radius of the opacity dominating grain population (Eq. 6.23). Thus, if the bouncing barrier is located at a large enough grain size, photolysis will no longer be residence time limited because $t_{\rm ph} > t_{\rm res}$. For an illustrative example, we assume the grains to grow until the bouncing barrier at size a_B. Then, the grain destruction time of a grain in the exposed layer is

$$t_{\rm ph,B} = \frac{m}{m_c R_{\rm UV}} = \frac{4}{3}\frac{a_B \rho_\bullet}{m_c Y_{\rm ph} F_{\rm UV}} \tag{6.47}$$

For simplicity, we assume, the size a_B of grains at the bouncing barrier, to be equal to the grains at the (hypothetical) fragmentation barrier, i.e., the only grain size we consider is

$$a_B = \frac{2}{3\pi}\frac{f_f m_g v_f^2}{\alpha k_B}\frac{\Sigma_g}{T} \tag{6.48}$$

Then, the depletion time for bouncing $t_{\rm ph,B}$ scales with radius like the inverse of the Keplerian frequency

$$t_{\rm ph,B} = t_{\rm ph,B,0}\left(\frac{r}{r_0}\right)^{2-p_g+q} \tag{6.49}$$

with proportionality factor

$$t_{\rm ph,B,0} = \frac{8}{9\pi}\frac{f_f m_g \rho_c v_f^2 \Sigma_{g,0}}{\alpha k_B m_c Y_{\rm ph} F_{\rm UV,0} T_0} \tag{6.50}$$

In our fiducial model, we find $t_{\rm ph,B} = 76.6\,\Omega^{-1}$ which is equal to 12.6 yr at 1 au. The residence time is always smaller than half the mixing time, which in our fiducial model at 1 au is equal to $50\,\Omega^{-1}$. Thus, $t_{\rm res} > t_{\rm ph,B}$ and photolysis is not limited by vertical transport in this example and the effective depletion timescale is

$$\tau_{c,B} = \frac{\Sigma_{d,0}}{\Sigma_d^*} t_{d,B} \tag{6.51}$$

which does simplify to

$$\tau_{c,B}^{\rm ph} = \frac{\Sigma_d}{2 m_c Y_{\rm ph} \Phi F_{\rm UV}} \tag{6.52}$$

by plugging in Eq. 6.47 and using $\Sigma_d^* = \kappa_0^{-1} = 4\rho_\bullet a_B/3$. Equation 6.52 is identical to the unrestricted carbon depletion timescale (Eq. 6.25) in a coagulation-fragmentation distribution, i.e. $\tau_c^{\rm ph,B} = 40\,{\rm kyr}$.

To conclude, if bouncing does not heavily deplete the number of small grains, it does decrease the efficiency of photolysis. But, if it decreases the number density of small grains enough for large grains to become the dominant contributor to the FUV-opacity at the optical surface, it significantly decreases the depletion timescale of photolysis. The validity of this simple argument should be evaluated in a more detailed study.

6.6.2 Choice of Model Parameters

Dust Surface Density Σ_d

We showed that the carbon depletion timescale is sensitive to the dust surface density Σ_d and thus, indirectly also to the total dust mass contained in the disk. Hence, the carbon depletion efficacy is larger in less massive disks. However, the total dust mass in the early Solar disk is bound from below because there must be enough solid material in the inner disk to form the rocky objects in the Solar System. In our fiducial model, the total dust mass contained in the disk up to 200 au is 131 $M_\oplus$. Lenz et al. (2020) have constrained the parameter space for the Solar nebula and propose a lower bound for the total mass of planetesimals at 76 $M_\oplus$. If all the dust is converted into planetesimals, the initial global dust disk cannot be less massive than 76 $M_\oplus$, i.e., the dust surface density can, at most, be reduced by a factor of 1.7 compared to our fiducial model. A reduction by a factor of 1.7 in the dust surface density alone cannot reproduce the carbon abundance in the Solar System within 1 Myr.

Dust traps, on the other hand, can locally decrease the dust surface density also in more massive disks. A dust trap caused by a Jupiter-mass planet can decrease the dust surface density inside the orbit of the planet by a factor of 10 (Drążkowska et al., 2019). The local decrease does not contradict Lenz et al. (2020) who require a planetesimal mass of $0.1 - 8.77$ $M_\oplus$ in the inner Solar nebula between 0.7 and 4 au. In our fiducial model, the total dust mass between 0.7 and 4 au is 18.5 $M_\oplus$. Hence, a decrease only in the inner disk by a factor of 10 is consistent with constraints on the inner Solar Nebula. As a result, a dust trap is likely required to reproduce the observed carbon abundance in the inner Solar System. In other lower-mass protostellar systems, a dust trap is not necessary to reproduce similar carbon depletion levels. Of course, while a dust trap decreases the dust surface density in the inner disk, it increases the dust surface density at the location of the dust trap, effectively switching off carbon depletion there. Thus, planetesimals that form inside the dust traps are likely less depleted in carbon. Therefore, if planetesimals mainly form in dust traps, carbon must be removed from the dust before it accumulates in the trap.

Opacity κ

The depletion timescale τ_c sensitively depends on the UV-opacity of the disk atmosphere. Carbon depletion itself can reduce the opacity in the exposed layer by releasing solid material into the gas. An effect that we do not take into account in our model. As carbonaceous material initially contributes 29 % to the total dust mass, it contributes about the same amount to the total opacity. Hence, the destruction of all the carbon would decrease the opacity in the exposed layer by 29 %. Furthermore, there are large uncertainties in the exact opacity of the solid disk material because it sensitively depends on the composition and the local size distribution of the material (Birnstiel et al., 2018). We expect a detailed opacity treatment could easily introduce corrections by a factor of a few compared to our crude model assumptions.

Turbulent Alpha Parameter α

We use a relatively large value for the turbulent alpha parameter ($\alpha = 10^{-2}$), which we show is needed for efficient carbon depletion in the exposed layer. Observationally, it is difficult to directly infer the levels of turbulence in protoplanetary disks. However, measurements and modeling of the widths of dust rings in mm-continuum observations consistently report relatively strong levels of turbulence $\alpha/St \gtrsim 10^{-2}$ (Dullemond et al., 2018; Rosotti et al., 2020).

6.6.3 Other Carbon Depletion Mechanisms

In this work, we have only focused on photolysis and irreversible sublimation as refractory carbon depletion mechanisms. There are other mechanisms that could potentially increase the carbon depletion efficiency (e.g., photo-/thermochemically induced processes). However, they will likely only further decrease the carbon fraction if they are active in the denser disk regions close to the midplane. Any photo-induced mechanism that is active in the UV-irradiated layers of the disk, suffers from the same limitations as photolysis and will be residence-time-limited. As for thermal decomposition mechanisms, irreversible sublimation is already very efficient in the inner disk, but suffers from the problem that it does not decompose the amorphous carbon compounds. Amorphous carbon only decomposes at temperatures beyond 1200 K when enough oxygen is available for its oxidation (Gail & Trieloff, 2017). In our models, the 1200 K line only reaches out to ~ 0.85 au during an FU Ori-type outburst, which is well within the expected formation region of the solid objects in the asteroid belt. Further, it is not clear whether oxidation is efficient enough to significantly deplete the disk during short-lasting outbursts.

6.6.4 Timing of Planetesimal Formation

In Sec. 6.5.4 we showed that it is in principle possible to deplete the disk in a coagulation-fragmentation equilibrium to values as observed in the Solar System. However, the coagulation-fragmentation equilibrium will only persist as long as planetesimal formation has not yet commenced. Refractory carbon depletion by externally induced photo- and/or thermal decomposition will likely cease to operate efficiently once the material is locked in planetesimals with a small surface-to-mass ratio and very little internal mixing. Thus, planetesimals inherit the local carbon fraction of the dust at their formation location in space and time. Depending on the details of the planetesimal and/or planet formation process, Solar System objects are built from planetesimals formed over an extended period of time at different locations in space. The resulting carbon fraction of the body will then be an average over all the planetesimals the body has formed from. The timing and location of planetesimal formation is therefore critical (Lichtenberg et al., 2021). Further decomposition of refractory compounds as a result of internal heating processes after the incorporation of the material into planetesimals is also possible, but beyond the scope of this project (see e.g. Lichtenberg & Krijt, 2021).

Radial Turbulent Diffusion

In Sec. 6.3.3, we have discussed the effects of vertical transport as a result of turbulent mixing. However, turbulence also causes radial dust transport in addition to radial drift. In our simplified model, we have ignored the effects of radial turbulent mixing. Turbulent diffusion, which is most effective at large values of α, is capable of mixing carbon-rich material from outside the soot line to the inner disk and replenishing the inner disk after a FU Ori-type outburst even when radial drift is slow. With a simple timescale argument, we expect replenishment via radial diffusion to become relevant in the region between 1 au and 5 au when the radial component of the turbulent alpha is larger than $\sim 6 \cdot 10^{-3}$. Hence, the results in the first subplot of Fig. 6.9 are only reasonable if the underlying turbulent mixing is anisotropic, something that could be expected, for example, from hydrodynamic turbulence caused by vertical shear instability (Stoll et al., 2017).

6.7 Summary

In this work, we build upon the model of Klarmann et al. (2018) and study the depletion of refractory carbon in the solid material of the early Solar System by means of an analytical model of the young Solar disk. In Sec. 2.4.4, we provide an overview of the problem and, in Sec. 2.4.5, we estimate Bulk Earth to be depleted in carbon by at least two orders of magnitude (by mass) when comparing to the ISM. Based on detailed models, bulk Earth could even be depleted by almost three orders of magnitude (see Table 2.1). We expect solid refractory carbonaceous material to be selectively decomposed and lost to the gas phase, i.e., it is *destroyed*, in the time between the infall of interstellar material and the formation of the parent bodies of today's rocky Solar System objects (terrestrial planets, asteroids, etc.), i.e., within the first 10^6 years of Solar

System formation.

In Sec. 6.2.1, we introduce a compositional model of the solid material that was delivered to the early Solar System based on literature values (see illustration in Fig. 6.2.1) and illustrate how it is radially distributed among today's Solar System bodies in Fig. 2.8. We aim to reproduce current Solar System abundances via the selective removal of carbonaceous material in the early Solar disk by photo-induced and/or thermally-induced decomposition processes.

In Sec. 6.3.2, we study *photolysis* as a specific example of a photo-induced carbon decomposition mechanism that is active in the UV-irradiated *exposed layer* of the disk atmosphere. We derive an analytical solution that describes the decreasing carbon fraction $f_c(r,t)$ as a function of heliocentric radius r and time t (see Eq. 6.32, Eq. 6.33 and Eq. 6.36) and identify a characteristic carbon depletion timescale τ_c (see Eq. 6.16). In our most detailed model, which considers both radial and vertical transport of the solid material, as well as photon forward scattering, we find the carbon depletion timescale by solving Eq. 6.30 which results in a value of $\tau_c^{\mathrm{res}} = 695\,\mathrm{kyr}$ at 1 au. That is a value too large to reproduce Solar System abundances within the disk lifetime (see the third column of Fig. 6.6). While radial transport mainly determines the steady-state solution on long timescales (gray dashed lines in Fig. 6.7 and Fig. 6.10), it only marginally influences our result on the timescales relevant for our problem (in contrast to the model in Klarmann et al., 2018). It is only the inefficient vertical transport that limits the carbon depletion in our model because the UV-irradiated exposed layers of the disk are depleted in carbon faster than they can be replenished by vertical mixing (see the sketch in Fig. 6.3). This limitation does not only hold for the specific example of photolysis but for any photo-induced carbon depletion mechanism which is active in the UV-irradiated *exposed layers* of the disk.

In Appendix 6.B and Eq. 6.46, we explicitly show that the carbon depletion timescale τ_c^{res} can either be increased by decreasing the vertical mixing timescale $t_{\mathrm{mix}} = 1/\alpha\Omega$ or increasing the extent of the exposed layer. Thus, to first order, the depletion timescale is directly proportional to the total dust surface density Σ_d and the dust opacity at UV wavelengths κ_0, and inversely proportional to the disk flaring angle Φ. Furthermore, there is a minor (higher-order) dependency on the mass fraction of small grains relative to large grains $f_{\leqslant a_s}$. We find no other parameters to influence the carbon depletion timescale τ_c^{res} in our model, this includes the stellar UV flux F_{UV}. Furthermore, we find a combined change by a factor of order ten compared to our fiducial values (see Table 6.1) in any of the main parameters $(\alpha \uparrow, \Sigma_d \downarrow, \kappa_0 \downarrow, \Phi \uparrow)$ in a direction that decreases the depletion timescale τ_c^{res}, does reproduce Solar System abundances via photolysis, even when considering radial and vertical dust transport. In Sec. 6.6.2, we discuss our choice of initial parameters and find them to be only weakly constrained such that, even though a combined change by a factor of ten is not well justified, it is entirely plausible based on our current limited understanding.

The second depletion mechanism that we study is the thermally induced irreversible sublimation (pyrolysis) of carbonaceous material (see Sec. 6.4). We describe the evolution of the carbon fraction $f_c(r,t)$ under the influence of irreversible sublimation in a kinetic approach with Eq. 6.45 and different thermal decomposition parameters for each carbonaceous compound (see Eq. 6.42 and Fig. 6.2.1). We find a steady state to form within 10^4 years when the outward radial motion of the soot line is balanced by inward drift, such that static soot lines, corresponding to the different carbonaceous compounds, in a radial range between 0.25 au and 0.5 au, divide the disk into a depleted and an undepleted region (see Fig. 6.8). As a result of the disk temperature profile, the region, where we expect Earth and chondrite parent bodies to have formed ($\sim 1-3$ au), remains entirely undepleted. Further, the carbon fraction in the depleted region only decreases to a floor value of $f_c = 0.03$ i.e., an order of magnitude above Earth's abundance, which corresponds to the abundance of highly refractory amorphous carbon compound. This compound does not thermally decompose at temperatures below ~ 1200 K (see Sec. 6.4.1). The initial abundance of amorphous carbon in our model is only constrained by a single source, based on in situ measurements on comet Halley. Thus, the general abundance in the material that was delivered to the early Solar System could very well be much lower, decreasing the resulting floor value. Otherwise, the amorphous carbon must be decomposed by other means to reproduce Earth's carbon abundance. Moreover, increased disk temperatures are required to shift the soot lines of the less refractory carbonaceous compounds radially outward such that disk regions beyond 1 au are depleted. We expect viscous heating to not sufficiently increase the disk temperature to also affect the formation region of chondrites. Therefore, we additionally study the effects of frequent and short-lived stellar luminosity outbursts (*FU Ori-type outbursts*) on the location of the soot lines in Sec. 6.5.3. We find that in our fiducial setup, one outburst every 100 kyr is enough to permanently move the soot lines from the range between $\sim 0.25 - 0.5$ au to $\sim 4.5 - 10$ au even when radial drift acts to replenish the inner disk in between individual outbursts (see Fig. 6.9). The soot lines only return to their original steady state location if the radial drift speed is large enough, which is the case for $\alpha \lesssim 4 \cdot 10^{-4}$. A further complication arises for $\alpha \gtrsim 6 \cdot 10^{-3}$ and isotropic turbulence, for which we expect radial diffusion to replenish the inner disk in between individual outbursts. In our analytical approach, we do not include the effects of radial turbulent diffusion. Nonetheless, there is a range around $\alpha \approx 10^{-3}$ in which neither radial drift nor turbulent diffusion can efficiently replenish the disk to the inside of 4.5 au in between stellar outbursts. In conclusion, a reproduction of Solar System abundances via irreversible sublimation requires high temperatures (> 500 K) that move the soot lines beyond the formation region of the parent bodies of the rocky objects of the inner Solar System (> 3 au), in combination with a low abundance of the most refractory carbonaceous compounds ($f_c < 0.4\%$). If these temperatures are reached only temporarily like in FU Ori-type outbursts, the turbulent alpha parameter must be on the order of 10^{-3} such that the inner disk regions are not replenished by radial drift or diffusion.

Another class of depletion mechanisms that can be active in the disk midplane (and thus not suffering from vertical transport restrictions like photolysis) are thermally induced chemical decomposition processes. However, the most promising example, oxidation via OH, only becomes efficient at midplane temperatures > 1200 K, and thus, is not relevant in the formation region of Earth or chondrites.

In Sec. 6.5.4, we find the combined effects of photolysis, irreversible sublimation and FU Ori-type outbursts to reproduce Solar System abundances within 700 kyr when the depletion timescale of photolysis is decreased by a factor of five compared to our fiducial model. Specifically, we achieve this by decreasing the dust surface density Σ_d by a factor of five (see Fig. 6.10).

In Sec. 6.6.1, we argue that, if large dust grains become the dominant contributor to the UV-opacity as a result of bouncing, the carbon depletion timescale of photolysis can become as low as $\tau_c^{\mathrm{ph,B}} = 40\,\mathrm{kyr}$. However, the effects of bouncing collisions are beyond the scope of this chapter.

Even though our fiducial setup does not reproduce carbon abundances of the Solar System, we demonstrate that, under specific but plausible conditions, photo- and/or thermally induced decomposition processes of carbonaceous material in the disk phase of the early Solar System, do reproduce carbon abundances that are observed today.

Table 6.2: List of notations of Chapter 6

symbol	description [cgs unit]
Σ_c	Surface density of carbonaceous material [g cm^{-2}]
Σ^*	Surface density in the exposed layer, Eq. 6.20 [g cm^{-2}]
$\dot{\Sigma}_c$	Destruction rate of carbonaceous material [g cm^{-2}s^{-1}]
Σ_d	Dust surface density, Eq. 6.3 [g cm^{-2}]
$\dot{\Sigma}_d$	Destruction rate of the i-th dust compound [g cm^{-2}s^{-1}]
$\dot{\Sigma}_d$	Dust destruction rate [g cm^{-2}s^{-1}]
Σ_g	Gas surface density, Eq. 6.1 [g cm^{-2}]
Σ_s	Surface density of silicate material [g cm^{-2}]
Φ	Disk flaring angle [rad]
Ω	Keplerian angular frequency [s^{-1}]
α	Dimensionless turbulence parameter [1]
β	Power-law exponent defined in Eq. 6.117 [1]
γ	Modulus of the power-law exponent of the gas pressure [1]
η	Settling rate as defined in Eq. 6.70 [s^{-1}]
κ	Opacity [cm^{2}g^{-2}]
κ_0	UV-opacity [cm^{2}g^{-2}]
λ	Wavelength [cm]
ρ_g	Gas volume density, Eq. 3.8 [g cm^{-3}]
σ	Geometrical cross-section [cm^2]
τ	Optical depth in radial direction [1]
τ_c	Carbon depletion timescale, Eq. 6.16 [s]
τ_c^{ph}	Unrestricted photolysis carbon depletion timescale, Eq. (6.24) [s]
τ_c^{res}	Residence time limited carbon depletion timescale, Eq. (6.26) [s]
τ_c^{eff}	Effective carbon depletion timescale, Eq. 6.39 [s]
τ_c^{sub}	Sublimation depletion timescale, Eq. 6.43 [s]
τ_z	Vertical optical depth [1]
υ	Standard deviation (variance) of Eq. 6.71 [cm]
χ	Dimensionless vertical coordinate defined in Eq. 6.28 [1]
A	Exponential prefactor in the Arrhenius law [s^{-1}]
B	Dimensionless constant defined in Eq. 6.104 [1]
C', C''	Integration constants [g cm^{-2}]
D_d	Dust diffusivity [cm^2 s^{-1}]
E_a	Activation energy of sublimation [erg]
F_{UV}	FUV flux [cm^{-2}s^{-1}]
L_*	Stellar luminosity [erg s^{-1}]
L_{UV}	Stellar UV luminosity [erg s^{-1}]
M_*	Stellar mass [g]
M_c	Total mass of carbonaceous material [g]
$\dot{M}_d$	Dust mass accretion rate [g s^{-1}]
M_s	Total silicate mass [g]
$\dot{M}_s$	Non-carbon grains mass accretion rate [g s^{-1}]
$M_{g,\mathrm{tot}}$	Total gas mass [g]
$\mathcal{N}$	Normal distribution
P_g	Gas pressure [dyn cm^{-2}]
R	Gas constant [erg K^{-1}mol^{-1}]
R_{UV}	Photolysis rate [s^{-1}]
St	Stokes number, Eq. 6.8 [1]

Table 6.2 – continued from previous page

symbol	description [cgs unit]
T	Disk temperature, Eq. 6.2 [K]
T_{burst}	Elevated disk temperature during an FU Ori-type outburst [K]
W_t	Wiener process
Y_{ph}	Photolysis yield [1]
a	Dust grain radius [cm]
a_B	Dust grain radius at the bouncing barrier, Eq. 6.48 [cm]
a_s	Radius of opacity dominating small grains [cm]
b	P.l.i. of the carbon grain destruction time t_d [1]
b_{res}	Fit parameter power law index of the residence time [1]
c_s	Isothermal sound speed [$\mathrm{cm\,s^{-1}}$]
f	Probability density function
f_Σ	Surface density ratio, Eq. 6.33 [1]
f_c	Carbon fraction [1]
f_{f}	Fragmentation limit calibration factor [1]
f_s	Silicate mass fraction [1]
$f_{\leqslant a_s}$	Mass fraction of grains smaller or equal to a_s
$f_{\geqslant z}$	Dust surface density fraction above height z
h_g	Vertical gas scale height [cm]
k	Rate of sublimation, Eq. 6.41 [$\mathrm{s^{-1}}$]
k_B	Boltzmann constant [$\mathrm{cm^2\,g\,s^{-2}\,K^{-1}}$]
l	P.l.i. of the radial drift velocity v_r [1]
m	Mass of a dust grain [g]
m_c	Mass of a carbon atom [g]
m_g	Mean weight of a gas molecule [g]
$\rho_\bullet$	Dust grain solid density [$\mathrm{g\,cm^{-3}}$]
p_d	Dust surface density p.l.i., Eq. 6.3 [1]
p_g	Gas surface density p.l.i., Eq. 6.1 [1]
q	Gas temperature p.l.i., Eq. 6.2 [1]
r	Radial coordinate (distance from the star) [cm]
r'	Position of a drifting grain at $t = t'$, Eq. 6.32 [cm]
r''	Integration variable [cm]
r_0	Reference radius (1 au) [cm]
r_{out}	Outer edge of the disk [cm]
s	Stokes number p.l.i., Eq. 6.8 [1]
t	Time [s]
t'	Initial time [s]
t_d	Carbon grain destruction time, Eq. 6.15 [s]
t_{ph}	Photolysis destruction time, Eq. 6.23 [s]
$t_{\mathrm{ph,B}}$	Photolysis destruction time for bouncing, Eq. 6.47 [s]
t_{res}	Residence time, Eq. 6.27 [s]
t_{mix}	Mixing time [s]
t_d^{sub}	Sublimation destruction time, Eq. 6.42 [s]
v_f	Fragmentation velocity [$\mathrm{cm\,s^{-1}}$]
v_r	Radial drift velocity, Eq. 6.10 [$\mathrm{cm\,s^{-1}}$]
x	Dimensionless radial coordinate [1]
z	Vertical coordinate (distance above the midplane) [cm]
z_1	Lower boundary of the exposed layer [cm]
z_τ	Height of the $\tau = 1$-surface, Eq. 6.21 [cm]
z_{dec}	Height at which dust grains decouple, Eq. 6.22 [cm]

Table 6.2 – continued from previous page

symbol	description [cgs unit]
$[.]_0$	Arbitrary quantity [.] evaluated at the reference radius r_0
$[.]_i$	Arbitrary quantity [.] describing the i-the dust compound

Appendices

6.A Derivation of the Location of the Optical Surface

In this section, we derive an analytical (but approximate) expression of the location of the $\tau = 1$-surface of stellar FUV photons. That is, we solve the following equation

$$1 = \tau(r, z) \tag{6.53}$$

We first use the disk flaring angle Φ and a geometric argument to convert the optical depth in the radial direction (τ) to the optical depth in the vertical direction (τ_z):

$$\tau = \frac{1}{\Phi}\tau_z \tag{6.54}$$

To compute the optical depth at height z along an optical path in the vertical direction, we assume grains of size a_1 at the geometrical optics limit dominate the FUV opacity κ_0. Then we integrate along the vertical axis from $z' = z_\tau$ to $z' = \infty$, to calculate the value of the vertical optical depth at height z

$$\tau_z(z) = \kappa_0 \int_z^\infty \rho_{a_1} \mathrm{d}z' \tag{6.55}$$

where ρ_{a_1} is the local volume density of dust grains of size a_1 or smaller. The integral on the right-hand side of Eq. 6.55 is the fraction of surface density of grains smaller or equal to a_1 above height z, which we set equal to $f_{\leqslant a_1} f_{\geqslant z} \Sigma_d$. Here, $f_{\leqslant a_1}$ is the mass fraction of grains of size a_1 or smaller. Assuming a grain size distribution between $a_{\min}$ and $a_{\max}$ that follows a power-law as $n \propto a^{-p}$ we calculate $f_{\leqslant a_1}$ with

$$f_{\leqslant a_1} = \frac{a_{\max}^{-p+4} - a_{\min}^{-p+4}}{a_1^{-p+4} - a_{\min}^{-p+4}} \approx \left(\frac{a_{\max}}{a_1}\right)^{-p+4} \tag{6.56}$$

where we have assumed $a_{\min} \ll a_1 < a_{\max}$. We set $p = 3.5$.
The expression $f_{\geqslant z}$ stands for the dust surface density fraction in the layers between z and $z = \infty$. We first assume that the vertical dust distribution is Gaussian, i.e., grains do not decouple from the gas in the upper disk layers. Then we calculate the dust surface density fraction in the layers between z and $z = \infty$ as

$$f_{\geqslant z} = \frac{1}{2}\mathrm{erfc}\left(\frac{z}{\sqrt{2}h_d}\right) \tag{6.57}$$

Assuming the grains smaller or equal to a_1 are well coupled to the gas, their vertical distribution is Gaussian with a scale height equal to the gas scale height $h_d \sim h_g$. The factor 1/2 in Eq. 6.57 comes from the fact that we only consider one side of the disk. We define a new dimensionless variable $X := z/(\sqrt{2}h_d)$ and rewrite Eq. 6.53, with the definitions made above:

$$1 = \frac{\kappa_0}{\Phi} f_{\leqslant a_1} f_{\geqslant z_\tau} \Sigma_d = \frac{\kappa_0}{2\Phi} f_{\leqslant a_1} \Sigma_d \mathrm{erfc}\big(X\big) \tag{6.58}$$

This equation can easily be solved numerically, however, we will now make some approximations to obtain an explicit expression. For $X \gg 1$, the complementary error function can be approximated using its asymptotic expansion

$$\mathrm{erfc}\big(X\big) \approx \frac{e^{-X^2}}{\sqrt{\pi}X} \tag{6.59}$$

We replace the complementary error function in Eq. 6.58 with this approximation and define a function

$$g(X) := \frac{\kappa_0}{2\sqrt{\pi}\Phi} f_{\leqslant a_1} \Sigma_d e^{-X^2} \tag{6.60}$$

Then Eq. 6.58 becomes

$$X - g(X) = 0. \tag{6.61}$$

This equation is still not solvable explicitly. Therefore, we Taylor expand $g(X)$ about $X = X_0$ to second order. We find the most accurate results across a large range of parameters if we chose X_0 such that $g(X_0) = 1$. Then, X_0^2 can be written as

$$X_0^2 = \ln \frac{f_{\leqslant a_1} \Sigma_d \kappa_0}{2\sqrt{\pi}\Phi}. \tag{6.62}$$

The Taylor expansion of Eq. (6.61) and solving the quadratic equation in X gives us the following results for X:

$$X = \frac{2X_0 + \frac{1}{2}X_0^{-2} - \sqrt{2X_0^{-1} - X_0^{-2} + \frac{3}{2}X_0^{-4}}}{2 - X_0^{-2}} \tag{6.63}$$

For $X_0 \gg 1$, we simplify the above equation to

$$X \simeq X_0 - \frac{1}{5} \tag{6.64}$$

where we chose the subtrahend such that it minimizes the error in the range between 3 and 5 times the gas pressure scale height h_g. In terms of z_τ and model parameters, Eq. (6.64) is equivalent to

$$\frac{z_\tau}{h_d} \simeq \sqrt{2 \ln \frac{f_{\leqslant a_1} \Sigma_d \kappa_0}{2\sqrt{\pi}\Phi}} - \frac{1}{5} \tag{6.65}$$

In the derivation up to now, we have not considered the effects of dust grains decoupling from the gas at large z. Next, we also consider the effects of decoupling in the upper disk layers when calculating the $\tau = 1$-surface. In that case, the vertical dust density profile does not follow a Gaussian anymore. In the upper disk layers, the dust density drops off more steeply than a Gaussian profile. We consider the effects of decoupling by calculating $f'_{\geqslant z}$ with the following integral (Fromang & Nelson, 2009):

$$f'_{\geqslant z} = \frac{f_0}{2} \int_z^\infty \exp\left[- \frac{St_{\mathrm{mid}}}{\alpha} \left(\exp\left(\frac{z^2}{2h_g^2} \right) - 1 \right) - \frac{z^2}{2h_g^2} \right] \mathrm{d}z \tag{6.66}$$

where f_0 is a normalization constant such that $f'_{\geqslant 0} = 1/2$. Similar to the case without decoupling in Eq. 6.58, the solution to equation

$$1 = \frac{\kappa_0}{\Phi} f_{\leqslant a_1} f'_{\geqslant z} \Sigma_d \tag{6.67}$$

will provide height of the $\tau = 1$-surface when also considering decoupling. In Fig. 6.2, we plot the radial dependence of the solution to Eq. 6.67 in our fiducial model with the solid blue line. Due to the effects of decoupling, the $\tau = 1$-surface lies lower than when decoupling is ignored.
To evaluate when the effects of decoupling become important, we evaluate at which height small grains decouple from the gas. The gas density drops away exponentially at large z, as shown in Eq. 3.8. Hence, there is a height z_{dec} above which the gas density is low enough for even the smallest dust grains to decouple from the gas. We consider a grain to be decoupled if the local Stokes number of a grain is equal or smaller than the turbulent α-parameter: $St(z_{\text{dec}}) \simeq \alpha$. Solving for z_{dec} provides an upper limit, above which Eq. 6.65 is only accurate if one does not consider the decoupling of dust grains. The explicit expression for z_{dec} is the following:

$$\frac{z_{\text{dec}}}{h_g} = \sqrt{2 \ln \frac{2\alpha\Sigma_g}{\pi \rho_\bullet a}} \tag{6.68}$$

The height above which small grains decouple, calculated with Eq. 6.68 is shown in the top panel of Fig. 6.2 in black color. Studying Eq. 6.68, it becomes clear that larger particles with a larger solid density are more weakly coupled to the gas and therefore decouple at smaller z/h_g. On the other hand, particles decouple at larger z/h_g if the gas surface density Σ_g or the alpha turbulence parameter α are large. We find that the solution to Eq. 6.65 deviates from the solution to Eq. 6.67 when $z_\tau \gtrsim z_{\text{dec}}$ and decoupling becomes important. In Fig. 6.2, z_{dec} lies close to the solution of Eq. 6.65 which is the reason the solution of Eq. 6.65 and Eq. 6.67 deviate slightly in our fiducial model. Nonetheless, Eq. 6.65 provides valuable scaling relations for our analysis. However, we use the exact numerical solution of Eq. 6.67 in all our quantitative results.

6.B Derivation of the Residence Time

In this section, we derive an expression to calculate the residence time, i.e., the time a grain spends in the exposed layer before being mixed back into the denser disk regions closer to the midplane. We model vertical motions of dust particles in the strong coupling approximation with a stochastic equation of motion (e.g. Ciesla, 2010; Ormel & Liu, 2018)

$$\mathrm{d}z = -\eta z \mathrm{d}t + \sqrt{2D_d}\mathrm{d}W_t \tag{6.69}$$

where D_d is the dust diffusivity and W_t denotes a Wiener process. We define the dust diffusivity as $D_d = \alpha c_s h_g$. The differential of the Wiener process is $\mathrm{d}W_t = \sqrt{\mathrm{d}t}\mathcal{N}(0,1)$ where $\mathcal{N}(0,1)$ is the normal distribution with zero mean and unit variance. The effective velocity term ηz is the sum of the vertical settling velocity at height z and a correction accounting for the gas density gradient

$$\eta = St\Omega + \frac{D_d}{h_g^2} \tag{6.70}$$

For $z \ll z_{\text{dec}}$ the correction term is generally much larger than the settling term. Hence, $\eta \simeq D_d/h_g^2$ in these regions.
If we assume η is independent of z (e.g., by approximating $St(z) \sim St(z_{t=0})$), Eq. 6.69 denotes an Ornstein-Uhlenbeck process (Uhlenbeck & Ornstein, 1930) for which the probability density

function f as a function of z is a time-dependent Gaussian

$$f(z,t) = \frac{1}{\sqrt{2\pi \upsilon^2(t)}} \exp\left(\frac{(z-\bar{z}(t))^2}{2\upsilon^2(t)}\right) \tag{6.71}$$

with mean $\bar{z}(t) = z_{t=0}e^{-\eta t}$ and variance $\upsilon^2(t) = \frac{D_d}{\eta}\left(1-e^{-2\eta t}\right)$ where $z_{t=0}$ is the location of the particle at time $t = 0$.

We now assume that z_1 is the lower boundary of the exposed layer in the disk. Then for every $t > 0$, the following integral

$$P_{\geqslant z_1}(t) = \int_{z_1}^{\infty} f(z,t)\mathrm{d}z \tag{6.72}$$

is the probability of finding a particle that had started at $z = z_{t=0}$ at $t = 0$ above z_1 at time $t > 0$. For an ensemble of N particles, all starting at $z = z_{t=0}$ at $t = 0$, the average number of particles in the active layer above $z_{t=0}$ at time $t > 0$ then becomes $NP_{\geqslant z_1}(t)$. The number of particles outside the exposed layer is $N(1-P_{\geqslant z_1}(t))$. In the time interval $(t, t+\mathrm{d}t)$, the particles in the exposed layer spend a time of $\mathrm{d}t$ in the exposed layer. The particles outside the active layer spend a total time 0 in the exposed layer during that interval. Thus, the average time spent in the active layer in the time interval $(t, t+\mathrm{d}t)$ across the entire ensemble is

$$\langle \mathrm{d}t_{\mathrm{res}} \rangle = \frac{NP_{\geqslant z_1}(t)\cdot \mathrm{d}t + N(1-P_{\geqslant z_1}(t))\cdot 0}{N} \tag{6.73}$$

Here, $\langle\cdot\rangle$ denotes the ensemble average. The above equation simplifies to

$$\langle \mathrm{d}t_{\mathrm{res}} \rangle = P_{\geqslant z_1}(t)\mathrm{d}t \tag{6.74}$$

In order to calculate the total time spent in the active layer across all times t, we integrate Eq. 6.74 from $t = 0$ to $t = \infty$

$$\int_0^{\infty} P_{\geqslant z_1}(t)\mathrm{d}t \tag{6.75}$$

However, this integral does generally not converge. This is not a problem because we are not interested in the total time spent in the active layer across all times t but only up to the point when the ensemble equalizes its carbon fraction in collisions, typically in the dense midplane regions. This typically happens within one mixing time t_{mix}. Thus, we define the residence time as the integral between 0 and t_{mix}

$$\langle t_{\mathrm{res}} \rangle = \int_0^{t_{\mathrm{mix}}} P_{\geqslant z_1}(t)\mathrm{d}t \tag{6.76}$$

One might choose a different value for the upper limit of the integral. However, the above integral is very insensitive to the exact choice of its upper limit as long as the upper limit is larger than $\sim t_{\mathrm{mix}}/2$. Next, we assume the ergodic hypothesis to be true. Then, the ensemble-averaged residence time $\langle t_{\mathrm{res}} \rangle$ is equal to the time-averaged residence time t_{res} i.e., the average time a single particle spends, in the active layer above z_1, before it is recycled through collisions under the condition that it reaches height z_1 at least once before the recycling happens. The residence time t_{res} is then defined as

$$t_{\mathrm{res}} = \int_0^{t_{\mathrm{mix}}} P_{\geqslant z_1}(t)\mathrm{d}t \tag{6.77}$$

By defining a dimensionless variable

$$\chi(t) = \frac{z_1 - \bar{z}(t)}{\sqrt{2}\upsilon(t)} \tag{6.78}$$

we rewrite Eq. 6.77 as an integral over the complementary error function

$$t_{\mathrm{res}} = \frac{1}{2}\int_0^{t_{\mathrm{mix}}} \mathrm{erfc}\big(\chi(t)\big)\mathrm{d}t \tag{6.79}$$

where $t_{\mathrm{mix}} = 1/\alpha\Omega$, $\bar{z}(t) = z_1 e^{-\eta t}$ is the time-dependent mean and $\upsilon^2(t) = \frac{D_d}{\eta}\left(1 - e^{-2\eta t}\right)$ is the time-dependent variance.
Unless otherwise stated, we will use Eq. 6.79 in our analysis to calculate the residence time. However, due to its implicit form, we cannot gain much insight into the dependence on model parameters from Eq. 6.79. Therefore, we now aim to find an explicit, but approximate, expression of the residence time which we will use to study how the residence time depends on the chosen model parameters. This will be useful because the residence time is a limiting factor in the efficiency of the photolysis of carbonaceous material.
First, we assume dust grains to be perfectly coupled to the gas. Then, their residence time follows the green colored line in Fig. 6.4 and $D_d/h_g^2 \gg St\Omega$ holds. Thus, the first term in Eq. 6.70 does not contribute, and we approximate Eq. 6.70 with $\eta \simeq D_d/h_g^2$. Furthermore, in this perfectly coupled case, we approximate the residence time in Eq. 6.79 for $z \gg h_g$ as

$$t_{\mathrm{res}} \simeq \left(\frac{h_g}{z}\right)^2 t_{\mathrm{mix}} \tag{6.80}$$

We plot this dependence in blue in Fig. 6.4. This is the same expression as the definition of the residence time in Klarmann et al. (2018) (see their equation (6)). However, in comparison to Eq. 6.27, Eq. 6.80 is divergent for $z \to 0$. Further, we assume the lower edge of the exposed layer to be identical to the τ=1-surface ($z_1 \sim z_\tau$), which holds in the absence of photon forward scattering. Then we plug Eq. 6.21 into Eq. 6.80 and find a rough scaling relation between the residence time of perfectly coupled grains and the model parameters

$$t_{\mathrm{res}} \simeq \left(\sqrt{2\ln\frac{f_{\leqslant a_1}\Sigma_d\kappa_0}{2\sqrt{\pi}\Phi}} - \frac{1}{5}\right)^{-2} \alpha^{-1}\Omega^{-1}. \tag{6.81}$$

In a residence-time-limited case, i.e., when τ_c^{res} is larger than the unrestricted depletion time, we know from Eq. 6.26, carbon depletion is more efficient if t_{res} is small. The residence time, as expressed in Eq. 6.81, becomes small if the ratio inside the logarithm is large. However, this ratio is generally larger than unity and, because it is inside the natural logarithm, its impact on the residence time is small. The residence time is more sensitive to the alpha turbulence parameter, to which it is inversely proportional. It becomes clear that the residence time can be most efficiently decreased, and consequently carbon depletion increased, if the alpha parameter is increased.
In Fig. 6.4, we plot the z-dependence of the residence time. There, Eq. 6.80 is plotted in blue. The exact solution to Eq. 6.27, for perfectly coupled grains ($\eta = D_d/h_g^2$), is plotted in green. The exact and the approximate solutions agree well for $z \gg h_g$. Using our fiducial parameters, Eq. 6.80 overestimates the residence time for $z < 3h_g$. In Fig. 6.4, we also plot the exact solution of the residence time for grains that decouple at large z in orange color. It clearly deviates above z_{dec} which is indicated by the vertical dashed black line. When including the effects of decoupling, the residence time becomes more than an order of magnitude smaller for $z > z_{\mathrm{dec}}$ than without considering the decoupling. The dashed orange vertical line shows the

location of the exposed layer. It is clearly below $z_{\rm dec}$. By choosing appropriate parameters, we could push z_1, as calculated with Eq. 6.21, to larger z, beyond $z_{\rm dec}$ where the residence time becomes very low. However, when considering decoupling, it becomes very difficult to push z_1 beyond $z_{\rm res}$ (at least by choosing physically plausible parameters). At heights close to $z_{\rm dec}$, grains settle vertically so efficiently that only a few grains are diffused beyond $z_{\rm dec}$. Hence, the dust density in layers beyond $z_{\rm dec}$ is so low that these layers remain optically thin, and consequently $z_1 < z_{\rm dec}$ holds. Thus, the no-decoupling assumption in the derivation of Eq. 6.81 is generally justified.

6.C Derivation of the Analytical Solution of the Carbon Fraction

In this section, we derive the solutions given by Eq. 6.32, Eq. 6.33, and Eq. 6.36 as discussed in Sec. 6.3.5 based on the radial transport equations presented in Sec. 6.2.3.

Solution without Radial Transport ($v_r = 0$)

First, we derive the solution to Eq. 6.14 without radial transport, i.e., by setting $v_r = 0$. For the silicate component ($i = 0$), the solution is simply

$$\Sigma_s(r,t) = \Sigma_s(r,t') \tag{6.82}$$

where t' is an arbitrary time with $t' < t$, most commonly identified as the initial time $t' = 0$. Due to the absence of a mechanism that depletes silicate in our model, the silicate surface density remains constant in the absence of radial transport. Assuming the carbon depletion timescale for all the carbonaceous components is identical ($\tau_{c,i} = \tau_c$), the solution to Eq. 6.14 summed up over all the carbonaceous components is

$$\Sigma_c(r,t) = \Sigma_c(r,t') \exp\Big(-\frac{t-t'}{\tau_c}\Big(\frac{r}{r_0}\Big)^{p_d-b}\Big) \tag{6.83}$$

where we have assumed $\Sigma_c \ll \Sigma_s$. The surface density ratio f_Σ between carbon and silicate grains then becomes

$$f_\Sigma(r,t) = \frac{\Sigma_c(r,t)}{\Sigma_s(r,t)} = f_\Sigma(r,t') \cdot \exp\Big(-\frac{t-t'}{\tau_c}\Big(\frac{r}{r_0}\Big)^{p_d-b}\Big) \tag{6.84}$$

and the carbon fraction f_c as a function of radius and time is

$$f_c(r,t) = \Big(1 + \Big(f_\Sigma(r,t)\Big)^{-1}\Big)^{-1} \tag{6.85}$$

Steady State

The steady-state solution of the silicate components in Eq. 6.14 can be found by setting $d\Sigma_s/dt = 0$. Thus, $r\Sigma_s v_r = const.$ and we identify the constant as $\dot{M}_s/2\pi$. Hence, the steady-state solution of the silicate component in Eq. 6.14 is:

$$\Sigma_s = \frac{\dot{M}_s}{2\pi r_0 |v_0|}\Big(\frac{r}{r_0}\Big)^{-(l+1)} \tag{6.86}$$

Hence, $p_d = l + 1 = s - q + 3/2$. In the fragmentation limit (s=q), we find $p_d = 3/2$.

Grain Trajectory

We now aim to solve Eq. 6.14 for the carbonaceous components, including radial transport. For this, we first follow a trajectory of an arbitrary grain in the disk, moving at radial velocity described by Eq. 6.11. We rewrite Eq. 6.11 as

$$v_0 dt = \left(\frac{r}{r_0}\right)^{-l} dr \tag{6.87}$$

and assume a grain to start at radius r' at time $t' \geqslant 0$ and radially drift towards $r(t)$ where the grain arrives at time $t > t'$. We integrate Eq. 6.87 from r' to r

$$\int_{t'}^{t} v_0 dt = \int_{r'}^{r} \left(\frac{r''}{r_0}\right)^{-l} dr'' \tag{6.88}$$

where r'' is the integration variable, and solve for r' to find the initial radius as a function of the grain position r at time t. For $l \neq 1$ we find

$$r'(r, t, t') = \Big(r^{1-l} - (1-l) r_0^{-l} v_0 (t - t')\Big)^{1/(1-l)}. \tag{6.89}$$

Note that this equation has a physical solution for all times t only if $l < 1$ (assuming $v_0 < 0$). For $l > 1$, there is a maximum time t_max for any given r and t' at which the initial radius diverges $r' = \infty$:

$$t_\text{max}(r, t') = t' + \frac{r^{1-l} r_0^{l}}{(1-l) v_0} \tag{6.90}$$

meaning, grains can drift from an infinite distance to radius r in a finite amount of time. This solution can still be physical if the disk itself is finite. The solution to Eq. 6.88 for $l = 1$ is:

$$r'(r, t) = r \cdot \exp\big(-\frac{v_0}{r_0}(t - t')\big) \tag{6.91}$$

We want to highlight that for most cases, it is sufficient to choose $t' = 0$ which simplifies the solution. However, carrying on with t' will allow us to apply this solution to problems that are piece-wise defined by power-law dependencies instead of a single, global power law.

Characteristic Equations

For the next steps in the derivation, it is convenient to introduce the dimensionless variable $x = r/r_0$ such that Eq. 6.14, summed over all the carbonaceous components, becomes

$$\frac{\partial \Sigma_c}{\partial t} + \frac{1}{x r_0} \frac{\partial}{\partial x}(x \Sigma_c v_r) = \dot{\Sigma}_c \tag{6.92}$$

Following the approach in Birnstiel & Andrews (2014) appendix A, we solve the partial differential equation (PDE) in Eq. 6.92 with the method of characteristics. Along characteristic trajectories, the PDE simplifies to a system of ordinary differential equations (ODE) which we solve analytically. The three characteristic equations of Eq. 6.92 are:

$$\frac{dt}{ds} = 1 \tag{6.93}$$

$$\frac{dx}{ds} = \frac{v_r}{r_0} \tag{6.94}$$

$$\frac{d\Sigma_c}{ds} = -\frac{\Sigma_c}{xr_0}\frac{\partial(v_r x)}{\partial x} + \dot{\Sigma}_c \tag{6.95}$$

Homogeneous Solution

The homogeneous solution ($\dot{\Sigma}_c = 0$) of Eq. 6.92 can be found by using $d(v_r x) = \partial(v_r x)/\partial x \cdot dx$ and rewriting Eq. 6.95 as

$$\frac{d\Sigma_c}{\Sigma_c} = -\frac{1}{xr_0}d(v_r x)\frac{ds}{dx} \tag{6.96}$$

and using Eq. 6.94 to write the above expression as

$$\frac{d\Sigma_c}{\Sigma_c} = -\frac{d(v_r x)}{v_r x} \tag{6.97}$$

which is equivalent to

$$d\ln\Sigma_c = -d\ln(v_r x). \tag{6.98}$$

From Eq. 6.98, we see that the solution is $\Sigma_c \propto 1/(v_r x)$ and thus:

$$\Sigma_c(r,t) = \Sigma_c(r',t')\frac{v_r(r')r'}{v_r(r)r} \tag{6.99}$$

With using definition in Eq. 6.11, this simplifies to:

$$\Sigma_{c,\mathrm{hom.}}(r,t,t') = \Sigma_c(r',t') \cdot \left(\frac{r'}{r}\right)^{l+1} \tag{6.100}$$

where r' is the initial radius of the particle at time t' as found in Eq. 6.89. Coincidentally, this is also the general form of the solution to the silicate component in Eq. (6.14)

$$\Sigma_s(r,t,t') = \Sigma_s(r',t') \cdot \left(\frac{r'}{r}\right)^{l+1} \tag{6.101}$$

Inhomogeneous Solution

We continue with Eq. 6.95 to find the inhomogeneous solution and rewrite the equation as

$$\begin{aligned} dln\Sigma_c &= -\frac{1}{xr_0}\Big(x\frac{\partial v_r}{\partial x} + v_r\Big)ds + \frac{\dot{\Sigma}_c}{\Sigma_c}ds \\ &= -\Big(l\frac{v_0}{r_0}x^{l-1} + \frac{v_0}{r_0}x^{l-1} + x^{p_d-b}/\tau_{c,0}\Big)ds \end{aligned} \tag{6.102}$$

Case I $(l-1 = p_d - b)$
First, we consider the case when $l-1 = p_d - b$, this is equivalent to an (initial) steady-state surface density distribution. In this case, we can rewrite Eq. 6.102 as

$$\begin{aligned} dln\Sigma_c &= -x^{l-1}\frac{v_0}{r_0}\Big(l+1+\frac{r_0}{v_0\tau_{c,0}}\Big)ds \\ &= -x^{-1}\Big(l+1+\frac{r_0}{v_0\tau_{c,0}}\Big)dx \end{aligned} \tag{6.103}$$

where we have used the relation $ds = (r_0/v_0)x^{-l}dx$ in the second line. With defining

$$B = l + 1 + \frac{r_0}{v_0\tau_{c,0}} \tag{6.104}$$

we rewrite Eq. 6.103 as

$$dln\Sigma_c = -B\, dlnx \tag{6.105}$$

The solution to Eq. 6.105 is:

$$\Sigma_c(r,t) = C' \cdot \left(\frac{r}{r_0}\right)^{-B} \tag{6.106}$$

where C' is a constant (in r) that can depend on time t. We require $\Sigma_c(r, t = t') = \Sigma_c(r', t')$ because $r = r'(t = t')$. Hence, $C' = \Sigma_c(r', t')(r_0/r')^{-B}$ and the solution to the inhomogeneous equation for $l - 1 = p_d - b$ is:

$$\Sigma_c(r,t) = \Sigma_c\big(r'(r,t,t'),t'\big) \cdot \left(\frac{r}{r'(r,t,t')}\right)^{-B} \tag{6.107}$$

Combining Eq. 6.107 and Eq. 6.101, we can also find the solution for the surface density ratio

$$f_\Sigma(r,t) = \frac{\Sigma_c(r,t)}{\Sigma_d(r,t)} = f_\Sigma\big(r'(r,t,t'),t'\big) \cdot \left(\frac{r}{r'(r,t,t')}\right)^{-\frac{r_0}{v_0\tau_{c,0}}} \tag{6.108}$$

from which the carbon fraction f_c follows directly from Eq. 6.85.

Case II ($l - 1 \neq p_d - b$) We start again with Eq. 6.102 and use the relation $ds = (r_0/v_0)x^{-l}dx$ to write the equation as following:

$$dln\Sigma_c = -\Big(l + 1 + \frac{r_0}{v_0\tau_{c,0}} x^{p_d-b-l+1}\Big) dlnx \tag{6.109}$$

We now substitute $x = \exp(\tilde{x})$ ($x > 0$ holds) and define $\beta := p_d - b - l + 1$ and find

$$\frac{dln\Sigma_c}{d\tilde{x}} = -(l+1) - \frac{r_0}{v_0\tau_{c,0}} \exp\big(\tilde{x}\beta\big) \tag{6.110}$$

The solution to Eq. 6.110 can be identified as

$$ln\Sigma_c = -(l+1)\tilde{x} - \frac{r_0}{v_0\tau_{c,0}\beta} \exp\big(\tilde{x}\beta\big) + lnC'' \tag{6.111}$$

where C'' is a (yet unidentified) constant which can depend on t. Then we substitute back by using $\tilde{x} = lnx$ and find

$$ln\Sigma_c = ln\Big(x^{-(l+1)}\Big) - \frac{r_0}{v_0\tau_{c,0}\beta} x^\beta + lnC'' \tag{6.112}$$

which we solve for Σ_c by applying the exponential function

$$\Sigma_c = x^{-(l+1)} \exp\Big(-\frac{r_0}{v_0\tau_{c,0}\beta} x^\beta\Big) \cdot C'' \tag{6.113}$$

Next, we evaluate this equation at $r = r'$ and $t = t'$ to find an expression for the constant C'':

$$C'' = \Sigma_c(r',t')\Big(\frac{r_0}{r'}\Big)^{-(l+1)} \exp\Big(\frac{r_0}{v_0\tau_{c,0}\beta}\Big(\frac{r'}{r_0}\Big)^\beta\Big) \tag{6.114}$$

inserting Eq. 6.114 back into Eq. 6.113 leads to the inhomogeneous solution for the surface density Σ_c:

$$\Sigma_c(r,t) = \Sigma_c(r',t')\Big(\frac{r}{r'}\Big)^{-(l+1)} \exp\left(\frac{r_0}{v_0\tau_{c,0}\beta}\Big[\Big(\frac{r'}{r_0}\Big)^{\beta} - \Big(\frac{r}{r_0}\Big)^{\beta}\Big]\right) \tag{6.115}$$

And from this, we can also find the solution for the surface density ratio:

$$\begin{aligned} f_\Sigma(r,t) &= \frac{\Sigma_c(r,t)}{\Sigma_s(r,t)} \\ &= f_\Sigma(r',t') \cdot \exp\left(\frac{r_0}{v_0\tau_{c,0}\beta}\Big[\Big(\frac{r'}{r_0}\Big)^{\beta} - \Big(\frac{r}{r_0}\Big)^{\beta}\Big]\right) \end{aligned} \tag{6.116}$$

where
$l = s - q + 1/2$

$$\beta = p_d - b - l + 1 = p_d - b - s + q + 1/2 \tag{6.117}$$

Note; by taking the limit $v_0 \rightarrow 0$ in Eq. 6.116 we obtain Eq. 6.84, i.e., the solution without radial transport. The same is true for taking the limit $v_0 \rightarrow 0$ of Eq. 6.108.

6.D Derivation of the Analytical Solution for Irreversible Sublimation

In this section, we derive the analytical solution to the carbon fraction considering the carbon depletion via irreversible sublimation, analogous to Sec. 6.C, but with a source term that follows an exponential law rather than a power law.

Steady-State Solution

First, we search for the steady state solution of Eq. 6.14 with a source term of the form as in Eq. 6.44. I.e., the equation we want to solve is

$$\frac{\partial \Sigma_{d,i}}{\partial t} + \frac{1}{r}\frac{\partial}{\partial r}(r\Sigma_{d,i}v_r) = -\Sigma_{d,i}A_i \exp\left(-\frac{E_{a,i}}{RT(r)}\right) \tag{6.118}$$

In the steady state, we require the time derivative to vanish. With using the dimensionless radius $x = r/r_0$, the steady state condition becomes

$$\frac{\partial}{\partial x}(x\Sigma_{d,i}v_r) = -\Sigma_{d,i}r_0 x A_i \exp\left(-\frac{E_{a,i}}{RT_0}x^q\right) \tag{6.119}$$

By defining $g(x) = x\Sigma_{d,i}v_r$, we rewrite the equation above to read

$$\frac{\partial}{\partial x}(\ln g) = \frac{r_0}{v_0}A_i x^{-l} \exp\left(-\frac{E_{a,i}}{RT_0}x^q\right) \tag{6.120}$$

Case I $(1 - q - l = 0)$
If we assume $1 - q - l = 0$, the above equation can easily be integrated:

$$\ln g(x) = -\frac{r_0}{v_0 q}\frac{A_i R T_0}{E_{a,i}} \exp\left(-\frac{E_{a,i}}{RT_0}x^q\right) + \text{const.} \tag{6.121}$$

Hence,

$$r\Sigma_{d,i}v_r = \exp\left[-\frac{r_0}{v_0 q}\frac{A_i R T_0}{E_{a,i}}\exp\left(-\frac{E_{a,i}}{RT(r)}\right)\right]\cdot\text{const.} \tag{6.122}$$

We require $\Sigma_{d,i} = \text{const.}$ as $T_0 \to 0$, thus,

$$\Sigma_{d,i}(r,t) = \Sigma_{d,i}(r,t')\exp\left[-\frac{r_0}{v_0 q}\frac{A_i R T_0}{E_{a,i}}\exp\left(-\frac{E_{a,i}}{RT(r)}\right)\right] \tag{6.123}$$

which results in the steady-state surface density ratio

$$f_{\Sigma_{d,i}}(r,t) = f_{\Sigma_{d,i}}(r',t')\exp\left[-\frac{r_0}{v_0 q}\frac{A_i R T_0}{E_{a,i}}\exp\left(-\frac{E_{a,i}}{RT(r)}\right)\right] \tag{6.124}$$

Inhomogeneous Solution

In the next step, we search for the inhomogeneous solution of Eq. 6.118. We use dimensionless radius $x = r/r_0$ and the characteristic equations:

$$\frac{dt}{ds} = 1 \tag{6.125}$$

$$\frac{\partial x}{\partial s} = \frac{v_r}{r_0} \tag{6.126}$$

$$\frac{\partial \Sigma_{d,i}(s)}{\partial s} = -\frac{\Sigma_{d,i}}{x r_0}\frac{\partial(v_r x)}{\partial x} - \Sigma_c A_i \exp\left(-\frac{E_{a,i}}{RT(x)}\right) \tag{6.127}$$

With the equations above, we find

$$ds = dx\cdot r_0/v_r \tag{6.128}$$

and thus

$$dln\Sigma_{d,i} = -\left[(l+1) + \frac{r_0}{v_0}x^{-l+1}A_i\exp\left(-\frac{E_{a,i}}{RT_0}x^q\right)\right]d\ln x \tag{6.129}$$

which we rewrite to

$$dln\Sigma_c = -\left[(l+1)\frac{1}{x} + \frac{r_0}{v_0}x^{-l}A_i\exp\left(-\frac{E_{a,i}}{RT_0}x^q\right)\right]dx \tag{6.130}$$

We define a variable $\tilde{x} = x^q$ and write the equations in terms of $\tilde{x}$:

$$dln\Sigma_c = -(l+1)\tilde{x}^{-1/q}d\tilde{x} - \frac{r_0}{v_0}\tilde{x}^{(1-q-l)/q}A_i\exp\left(-\frac{E_{a,i}}{RT_0}\tilde{x}\right)d\tilde{x} \tag{6.131}$$

Case I $(1-q-l=0)$
Then the equation simplifies to:

$$dln\Sigma_{d,i} = -(l+1)x^{-1}dx - \frac{r_0}{v_0}\frac{A_i}{q}\exp\left(-\frac{E_{a,i}}{RT_0}\tilde{x}\right)d\tilde{x} \tag{6.132}$$

which can be integrated to give:

$$ln\Sigma_{d,i} = -(l+1)\ln x + \frac{r_0}{v_0}\frac{A_i R T_0}{q E_{a,i}}\exp\left(-\frac{E_{a,i}}{RT_0}x^q\right) + const. \tag{6.133}$$

and then

$$\Sigma_{d,i}(x,t) = C' \cdot x^{-(l+1)} \exp\left[\frac{r_0}{v_0}\frac{A_i R T_0}{q E_{a,i}} \exp\left(-\frac{E_{a,i}}{RT_0}x^q\right)\right] \tag{6.134}$$

Next, we evaluate the above equation at $r = r'$ and $t = t'$ to find an expression for the constant C':

$$C' = \Sigma_{d,i}(r',t') \cdot \left(\frac{r'}{r_0}\right)^{l+1} \exp\left[-\frac{r_0}{v_0}\frac{A_i R T_0}{q E_{a,i}} \exp\left(-\frac{E_{a,i}}{RT_0}\left(\frac{r'}{r_0}\right)^q\right)\right] \tag{6.135}$$

which leads to the full solution

$$\begin{aligned} &\Sigma_{d,i}(r,t) = \Sigma_{d,i}(r',t')\left(\frac{r}{r'}\right)^{-(l+1)} \cdot \\ &\exp\left\{\frac{r_0}{v_0}\frac{A_i R T_0}{q E_{a,i}}\left[\exp\left(-\frac{E_{a,i}}{RT_0}\left(\frac{r}{r_0}\right)^q\right) - \exp\left(-\frac{E_{a,i}}{RT_0}\left(\frac{r'}{r_0}\right)^q\right)\right]\right\} \end{aligned} \tag{6.136}$$

and also the solution of the surface density ratio:

$$\begin{aligned} &f_{\Sigma_{d,i}}(r,t) = f_{\Sigma_{d,i}}(r',t') \cdot \\ &\exp\left\{\frac{r_0}{v_0}\frac{A_i R T_0}{q E_{a,i}}\left[\exp\left(-\frac{E_{a,i}}{RT_0}\left(\frac{r}{r_0}\right)^q\right) - \exp\left(-\frac{E_{a,i}}{RT_0}\left(\frac{r'}{r_0}\right)^q\right)\right]\right\} \end{aligned} \tag{6.137}$$

Chapter 7

Three-dimensional Grid-Based Gas-Dust Simulations of Protoplanetary Disks with an Embedded Planet

The content of this chapter was published in:

Binkert F., Szulágyi, J., Birnstiel, T. (2021), *First 3D grid-based gas-dust simulations of circumstellar discs with an embedded planet*[1]*, Monthly Notices of the Royal Astronomical Society, Volume 506, Issue 4, April 2023, Pages 5969-5988*

Abstract

Substructures are ubiquitous in high-resolution (sub-)millimeter continuum observations of protoplanetary disks. They are possibly caused by forming planets embedded in their disk. To investigate the relation between observed substructures and young planets, we perform novel three-dimensional two-fluid (gas+1-mm-dust) hydrodynamic simulations of protoplanetary disks with embedded planets (Neptune-, Saturn-, Jupiter-, 5 Jupiter-mass) at different orbital distances from the star (5.2 au, 30 au, 50 au). We turn these simulations into synthetic (sub-)millimeter ALMA images. We find that all but the Neptune-mass planet open annular gaps in both the gas and the dust component of the disk. We find that the temporal evolution of the dust density distribution is distinctly different from the gas'. For example, the planets cause a significant vertical stirring of the dust in the protoplanetary disk, which opposes the vertical settling. This creates a thicker dust disk than disks without a planet. We find that this effect greatly influences the dust masses derived from the synthetic ALMA images. Comparing the dust disk masses in the 3D simulations to the ones derived from the 2D ALMA synthetic images, we find the former to be a factor of a few (up to 10) larger, pointing to the conclusion that real disks might be significantly more massive than previously thought, based on ALMA continuum images using the optically thin assumption and equation. Finally, we analyze the synthetic ALMA images

---

[1] This work is a continuation of my Master's thesis (Binkert, 2019) which can be accessed here. Within the framework of my Master's thesis, I developed and tested the hydrodynamic dust solver and developed numerical scripts for post-processing simulations used in this chapter. Within the framework of my doctorate, I improved the design of the study, carried out all the hydrodynamical simulations shown in this chapter, and performed the data analysis and interpretation of the results.

and provide an empirical relationship between the planet mass and the width of the gap in the ALMA images, including the effects of the beam size.

7.1 Introduction

Substantial theoretical work on the interaction between young planets and their host protoplanetary disk has been carried out over the past decades. Both analytical and numerical approaches have led to an improved understanding of the problem (e.g. Goldreich & Tremaine, 1980; Lin & Papaloizou, 1986; Tanaka et al., 2002; Paardekooper & Mellema, 2004, 2006; de Val-Borro et al., 2006; Kley & Nelson, 2012). Today, it is widely accepted that a young planet embedded in a protoplanetary disk can open one or even multiple annular gaps and/or rings in the gaseous and dusty components of the disk (e.g. Dong et al., 2015b; Picogna & Kley, 2015; Jin et al., 2016; Fedele et al., 2017; Bae et al., 2017). However, it is still up for debate whether the annular structures, seen in scattered light and mm-continuum observations of protoplanetary disks, are indeed of planetary origin or if they have formed via other processes, e.g., dust pile-up at condensation fronts (Zhang et al., 2015), dead zones (Ruge et al., 2016) or large-scale vortices (Barge et al., 2017). However, the planetary hypothesis is plausible because planets are found to be common around stars. Yet, it remains difficult to directly observe young planets embedded in the host protoplanetary disk. Only a few planetary candidates still embedded in their protoplanetary disk have been observed, e.g., PDS 70 b, c (Müller et al., 2018; Keppler et al., 2018). Therefore, studies have focused on observable disk substructures to indirectly probe the properties of the unseen planet population and to establish a link between observations and planet formation theory. Current efforts mainly focus on near-IR scattered light images (Dong et al., 2015b; Avenhaus et al., 2018; Szulágyi et al., 2019), (sub-)mm dust thermal continuum images (Zhang et al., 2018; Szulágyi et al., 2018), or molecular line channel maps which trace the gas kinematics (Perez et al., 2015; Pinte et al., 2018; Teague et al., 2018a).

The planetary gaps in disks exist due to the exchange of angular momentum between a planet and the surrounding disk. The radial distribution of the disk material adjusts due to the gravitational transfer of angular momentum, i.e., via gravitational torques from the inner part of the disk to the planet and from the planet to the outer part of the disk(Goldreich & Tremaine, 1980; Lin & Papaloizou, 1984). Hence, disk material is radially pushed away from the planet. In gas, a gap opens if the gravitational torques win over the counterbalancing viscous torques. In addition to these two torques, the gas near the planet also feels a torque due to pressure due to the non-axisymmetric nature of the planetary wakes (Crida et al., 2006). In a steady state, viscous torques, gravitational torques caused by the planet, and torques due to pressure all balance each other. Hence, gap opening in gas does, in addition to its dependence on the planetary mass, depend on disk properties such as temperature (Crida et al., 2006; Szulágyi, 2017; Zhang & Zhu, 2020; Ziampras et al., 2020) and turbulent viscosity (Lin & Papaloizou, 1993). In other words, gap opening is more efficient, i.e. leads to deeper and wider gaps, for more massive planets in low viscosity gas with a larger Mach number (Crida et al., 2006).

In addition to gas, protoplanetary disks consist of about 1 % of their mass of solid material. In early phases, most of the solid material is present in the form of dust, i.e., solid grains of sizes ranging from below microns up to a few centimeters. These particles are suspended in the mass-dominating gaseous component of the disk and are coupled to the gas via aerodynamic drag forces. Drag forces and gravitational forces of the central star cause the dust grains to radially drift and vertically settle. In addition to these two transport mechanisms, dust grains experience turbulent diffusion due to their coupling to the gas' turbulent motion. Turbulent diffusion smooths out gradients in the local dust-to-gas ratio and, thus, can counteract radial drift or vertical settling. The result is a finite vertical thickness of the dust layer and the absence of sharp features in the dust distribution. Generally, turbulent diffusion is the dominant process for small dust grains, whereas radial drift and vertical settling are more dominant for large dust

grains. (Dubrulle et al., 1995; Youdin & Lithwick, 2007)
Due to its different nature, gap opening in the dust is somewhat different from gap opening in gas. Dipierro et al. (2016) differentiate two mechanisms. Small dust particles, which strongly couple to the gas, move along with the gas and therefore show similar gap-opening characteristics as the gas. Larger dust grains, however, decouple from the gas and drift in the direction of the disk pressure gradient. If a planet has already opened a gap in the gas, weakly coupled dust grains accumulate at the pressure maxima located at the gap edges. The result is a depletion of larger dust grains in the gap region due to radial drift (Paardekooper & Mellema, 2004, 2006; Fouchet et al., 2007, 2010). However, the presence of a gap in the gas is not a necessary condition for gap opening in dust. For low-mass planets, a gap can be present in the dust only (Dipierro & Laibe, 2017). Similar to the case in gas, gap opening in dust also occurs when gravitational torques push away dust from the planetary orbit. However, unlike in gas, viscous torques are not present in the dust when it is treated as a pressureless inviscid fluid. In a disk without a planet, the aerodynamic drag torque acting on dust particles due to the interaction with the gas is in general negative, resulting in a radial inward drift (Nakagawa et al., 1986). When a planet is present, gravitational torques also contribute. In the inner disk (inside the planetary orbital radius), gravity and aerodynamic torques add up and lead to an inward drift of the dust. In the outer disk, the two torques counteract each other. Hence, if the gravity torque is strong enough, i.e., the planet is massive enough, it can prevent dust from drifting from the outer disk to the inner disk and a gap opens in the dust without the need for a pressure bump in the gas (Johansen et al., 2009). Therefore, gap opening in dust depends, besides on the mass of the planet, on the degree of coupling between dust and gas, and also on the size of the dust particles. This has been shown in various numerical studies (e.g. Paardekooper & Mellema, 2004, 2006; Fouchet et al., 2007, 2010; Rosotti et al., 2016).
Planetary gaps and rings are predicted to be detectable in (sub-)mm continuum observations using the latest generation of radio interferometers such as the Atacama Large Millimeter/submillimeter Array (ALMA) (e.g. Pinilla et al., 2012; Gonzalez et al., 2012, 2015; Pineda et al., 2019). More recently, high-resolution ALMA observations have indeed revealed a multitude of substructures such as gaps, rings, spirals, and large-scale asymmetries in protoplanetary disks, e.g., Van Der Marel et al. (2013); ALMA Partnership et al. (2015); Andrews et al. (2018b). Even though the planetary origin of the observed features is still being debated, and young planets remain difficult to detect, the observed substructures can be used to indirectly probe the properties of the unseen population of forming planets. Continuum observations at (sub-)mm-wavelength most efficiently probe the thermal emission of mm-sized dust grains (Draine, 2006) coming from the cold midplane region of a protoplanetary disk. In this region, even low-mass giant planets can cause substructures in mm-sized dust. Typically, the lower mass limit for a planet to open a gap in 1 mm-sized dust is on the order of a Neptune-mass (e.g Paardekooper & Mellema, 2006; Fouchet et al., 2007)
A lot of work has been put into making observational planet-disk-interaction predictions for ALMA based on hydrodynamic models (e.g. Gonzalez et al., 2012; Ruge et al., 2016; Szulágyi et al., 2018; Zhang et al., 2018; Isella & Turner, 2018; Dipierro et al., 2018). In these models, an accurate dynamic and thermal treatment of the dust component in the disk is crucial to produce realistic observational predictions in (sub-)mm continuum observations. Moreover, radiative transfer methods are necessary to create synthetic ALMA images because there is no one-to-one relation between hydrodynamic features and observed features. Thermal emissions are dependent on a combination of density, temperature, and optical properties of the emitting region. An accurate computational treatment of all these quantities is therefore crucial for making accurate observational predictions. However, most studies compromise on physical accuracy in favor of computational efficiency.
In this work, we aim to improve upon some shortcomings of previous studies and create physically accurate observational predictions for planet-induced substructures in protoplanetary disks. Rather than using a particle-based approach for the dust component in the hydrodynamical mod-

els, we use a grid-based approach for both the gas and dust components. A grid-based approach does not suffer from a lack of resolution in low-density regions. Moreover, we perform global hydrodynamical simulations in three dimensions instead of two dimensions because planet-disk interaction is inherently a three-dimensional problem. We also avoid the common isothermal assumption in gas and include heating (adiabatic heating, viscous heating, stellar irradiation) and cooling processes (adiabatic, and radiative cooling) in our thermal simulations. To our knowledge, no global three-dimensional grid-based dust and gas planet-disk-interaction simulations have yet been published. We carry out a total of 12 hydrodynamic simulations using two fluids (gas + mm-sized dust) in which we embed a planet in the disk. We use different planetary parameters (mass, orbital radius) in each simulation and produce synthetic mm-continuum observations for ALMA with realistic beam sizes from the hydrodynamical models. This allows us to study the observable disk features in the mm-continuum induced by the planets. We derive an empirical formula that relates the planet mass to the width of the observed gaps. We also compare total dust masses derived from the synthetic observations to the actual total dust masses present in the disk.

In Sec. 7.2, we describe our methods. The results are presented in Sec. 7.3. In Sec. 7.4 we include a short discussion before we conclude the chapter in Sec. 7.5.

7.2 Methods

We carry out three-dimensional thermal two-fluid (gas+dust) hydrodynamic simulations of protoplanetary disks with an embedded planet. We use the grid-based code JUPITER (Szulágyi et al., 2016) and implement a pressureless solver to solve the dynamics of a dust fluid (assumed mm-sized grains) in addition to the gas fluid. We then processed the hydrodynamic simulation outputs with RADMC-3D (Dullemond et al., 2012), a wavelength-dependent radiative transfer tool, to obtain intensity images on a given wavelength. In a second step, we used the Common Astronomy Software Applications package (CASA) (Mcmullin et al., 2007) to create the final synthetic mm-continuum images of the protoplanetary disks with an embedded giant planet for the Atacama Large Millimeter/submillimeter Array (ALMA). In Sec. 7.2.1 we present the physical models of the gas and dust components and introduce the interaction terms, which also include the back-reaction from dust onto the gas. We also introduce the treatment of radiation and cooling/heating mechanisms for the two fluids. In Sec. 7.2.2 we describe the numerical methods used to solve the hydrodynamic equations introduced in Sec. 7.2.1. The details of our sets of thermal hydrodynamic simulations are presented in Sec. 7.2.3. To conclude the method section, we present the two post-processing steps in Sec. 7.2.4.

7.2.1 Physical Model

Gas and Radiation

We use the radiative hydrodynamics code JUPITER as presented in Szulágyi et al. (2016) to solve the hydrodynamic equations of the gas and radiation components in three dimensions on a spherical grid. In addition to the mass, momentum, and energy equations (see equations (1) to (3) in Szulágyi et al., 2016), we describe the gas with an equation of state of an ideal gas. It relates the gas pressure p_g to the internal energy density of the gas e_g as

$$p_g = (\gamma - 1)e_g \tag{7.1}$$

with $\gamma = 1.43$ being the adiabatic index. The energy equation describes the time evolution of the total energy of the gas per unit volume E_g as the sum of radiation energy per unit volume

e_{rad}, the internal energy per unit volume e_g and the kinetic energy per unit volume of the gas

$$E_g = e_{\text{rad}} + e_g + \frac{1}{2}\rho_g \mathbf{u}^2 \tag{7.2}$$

where ρ_g is the density and $\mathbf{u}$ is the three-dimensional velocity vector of the gas. The fourth equation which governs the dynamics is the radiation equation (see Eq. 4 in Szulágyi et al., 2016). It describes the dynamics of the radiation energy e_{rad} and contains the flux-limited diffusion approximation with the two-temperature approach (e.g. Commerçon et al., 2011).
The central star is assumed to be solar-like with radius $R_\star = R_\odot$, mass $M_\star = M_\odot$ and surface temperature $T = 5780$ K.

Dust

In this work, we model a single dust size species of size a as an additional pressureless fluid that has its distinct dynamics described by Eq. 5.3 and Eq. 5.4. Due to the ALMA continuum images we wanted to create, we chose the grain size to be 1 mm.
In our models, these particles have Stokes number in the range $9 \cdot 10^{-3} < St < 7 \cdot 10^{-2}$ in the disk midplane before inserting the planet. After the insertion of the planet, this range will become much broader due to the density fluctuation in gas. Moreover, in the disk regions above and below the midplane where the gas density drops off, the particles are less coupled and the Stokes numbers are generally larger than in the midplane.
For the grain composition, we assume a fractional abundance of 70 % silicate of solid density 3.5 g/cm^3 and 30 % refractory carbon of solid density 1.8 g/cm^3 (Zubko et al., 1996; Li & Greenberg, 1997) which results in a solid density of the dust grains of $\rho_\bullet = 3$ g/cm^3.
The Stokes number, as defined in Eq. 4.2, is used to parametrize the drag force $\mathbf{f}^{\text{drag}}$ which is responsible for the exchange of momentum between gas and dust (Weidenschilling, 1977a). The drag contributions to the gas and the dust fluid are symmetric and also depend on the relative velocity between the two fluids $\mathbf{v} - \mathbf{u}$ (Eq. 4.3)

Planet

The embedded planet is modeled solely via its gravitational potential as a point mass:

$$U_p(x, y, z) = \frac{GM_p}{\sqrt{(x - x_p)^2 + (y - y_p)^2 + (z - z_p)^2 + r_s^2}} \tag{7.3}$$

where G is the gravitational constant, M_p is the mass of the planet, (x_p, y_p, z_p) are the coordinates of the planet in Cartesian coordinates. r_s is a smoothing length to avoid singularities in the potential at the location of the planet. We set the smoothing length to the length of one cell diagonal of the computational grid (see Sec. 7.2.3).

7.2.2 Numerical Method

The main computational tool which we use to solve the hydrodynamic equations is the JUPITER code. It was originally developed by F. Masset and J. Szulágyi. For this study, we added a numerical dust solver to solve for a second (pressureless) fluid (dust) and its interaction with the gas. The JUPITER code is a three-dimensional Godunov-type code that solves the hydrodynamic equations on a grid using Riemann solvers. Even though the JUPITER code has nested mesh capability, it is not used in this study, so the planet vicinity is unresolved. The radiative module of the code applies a flux-limited diffusion approximation with the two-temperature approach as described in Szulágyi et al. (2016) and Szulágyi et al. (2018). We include thermal processes in the gas such as adiabatic heating/cooling, viscous heating, and radiative cooling, as well as stellar irradiation. For both, the gas and the dust, we use an operator splitting method to solve advection terms separately from the source terms. When solving the pressureless equations, we apply the method described by LeVeque (2004) which was also used by Paardekooper & Mellema (2006) to run two-fluid (gas+dust) simulations of protoplanetary disks. As in other Riemann solvers (Toro, 2009), the analytic solution to the Riemann problem of the system of Eq. 5.3 and Eq. 5.4 is the basis of the numerical method. The solution to the Riemann problem for a pressureless fluid is significantly different from the solution in gas, which includes pressure (Bouchut et al., 2003; LeVeque, 2004). It consists of a single wave moving from the Riemann interface at speed

$$\hat{v} = \frac{\sqrt{\rho_L} v_L + \sqrt{\rho_R} v_R}{\sqrt{\rho_L} + \sqrt{\rho_R}} \tag{7.4}$$

where ρ_L and v_L are the density and velocity on the left-hand side of the Riemann interface and ρ_R and v_R are the density and velocity on the right-hand side of the interface. The Riemann fluxes are determined based on the sign of $\hat{v}$ at every interface according to the following scheme:

$$\mathbf{F}_{\text{int}} = \begin{cases} \mathbf{F}_L & \text{if } \hat{v} > 0 \\ \frac{1}{2}\big(\mathbf{F}_L + \mathbf{F}_R\big) & \text{if } \hat{v} = 0 \\ \mathbf{F}_R & \text{if } \hat{v} < 0 \end{cases} \tag{7.5}$$

Following LeVeque (2004), we add correction terms to the interface flux to achieve second-order accuracy on smooth solutions and apply the *minmod* flux-limiter to avoid spurious oscillations around discontinuities (LeVeque, 2002).

In the numerical source step, we deal with the interaction between dust and gas. Following the operator splitting scheme, the two equations which we solve are:

$$\frac{\partial \mathbf{u}}{\partial t} = -\frac{1}{\rho_g}\mathbf{f}^{\text{drag}} \tag{7.6}$$

and

$$\frac{\partial \mathbf{v}}{\partial t} = \frac{1}{\rho_d}\mathbf{f}^{\text{drag}} \tag{7.7}$$

with definitions of the drag force $\mathbf{f}^{\text{drag}}$ as in Eq. 4.3. We find the solutions to Eq. 7.6 and Eq. 7.7 using an implicit finite difference scheme as described in Benítez-Llambay et al. (2019). The scheme leads to an update formula for the velocities **u** and **v** as in Stone (1997) and their Eq. 6 and Eq. 7. The velocities are updated in the source step along with the other source terms (gravitational and fictitious force terms). The implementation of the dust solver was tested[2] against analytic Riemann solutions, as suggested in (LeVeque, 2004) and compared to previous two-fluid studies (e.g. Paardekooper & Mellema, 2006). Further, we modified the opacity $\kappa(T, \rho_g)$ used in Szulágyi et al. (2016). In the one-fluid code, the opacity is calculated based on the local gas density ρ_g, assuming a dust-gas mixture with a locally constant dust-to-gas ratio $\epsilon = 0.01$. In the two-fluid simulations, we reduce the opacity where the dust-to-gas ratio is smaller and increase the opacity where the dust-to-gas ratio is larger. We computed the local two-fluid opacity $\kappa_{2\text{f}}$ based on the local dust density ρ_d and gas density ρ_g as

$$\kappa_{2\text{f}}(T, \rho_g, \rho_d) = \kappa\Big(T, 0.01\rho_g + 0.99\frac{\rho_d}{\epsilon}\Big) \tag{7.8}$$

where $\epsilon = 0.01$ is the dust-to-gas ratio assumed in the one-fluid dust-gas-mixture.

---

[2] Tests were performed within the framework of my master's thesis at ETH Zürich. The thesis can be found here.

7.2.3 Hydrodynamic Simulation Setup

Disk Setup and Simulation Domain

We set up a disk with a gas surface density following a power law as

$$\Sigma_g(r) = \Sigma_{g,0} \cdot \left(\frac{r}{\mathrm{au}}\right)^{-1/2} \tag{7.9}$$

where $\Sigma_{g,0} = 80\mathrm{g/cm}^2$ is the gas surface density at 1 au. This disk contains a total gas mass of $\sim 0.05\ \mathrm{M}_\odot$ ($\sim$52 $\mathrm{M}_{\mathrm{jup}}$) between 1 au and 120 au. With this disk setup, the Toomre Q parameter, which is a criterion for disk instability (Toomre, 1964), remains well above Q $>$ 1.7 in all our simulations. Hence, it can be expected that the disk self-gravity is negligible. Humphries & Nayakshin (2018, 2019) have conducted three-dimensional global (SPH) disk simulations, including a planet in situations where gravitational instability is important.

We use a constant kinematic viscosity $\nu = 3.15{\cdot}10^{15}\mathrm{cm}^2/\mathrm{s}$. Assuming an isothermal disk with aspect ratio H = 0.05, this is equivalent to a Shakura & Sunyaev α-parameter of $\alpha = 4.0{\cdot}10^{-3}$ at 50 au from a solar-mass star or $\alpha = 5.2{\cdot}10^{-3}$ at 30 au or $\alpha = 1.2{\cdot}10^{-2}$ at 5.2 au respectively (Shakura & Sunyaev, 1973). We note here that our disk is not isothermal and that the aspect ratio varies depending on the local heating and cooling conditions, ranging between 0.025 and 0.05.

In addition to the gas fluid, we initialize a dust fluid that represents a single dust size species of 1 mm-sized dust particles. Initially, the dust-to-gas mass ratio is 0.01 everywhere, but during the disk evolution, this ratio changes from location to location.

The computational grid is set up identically to Szulágyi et al. (2016), meaning we solve the hydrodynamic equations on a spherical grid (r, ϕ, θ) centered on the star. The frame of reference is co-rotating with the planet which orbits at distance r_p with Keplerian angular frequency $\Omega_K = \left(G(M_* + M_p)/r_p^3\right)^{1/2}$ where $M_* = M_\odot$ is the mass of the central star. Hence, the planet always remains fixed on the grid. To save computational costs, we do not simulate the entire disk between 1 au and 120 au in every simulation, but only the range between $0.4r_p$ to $2.4r_p$. In the case of a planet orbiting at $r_p = 50$ au, this corresponds to a range between 20 au and 120 au. In the azimuthal direction, the simulation covers the full range from $\phi_{min} = -\pi$ to $\phi_{max} = \pi$. The opening angle of the grid is set to $\theta_0 = 7.4°$. We assume the disk to be symmetric about the midplane and constrain the simulation to polar angles between $\theta_{min} = \pi/2 - \theta_0$ and $\theta_{max} = \pi/2$ to further save computational time. Our grid consists of $N_r = 215$ radial, $N_\phi = 680$ azimuthal and $N_\theta = 20$ polar cells , which creates roughly cubical grid-cells. Any further increase in resolution would increase the computational cost for this study by an unreasonable amount.

Initial/Boundary Conditions and Simulation Procedure

We initialize the gas disk with a constant aspect ratio $H = h_g/r = 0.05$ and the 1-mm sized dust so that the dust-to-gas ratio is uniformly at 0.01. This all of course evolves during the simulation, as the disk evolves. Before we introduce the planet to the disk, we evolve the disk without the planet and only 2 cells in the azimuthal direction (since the disk without the planet is azimuthally symmetric) for 150 planetary orbits. This allows the system to reach thermal equilibrium and the 1 mm-sized dust to settle vertically to reach a quasi-steady state. Then, we divide the 2 azimuthal cells into 680 cells and introduce the planet. We increase the mass of the planet over the following 100 orbits until it reaches its final mass so as not to introduce unwanted perturbations. We then evolve the system for another 100 orbits to arrive at a total of 200 planetary orbits. The boundary conditions for the gas are identical to Szulágyi et al. (2016). In detail, at the radial boundaries, the density and energy were extrapolated based on the initial slope and the value in the adjacent active cell. At the radial boundaries, the radial, and polar

simulation	r_p (au)	M_p ($\mathrm{M_{jup}}$)	$\Sigma_{g,t=0}(r = r_p)$ (g/cm^2)
`m5au1nep`	5.2	0.05	35
`m5au1sat`	5.2	0.3	35
`m5au1jup`	5.2	1	35
`m5au5jup`	5.2	5	35
`m30au1nep`	30	0.05	15
`m30au1sat`	30	0.3	15
`m30au1jup`	30	1.0	15
`m30au5jup`	30	5.0	15
`m50au1nep`	50	0.05	11
`m50au1sat`	50	0.3	11
`m50au1jup`	50	1.0	11
`m50au5jup`	50	5.0	11

Table 7.2.1: This table provides an overview of the 12 hydrodynamic simulations which we carried out and the parameters used. We varied the planetary orbital radius r_p between 5.2 au and 50 au and the planetary mass M_p between Neptune mass (0.05 $\mathrm{M_{jup}}$) and 5 Jupiter masses, as shown in the second and third column. The last column shows the initial gas surface density $\Sigma_{g,t=0}$ at the location of the planet.

velocity components in the ghost cells were set equal to the value in the adjacent active cell, i.e., symmetric boundary conditions. The azimuthal velocity component was extrapolated based on the local Keplerian velocity and the value in the adjacent active cell. In the polar direction, we used reflective, i.e., antisymmetric, boundary conditions. At the upper polar boundary, the temperature in the ghost cells was fixed at 3K which accounts for the radiative cooling of the disk to outer space. We used periodic boundary conditions in the azimuthal direction. For the dust fluid, at the radial boundaries, we also used antisymmetric boundary conditions for the radial velocity component. This prevents the inflow and outflow of dust in the simulation domain. The density and the other velocity components have symmetric boundary conditions at the radial boundaries. The boundaries condition in the azimuthal and polar direction were set equal to the boundary conditions in gas, except for the dust density at the polar boundary opposite to the midplane. There, the dust density was set to a floor value. The floor value corresponds to about one mm-sized dust grain per computational cell.

Simulation Sets

We carry out a set of twelve radiative hydrodynamic simulations, which are summarized in Table 7.2.1. We choose four different planetary masses (5 $\mathrm{M_{jup}}$, 1 $\mathrm{M_{jup}}$, 0.3 $\mathrm{M_{jup}}$, 0.05 $\mathrm{M_{jup}}$, the latter two are equivalent to the mass of Saturn and the mass of Neptune respectively) which we place at three different radii (5.2 au, 30 au, and 50 au). After injecting a planet, we evolve each simulation for 200 planetary orbits as described in Sec. 7.2.3.

7.2.4 Post-Processing

For each of the hydrodynamic simulations, we created synthetic ALMA mm-continuum observations. As in Szulágyi et al. (2018), we process our models with RADMC-3D (v0.41), a radiative transfer tool developed by Dullemond et al. (2012) and the Common Astronomy Software Applications package[3] (CASA). In the first step, we compute the dust temperature with a thermal Monte Carlo approach using RADMC-3D which assumes that the dust is in radiative equilibrium with the radiation field. Then, we perform ray-tracing with RADMC-3D to generate intensity images of our disk models at different wavelengths and create synthetic ALMA images of the disks using CASA.

RADMC-3D

Not only the density distribution in the disk has a large impact on the mm-continuum observations but also the temperature structure. We determine the dust temperature in the disk using the `mctherm` task of RADMC-3D which performs a thermal Monte Carlo simulation. As in the hydrodynamic simulations, we assume the radiation source to be a solar-like star of mass 1 $M_\oplus$, radius 1 $R_\oplus$ and temperature $T_{\text{eff}} = 5780$K. The radiation field of the star is represented by $2.1 \cdot 10^9$ photon packages which are emitted isotropically before they travel through the disk and are scattered, absorbed, and re-emitted along their path by dust grains until they eventually leave the model. The temperature computed in this process is the equilibrium temperature of the dust in the radiation field of the central star. In our setup, the dust does not acquire thermal energy from the gas.

Even though the hydrodynamic simulations are radiative, the radiation is treated in a wavelength-independent way. To obtain wavelength-dependent intensity images of our disk models, we apply the RADMC-3D `image` task for which we also set scattering to be isotropic. The Python pipeline used to convert the JUPITER code output files is based on Szulágyi et al. (2018). We set up the radiative transfer with the same stellar source as in the thermal Monte Carlo simulation to be consistent throughout our hydrodynamic simulations and post-processing steps. For the dust temperature, we use the temperature determined in the previous thermal Monte Carlo simulation, which is not necessarily equal to the gas temperature. The opacity table provided to RADMC-3D is identical to the one used in Szulágyi et al. (2018) and is based on a dust mixture of 70 % silicate and 30 % carbon. It was computed considering Mie theory using the BHMIE code of Bohren & Huffman (1984) assuming a dust grain size distribution of 0.1 μm and 1 cm with a power-law index of 3.5. The size of the intensity image is set to 1000 × 1000 pixels and the distance between the observer and the disk is assumed to be 100 parsec which is similar to the distance to the closest star-forming regions.

Synthetic ALMA Observations

We process the intensity images as generated byRADMC-3D with CASA and create synthetic ALMA observations using the `simobserve` and `simanalyze` tasks. Furthermore, we use ALMA cycle 7 array configurations which have baselines ranging from 0.16 km to 16.2 km and allow us to explore different beam sizes. For each antenna configuration, we create observations at different wavelength bands to explore the optimal observing setups. The channel bandwidth of our continuum observations is 7.4GHz. The integration time is chosen to be 300s per pointing with a total integration time of 3h. We add thermal noise to the synthesized images using the tsys-atm parameter which constructs an atmospheric profile at the ALMA site at an altitude of 5000 m, atmospheric pressure of 650mBar, and 20 % relative humidity. The precipitable water vapor is set to 0.475 mm and the ambient temperature is 269K.

7.3 Results

In the following section, we present the results of our three-dimensional two-fluid hydrodynamic simulations. This is followed by the results of the synthetic observations for ALMA. Analysis

---

[3] `casa.nrao.edu`

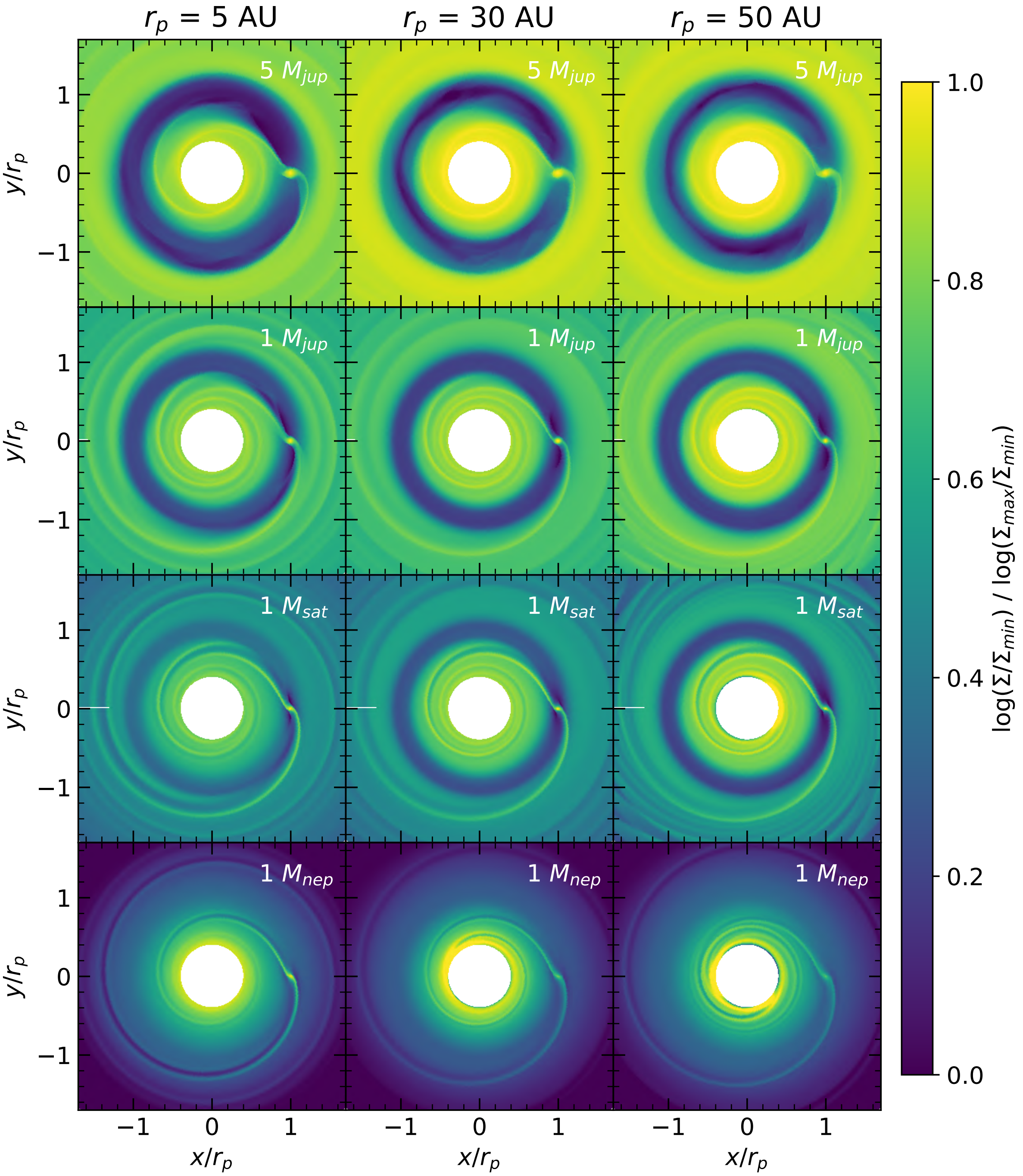

Figure 7.2.1: The figure shows the normalized gas surface density distribution in logarithmic scale of our 12 hydrodynamic two-fluid simulations of a protoplanetary disk with an embedded planet at 200 planetary orbits in a face-on view. In each panel, the columns show simulations with planets orbiting at different radii, r_p = 5 au, 30 au, 50 au. Each row shows the disk containing a planet with different mass ($M_p = 5\ M_{\rm jup}$, $1\ M_{\rm jup}$, $1\ M_{\rm sat}$, $1\ M_{\rm nep}$). The mass of the planet is indicated in the upper right corner of each subplot. The x and y coordinates are normalized with the planetary orbital radius r_p.

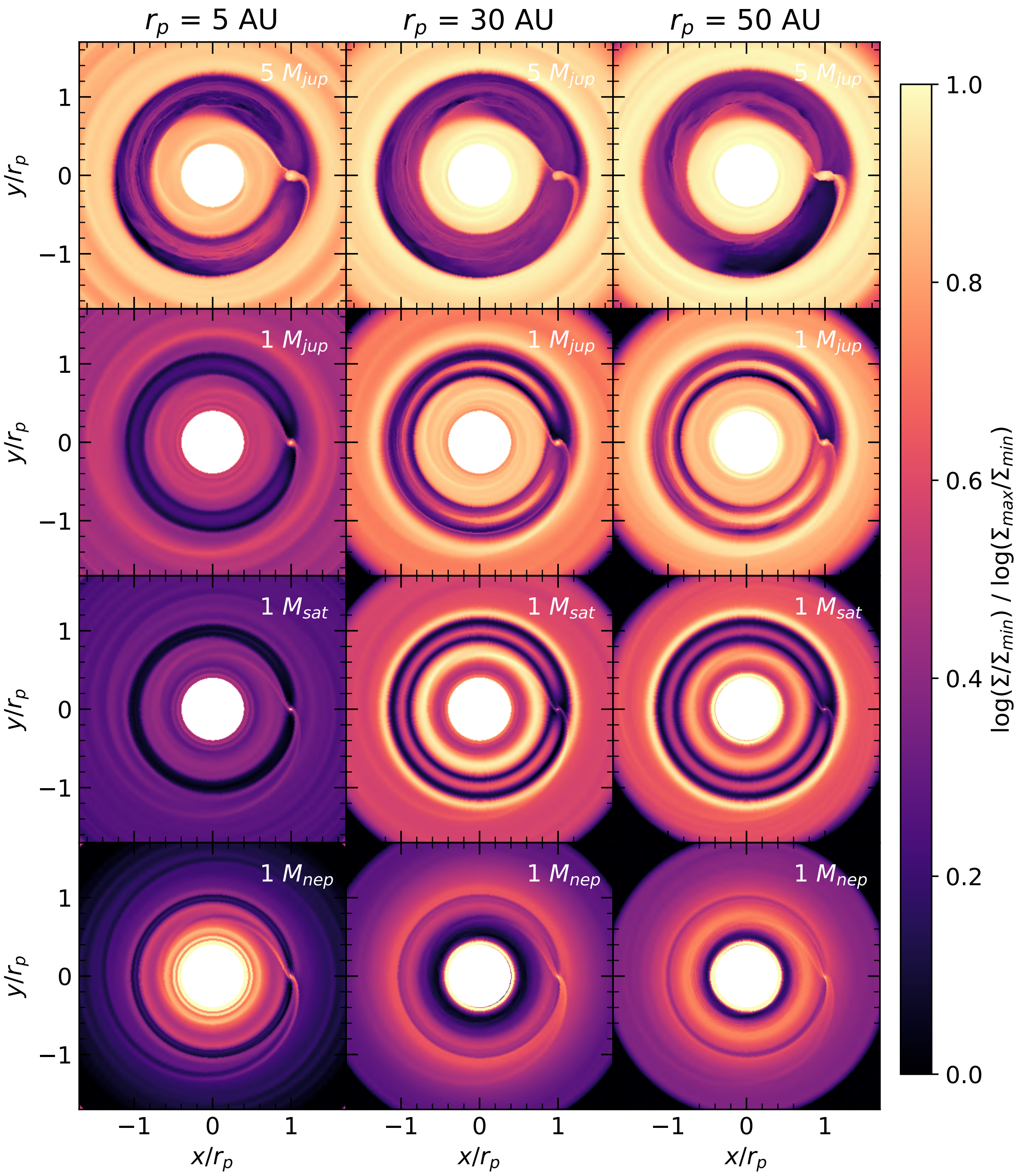

Figure 7.2.2: The figure shows the normalized surface density distribution of 1 mm-sized dust in logarithmic scale of our 12 hydrodynamic two-fluid (gas+dust) simulations of a protoplanetary disk with an embedded planet at 200 planetary orbits in a face-on view. In each panel, the columns show simulations with planets orbiting at different radii, $r_p = 5$ au, 30 au, 50 au. Each row shows the disk containing a planet with different mass ($M_p = 5\ M_{\rm jup}$, 1 $M_{\rm jup}$, 1 $M_{\rm sat}$, 1 $M_{\rm nep}$). The mass of the planet is indicated in the upper right corner of each subplot. The x and y coordinates are normalized with the planetary orbital radius r_p.

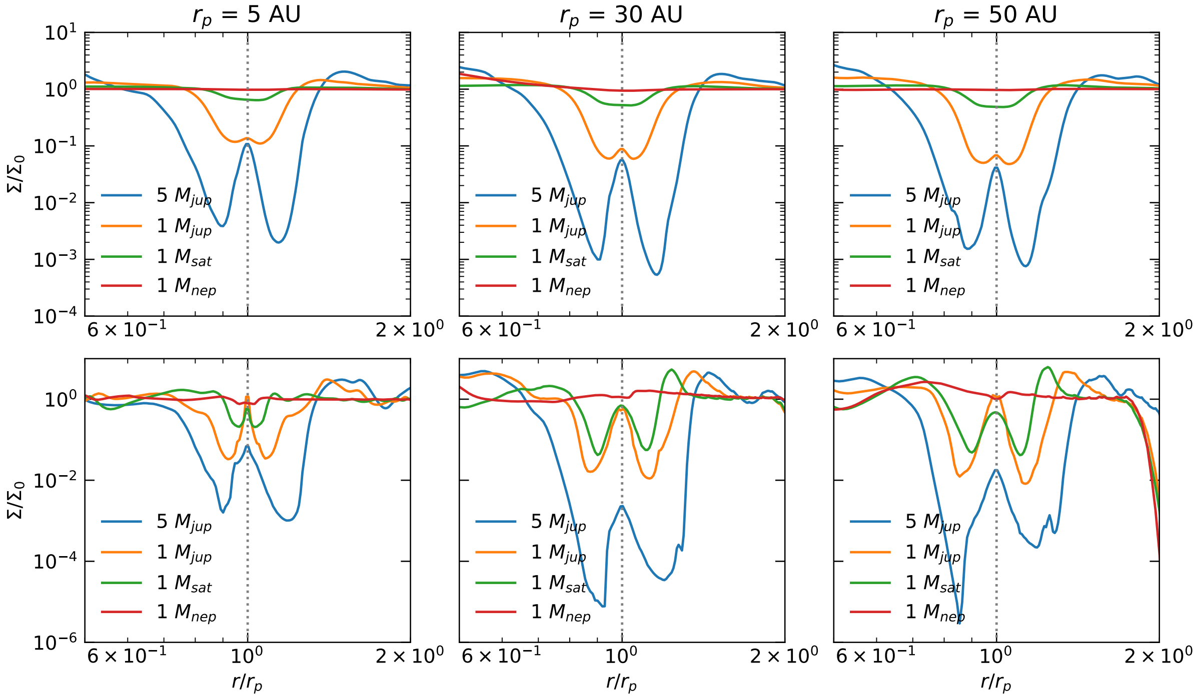

Figure 7.2.3: The azimuthally averaged surface density in gas (top row) and 1 mm-sized dust (bottom row) of our 12 hydrodynamic simulations are shown here. Each panel shows profiles of 4 identical disks, each containing a planet of different mass ($M_p = 5\ M_{\rm jup}$, 1 $M_{\rm jup}$, 1 $M_{\rm sat}$, 1 $M_{\rm nep}$). From left to right, the panels show planets orbiting at different radii, $r_p = 5$ au, 30 au, 50 au. The location of the planet is indicated with a dashed vertical line.

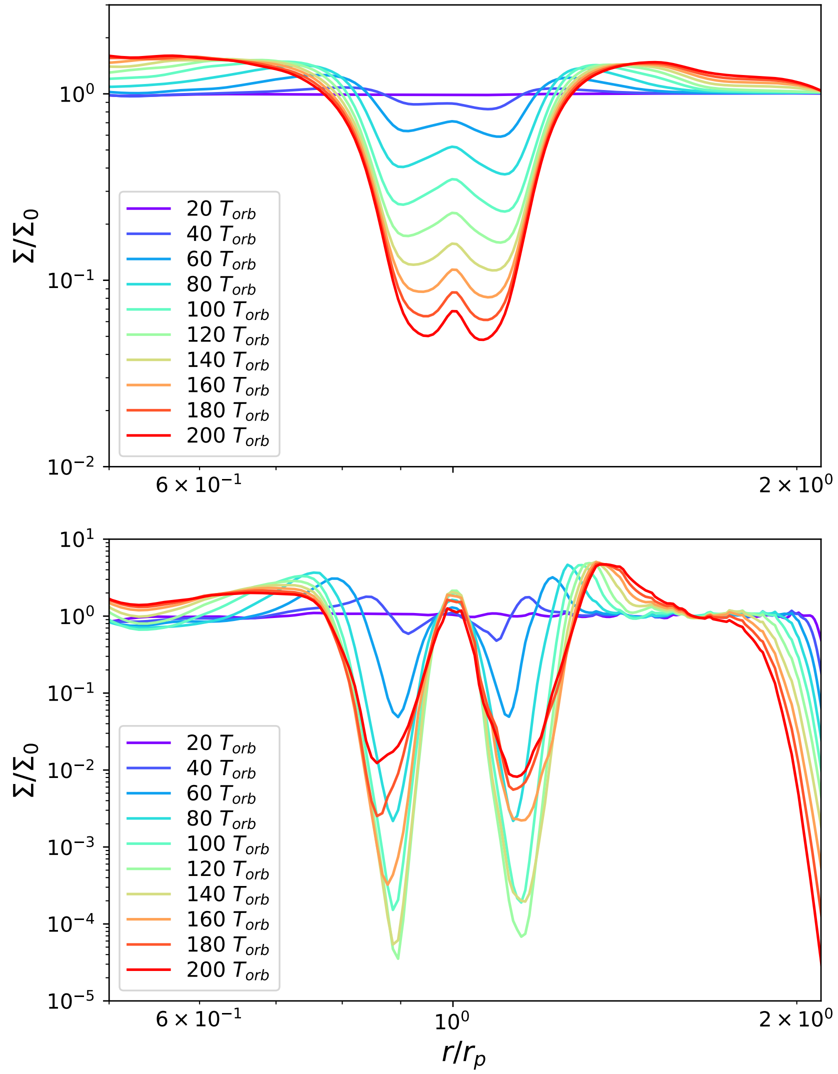

Figure 7.2.4: Temporal evolution of the azimuthally averaged surface density profile in gas (top) and dust (bottom) in our `m50au1up` simulation containing a 1 Jupiter-mass planet orbiting at $r_p = 50$ au over the period of 200 planetary orbits. Plotted are the surface density profiles after every 20 orbits.

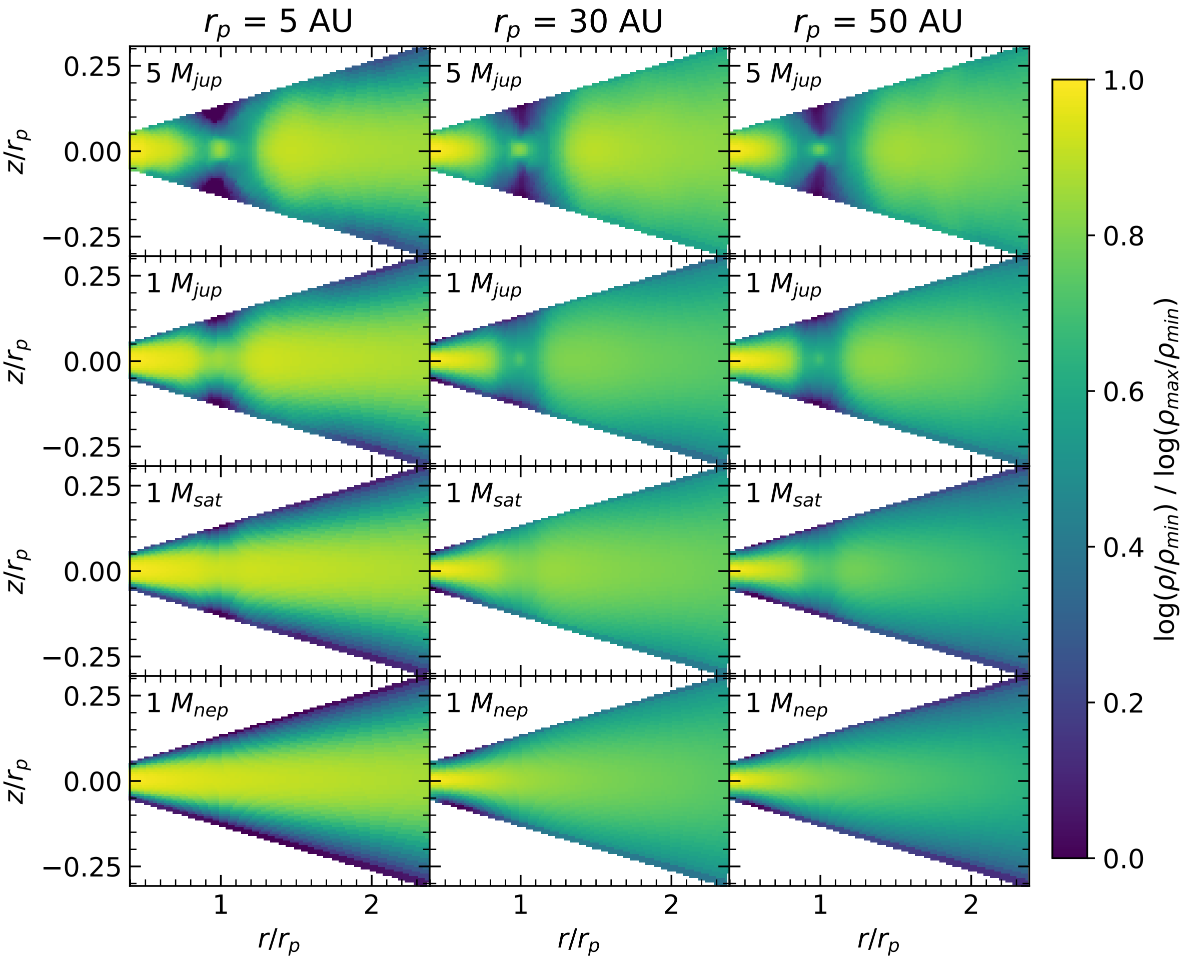

Figure 7.2.5: Here we show the normalized vertical distribution of the azimuthally averaged gas volume density of our 12 hydrodynamic two-fluid simulations of a protoplanetary disk with an embedded planet at 200 planetary orbits in a side-on view. The opening angles of the disks are enlarged for better visualization, i.e., the aspect ratio of the disk is plotted larger. In the left panel, we show the surface density in gas, in the right panel we show the surface density in 1 mm-sized dust. In each panel, the columns show simulations with planets orbiting at different radii, $r_p = 5$ au, 30 au, 50 au. Each row shows the disk containing a planet with different mass ($M_p = 5\ M_{\rm jup}$, $1\ M_{\rm jup}$, $1\ M_{\rm sat}$, $1\ M_{\rm nep}$). The mass of the planet is indicated in the upper left corner of each subplot.

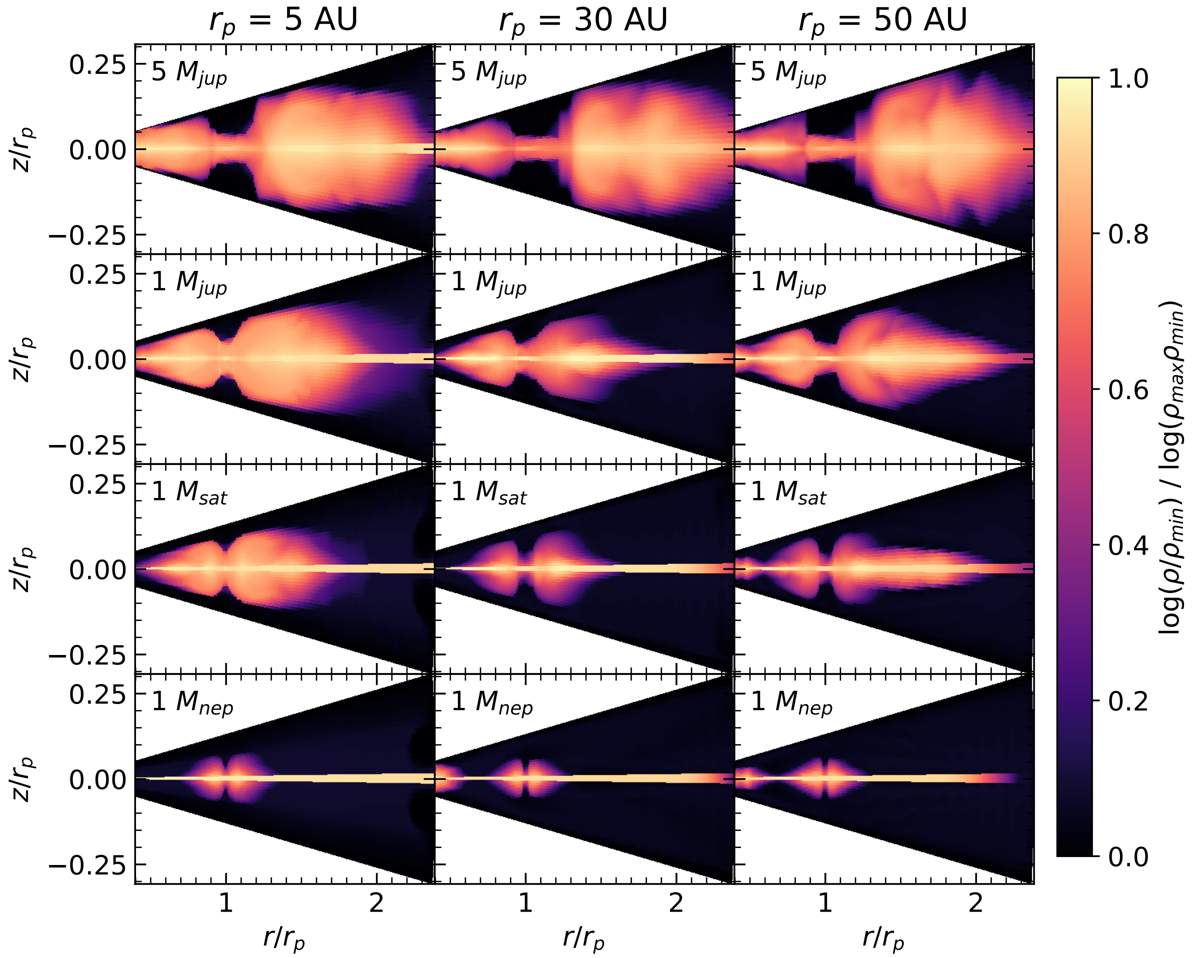

Figure 7.2.6: Here we show the normalized vertical distribution of the azimuthally averaged volume density of our 12 hydrodynamic two-fluid simulations of a protoplanetary disk with an embedded planet at 200 planetary orbits in a side-on view. The opening angle of the disks is enlarged for better visualization, i.e., the aspect ratio of the disk is plotted larger. In the left panel, we show the surface density in gas, in the right panel we show the surface density in 1 mm-sized dust. In each panel, the columns show simulations with planets orbiting at different radii, r_p = 5 au, 30 au, 50 au. Each row shows the disk containing a planet with different mass (M_p = 5 M_{jup}, 1 M_{jup}, 1 M_{sat}, 1 M_{nep}). The mass of the planet is indicated in the upper left corner of each subplot.

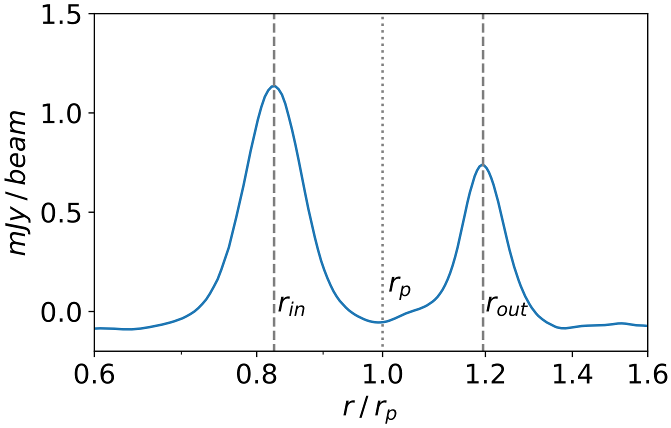

Figure 7.2.7: Example of the gap width Δ as defined in Eq. 7.12. Shown is the azimuthally averaged intensity profile computed using the CASA output. We identify r_{out} and r_{in} as the location of the local maxima in the intensity profile. This particular figure shows the intensity profile of the simulation `m30au1sat` observed in ALMA band 9 (400-500μm) with antenna configuration C43-8.

and discussion of the results will be presented in the next section.

7.3.1 Hydrodynamic Simulations

We run a set of twelve three-dimensional two-fluid (gas + 1 mm-sized dust) hydrodynamic simulations of a protoplanetary disk with an embedded planet. We place a planet of four different masses in an orbit at three different semi-major axes. In this section, we present the resulting effects that the planets have on the gas and dust distribution on their hosting protoplanetary disk.

Surface Density

In Fig. 7.2.1 we plot the vertically integrated volume density, i.e., the surface density, of the gas component at 200 planetary orbits. In Fig. 7.2.2 we show the corresponding surface density in 1 mm-sized dust. The figures show the surface density in Cartesian coordinates, even though the computations are carried out on a spherical grid, with the star located at the center of each sub-panel and the planet at the three-o'clock position, orbiting in a counterclockwise direction. In both Fig. 7.2.1 and Fig. 7.2.2, the columns show the simulations containing planets with different semi-major axis (r_p = 5 au, 30 au, 50 au). At these orbital radii, a period of 200 planetary orbits is equivalent to $\sim$ 2.4 kyr, $\sim$ 33 kyr or $\sim$ 71 kyr respectively. The four rows show the simulations containing a planet with mass $M_p = 5\ M_{\text{jup}}$, 1 M_{jup}, 1 M_{sat}, 1 M_{Nep}. The color map of the figures has a logarithmic scale and is normalized so that we can use the same color map for all the sub-panels in gas and dust respectively. In both, the gas and the dust disk, the planet creates distinctive disk morphologies. While for planets masses $M_p \geqslant 1 M_{\text{sat}}$, a gap is seen in the gas, a gap is seen in dust also when $M_p = 1 M_{\text{nep}}$.
In Fig. 7.2.3 we show the azimuthally averaged surface density profiles in gas (*top row*) and dust (*bottom row*). From left to right, we plot the surface density profiles with the planet at r_p = 5.2 au, 30 au, and 50 au at 200 planetary orbits.
Across our simulations, we vary the planet mass from 1 $M_{\text{nep}} \approx 0.05\ M_{\text{jup}}$ to 5 M_{jup}. Similar to Paardekooper & Mellema (2006), we find that the M_p = 1 M_{nep} planet does only open a

gap in 1 mm sized dust, but not in gas. The Neptune-mass planet is able to disturb the gas surface density by producing distinct spiral waves. However, the gravitational torque caused by the planet is not large enough to overcome the viscous effects in the gas. The gap which is opened by the 1 M_{nep} in the dust is very shallow. Increasing the planet mass decreases the gas surface density in the vicinity of the planetary orbital radius because gravitational torques increase and push the gas away from the planetary orbit. As expected, the depth and width of the gap increase with the mass of the planet. We find that the depth of the dust gap is generally deeper than the depth in gas.

At the outer edge of the dust gap, a density enhancement forms which coincides with a pressure maximum in gas. From both sides of the pressure maximum, dust drifts towards it. Hence, dust in the outer disk which drifts inwards gets trapped at this location, steadily increasing the local dust density. We show this effect in Fig. 7.2.4 where we plot the temporal evolution of the azimuthally averaged surface density distribution in gas (*top*) and dust (*bottom*) for every 20 orbits in the case of the 1 Jupiter-mass planet orbiting at 50 au. The dust enhancement at the outer edge of the gap also becomes broader with time and moves outward following the gas pressure maximum. The dust enhancement is generally broader for more massive planets. The maximum dust density remains roughly constant for different planetary masses for $M_p \geqslant 1\ M_{\mathrm{sat}}$.

As shown in Fig. 7.2.4, we find that the width of the gas gap quickly approaches a quasi-steady state. The depth of the gas gap increases monotonically over time and the width of the gap approaches its final value after about 100 orbits when the planet reaches its final mass. The gas disk still continues to evolve viscously, and we expect a true steady-state to be reached in the gas after one viscous timescale $t_{\mathrm{vis}} = x^2/\nu$ (e.g. Lynden-Bell & Pringle, 1974). Over the length scale of a gas gap with width $\Delta_{\mathrm{gas}} = 0.5 \cdot r_p = 0.5 \cdot x$, the viscous timescale in our simulations is $\sim 2 \cdot 10^3$ orbital timescales at 5.2 au. However, Kanagawa et al. (2017) find that the width of the gas gap does change only about 10 % after $0.1 \cdot t_{\mathrm{vis}}$ which is equivalent to $\sim$ 200 orbital timescales at 5.2 au. On the other hand, the gap profile in dust evolves continuously and the features in the 1 mm-sized dust disk change over time. Interestingly, the depth of the dust gap in our `m50au1jup` simulation does reach a maximum already after about 120 orbits, after which the depth decreases again. We find this behavior in all our simulations with $M_p \geqslant 1\ M_{\mathrm{jup}}$. In some cases, a pressure maximum also forms in the inner disk, e.g., in the `m30au1sat` simulation. In that case, a dust density enhancement also forms in the inner disk because the 1 mm-sized dust drifts towards the pressure maximum at this location as well.

Intermediate mass planets ($M_p = 1\ M_{\mathrm{sat}}$, $1\ M_{\mathrm{jup}}$) show the distinct W-shaped dust surface density profile as found in previous studies, e.g., by Dipierro et al. (2016). There exists a substantial amount of dust in the co-orbital region of the planet, which also causes a peak in the surface density profile in Fig. 7.2.3 at the location of the planet. Since for these masses, a gap is also opened in the gas, drag is reduced due to the low gas density and there exists a region around the orbital radius of the planet where the effects of radial drift are smaller, and dust can temporarily accumulate. We find that the 1 mm-sized dust remains in the co-orbital region of the planet as long as $1 \gg St$. If the gas density in the co-orbital regions decreases enough for the Stokes number to reach about order unity, dust is removed from the co-orbital region and the entire gap empties out. The onset of this process can also be seen in Fig. 7.2.4 where dust in the co-orbital region is stable until about 120 planetary orbits. At that point, the depth of the gap edges reaches a temporary maximum (largest depth). After that, dust from the co-orbital region is lost and fills the edges of the gap. The gap depth only grows again after all the dust from the co-orbital region is lost. This effect can be seen in all our simulations. However, it happens sooner in simulations containing a more massive planet or planets orbiting at smaller semi-major axes where dynamical timescales are smaller. We also expect the onset of this process to occur sooner, the flux of dust through the gap to be increased and the peaks in the gap profile to be smoothed if dust turbulent diffusion is included (see e.g. Zhu et al., 2012; Weber et al., 2018, for a comparison with and without diffusion in 2D). The outer edge of the planet also acts as a barrier for 1 mm-sized dust particles drifting inwards (Rice et al., 2006). Hence, without diffusion, there is no inward drift from the outer part of the disk to the co-orbital region. While, for the Saturn-mass simulations, the dust is evenly distributed along the co-orbital radius, there are dust enhancements just before and after the location of the planet (around the Lagrange points L4 and L5) in the 1 Jupiter-mass simulations. This is also consistent with earlier work in 2D, e.g., Zhang et al. (2018).

For $M_p = 5M_{\rm jup}$, the dust surface density at the location of the planet is much lower than in the other simulations because dust in the co-orbital region is lost. The gap region in these simulations still contains dust, but it is not confined to the co-orbital radius. Instead, it is more evenly distributed across the gap, but at very low densities. Looking at the temporal evolution of these simulations, we find that the 5 $M_{\rm jup}$ simulations also produce distinct co-orbital dust accumulation features early in the simulations. However, dust originally trapped in this region vanishes after about 150 planetary orbits and is therefore not seen in Fig. 7.2.2 and Fig. 7.2.3 where we plot a snapshot of the density distributions at 200 planetary orbits. We would like to highlight again that the dust disk has a more complex temporal evolution than the gas disk without any sort of steady state. Hence, the dust disk morphologies heavily depend on the age of the simulated systems. We expect the simulations containing a lower mass planet to also lose its dust from the co-orbital region at later times ($>$ 200 orbits). Moreover, for $M_p = 5\ M_{\rm jup}$, we find the mass of the planet to be large enough to make the disk slightly eccentric, leading to non-axisymmetric gap structures (Kley & Dirksen, 2006; Szulágyi, 2017).

At $M_p = 5\ M_{\rm jup}$ the surface density profile in gas (see Fig. 7.2.3) also has a W-shape. However, its origin is different from the situation explained above. Even though the dips adjacent to the planetary orbital radius become significantly deeper with the increase of the planetary mass from 1 $M_{\rm jup}$ to 5 $M_{\rm jup}$, the surface density at the orbital radius only decreases slightly. This is because gas efficiently accumulates in the planet's circumplanetary disk. With the azimuthal averaging, the gas in the potential well contributes to the surface density profile at the planetary orbital radius even though, away from the planet, the gap is much deeper.

When comparing the gap at different orbital distances, we find that the depth of the gap at 200 planetary orbits increases with planetary orbital radius. One factor which favors gas gap formation at large radii in our models, is the adoption of constant kinematic viscosity. This becomes clear by studying the dimensionless P-parameter

$$P = \frac{3}{4}\frac{h_g}{R_H} + \frac{50}{q\mathcal{R}} \tag{7.10}$$

introduced by Crida et al. (2006) which measures the ability of a planet to carve a gap in gas. The smaller this parameter, the easier it is to carve a gap. Here, $q = M_p/M_*$ is the planet-to-star mass ratio, $R_H = r_p(q/3)^{1/3}$ is the Hill radius of the planet and $\mathcal{R} = r^2\Omega/\nu$ is the Reynolds number. The first term on the r.h.s. of Eq. 7.10 scales as the aspect ratio h_g/r and, for flared disks, increases with radius. With constant kinematic viscosity, the second term on the r.h.s. of Eq. 7.10 decreases as $r^{-1/2}$ i.e., it contributes less at large radii. In our models, the decrease of the second term dominates over the increase of the first term. Therefore, the P-parameter decreases with radius and gap formation in gas is easier in the outer disk.

The outermost regions of the disk are depleted in dust. This is most noticeable for simulations with planets at large radii and small planet mass, (e.g., `m50au1nep` in Fig. 7.2.2). The dust depletion is due to radial inward drift of the 1 mm-sized dust and no replenishment through the closed outer radial boundary. We expect the entire outer disk to empty out eventually and drift inward to be trapped in a pressure maximum or at the inner boundary of our simulation domain.

Vertical Distribution

We also investigate the vertical distribution of the gas and dust components. In Fig. 7.2.5 we plot the azimuthally averaged distributions of the volume density in gas. In Fig. 7.2.6 we plot the azimuthally averaged distributions of the volume density in dust. Both figures are plotted in a normalized logarithmic color scale. The layout of the sub-panels in both figures is identical to Fig. 7.2.1 and Fig. 7.2.2, i.e., the planet mass decreases from top to bottom, and the orbital distance increases from left to right.

Similarly to Fig. 7.2.1, the gap in the vertical gas distribution is noticeable in all the simulations except in the Neptune-mass simulations. If a gap is present, it extends the full height of the disk. For more massive planets, the gap is wider at larger altitudes. For 1 M_{jup} planets and especially at 5 M_{jup} planets, an accumulation of gas at the center of the planetary potential is visible where gas accumulates in the circumplanetary disk. However, since we underestimate the gravitational potential at the location of the planet due to the smoothing length, we expect this effect to be even more prominent in reality.

The azimuthally averaged vertical dust density distribution (Fig. 7.2.6) is very different from the distribution in gas. This is mainly because dust is not pressure supported. The 1 mm-sized particles, which are not perfectly coupled to the gas settle vertically. In a disk without a planet, all the 1 mm-sized dust does settle onto the midplane because we do not include turbulent diffusion in the simulations, which would counteract the settling at some point. In Fig. 7.2.6, the effect of settling is seen most clearly in the outermost regions of the disks containing a low-mass planet. There, the dust disk is very thin. Its thickness is not vanishingly small because the computational cells at the midplane have a non-vanishing size.

Fig. 7.2.2 shows that vertical settling is counterbalanced by vertical stirring around the gap edges, as predicted by Edgar & Quillen (2008). The vertical stirring is caused by the meridional flows in the gas (Szulágyi et al., 2014; Fung & Chiang, 2016; Szulágyi & Garufi, 2021). In the midplane where the mm-sized grains are most tightly coupled to the gas, they are dragged along with the vertical upward flow of the gas until they reach a height at which the grains decouple enough for them to settle toward the midplane again. The vertical stirring is not uniform along the entire edge (in azimuthal direction) but it is strongest at the location where the planetary wake meets the edge of the gap and decreases in strength further away from the planet. Due to the differential rotation of the disk, the material at the gap edge has a different angular velocity than the planet. Therefore, in the rest frame of the gap edge, the vertical stirring is periodic with a period $t_{\mathrm{stir}} \simeq 2\pi/|\Omega_K(r_P) - \Omega_K(r_{\mathrm{edge}})|$ where r_{edge} is the radius of the gap edge. Low-mass planets, like the Neptune-mass planets, only disturb the dust vertically in regions close to the orbit of the planet. The larger the planet's mass, the thicker the dust disk becomes, and regions farther away from the planetary orbit are affected. Similar effects were found by Fouchet et al. (2010) in their 3D gas+dust simulations but using the smoothed particle hydrodynamics (SPH) approach. In the simulations containing a larger mass planet, dust is present in a large vertical fraction of the simulation domain, also far away from the planet and the midplane. We discuss the effects of turbulent diffusion on the vertical dust distribution in Sec. 7.4.2.

In some panels in Fig. 7.2.6, the dust gets puffed up at the inner computational boundary. This can be seen, for example, in the simulations containing a Neptune mass planet at 30 au and 50 au and is caused by direct stellar irradiation of the inner edge of the disk.

7.3.2 Synthetic ALMA Observations

In this section, we study the synthetic ALMA mm-continuum observations created with RADMC-3D and CASA.

In Fig. 7.3.1, we show normalized mm-continuum maps for each of our 12 hydrodynamic simulations in the same layout as in Fig. 7.2.1. For each simulation, we chose the observation band and antenna configuration that produces the most detailed intensity map. In detail, this

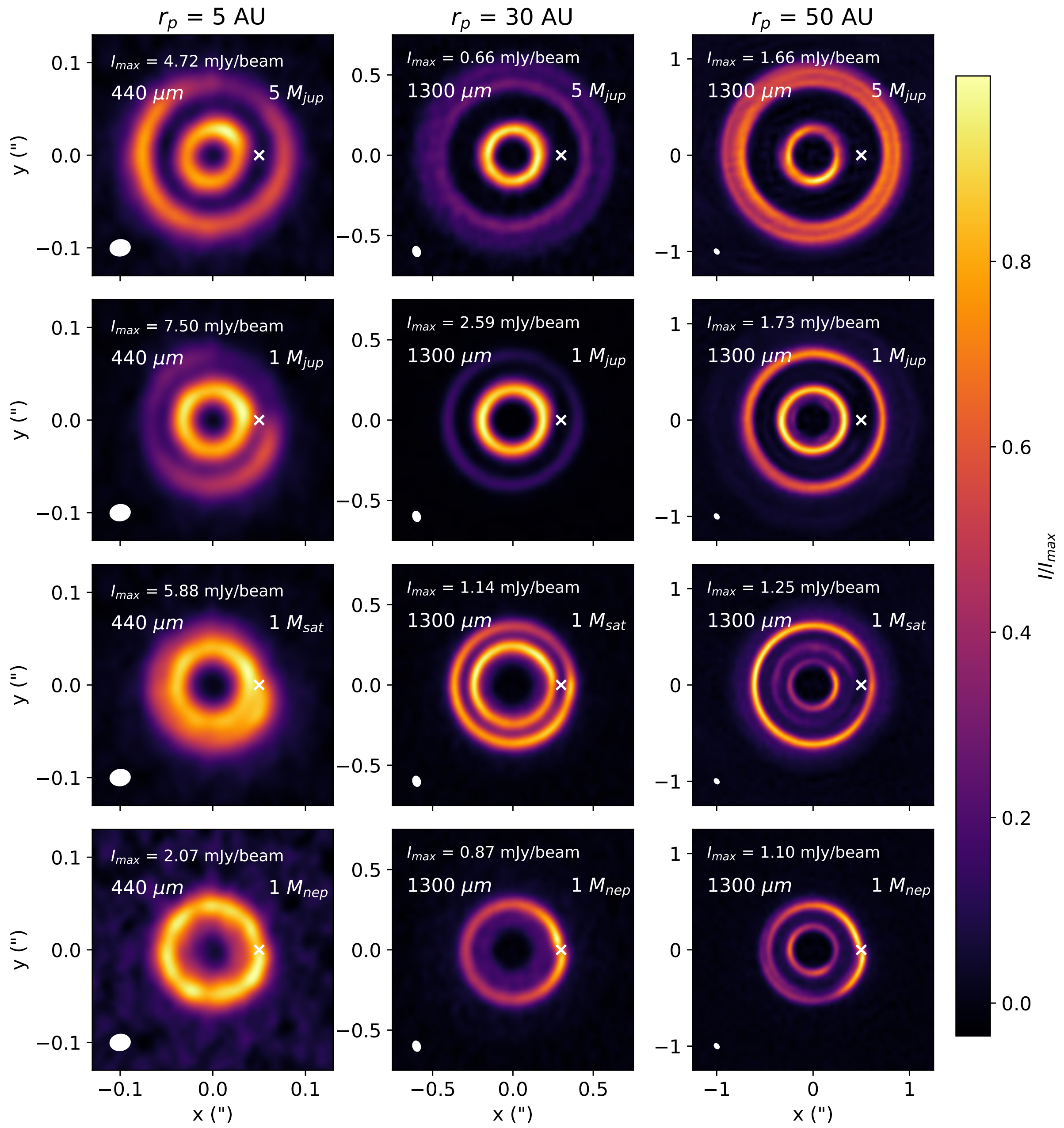

Figure 7.3.1: For each of our 12 hydrodynamic simulations, we show one synthetic ALMA observation. Each image is normalized to its peak intensity, which is indicated in the upper-left corner of each image. From left to right, we show the disk containing a planet at $r_p = 5$ au, 30 au, 50 au. The rows show the disks with a planet of equal mass, $M_p = 5\ M_{\mathrm{jup}}$, 1 M_{jup}, 1 M_{sat}, 1 M_{nep}. In each image, the mass of the planet is indicated in the upper right corner. The central wavelength of the observation band is indicated in the upper-left corner. The beam size is indicated in the lower-left corner.

is antenna configuration C43-8 and ALMA band 9 ($\sim$ 440 μm) for simulations with $r_p = 5$ au and ALMA band 6 ($\sim$ 1300 μm) for simulations with $r_p \geqslant 30$ au. The intensity maps are normalized with the peak intensity. We place the value of the peak intensity in the upper left corner of every individual map. The beam size is indicated with a white ellipse in the bottom left corner of each map and the location of the planet is indicated with a white `x`.

The intensity maps containing $M_p = 5M_{\rm jup}$ planets (first row in Fig. 7.3.1) all show a clear gap with a wide outer ring and a narrower inner ring. At $r_p = 5$ au the inner and outer rings show asymmetric brightness distributions. The outer ring is brightest on the opposite side of the planet whereas the inner ring is brightest about 45 degrees in front of the planet. This is the location where the inner spiral arm meets the inner disk and stirs up the dust. The asymmetry is further enhanced due to beam dilution, especially at $r_p = 5$ au, where the beam is notably large and elongated. At $r_p \geqslant 30$ au, the outer rings are more azimuthally symmetric. Generally, the inner ring is brighter than the outer ring.

The outer ring in the simulation containing a $M_p = 5M_{\rm jup}$ planet at $r_p = 50$ au, shows two rings separated by a depletion. The origin of this feature is most apparent in the vertical density distribution in figure 7.2.7 where the outer disk exhibits a vertical notch at around 1.7 r_p. This notch can also be seen in the vertical distribution of the disks containing a $M_p = 5M_{\rm jup}$ planet at $r_p = 30$ au and in the disk containing a $M_p = 1M_{\rm jup}$ planet at $r_p = 50$ au. However, in both other cases, the notch is not prominent enough to appear in the synthetic intensity map. One must be careful when interpreting the inner ring. We found that in all the $M_p = 5M_{\rm jup}$ maps, the inner ring is caused by an accumulation of dust at the inner computational boundary rather than at a gas pressure maximum. No matter where the inner boundary would lie, there would be naturally a ring in the inner boundary, where dust accumulates, due to the mass-conservation simulations, (i.e., we do not allow outflow). In the maps containing lower-mass planets ($M_p < 5M_{\rm jup}$), there are maps with either one or two inner rings. If only one ring is present, it has a physical origin. If there are two inner rings, (e.g., Jupiter mass, Saturn mass, and also Neptune mass at 50 au), the outermost of the two inner rings is physical, and the innermost ring is an artifact.

In the second row of Fig. 7.3.1 we show the $M_p = 1M_{\rm jup}$ planets which all produce two rings in the disk. At $r_p = 5$ au, the inner ring has an asymmetric azimuthal brightness profile with a peak in front of the planet (in an anticlockwise direction). At this location, the inner planetary wake meets the inner edge of the gap and stirs up dust above the midplane. Exposed to direct stellar radiation, dust above the midplane is warmer and, hence, brighter in the intensity map. The puffed-up dust disk at this location also casts a shadow on the outer disk and the outer ring. Therefore, the outer ring is darker in the upper-right quadrant. Vertical stirring also occurs when the outer planetary wake meets the outer edge of the gap. Similarly to the inner ring, the outer ring is warmer and therefore brighter in the lower-right quadrant. As shown in Fig. 7.2.5, stirring is much more effective at 5.2 au compared to 30 au and 50 au because the mm-sized grains are more strongly coupled to the gas' meridional flows due to the larger gas density closer to the star. Therefore, at 30 au and 50 au less dust is stirred above the midplane which can cause shadowing. Hence, asymmetries due to absorption and shadowing are much less pronounced at larger orbital radii. Comparing the intensity map containing the $M_p = 1M_{\rm jup}$ planet at 30 au and 50 au it becomes apparent that the outer ring at 30 au is dimmer than at 50 au. This is because the Saturn-mass planet is able to stir up more dust in the inner disk than when it orbits at 50 au. Again, this is due to better coupling to the gas. The puffed-up inner edge of the gap then casts a shadow over the vertically stirred dust at the outer ring. This shadow is slightly larger in the upper-right quadrant, but generally, the brightness distribution is more symmetric than with the planet at 5 au. When the Saturn-mass planet orbits at 50 au, the inner edge of the gap casts a smaller shadow and the outer ring is brighter. Hence, even though the dust at the location of the outer ring is similar in both cases, the emission of the outer ring is different due to temperature differences as a result of the vertical structure of the disk. In all the $M_p = 1M_{\rm jup}$ maps, the inner ring is clearly separated from our inner computational boundary.

In the models containing the $M_p = 1M_{\rm sat}$ at $r_p = 5$ au it is difficult to resolve the gap due

to the combination of small gap width and large beam size. However, an asymmetry can be seen in cases with more massive planets. Most prominent is the crescent-shaped asymmetry in the lower-right quadrant due to the vertical stirring at the location where the outer planetary wake meets the gap edge. The asymmetry arises because in the upper-right quadrant, the outer edge of the gap lies in the shadow of the puffed-up inner edge section of the disk. Here, the asymmetries are also less pronounced at 30 au and at 50 au compared to when the planet orbits at 5 au because grains are less strongly coupled to the meridional flows. Similarly to the case with $M_p = 1 M_{\mathrm{jup}}$, the inner gap edge is less puffed up when the Saturn-mass planet orbits at 50 au than at 30 au. Therefore, the inner ring is less pronounced in the intensity map. For $r_p \geqslant 30$ au, the gap is clearly resolved. At $r_p = 30$ au, there are two rings with roughly equal brightness. At $r_p = 50$ au, the ring to the inside of the gap is barely visible. Moreover, there is a third ring right at the inner boundary of our computational domain caused by accumulating dust. Also, faint emission from the disk outside the outer ring is visible.
As mentioned in Sec. 7.3.1, the Neptune mass planet barely opens a gap in the dust. There is no gap in the gas and hence, no pressure bump in which dust can accumulate. The features which we see in the disks containing a Neptune-mass planet are traces of the spiral wakes caused by the planet. The spiral wakes stir up dust from the midplane which gets illuminated and subsequently heated by the central star.

7.3.3 Gap-Widths in Gas

Before we present our results on gap width measurements in the synthetic ALMA intensity maps, which we will do in the following section, we will present gap width measurements in gas. For this, we measured the gap widths Δ_g in the hydrodynamic gas density distribution. These measurements allow us to better understand the results and enable direct comparison with previous studies. Our approach for the gas gap measurements is identical to Zhang et al. (2018). We find the following relation between the gas gap width Δ_g and model parameters:

$$\Delta_g = 0.27 \left(\frac{M_p}{M_*}\right)^{0.21} \left(\frac{h_g}{r}\right)^{-0.30} \alpha^{-0.15} \tag{7.11}$$

Compared to Kanagawa et al. (2016), the gap-width in gas Δ_g is, with a power law index 0.21, less sensitive to the planet-to-star mass-ratio (0.5 in Kanagawa et al., 2016) but is in rough agreement with Zhang et al. (2018) who find a similar value (0.26). The gap width in gas is also less sensitive to h_g/r and to α compared to Kanagawa et al. (2016). They find power law indices -0.75 and -0.25 respectively. The difference to Kanagawa et al. (2016) is likely due to our different definition of the gap width in gas. Our definition is identical to the definition in Zhang et al. (2018) which is smaller for wide gaps. Nevertheless, our gap width in gas is more sensitive to h_g/r and α compared to what is found in Zhang et al. (2018). They find values of -0.05 and -0.08 respectively. The differences likely arise due to a combination of 3-D and radiative effects.

7.3.4 Gap Widths in Intensity Maps

We measure the widths of the gaps (Δ) in azimuthally averaged intensity profiles (see Fig. 7.2.7).

Measuring Gap Widths

We first identify the gap caused by a planet around r_p and then find the first local maximum outside and inside the center of the gap. In the case of Neptune mass planets, which do not open observable gaps, we do not measure a gap width. In all other cases, we fit a Gaussian profile to the observed maxima and identify the radii at which the emission peaks as r_{out} and

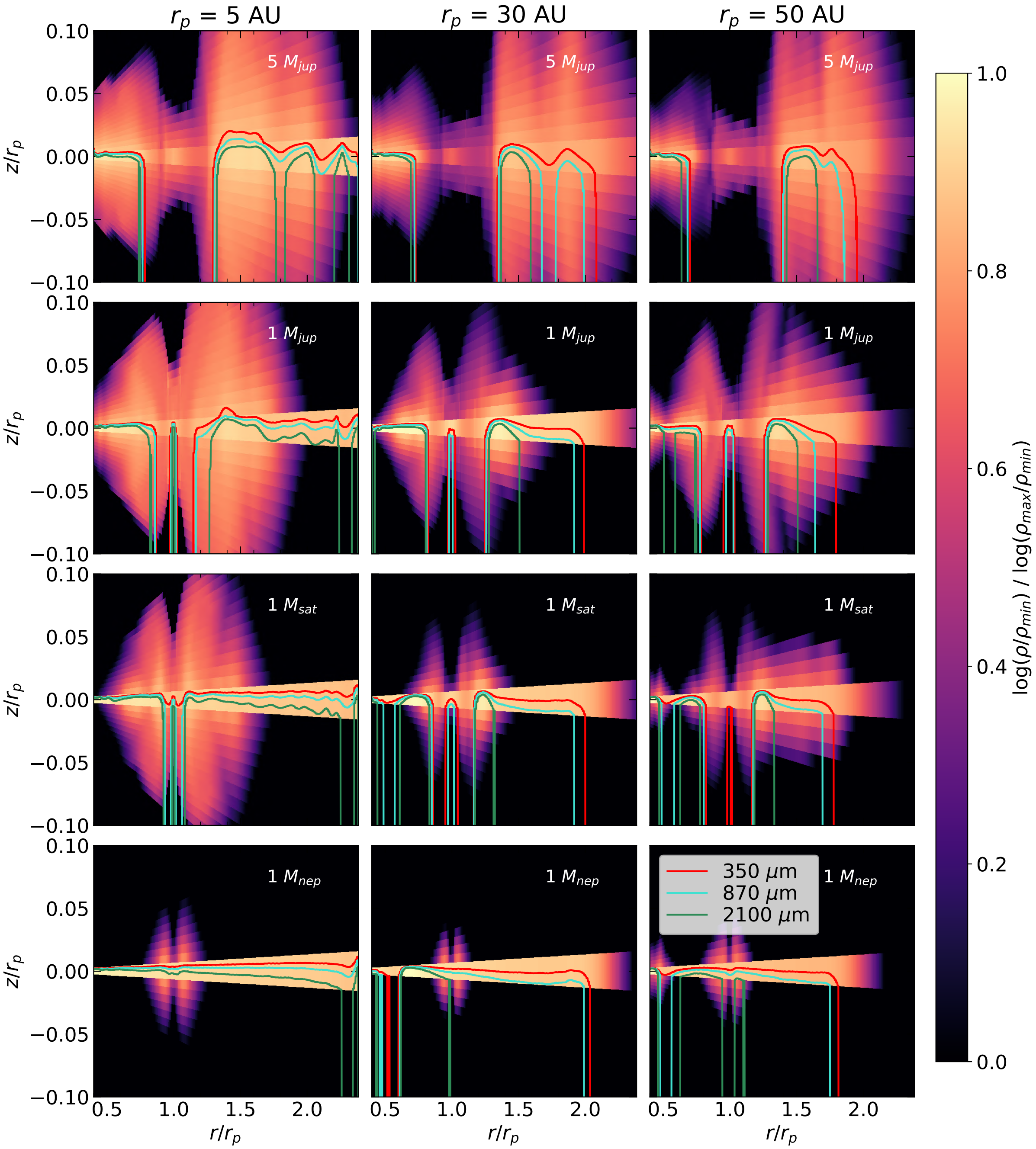

Figure 7.3.2: This figure shows for each of our 12 models the contour $z_1(r)$ of the surface where the optical depth $\tau = 1$. Each panel shows a vertical cut of the volume density in the dust at the location of the planet ($\phi = 0$). In each panel we show the $\tau = 1$ contour for three wavelengths: 350 μm , 870 μm , and 2100 μm respectively. At each radius, we integrate along the z-axis from z = $+\infty$.

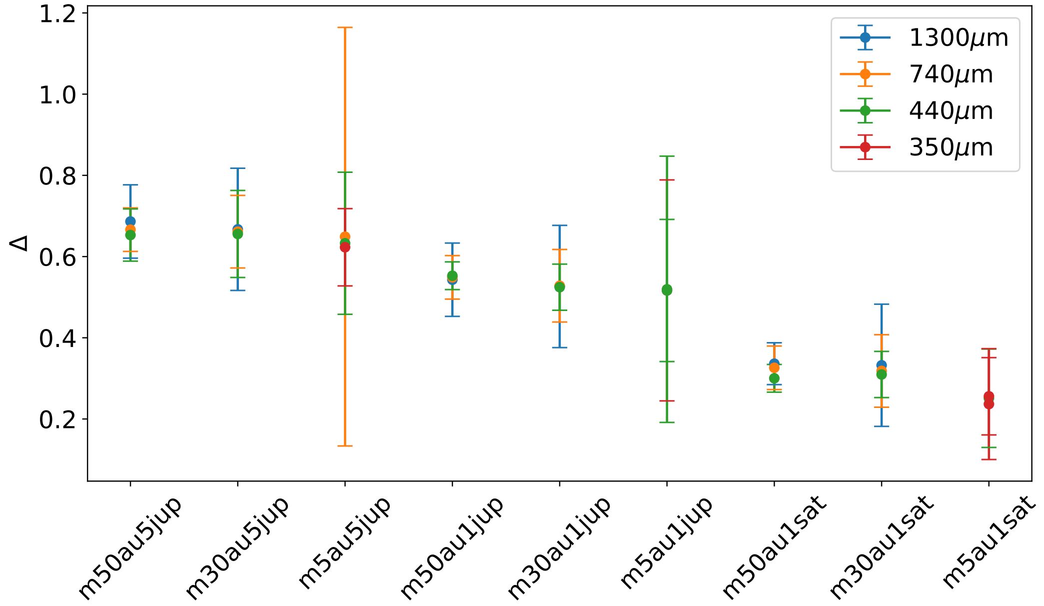

Figure 7.3.3: Gap width measurements (Δ) as defined in Eq. 7.12. In all our models which contain a planet massive enough to open an observable gap, we show the gap width measured in synthetic observations at different wavelengths. The vertical error bars correspond to the size of the beam in the synthetic ALMA observation.

$r_{\rm in}$ respectively. We then define the gap width Δ as

$$\Delta = \frac{r_{\rm out} - r_{\rm in}}{r_{\rm out}}. \tag{7.12}$$

This has the advantage that it does not depend on r_p. In some cases, we cannot identify a clear gap in our synthetic images, but only a single ring located on the inside or on the outside of the planetary orbital radius. In these cases, we assume the gap to be symmetric about the planetary orbital radius r_p, i.e.,

$$r_{\rm out} - r_p = r_p - r_{\rm in}. \tag{7.13}$$

If the ring is located to the inside of the planetary radius, we use Eq. 7.13 and express $r_{\rm out} = 2r_p - r_{\rm in}$ which we then plug into the definition of the gap width (Eq. 7.12) and use the value for r_p which we know from the hydrodynamic simulations. If only an outer ring is visible, we use $r_{\rm in} = 2r_p - r_{\rm out}$. Thus, we can always define a gap width Δ even if only a single ring is visible in the synthetic images.

For the gap width measurements, we use the locations of the local maximum of the intensity to define a gap width instead of the locations of the edge at half of the peak value, as done by, e.g., Zhang et al. (2018). We found that the radial locations of the local maxima are less sensitive to the size of the beam. Furthermore, our definition is independent of the emission at the bottom of the gap which, for resolved gaps, can drop below the noise level. In Fig. 7.3.3, we show the measured gap width Δ for all our models containing a planet more massive than Neptune. For each model, we measure the gap width (Δ) at three different beam sizes. The vertical lines represent the size of the corresponding beam. We list the average values of the measured gap width in Table 7.3.1. We later use these values in the fitting procedure in Sec. 7.3.4.

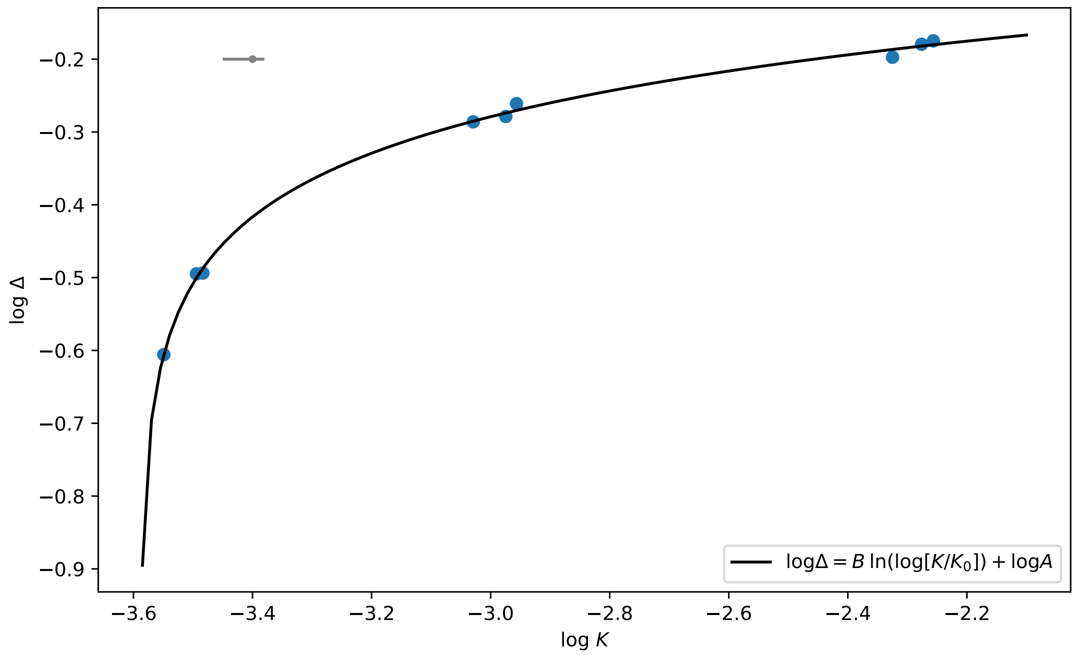

Figure 7.3.4: $\Delta - K$-relation and best fit using Eq. 7.17. The gray error bar in the upper left corner shows the error in log K.

Fitting Gap Widths

We derive an empirical relationship between the gap width Δ, as measured from the intensity profiles in continuum images, and the planet mass M_p similarly to what has been done in previous studies (e.g. Kanagawa et al., 2016; Rosotti et al., 2016; Dong & Fung, 2017; Zhang et al., 2018). While Kanagawa et al. (2016) focused on the planetary gaps in gas, Dong & Fung (2017) focused on planet opened gaps in near-infrared scattered-light images. Zhang et al. (2018) have previously studied the relationship between gap widths and planetary mass in continuum intensity maps. Our aim for this section is to do the analysis, for the first time, based on three-dimensional simulations, and to improve upon the previous approaches by providing a method tailored towards observations rather than hydrodynamic simulations. Following previous studies, we define a dimensionless parameter K which is proportional to the mass ratio between the planet and the star M_p/M_*, and has a power-law dependence on the parameters H_B and α as

$$K = \frac{M_p}{M_*} \cdot H_B^a \cdot \alpha^b. \tag{7.14}$$

The dimensionless parameter H_B can be regarded as an aspect ratio H of the disk ($H = h_g/r$ and $h_g = c_s/\Omega$). We do not define H_B in terms of hydrodynamic quantities in order to make this approach more tailored toward real observations. Therefore, we define H_B as

$$H_B = \sqrt{\frac{\gamma k_B}{G M_* m_\mu} \cdot r T_B}. \tag{7.15}$$

Here, k_B is the Boltzmann constant. The parameter H_B is defined in a way that, for a vertically isothermal disk of temperature T_B at radius r, $H_B = H$ holds. We determine the parameter H_B for a given disk by measuring the (azimuthally averaged) brightness temperature T_B of the dust emission at distance r from the central star. We measure the brightness temperature T_B instead of the physical temperature T because, similar to the aspect ratio of the disk, we do not have direct observational access to the physical temperature in images of marginally optically thin regions. In optically thick regions, the brightness temperature is equal to the physical temperature of the emitting material at the $\tau = 1$-surface. We choose $r = r_{\text{out}}$ to be the radius of the ring outside the planetary orbit r_p where the dust emission is most optically thick and the brightness temperature approaches the physical temperature of the emitting material.

The second dimensionless parameter in Eq. 7.14 is the Shakura and Sunyaev α-parameter of turbulent viscosity (Shakura & Sunyaev, 1973). It is usually not directly measurable from mm-continuum observations but requires additional modeling as done by, e.g., Pinte et al. (2016) for HL Tau. Therefore, the value of the α-parameter usually assumed to be in the range of 10^{-3} to 10^{-2} for typical disks. The α-turbulence parameter is also not a predetermined quantity in our radiative hydrodynamic simulations, where we have adopted a constant kinematic viscosity instead of the alpha prescription typically used in isothermal hydrodynamic simulations. Here, we estimate the α-parameters from the scale height h_g of a Gaussian fit to the vertical gas density in the initial hydrodynamic thermal equilibrium density field (without a planet) at the orbital radius of the planet r_p. We do that before the injection of the planet because in our radiative disk, the vertical gas profile can deviate from a Gaussian depending on the local heating and cooling in the gas. In addition to that, unlike in isothermal simulations, the local gas scale height sensitively depends on the radius at which it is measured due to the perturbation of the planet. We then use the kinematic viscosity ν to compute the α-parameter with the following formula:

$$\alpha = \frac{\nu}{\Omega h_g^2} \tag{7.16}$$

We list the α-parameters for each model in the third column of Table 7.3.1.

In the next step, we find the best fitting parameters a and b in Eq. 7.14 which relate the K-parameter to the gap width Δ via the following relation

$$\log \Delta = B \cdot \ln \left[\log \left(K/K_0 \right) \right] + \log A \tag{7.17}$$

where A, B and K_0 are fitting coefficients. Here we highlight that we use the intensity profile of the synthetic continuum intensity maps to find the fitting parameters a and b. This is in contrast to the previous work of Kanagawa et al. (2016) and Zhang et al. (2018) which used the gas surface density to calibrate their parameters. We do not use the gas surface density in the fitting process here because we aim to produce a formula that is as independent as possible from hydrodynamic quantities. In Eq. 7.17, *log* is the logarithm with base 10 and *ln* is the natural logarithm. We chose a ln-dependence between $\log \Delta$ and $\log K$ because we found it to be the functional dependence that minimizes the fitting error out of any monotonic functional dependence we tested (1st, 2nd order polynomial, exponential, root). The ln functional dependence is also physically motivated because there exists a minimum planetary mass, which lies somewhere between a Neptune mass and a Saturn mass, below which no planetary gap is opened in a disk (e.g. Paardekooper & Mellema, 2006). The ln-dependence naturally provides a minimum value for K below which a gap is not observable unlike the linear dependence used in previous studies. In Eq. 7.17 the lower bound is reached when $K = K_0$.

In practice, we first find the best fitting coefficient K_0 for the case when $a = b = 0$ using a least square fit. We find $K_0 = 2.58 \cdot 10^{-4}$ which we fix at this value. It is equivalent to $\sim 5.2\ M_{\text{nep}}$ which lies below a Saturn-mass. We do not yet fix the coefficients A and B in this process.

In a second step, after fixing K_0, we find the best fitting parameters a and b as defined in Eq. 7.14. For this, we assign values to a and b and perform additional least square fits with A and B as free parameters using the $\Delta - K$ relation in Eq. 7.17. We obtain a fitting error σ from the sum of the square difference between the measured values of the gap width Δ and the fit. We then vary a and b to minimize σ. At the minimum σ, we find the optimal parameters a,

b and the corresponding coefficients A and B. Our results are A = 0.61 and B = 0.12 and the K-parameter is:

$$K = \frac{M_p}{M_*} \cdot H_B^{0.086} \cdot \alpha^{-0.066} \tag{7.18}$$

We list the values of $\log K$ for each of the models in the fifth column of Table 7.3.1. To compute the uncertainty of the fitting in $\log K$, we calculate the residual between each measurement and the fitting curve. From the distribution, the lower bound is estimated by the 15.9 percentile, and the upper bound by the 84.1 percentile. We find an uncertainty in $\log K$ of $^{+0.02}_{-0.05}$. We indicate this uncertainty with the gray error bar in the upper left corner of Fig. 7.3.4.

We can not immediately compare the relationship in gas in Eq. 7.11 with the observational relationship in Eq. 7.17 because of the different functional dependence (linear vs. ln). However, because close to $\log K = -2.36$, the relation $\ln[\log(K/K_0)] \sim \log(K/K_0)$ holds, we can restrict ourselves to this value of $\log K$ and compare the power-law exponents there. For example, the parameter B provides the gap-width-dependence on the planet-to-star mass ratio, and the product aB represents the dependence on H_B or h_g/r respectively. The product bB provides the dependence on the α-parameter. The dependence on M_p/M_* is weaker in the observed gaps ($B = 0.12$) than in gas ($B = 0.21$). This is in agreement with Zhang et al. (2018), who also found a weaker dependence for moderately coupled grains. The dependence on α is also weaker in our observational relationship ($bB = -0.008$) compared to the dependence on gas ($bB = -0.15$). It is also about a factor of two lower than for the moderately coupled large grains in Zhang et al. (2018) ($bB = 0.016$). The dependence on H_B is weaker and has the opposite sign ($aB = 0.01$) than the dependence on h_g/r in gas ($aB = -0.3$). Here, Zhang et al. (2018) find $aB = -0.01$ for their moderately coupled large grains. Hence, the magnitude of our value of aB is in agreement with previous work, but it has the opposite sign. This is a result of our definition of H_B and the fact that the brightness temperature T_B is not always an accurate tracer of the gas temperature. In our case, T_B decreases faster with radius than the gas temperature, resulting in the opposite sign in the power law exponent of H_B (to be precise, rT_B is a decreasing function of radius, while in flared disks, rT is generally an increasing function of radius for T being the physical gas temperature).

Eq. 7.17 can be solved for the planet-to-star mass ratio $\log\left(M_p/M_*\right)$ from which we can directly compute planet masses M_p from gap widths Δ in ALMA observations:

$$\log\left(M_p/M_*\right) = \exp\left[\left(\log\Delta - \log A\right)/B\right] + \log\left(K_0 H_B^{-a} \alpha^{-b}\right) \tag{7.19}$$

Where A = 0.61, B = 0.12, $K_0 = 2.58 \cdot 10^{-4}$, a = 0.086, b = -0.066. We list the ratio M_p/M_* found using Eq. 7.19 in the last column of Table 7.3.1. We find a standard deviation of 10.1 % in the planet mass. Smaller deviations at smaller planet masses and larger deviations at larger planet masses. The maximum deviation is 21.9 %. When comparing the mass ratios obtained with Eq. 7.19, we generally find a good agreement with the mass ratio used in the hydrodynamic simulations. We find a better agreement for low-mass planets and a worse agreement for high-mass planets when compared to the actual value used in the simulation. This is likely due to the fact that the slope of the fitting function decreases with increasing planet mass (see figure 7.3.4). Hence, small deviations in gap width measurements translate into larger mass deviations in the high-mass range compared to the low-mass range.

simulation	M_p/M_* (hydro)	α (hydro)	T_B (K) (measured)	$\log \Delta$ (measured)	H_B Eq. 7.15	$\log K$ Eq. 7.14	M_p/M_* Eq. 7.19
`m5au1nep`	$5 \cdot 10^{-5}$	$2.1 \cdot 10^{-2}$	14.1	–	0.020	-4.34	–
`m5au1sat`	$3 \cdot 10^{-4}$	$2.1 \cdot 10^{-2}$	20.9	-0.61	0.027	-3.55	$2.99 \cdot 10^{-4}$
`m5au1jup`	$1 \cdot 10^{-3}$	$2.1 \cdot 10^{-2}$	15.2	-0.29	0.024	-3.03	$0.99 \cdot 10^{-3}$
`m5au5jup`	$5 \cdot 10^{-3}$	$2.1 \cdot 10^{-2}$	18.1	-0.20	0.028	-2.32	$3.91 \cdot 10^{-3}$
`m30au1nep`	$5 \cdot 10^{-5}$	$4.4 \cdot 10^{-3}$	5.6	–	0.030	-4.28	–
`m30au1sat`	$3 \cdot 10^{-4}$	$4.4 \cdot 10^{-3}$	5.8	-0.49	0.034	-3.49	$3.02 \cdot 10^{-4}$
`m30au1jup`	$1 \cdot 10^{-3}$	$4.4 \cdot 10^{-3}$	4.4	-0.28	0.031	-2.97	$0.94 \cdot 10^{-3}$
`m30au5jup`	$5 \cdot 10^{-3}$	$4.4 \cdot 10^{-3}$	3.7	-0.18	0.031	-2.28	$5.32 \cdot 10^{-3}$
`m50au1nep`	$5 \cdot 10^{-5}$	$4.5 \cdot 10^{-3}$	5.4	–	0.038	-4.27	–
`m50au1sat`	$3 \cdot 10^{-4}$	$4.5 \cdot 10^{-3}$	6.2	-0.49	0.046	-3.48	$2.96 \cdot 10^{-4}$
`m50au1jup`	$1 \cdot 10^{-3}$	$4.5 \cdot 10^{-3}$	6.6	-0.26	0.052	-2.96	$1.12 \cdot 10^{-3}$
`m50au5jup`	$5 \cdot 10^{-3}$	$4.5 \cdot 10^{-3}$	6.5	-0.17	0.053	-2.25	$5.74 \cdot 10^{-3}$

Table 7.3.1: We present the results of the gap width fitting. The second and third columns list the planet mass and α-turbulence parameter, as found in the hydrodynamic simulations for each model. The fourth column lists the brightness temperature T_B measured at the outer ring (r_{out}) at a wavelength of $870\,\mu m$ in the synthetic observations. The fifth column lists the gap widths $\log \Delta$ as measured in the azimuthally averaged intensity profiles. The sixth column lists, for each model, the parameter H_B which we calculated using Eq. 7.15. The seventh column lists the K parameter computed with Eq. 7.14 with the coefficients A, B, a, and b as found in the fitting procedure. The last column lists the planet masses computed with Eq. 7.19, using the fitting coefficients found in the fitting procedure.

7.3.5 Disk Masses from Synthetic Observations

Accurate accounting of bulk dust masses of protoplanetary disks is essential to understanding planet formation because it is the bulk reservoir of solid material from which terrestrial planets and the cores of giant planets form. There has been some discrepancy because recent observational studies (e.g. Andrews et al., 2013; Cieza et al., 2019; Ansdell et al., 2016) reveal that the total dust mass ($\lesssim$cm sized grains) in Class II disks is low if one wants to explain the typical exoplanet demographics as derived from results of the *Kepler* mission (e.g. Dong & Zhu, 2013). The shortage of solid material could be explained if the dust grains grow to larger sizes before the disk reaches the Class II stage. Larger grains remain hidden in the wavelength domains to which ALMA is sensitive. However, in this work, we focus on another explanation for the potential underestimation of the observed mass of the solid disk components.

Observationally, bulk dust masses are typically obtained by flux density measurements in (sub-)millimeter surveys and using the optically thin approximation (and making assumptions about opacity and temperature) (e.g. Tychoniec et al., 2020). Bulk dust masses can also be used as a proxy for bulk gas masses by assuming a dust-to-gas ratio. This indirect probe of bulk gas mass lends itself to the community because measuring bulk gas masses is difficult due to a lack of direct bulk gas mass tracers (e.g. Bergin & Williams, 2017).

To probe dust masses, dust emissions are typically observed in (sub-)millimeter wavelengths. The observed intensity of optically thin emissions coming from an isothermal region of dust depends on the dust temperature T_d and optical depth τ. The optical depth is in turn dependent on the dust mass M_d present along a line of sight and the opacity κ. As shown in Hildebrand (1983), the total dust mass M_d in an isothermal region can be estimated from optically thin (sub-)millimeter emissions by measuring the flux density F_ν and using the following relation:

$$M_d = \frac{F_\nu d^2}{\kappa_\nu B_\nu(T_d)} \tag{7.20}$$

Here, κ_ν is the dust absorption opacity at the observed frequency ν, B_ν is the Planck function at the dust temperature T_d and d is the distance between the emitting region and the observer. It is generally not easy to determine the opacity κ and temperature T_d of the emitting dust from observations. Hence, this approach of determining dust masses involves some uncertainties. However, we aim to apply this method here to investigate its validity and accuracy. As typically done in the community, we first approximate the dust opacity by a power law,

$$\kappa_\nu = \kappa_0 \left(\frac{\nu}{\nu_0}\right)^\beta \tag{7.21}$$

(e.g. Draine, 2006) and use a simple parametrization as used by, e.g., Beckwith et al. (1990) or Ansdell et al. (2016) with $\kappa_0 = 10\,\frac{\mathrm{cm}^2}{\mathrm{g}}$, $\nu_0 = 1000\,\mathrm{GHz}$ and power-law index $\beta = 1$. Furthermore, we assume a characteristic disk temperature $T_{\mathrm{dust}} = 20$ K as in Ansdell et al. (2016) for all our models. Using Eq. 7.20, we compute the total dust mass M_d from a synthetic image of each of our models. For this, we use synthetic images obtained at a wavelength of $\lambda = 870\ \mu m$ (ALMA band 7). We list the results of this dust mass estimate in Table 7.3.2 column 4. At this wavelength, the dust opacity, computed using Eq. 7.21, is $\kappa_\nu = 3.45\,\mathrm{cm}^2/\mathrm{g}$. For comparison, we list the actual dust mass present in the corresponding hydrodynamic model in the first third column of Table 7.3.2 and label it with $M_{d,\mathrm{hydro}}$. With this method, we recover, on average, 28.7 % of the total dust mass $M_{d,\mathrm{hydro}}$. The fraction is generally larger in models containing a planet at 5.2 au and lower in models at 30 au and 50 au. One obvious reason for the deviation is the fact that the crude assumptions for temperature T_d and opacity κ_ν are not perfectly representative of our models. The opacity used in the radiative transfer step at $\lambda = 870\ \mu m$ is with $\kappa_\nu = 10.2\,\mathrm{cm}^2/\mathrm{g}$ larger than what we assumed here. However, using a smaller opacity would lead to an overestimation of the recovered dust mass.

We compute a characteristic disk temperature $\bar{T}_{\rm dust}$ from the three-dimensional hydrodynamic temperature grid for each model, to assess the validity of the assumption of the characteristic temperature above. We compute $\bar{T}_{\rm dust}$ as a mass-weighted average temperature

$$\bar{T}_{\rm d} = \frac{1}{M_{d,\rm hydro}} \sum_i m_{d,i} T_{d,i} \tag{7.22}$$

where we sum over all the computational cells. Here, $m_{d,i}$ is the dust mass and $T_{d,i}$ is the dust temperature in cell i. As found by Ballering & Eisner (2019), the radial extent of the disk has a large impact on the mass averaged dust temperature $\bar{T}_d$ and we find that smaller disks are significantly warmer than larger disks. The characteristic dust temperatures are listed for each disk model in Table 7.3.2 column 2. Except in `m5au1nep`, the characteristic dust temperatures are larger than 20 K in all the models containing a planet at 5.2 au. In all other cases, the characteristic temperature is smaller as the disk extends farther away from the star. Characteristic temperatures below 20 K counteract the effect of the larger opacity used in our models compared to the initially assumed value of $\kappa_\nu = 3.45\,\rm cm^2/g$.

We repeat the dust mass calculations using the more suitable temperature and opacity values to compare with the crude estimates. We can only do this because we have the advantage over real observations to have perfect knowledge of opacity and temperature in our computational models. The results of this first improvement are listed in Table 7.3.2 column 5. On average, we recover only 30.3 % of the total dust mass with this approach. The fact that we can not significantly increase the recovered dust mass points to a weakness in the applied approach itself, and we point out several difficulties here.

In the Rayleigh-Jeans tail of the Planck function, the sensitivity to changes in temperature increases the closer the peak wavelength is to the observed wavelength. At $T_d = 3.3$ K, the peak of the Planck function is at the observed wavelength $\lambda = 870\ \mu m$. Therefore, characteristic temperatures close to 3.3 K introduce larger uncertainties in Eq. 7.20 than larger temperatures. Consequently, dust mass estimates will be more accurate for disks with larger characteristic temperatures and observations at longer wavelengths. Hence, dust mass estimates with $\bar{T}_{\rm d} \sim 3.3\,K$ rely on a very accurate estimation of the characteristic disk temperature. Generally, it is a difficult task to assign a single characteristic temperature to a disk because disks have diverse temperature profiles. Moreover, the assumption of optically thin emissions is not valid for large regions in the models. At a wavelength of 870 μm, the emission becomes optically thick for surface densities $\Sigma_{\rm d} > 1/\kappa_\nu \sim 0.1\,\rm g/cm^2$. In our initial conditions, this is the case in the inner disk for $r < 64$ au. Emissions at longer wavelengths are more optically thin (e.g. Liu, 2019; Zhu et al., 2019). At a longer wavelength of 1300 μm, where we use $\kappa_\nu = 7.8\,\rm cm^2/g$, the optically thick regions in the inner disk only reach up to $r < 39$ au. As shown in Fig. 7.2.3, the surface density can also increase by a factor of a few in the rings at the edges of the disk gaps when the disks evolve away from their initial condition. Because optically thick emissions are independent of surface density, they can lead to an underestimation of the bulk dust mass. Furthermore, the temperature in large regions of the models is so low that the emission at the observed wavelength is lost in the observational noise. Hence, dust in these regions remains undetected in the synthetic observations which further decreases the recovered dust mass fraction.

We repeat the dust mass measurements at longer wavelengths of $\lambda = 1300\ \mu m$ (ALMA band 6) and $\lambda = 2100\ \mu m$ (ALMA band 4) (using identical estimates for $\bar{T}_{\rm d}$ as before) and list the results in Table 7.3.2 column 6 and 7. Longer wavelengths are more favorable here because, firstly, the Planck function is less sensitive to temperature at longer wavelengths (in the Rayleigh-Jeans tail). Secondly, emission at longer wavelengths are more optically thin and thirdly, the cold outer regions of the disk emit at longer wavelengths. At $\lambda = 1300\ \mu m$ we recover, on average, 30.2 % of the total dust mass and at $\lambda = 2100\ \mu m$ we recover on average 33.7 % of the total dust mass.

In this section, we applied a typical method used in the observational community to measure bulk dust masses by assuming optically thin emission and using Eq. 7.21. This allows us to evaluate the typical assumption of dust opacity and temperature made in previous studies. We showed a significant underestimation of the total dust mass, even under ideal conditions where opacity and dust temperature are well known. The assumption of optically thin emission fails in large fractions of the disk. Moreover, the signal-to-noise ratios in the ALMA bands used here are not large enough to recover dust emissions from cold outer disk regions. Generally, the characteristic disk temperature we find increases with the mass of the planet. This is because a more massive planet stirs up more dust above the midplane which is then illuminated directly by the central star. This also leads to a trend that we recover more dust mass from disks with a low-mass planet. By assuming a constant $T_d = 20$ K for all disks, we recover more dust from the disks containing a planet at a smaller semi-major axis than at a larger semi-major axis. By computing a characteristic dust temperature for every model individually, we see that the disks with a planet at larger radii are generally colder than 20 K and we do not see a significant difference in recovered disk mass for disks with planets at different radii anymore (Ballering & Eisner, 2019). The dust contained in the hidden optically thick regions in the disk can potentially account for the missing dust mass.

Photon scattering can be an additional reason for the underestimation of the total dust mass. It decreases the maximum depth from which photons can escape and can make an optically thick region look optically thin (e.g. Rybicki & Lightman, 1979). The reduction of emission due to scattering is largely ignored in observations but can have an important impact (e.g. Zhu et al., 2019).

simulation	$\bar{T}_{\mathrm{dust}}$ (K)	$M_{d,\mathrm{hydro}}$ ($M_{\oplus}$)	$M_{d,\mathrm{obs.}}$ ($M_{\oplus}$) $\lambda =$ 870 μm	M_d ($M_{\oplus}$) $\lambda =$ 870 μm	M_d ($M_{\oplus}$) $\lambda =$ 1300 μm	M_d ($M_{\oplus}$) $\lambda =$ 2100 μm	$M_d^{\tau<1}$ ($M_{\oplus}$) $\lambda =$ 870 μm	$M_d^{\tau<1}$ ($M_{\oplus}$) $\lambda =$ 1300 μm	$M_d^{\tau<1}$ ($M_{\oplus}$) $\lambda =$ 2100 μm
`m5au1nep`	10.8	4.95	1.33	1.27	1.44	1.72	1.82	2.35	3.21
`m5au1sat`	23.2	4.95	3.57	0.98	1.21	1.53	1.81	2.31	3.12
`m5au1jup`	25.7	4.95	3.66	0.87	1.07	1.35	1.67	2.16	2.86
`m5au5jup`	25.4	4.95	3.14	0.76	0.95	1.22	1.46	1.87	2.43
`m30au1nep`	3.7	68.5	3.39	78.0	50.8	39.0	43.1	50.3	54.9
`m30au1sat`	7.2	68.5	10.9	23.6	23.7	23.9	38.2	44.2	48.4
`m30au1jup`	8.5	68.5	12.7	20.3	21.9	23.2	34.8	41.2	47.6
`m30au5jup`	15.5	68.5	4.21	2.13	3.3	9.33	32.1	38.1	45.0
`m50au1nep`	5.1	147	8.17	57.7	51.5	53.1	94.9	113	128
`m50au1sat`	8.5	147	15.2	27.0	35.7	45.0	76.8	88.9	100
`m50au1jup`	9.5	147	29.2	38.5	50.8	65.6	72.3	85.0	102
`m50au5jup`	12.8	147	39.3	31.5	43.0	53.5	70.2	84.7	102

Table 7.3.2: This table gives total dust masses in the disks obtained from our synthetic observations using Eq. 7.20. The second column lists mass-weighted average temperatures of the three-dimensional temperature field from RADMC-3D's mctherm. The third column lists the total dust mass present in the hydrodynamic models. These are the reference values that we want to retrieve. The fourth column lists dust masses retrieved at 870 μm using Eq. 7.20, identical dust temperature for all the models of $T_{\mathrm{dust}} = 20$ K and dust opacity $\kappa_\nu = 3.45$ cm^2/g. Columns 5 to 7 contain total dust masses retrieved from using mass the weighted temperatures as listed in column 2 and opacities as used in the radiative transfer. In the models containing a planet at 5.2 au, we used antenna configuration C43-10, for the other models we used antenna configuration C43-7. The last three columns contain the total dust mass above the $\tau = 1$-surface, i.e., the optically thin dust mass, at different wavelengths, computed using the hydrodynamic dust density fields and the opacities as used in the radiative transfer.

7.3.6 Optically Thin Dust and $\tau = 1$-Surfaces

In this section, we further explore the validity of the optically thin approximation and quantify the mass fraction of optically thin emitting dust. In Fig. 7.3.2, we show a vertical cut of the dust volume density at the location of the planet ($\phi = 0$) for each of our 12 hydrodynamical models. Overplotted are the contours $z_1(r)$ of the surfaces where the optical depth equals unity ($\tau = 1$) when integrated along the z-axis from z = $+\infty$ for three different wavelengths (350 μm , 870 μm , 2100 μm), i.e.:

$$\tau = \kappa_\nu \int_{\infty}^{z_1} \rho_d dz \tag{7.23}$$

All the areas below the contours are optically thick regions and hidden in face-on observations at the corresponding wavelengths.

We computed the azimuthally averaged height z_1 of the $\tau = 1$-surface at every radius and used it to compute the total dust mass which is optically thin$M_d^{\tau<1}$. The results at different wavelengths are listed in columns 8 to 10 of Table 7.3.2. Assuming perfect knowledge of the emission F_ν and temperature T_d, we would be able to also obtain these values using Eq. 7.20 as done in the previous section. Similar to the previous section, the total optically thin dust mass is larger at longer wavelengths and large radii because the dust is less optically thick at longer wavelengths and larger radii.

Even at longer wavelengths, a large mass fraction of the disk remains optically thick in all the models. Dust in optically thick layers of the disk remains hidden and cannot be recovered when doing bulk mass estimates using the optically thin assumption. The optically thin disk regions are mainly the gap regions and the outermost disk regions where the dust density has decreased due to radial inward drift.

7.4 Discussion

7.4.1 Dust Temperature

The method with which we compute the gas temperature is different from the method with which we compute the dust temperature. We compute the gas temperature self consistently during the radiative hydrodynamics simulations based on local cooling and heating. The dust temperature, on the other hand, we compute with RADMC-3D's `mctherm` in a post-processing step. The resulting mass-weighted averaged dust temperatures are are 25 % larger in the disks containing a planet at 50 au, 40 % lower in the disks containing a planet at 30 au and 41 % lower in the disks containing a planet at 5.2 au. To investigate the validity of our approach, we ran supplementary computations with RADMC-3D's `mctherm` and `image` tasks. In these test runs, we added a second dust species consisting of small (1 μm sized) dust particles. We assumed them to be well mixed with the gas with a local density $\rho_{\text{small}} = 10^{-4}\rho_g$, i.e., the global mass ratio between the small and the 1 mm-sized grains is 0.01. For the small grains, we computed an additional opacity table using Mie theory and the BHMIE code. In this two-species setup, the upper disk layers are mainly filled with a small amount of μm-sized particles while the midplane is dominated by the larger mm-sized grains as is expected in real disks. The resulting dust temperature distribution of the mm-sized grains computed with the `mctherm` task using this setup was similar to the one-species setup. However, the midplane dust temperature was marginally larger due to more indirect radiation coming from the upper disk layers where the small grains are. Even though this approach probably represents a more realistic disk, it did not have any major effect on our results presented in this chapter.

7.4.2 Caveats

There are some caveats regarding the assumptions used in our models. Firstly, we investigate the observable disk features after 200 planetary orbits. i.e., a snapshot in time, we do not follow a longer disk evolution. Dust-included simulations are continuously evolving, it is well known that they could never reach steady-state, due to the nature of the dust-gas interaction. Therefore, the disk sub-structures, and especially the gap widths, somewhat change with time as mentioned in Sec. 7.3.1. Hence, the time of observation has a crucial impact on the resulting observed gap width. However, we usually only know little about the time when planets formed in disks. Zhang et al. (2018) have done some analytical estimates on how the gap width changes with time. They estimate that for marginally coupled dust particles ($St \gtrsim 10^{-2}$), the gap width is proportional to $St \times t$. This means that particles will drift twice farther over twice the amount of time. A detailed study that includes the change of the gap width over time is necessary to fully investigate this behavior.

Secondly, we only include one dust fluid in our simulations which represents 1 mm-sized dust. Also, it should be stressed that the empirical fit, found in Sec. 7.3.4, was derived based on only one dust fluid. This limitation is due to the enormous computational time needed for multi-fluid simulations of a global disk perturbed by a planet in three dimensions. Of course, in reality, the dust consists of a distribution of grain sizes. Dust-continuum observations at a given wavelength are most sensitive to emissions of a single particle size. However, larger and smaller sizes also contribute (see e.g. Draine, 2006). The populations of larger/smaller particles are more weakly/strongly coupled to the gas which will result in a different spatial distribution in the disk. Hence, we expect slightly different intensity distributions (e.g. Drążkowska et al., 2019). Including additional dust particle sizes is planned for future studies when computers will be able to handle such heavy computations in 3D.

Thirdly, we do not include turbulent diffusion in the dust. In the vertical direction, dust turbulent diffusion is responsible for the mixing of dust particles and can counterbalance vertical settling toward the midplane (Dubrulle et al., 1995). However, in this study, we focus on vertical mixing by a planet. An estimate of the scale height of dust grains, when turbulent diffusion is included, is given by Youdin & Lithwick, 2007:

$$h_d \approx h_g \sqrt{\frac{\alpha}{\alpha + St}\left(\frac{1+St}{1+2St}\right)}. \tag{7.24}$$

where the Stokes number St is typically evaluated at the midplane. In our simulations, before inserting the planet, the dust scale height calculated with Eq. 7.24 is $\sim 0.29\, h_g$ at 50 au which is ~2.0 times the vertical height of one grid cell. At 30 au $\sim 0.39\, h_g$ (~2.4 grid cells) and at 5.2 au it is $\sim 0.80\, h_g$ (~3.8 grid cells). The vertical extent of intermediately coupled grains ($St < 1$) is typically not Gaussian but follows a flatter distribution with a sharp cut-off due to the grains decoupling in the low gas density regions above the midplane (e.g. Fromang & Nelson, 2009). This is because grains tend to decouple in the low gas density regions and vertical downward settling becomes dominant over vertical upward diffusion. Hence, we expect only very few dust grains above h_d without additional stirring by a planet. Therefore, we expect dust which is stirred up significantly above h_d by a planet, to be only marginally affected by vertical diffusion because its dynamics is dominated by planetary stirring and vertical settling.

The finite thickness of the midplane in the vertical dust distribution in our simulations due to the finite size of the vertical grid spacing, is a crude representation of a flat distribution with a sharp cutoff. However, as stated above, it is a factor 2 to 4 thinner than when including dust turbulent diffusion.

We measured the ratio h_d/h_g in our simulations by fitting a Gaussian profile to the vertical density profiles and found that Jupiter-mass planets and 5 Jupiter-mass planets, at all orbital distances, are able to locally increase h_d/h_g to values larger than what is expected from Eq. 7.24

i.e., by turbulent diffusion only. We expect this to also be possible for Saturn-mass planets (and possibly below) if the magnitude of turbulent diffusion is decreased. In the case of the 5 Jupiter-mass planets, the peak value h_d/h_g is on average 0.75. In the case of the Jupiter-mass planets, it is 0.84 and in the case of Saturn-mass planets, it is 0.23. In the case of Neptune-mass planets, the vertical scale height is smaller than what we can resolve.

Studying the effects of dust turbulent diffusion will be a follow-up study to this project. Besides its influence on the vertical distribution, we expect dust turbulent diffusion to also affect the dust surface density distribution in a way that it smears out small-scale features, with a possible impact on gap width measurements. We ran an additional simulation identical to `m30au1jup` but with dust turbulent diffusion included as described in Appendix A of Weber et al. (2019). There, we found a difference in gap width Δ between the cases with and without dust turbulent diffusion of 7 %.

Furthermore, in our setup, there is no thermal coupling between dust and gas. The temperature of the gas as determined in the radiative hydrodynamics simulations is independent of the dust temperature determined with the Monte Carlo approach. Thermal coupling is generally strongest in regions where the gas density is large, and the dust temperature is low, which is most likely the case in the midplane of the disk (e.g. Armitage, 2010; Vorobyov et al., 2020).

Moreover, in our hydrodynamical simulations, there were no magnetic fields included. This could also heavily alter the dust and gas distributions.

We do not consider planetary migration in our simulations, even though gap-opening planets can undergo type II migration. However, the migration timescales of type II migration are on the order of the viscous timescale Dürmann & Kley (2015). As pointed out in Sec. 7.3.1, the viscous timescale across the length scale of a gap is considerably larger than the duration of our simulations. Hence, we do not expect type II migration to play a role. The Neptune-mass planets in our models can undergo type I migration because they perturb the gas disk only a little and do not open a gap in gas. However, the type I migration timescale of a Neptune-mass planet is on the order of 100 times longer than the simulation time considered here Tanaka et al. (2002). Therefore, we also expect type I migration to not change our results. A potentially relevant effect is the rapid type III runaway migration (Masset & Papaloizou, 2003). This type of planetary migration is especially relevant for the Saturn-mass planets in our models, which are in the transition region between type I and type II migration. Masset & Papaloizou (2003) found that for a disk with an aspect ratio of 0.05, which is approximately the case for our disk at 50 au, and kinematic viscosity identical to our value at 50 au, a Saturn-mass planet undergoes type III migration if the Toomre Q is below a value of ~ 10. At 50 au, we find $Q \sim 5$. Hence, the Saturn-mass planet at 50 au can potentially undergo type III migration. At 30 au, the Toomre Q is larger, but at the same time, the aspect ratio is smaller. We expect type III migration to be less likely for the Saturn-mass planet at 30 au. The Jupiter-mass planet at 50 au is close to the transition region between type III and type II migration. If a planet indeed undergoes type III migration, Masset & Papaloizou (2003) find different migration behavior depending on the slope of the gas surface density. For shallow profiles, as in our case, they find a 50 % increase of the planet's semi-major axis, i.e., outward migration, within 50 orbital periods. This is much shorter than the duration of our simulations.. Hence, we expect rapid type III migration to affect the gap structure in the disk and should be taken into account in future studies.

7.5 Conclusions

Using three-dimensional two-fluid hydrodynamic simulations of protoplanetary disks with an embedded planet, we investigate observable planetary features in synthetic (sub-)mm-continuum ALMA images of the disks. We choose the grain size to be 1 mm within the hydrodynamic simulations. The feedback of the dust onto the gas is included in our simulations. We specifically investigate the gap widths caused by planets of different masses (Neptune-, Saturn-, Jupiter, 5 Jupiter-mass) at different orbital distances to the central star (5.2 au, 30 au, 50 au). We summarize our results in the following points.

- Except for the Neptune mass planets, the planets in our disk model open an annular gap at their orbital radius in both the dust and the mm-sized dust. The Neptune mass-planet cannot disturb the gas enough to open a gap in the gas. In the dust, the Neptune-mass planets barely open a gap.

- The temporal evolution of the surface density profile in the dust is distinctly different from the surface density profile in gas. Whereas gap widths in both gas and dust steadily increase with time, the depth of the gap steadily increases with time only in the gas. The depth of the gap in dust can also decrease again with time after an initial increase in depth.

- The planets cause significant vertical stirring of the dust which opposes the vertical settling. This creates thicker dust disks than in disks without a planet. The amount of vertical stirring depends on the mass and orbital radius of the planet. Large dust particles in the upper layers of the disk potentially have observational consequences. We examine this effect further in Chapter 8.

- We find multiple rings in the synthetic ALMA images which are caused by dust concentrations at the edges of the planetary gaps.

- We examined the relationship between the gap width as observed in ALMA images and the planet mass. We fitted the results and created equations between the planetary mass and the ALMA gap width, based on the planetary orbital radius, the disk turbulence, and disk temperature. This relation can be used to constrain the planetary mass in future ALMA observations of gaps in protoplanetary disks.

- We derived the disk mass from the hydrodynamical simulations and from the ALMA mock images created from the same simulations (Table 7.3.2). We found a significant difference between the disk masses in the two cases: Using the usual disk mass formula with an optically thin dust emission assumption greatly underestimates the disk mass. The discrepancy of a factor of a few highlights that protoplanetary disks might be several (up to 10) times more massive than previously thought. This has a strong consequence on planet formation, and disk processes, including chemistry. Further, we found that the derived disk masses were generally larger in disks containing a low-mass planet, regardless of the orbital distance between the star and the planet.

Chapter 8

Three-Dimensional Dust Stirring by a Giant Planet Embedded in a Protoplanetary Disk

The content of this chapter was published in:

Binkert F., Szulágyi, J., Birnstiel, T. (2023), *Three-dimensional dust stirring by a giant planet embedded in a protoplanetary disk, Monthly Notices of the Royal Astronomical Society, Volume 523, Issue 1, Pages 55-79*

Abstract

The motion of solid particles embedded in gaseous protoplanetary disks is influenced by turbulent fluctuations. Consequently, the dynamics of moderately to weakly coupled solids can be distinctly different from the dynamics of the gas. Additionally, gravitational perturbations from an embedded planet can further impact the dynamics of solids. In this work, we investigate the combined effects of turbulent fluctuations and planetary dust stirring in a protoplanetary disk on three-dimensional dust morphology and on synthetic ALMA continuum observations. We carry out three-dimensional radiative two-fluid (gas+1-mm-dust) hydrodynamic simulations in which we explicitly model the gravitational perturbation of a Jupiter-mass planet. We use a new momentum-conserving turbulent transport model that introduces a turbulent pressure to the pressureless dust fluid to capture the turbulent transport of dust. The model implicitly captures the effects of orbital oscillations and reproduces the theoretically predicted vertical settling-diffusion equilibrium. We find a Jupiter-mass planet to produce distinct and large-scale three-dimensional flow structures in the mm-size dust, which vary strongly in space. We quantify these effects by locally measuring an effective vertical diffusivity (equivalent alpha) and find azimuthally averaged values in a range $\delta_{\text{eff}} \sim 5 \cdot 10^{-3} - 2 \cdot 10^{-2}$ and local peaks at values of up to $\delta_{\text{eff}} \sim 3 \cdot 10^{-1}$. In synthetic ALMA continuum observations of inclined disks, we find effects of turbulent transport to be observable, especially at disk edges, and effects of planetary dust stirring in edge-on observations.

8.1 Introduction

Protoplanetary disks consist of only one percent dust by mass. Even though the other 99 percent is gas, it is the small solid component in protoplanetary disks from which all rocky objects, such as rocky planets, form. Advanced radio interferometers, such as the Atacama Large Millimeter/submillimeter Array (ALMA), are capable of detecting and resolving the faint thermal emission of cold dust in protoplanetary disks. This provides direct insight into the earliest phase of planet formation. Continuum observations of protoplanetary disks with ALMA have revealed numerous substructures, such as gaps, rings, and asymmetries (see, e.g., the review by Andrews, 2020). Numerical studies predict a planet (or multiple planets) to be capable of producing many of the observed disk features via its gravitational interaction with the surrounding protoplanetary disk (e.g., Wolf & D'Angelo, 2005; Gonzalez et al., 2012; Perez et al., 2015; Dong et al., 2015b,a; Szulágyi et al., 2018, 2019; Weber et al., 2019). However, despite significant efforts, only a few observed disk substructures have been successfully linked to the presence of a planet (e.g., PDS 70b/c, Keppler et al., 2018; Isella et al., 2019; Haffert et al., 2019; Christiaens et al., 2019).

Most theoretical and observational studies on disk substructures have focused on radial structures, favoring low-inclination disks because the radial structure is more readily observable (e.g., ALMA Partnership et al., 2015; Pinte et al., 2016; Jin et al., 2016; Dong et al., 2017; Szulágyi et al., 2018; Dullemond et al., 2018; Ricci et al., 2018; Zhang et al., 2018; Andrews et al., 2018b; Dipierro et al., 2018; Wafflard-Fernandez & Baruteau, 2020). Even though, it is difficult to constrain the vertical extent of the millimeter continuum emission in low-inclination disks due to their geometrically thin shape, the study of the vertical structure of more inclined and/or edge-on disks offers additional opportunities to constrain disk properties.

The vertical extent of millimeter-sized dust grains, which are mainly probed with (sub-)millimeter continuum observations, is set by a balance of vertical settling and mixing. While small, micron-sized, dust grains are aerodynamically tightly coupled to their gaseous environment, the larger dust grains tend to decouple from the gas and settle towards the disk midplane, forming a geometrically thin midplane layer. However, these larger dust grains are still somewhat coupled to their environment and react to fluctuations in the gas. Thus, turbulent flows have the potential to counteract the vertical settling of moderately coupled dust grains, setting the vertical extent of the dust disk. Even though protoplanetary disks are generally found to be turbulent (e.g., Hughes et al., 2011; Guilloteau et al., 2012; Pinte et al., 2016; Teague et al., 2016; Dullemond et al., 2018), the driving mechanism of the turbulence is not yet fully understood despite the study of promising candidates such as the magneto-rotational instability (e.g., Flock et al., 2015) or purely hydrodynamic mechanisms such as the vertical shear instability (VSI) (e.g., Urpin, 2003; Nelson et al., 2013; Stoll & Kley, 2014; Schäfer et al., 2020). In addition to disk turbulence, it has been shown that a planet, embedded in a protoplanetary disk, can be an additional source of dust mixing (Binkert et al., 2021; Bi et al., 2021).

Due to the lack of full understanding regarding the origin of turbulence, the underlying driving mechanisms are often disregarded when studying the dynamics of gas in protoplanetary disks using hydrodynamical simulations. Instead, the net effects of the unspecified turbulence on gas are parametrized with an effective turbulent viscosity (Shakura & Sunyaev, 1973; Lynden-Bell & Pringle, 1974). On the other hand, the net effects of turbulent flows on dust have successfully been modeled by using a gradient-diffusion hypothesis, which models the turbulent mixing of dust grains in a turbulent environment (Cuzzi et al., 1993; Youdin & Lithwick, 2007; Carballido et al., 2006, 2010; Zhu et al., 2015). The subsequent comparison between such hydrodynamical models and the observed radial structure and/or the vertical extent of a protoplanetary disk allows for the constraint of the effective viscosity and/or diffusivity in the observed disks (e.g., Pinte et al., 2016; Villenave et al., 2022).

Motivated by such comparisons, we build upon the results of Binkert et al. (2021); Szulágyi et al. (2022), in which we studied observational disk features caused by a planet, using radiative hydrodynamic two-fluid simulations (gas + millimeter-size dust). For the current work, we expand the dust module of the Jupiter code (Szulágyi et al., 2014) by treating turbulent transport as a pseudo pressure in the otherwise pressureless dust fluid, as discussed in Chapter 5. Consequently, our approach ensures the conservation of angular and linear momentum in our simulations, a property that gradient diffusion approaches lack (Tominaga et al., 2019) and is crucial to correctly capture the dynamics of dust and gas within a protoplanetary disk. In the following work, we study the combined effects of turbulent mixing (parametrized by a diffusivity) and planetary mixing of millimeter-sized dust, on the global, three-dimensional dust distribution within a protoplanetary disk. Additionally, we study how turbulent stirring and planetary stirring affect the observed millimeter-continuum flux in synthetic ALMA observations of face-on and inclined disks.

The outline of this chapter is as follows. In Sec. 8.2, we describe the dynamical equations that govern dust, gas, and radiation in our hydrodynamic models. We also describe how we create synthetic ALMA continuum observations from these models. In Sec. 8.3, we present our results and in Sec. 8.4, we discuss and summarize our results.

8.2 Method

We run global three-dimensional radiative two-fluid (gas+mm-sized dust) hydrodynamic simulations of protoplanetary disks with an embedded planet, to investigate the effect of planetary stirring on the three-dimensional dust morphology in the presence of turbulent transport. Further, we employ radiative transfer calculations to turn the hydrodynamic simulations into synthetic continuum intensity maps, from which we generate synthetic ALMA observations to study observational signatures of planetary stirring and/or background turbulence. This section is structured as follows. We introduce the physical models of dust and turbulent transport in Sec. 8.2.1, and the hydrodynamic model of the gas and the radiation component in Sec. 8.2.2. In Sec. 8.2.3, we describe our simulation procedure and the numerical details. Sections 8.2.4 and 8.2.5 describe the post-processing steps. Namely, the radiative transfer calculations and the subsequent generation of synthetic ALMA continuum observations, respectively.

8.2.1 Dust and Turbulent Transport Model

Turbulent gas in protoplanetary disks contains a wide range of excited length scales, down to the molecular level. Dust grains embedded in these turbulent environments are aerodynamically coupled to the gas motion and, depending on their properties can be excited on a similar range of lengths scales. Thus, capturing the entire dynamics of the dust-gas interactions in numerical hydrodynamic simulations would require spatial resolution down to the molecular dissipation scale of turbulence. However, this is, with today's computational resources, not possible in global hydrodynamical simulations of protoplanetary disks, and, the smallest dynamical scales remain unresolved. As a workaround, gradient diffusion models are generally adopted to model the effects of unresolved small-scale gas motions on resolved large-scale dust flows (Cuzzi et al., 1993; Fan & Chao, 1998).

The gaseous component is generally modeled as a viscous fluid for which diffusive processes of unresolved turbulence are parametrized with an effective turbulent viscosity coefficient ν. Both the diffusion coefficient in the dust D and ν have the same dimensionality and are related via the dimensionless (hydrodynamic) Schmidt number Sc (Cuzzi et al., 1993):

$$Sc = \frac{\nu}{D} \tag{8.1}$$

Note, the hydrodynamic Schmidt number in this chapter is not identical to the Schmidt number in Chapter 5 and defined in Eq. 5.14. The latter relates the diffusivity of the dust to the diffusivity of the gas (and not the viscosity). See Sec. 5.2.2 for a more detailed discussion.

In Chapter 5 we derived a general turbulent transport model that we will now apply in this chapter. Specifically, we use the large grain limit described by the mass conservation equation

$$\frac{\partial \rho_d}{\partial t} + \nabla \cdot (\rho_d \mathbf{v}) = 0 \tag{5.57}$$

where we have removed the tilde above the velocity for ease of notation in this chapter. Note, the velocity should still be regarded as being Favre-averaged. The momentum equation reads:

$$\frac{\partial}{\partial t}(\rho_d \mathbf{v}) + \nabla \cdot \left(\rho_d \, \mathbf{v} \otimes \mathbf{v} + \frac{1}{3}\rho_d c_d^2 \mathbb{1}\right) = -\rho_d \nabla \Phi - \frac{\rho_d}{t_s}(\mathbf{v} - \mathbf{u}) + \frac{\rho_d}{\rho_g}\nabla\Big(\rho_g c_d^2\Big) \tag{8.2}$$

Here the *turbulent speed* c_d is defined as

$$c_d^2 = \frac{D}{t_s} \tag{8.3}$$

Equation 8.2 is identical to Eq. 5.99 except that the turbulent speed c_d^2 appears inside the spatial derivative on the r.h.s. of Eq. 8.2. This is to ensure that Eq. 8.2 fulfills the vertical equilibrium profile (Eq. 5.24) also for $St \ll 1$. We refer to Binkert et al. (2023) for a heuristic derivation of Eq. 8.2.

8.2.2 Gas and Radiation Model

The radiative gas model in this study is identical to the one used in Szulágyi et al. (2016), Binkert et al. (2021), and Chapter 7. Particularly, we model the gas with an adiabatic equation of state and a radiative transfer module to account for heating (adiabatic heating, viscous heating, stellar irradiation) and cooling (adiabatic cooling, radiative cooling). The mass- and momenta equations in conservation form are:

$$\frac{\partial \rho_g}{\partial t} + \nabla \cdot (\rho_g \mathbf{u}) = 0 \tag{8.4}$$

$$\frac{\partial}{\partial t}(\rho_g \mathbf{u}) + \nabla \cdot \left(\rho_g \, \mathbf{u} \otimes \mathbf{u} + \frac{1}{3}p_g \mathbb{1}\right) = -\rho_g \nabla \Phi + \nabla \cdot \bar{\bar{R}} - \frac{\rho_d}{t_s}(\mathbf{u} - \mathbf{v}) - \frac{\rho_d}{\rho_g}\nabla\Big(\rho_g c_d^2\Big) \tag{8.5}$$

Here, ρ_g is the volume density of the gas, and $\mathbf{u}$ is its velocity vector. The gas pressure p_g is coupled to the internal energy of the gas ϵ via the adiabatic equation of state:

$$p_g = (\gamma - 1)\epsilon \tag{8.6}$$

where $\gamma = 1.43$ is the adiabatic index. The first term on the r.h.s. of the momentum Eq. 8.5 accounts for the change in momentum due to gravitational acceleration. The third term accounts for the momentum exchange with the dust, i.e., the back reaction, due to aerodynamic drag. Compared to the equation without dust turbulent dust transport in Chapter 7, it contains an additional term on the r.h.s. to account for the drag interaction on the turbulent transport flux. The source term exactly cancels with the corresponding source term in the dust momentum equation, which ensures the conservation of momentum in the full system (gas+dust). It also becomes apparent that turbulent transport, like the explicit drag, in this formulation, has a back reaction from the dust onto the gas. The second term on the r.h.s. of the momentum equation contains the Reynolds stress tensor $\bar{\bar{R}}$, which is set equal to the viscous stress tensor as defined in Eq. 5.83.

The third conservation equation that we solve is the energy equation that governs the evolution of the total energy (internal and kinetic energy). We assume the thermal internal energy of the dust fluid to be zero at all times, thus, the energy equation describes the total energy of the gas

(E) only:

$$\frac{\partial E}{\partial t} + \nabla \cdot \left(\left(p_g \mathbb{1} - \bar{\bar{R}} \right) \cdot \mathbf{u} + E\mathbf{u} \right) = -\rho_g \mathbf{u} \cdot \nabla \Phi + S - \rho_g \kappa_P \big(B(T) - c\epsilon_{\rm rad} \big) \tag{8.7}$$

In addition to the term that accounts for the advection of the total energy E, the l.h.s. of Eq. 8.7 also includes terms that contain the pressure p_g and the stress tensor $\bar{\bar{R}}$. These terms describe the effects of adiabatic heating or cooling, and viscous heating. The first term on the r.h.s. of Eq. 8.7 accounts for the work done by gravity, and the second term (S) is the contribution from stellar heating. The last term on the r.h.s. of Eq. 8.7 accounts for radiative heating/cooling, where $B(T)$ describes the total emitted power of a blackbody at temperature T, κ_P is the Planck opacity, and c the speed of light. There is radiative cooling if the gas radiates more energy than it receives from the surrounding radiation field ($B(T) > c\epsilon_{\rm rad}$). The gas is radiatively heated if it receives more energy from the radiation field than it emits ($B(T) < c\epsilon_{\rm rad}$). The gas is in local thermodynamic equilibrium if the two terms balance each other, i.e., $B(T) = c\epsilon_{\rm rad}$ (assuming no other heating/cooling mechanisms are active). A fourth partial differential equation (PDE) describes the rate of change of the radiative energy density $\epsilon_{\rm rad}$:

$$\frac{\partial \epsilon_{\rm rad}}{\partial t} = -\nabla \cdot \mathbf{F}_{\rm rad} + \rho_g \kappa_P \big(B(T) - c\epsilon_{\rm rad} \big) \tag{8.8}$$

where the second term on the r.h.s. of Eq. 8.8 is identical to the third term of Eq. 8.7 and accounts for the contribution to the radiative energy from thermal emission and/or absorption of the gas. The first term on the r.h.s. of Eq. 8.8 contains the radiative flux $\mathbf{F}_{\rm rad}$, which we find using the flux-limited diffusion approximation (see e.g. Szulágyi et al., 2016). Specifically, the radiative flux can be expressed as

$$\mathbf{F}_{\rm rad} = -\frac{c\lambda}{\rho \kappa_R} \nabla \epsilon_{\rm rad} \tag{8.9}$$

where λ is the flux limiter of Kley (1989), and κ_R is the Rosseland mean opacity. The latter is a weighted average over frequency, defined as

$$\kappa_R(T, \rho_g)^{-1} = \frac{\int \kappa_\nu^{-1}(T, \rho_g) \frac{\partial B_\nu(T)}{\partial T} \mathrm{d}\nu}{\int \frac{\partial B_\nu(T)}{\partial T} \mathrm{d}\nu} \tag{8.10}$$

where κ_ν is the frequency dependent absorption opacity. More details about the opacities used here are given in Sec. 8.2.3.
Ultimately, we calculate the gas temperature T_g self-consistently with

$$T_g = (\gamma - 1) \frac{m_\mu \epsilon}{k_B \rho_g}. \tag{8.11}$$

We do not calculate the dust temperature during the hydrodynamic simulations because the thermal internal energy of the dust is assumed zero and consequently the dust temperature does not impact the dynamics of the dust fluid. The presence of the dust only implicitly affects the gas temperature via the opacity. Ultimately, the total system of coupled equations to solve for the gas and radiation components are Eqs. 8.4, 8.5, 8.7 and 8.8 which are in turn coupled to the dust Eq. 5.57 and Eq. 8.2 via the aerodynamic drag and turbulent transport terms. It is important to highlight that, in contrast to the dust fluid, we have not introduced a turbulent pressure term to the gas momentum Eq. 8.5, nor to the energy Eq. 8.7 under the assumption that the term is small compared to the thermal pressure p_g.

8.2.3 Hydrodynamic Simulations

As this work is a continuation of Chapter 7, we base the set of hydrodynamic simulations carried out in this chapter, on the set used in Chapter 7 and use identical setups and parameters but with the addition of turbulent transport. In particular, we run three-dimensional radiative two-fluid (gas+dust) hydrodynamic simulations of protoplanetary disks with an embedded planet. The simulations are carried out with the grid-based code JUPITER (Szulágyi et al., 2016) which solves the radiation and gas hydrodynamic equations, summarized in Sec. 8.2.2, and are fully described in Szulágyi et al. (2016). We modified the dust-solver of the JUPITER code, introduced in Binkert et al. (2021) and Chapter 7, to include the effects of turbulent transport on the dust fluid as described in Sec. 8.2.1. As a result, we model the effects of subgrid turbulence on the dust via a dynamical diffusion pressure that ensures the conservation of angular and linear momentum in the system.

In our simulations, we fix the dust grain size at $a = 1$ mm throughout this entire work. As a result, the Stokes number, i.e., the degree of dust-gas coupling, freely changes depending on the local hydrodynamic conditions.

Further, we set the Planck opacity equal to the Rosseland mean opacity $\kappa_P = \kappa_R$ in favor of a shorter computational time. The difference between the two opacities is not large, and thus our results are not affected by this approximation (Semenov et al., 2003; Bitsch et al., 2013). Henceforth, we drop the subscript R and only consider the frequency averaged gas opacity $\kappa(T, \rho_g)$ that is a function of the local gas density and temperature.

At temperatures below 1500 K, we assume dust to be the dominant contributor to the opacity, which is a valid approximation in the wavelength regime relevant for hydrodynamic heating and cooling. Further, we assume the gas to be thermally coupled to the dust. Based on these two assumptions, we calculate the frequency-dependent opacity κ_ν of three dust compounds (silicate, water ice, carbonaceous material) self-consistently with a version of the BHMIE code of Bohren & Huffman (1984). We then calculate a mass-weighted average of the individual Rosseland mean opacities for a combined dust composition of 40 percent silicates, 40 percent water ice, and 20 percent carbonaceous material (Zubko et al., 1996; Draine, 2003; Warren & Brandt, 2008), and a dust-to-gas ratio of $\rho_d/\rho_g = 0.01$.

Above, 1500 K, the opacity κ includes gas opacities from Bell & Lin (1994). In detail, the implemented opacity table accounts for the sublimation of water ice (170 K), carbonaceous material (1500 K), and silicate (2000 K) respectively. Above 2000 K, only gas opacities contribute. We refer to Szulágyi et al. (2019) for more details on the construction of the opacity table.

In our two-fluid setup, we modify the frequency averaged opacity $\kappa(T, \rho_g)$ compared to the one-fluid setup in Szulágyi et al. (2018), such that for $T < 1500$ K, it also includes the local dust density ρ_d. The two-fluid opacity $\kappa_{2\mathrm{f}}$ that we ultimately implemented is calculated as:

$$\kappa_{2\mathrm{f}}(T, \rho_g, \rho_d) = \kappa(T, 0.01\rho_g + 99\rho_d) \tag{8.12}$$

Note that for a local dust-to-gas ratio of 0.01, the two opacities are identical $\kappa_{2\mathrm{f}} = \kappa$.

As a result of the above definition (Eq. 8.12), the dust-to-gas ratio is not fixed at one percent, and regions with a large dust-to-gas ratio are more optically thick in our radiative simulations, while regions with a small dust-to-gas ratio are more optically thin.

In computational cells which are directly irradiated by stellar irradiation, i.e., cells in the disk surface, the opacity should not depend on the local gas temperature but on the temperature of the star T_*. We thus set the opacity in these cells to a constant value of $\kappa = 3.5\,\mathrm{cm}^2/\mathrm{g}$ which is consistent with $T_* = 5780$ K, i.e., a sun-like star (Bitsch et al., 2014).

Our model disk has a gas radial surface density profile Σ_g which follows a power law of the form

$$\Sigma_g(r) = 80\,\mathrm{g/cm}^2 \cdot \left(\frac{r}{1\,\mathrm{au}}\right)^{-1/2} \tag{8.13}$$

Initially, the dust follows an identical surface density profile but is scaled by a factor 0.01. Like in Binkert et al. (2021) and Chapter 7, the surface density profile corresponds to a total dust mass of $\sim 5 \cdot 10^{-4}\, M_{\odot}$ within 120 au, which is comparable to the most massive disks in the ALMA survey of Ansdell et al. (2016). In our models, the mm-sized particles experience Stokes numbers in the range $9 \cdot 10^{-3} < St < 7 \cdot 10^{-2}$ in the disk midplane (before the insertion of the planet).

Throughout our simulations, we keep the value of the kinematic viscosity constant at a value which corresponds to $\nu = 10^{-5} r_0^2 \Omega_0$ at a reference radius of $r_0 = 50$ au. This value corresponds to a Shakura & Sunyaev α-parameter of $\alpha = 4.0 \cdot 10^{-3}$ at $r = 50$ au, assuming a vertically isothermal disk with an aspect ratio of $H = 0.05$. We purposely set the viscosity at this relatively large value to isolate the effects of planetary stirring and suppress other sources of resolved hydrodynamic turbulence coming from, e.g., Rossby vortices at gap edges (Zhu et al., 2014) or the VSI (Flock et al., 2017; Lin, 2019), which, unavoidably, would impact our simulations at lower prescribed viscosity. Therefore, when studying the impact of different strengths of turbulent transport, we solely change the diffusion coefficient D and keep the gas viscosity ν constant to isolate the influence of turbulent transport. Throughout this work, we describe the ratio of the used parameters ν and D with the dimensionless Schmidt number Sc as defined in Eq. 8.1. However, we stress that in reality, it is the underlying turbulent viscosity that changes and governs the strength of turbulent transport and that the Schmidt is expected to always be on the order of unity (Cuzzi et al., 1993).

Like in Binkert et al. (2021) and Chapter 7, we assume the central star in our simulations to emit a blackbody spectrum with a solar effective temperature $T_{\text{eff}} = 5780\, K$ and have a mass and radius equal to the solar mass and solar radius, respectively ($M_* = M_{\odot}$, $R_* = R_{\odot}$). We solve the hydrodynamic equations in spherical coordinates in a rotating frame of reference. Because we are interested in the vertical disk structure, we mainly focus on the radially most extended disk domain presented in Binkert et al. (2021) and Chapter 7 where the vertical extent of the disk is the largest. This domain covers the radial domain between 20 au and 119 au from the central star, with a planet orbiting on a circular orbit with a fixed radius at $r_p = 50$ au. In azimuthal direction, we simulate the full 2π disk, while in polar direction, we assume mirror symmetry about the midplane and include the domain between the disk midplane and 0.13 rad above the midplane (corresponding to about three gas scale heights). We keep the numerical resolution of our base grid identical to the one used in our previous study, i.e. $N_\phi \times N_r \times 2N_\theta = 680 \times 215 \times 40$, linearly spaced along all dimensions. With this resolution, we vertically sample a gas scale height h_g with about eight numerical grid cells. In selected simulations, we locally refine the numerical grid in a comoving region surrounding the planet ($\phi = [-1.1, 1.1]$, $r = [0.5385, 1.4615] \cdot r_p$, $\theta = [\pi/2, \pi/2 - 0.116]$) doubling the resolution along each dimension, i.e., locally increasing the number of cells by a factor eight. We summarize our simulation parameters in Table 8.2.1. In this chapter, we are ultimately interested in observational features obtained from synthetic ALMA continuum observations, which are resolution limited by the size of the beam which has a size of about 35 mas (see Sec. 8.2.5). At 50 au from the central star, the vertical extent of a single grid cell of the base grid in our simulations is equal to 0.32 au, which subtends an angle of ~ 3.2 mas at a source-observer distance of 100 pc. Thus, our vertical numerical resolution of the base grid samples the beam about eleven times along one axis. The refined grid samples the beam about 22 times.

In Table 8.2.2, we compile a list of all the simulations that we ran for this study. As mentioned, we mainly focus on the `50au`-domain, for which we designate the simulation containing a Jupiter-mass planet our *fiducial* simulation. We ran this configuration three times with different values of the Schmidt numbers ($Sc = 1, 10, 100$), i.e., changing the value of the diffusion coefficient D, to study the influence of turbulent transport. We added a grid refinement patch to all three of these simulations. In addition to that, we ran the three identical simulations, but without an embedded planet. Furthermore, we ran simulations containing a more massive 5 Jupiter-mass planet and a less massive Saturn-mass planet with $Sc = 1$ in the `50au`-domain. For comparison,

Table 8.2.1: Overview of the physical disk parameters and the numerical grid parameters used in the three-dimensional radiative hydrodynamic simulations.

Gas surface density	$\Sigma_g = 80\mathrm{g/cm}^2 \cdot \left(\frac{r}{1\,\mathrm{au}}\right)^{-1/2}$
Global dust-to-gas ratio	0.01
Stellar parameters	$\mathrm{T}_{\mathrm{eff},*} = 5780\,K$, $\mathrm{M}_* = 1\,\mathrm{M}_\odot$ $\mathrm{R}_* = 1\,\mathrm{R}_\odot$
Base grid resolution	$N_\phi \times N_r \times 2N_\theta = 680 \times 215 \times 40$
ϕ-domain	0 - 2π rad
θ-domain	$\pi/2 - 0.129$ rad
r-domain "`50au`"	20.0 au - 119 au
r-domain "`5au`"	2.08 au - 12.4 au

Table 8.2.2: List of hydrodynamical simulations conducted in this study.

Model #	r-Domain	Planet Mass M_p	Sc	grid refinement
1	`50au`	1 M_{Jup}	1	✓
2	`50au`	1 M_{Jup}	10	✓
3	`50au`	1 M_{Jup}	100	✓
4	`50au`	no planet	1	×
5	`50au`	no planet	10	×
6	`50au`	no planet	100	×
7	`50au`	5 M_{Jup}	1	×
8	`50au`	1 M_{Sat}	1	×
9	`5au`	5 M_{Jup}	1	×
10	`5au`	1 M_{Jup}	1	×

we also ran the Jupiter-mass and 5 Jupiter-mass planet in the `5au`-domain with $Sc = 1$.

Initial/boundary conditions and simulation procedure

We initialize the gas disk with a constant aspect ratio $H = h_g/r = 0.05$, which then evolves depending on the local heating/cooling in the simulations. We initialize the mm-sized dust with a vertical profile equal to the vertical equilibrium distribution in Eq. 5.24. At each radius, the vertically integrated dust-to-gas ratio, i.e., the surface density ratio, initially is equal to 0.01. During the simulation, the distribution in the gas as well as the dust evolves according to the local thermohydrodynamic conditions and the local dust-to-gas ratio evolves accordingly. Before injecting the planetary gravitational potential, we first run the simulation with only 2 cells in the azimuthal direction for a duration equivalent to 150 planetary orbits to reach the thermodynamic equilibrium of the protoplanetary disk. We set the end of this run as $t = 0$. Then, we split the azimuthal domain into 680 cells and run the simulation up to $t = 200 \cdot 2\pi\Omega_0^{-1}$, 200 additional planetary orbits, while we increase the planet's potential to the desired value over the first 100 orbits as in Szulágyi et al. (2016). In the relevant simulations (see Table 8.2.2), we add the grid refinement patch at $t = 200 \cdot 2\pi\Omega_0^{-1}$ and run the simulation with the locally increased resolution until $t = 220 \cdot 2\pi\Omega_0^{-1}$.

The boundary conditions in the gas fluid are identical to Szulágyi et al. (2016), Binkert et al.

(2021) and Chapter 7. Particularly, this means symmetric boundary conditions in the vertical direction, where also the gas density is exponentially tapered based on the local gas temperature at the boundary opposite to the midplane. In Binkert et al. (2021) and Chapter 7, we imposed antisymmetric radial boundaries for the radial dust velocity component, which ensured mass conservation in the entire simulation domain. However, at the same time, it allowed dust accumulations to form at the radial boundaries. When including turbulent transport, these dust accumulations would diffuse back into the simulation domain. To prevent this, in this work, we also chose symmetric boundary conditions for the radial velocity component, identical to the boundary conditions of other two velocity components and the density. As a result, 3-8 percent of dust present in the domain is lost via the boundary during the entire evolution of our simulations (the degree of mass lost scales with the mass of the planet).

8.2.4 Radiative Transfer

After the hydrodynamic simulations, but before post-processing, we exponentially taper the dust density in the inner disk within a region $r < 0.5 \cdot r_p$, to decrease the impact of potential dust accumulations at the inner computational boundary and/or artifacts caused by the inner computational boundary.

The need for tapering arises because we do not have density-damping zones in our radiative hydrodynamic simulations. We find dust accumulations at the inner disk edge to build up during the simulations as a result of the incident stellar radiation and the consequent large disk temperature close to the inner disk edge. This is a result of the third term on the r.h.s. of Eq. 8.2. These accumulations resulted in an increased optical depth that affects the radiative transfer post-processing. Thus, we followed the approach of Speedie et al. (2022) and truncate the disk in between hydrodynamic simulations and radiative transfer post-processing. We experimented with different values of the truncation radius and found a value of $0.5 \cdot r_p$ to be the optimal tradeoff between decreasing the impact that these dust accumulations have on the synthetic observations, and not interfering with the domain of scientific interest.

We then post-process our set of hydrodynamic simulations with the Monte-Carlo radiative transfer code package RADMC-3D (Dullemond et al., 2012) in order to create synthetic ALMA observations in band 7 at 0.87 mm. The opacity provided to code is based on a dust grain size distribution of 0.1 μm and 1 cm with a power-law index of 3.5 (Pohl et al., 2017) assuming a mixture of silicate (Draine, 2003) and carbon (Zubko et al., 1996) with a fractional abundance of 70 percent and 30 percent, respectively. The absorption and scattering opacities as well as the g parameter of anisotropy were calculated using the BHMIE code of Bohren & Huffman (1984). The Bruggeman mixing formula was used to determine the opacity of the mixture. The resulting absorption and scattering opacity at the wavelength of 0.87 mm are κ_{abs}=10.1 cm^2/g and κ_{sca}=10.2 cm^2/g, respectively. This is comparable to the values in Birnstiel et al. (2018). Based on these opacities and the dust surface densities, we expect the disk models to be marginally optically thick at the observed wavelength.

The observed mm-continuum fluxes ultimately depend on the distribution of the dust density ρ_d and temperature T_d. However, unlike the gas temperature, the dust temperature is not directly calculated in the hydrodynamic simulations.

In low-density disk regions, e.g., in the disk atmosphere, we expect nonradiative heating/cooling effects to be small and thus the dust temperature to be close to the radiative equilibrium temperature. Complex thermochemical models confirm that this is at least a valid first-order assumption, as shown by e.g., Woitke et al. (2022) using ProDiMo models (Woitke et al., 2009). Models capturing the full disk thermochemistry are desirable but beyond the scope of our current work. In our work, we find the radiative equilibrium temperature using the thermal Monte Carlo tool `mctherm` within RADMC-3D. However, even in the outer disk, we find the disk midplane, where we expect the majority of the observed thermal emission to come from, to be too dense and consequently dust-gas collisions to be too frequent, to neglect nonradiative cooling/heating effects. Therefore, we refrain from setting the dust temperature equal to the radiative equilibrium temperature and, instead, set the dust temperature equal to the temperature calculated in the radiative hydrodynamic simulations which also accounts for nonradiative cooling/heating effects.

Based on the dust density and temperature distribution, we generate intensity maps at four different inclinations ($i = 0°$, $60°$, $80°$, $90°$) with the `image` task including the `fluxcons` argument to assure flux conservation. We assume anisotropic scattering using the Henyey-Greenstein approximation. The size of the intensity maps is 1000 × 1000 pixels, and we assumed the disk to be at a distance of 100 pc, about the distance to the closest star-forming region. In the `50au`-domain, this results in an angular resolution of 2.5 mas per pixel. In a subsequent step, the resulting wavelength-dependent intensity maps are processed to simulate ALMA observations (see Sec. 8.2.5).

8.2.5 Synthetic ALMA Continuum Observations

We study the observational signatures of a planet in a turbulent disk by generating synthetic continuum observations from the intensity maps using the Common Astronomy Software Applications package CASA (Mcmullin et al., 2007) to simulate ALMA observations. Particularly, we create observations in band 7 at a wavelength of 0.87 mm (345 GHz) and use antenna configuration C43-8, which provides sufficient resolution and signal-to-noise behavior to pick up small-scale features on the scale of a few au. With a maximum baseline of 8.5 km, configuration C43-8 allows for an angular resolution of up to 28 mas, which corresponds to a physical scale of 2.8 au at a distance of 100 pc. However, configuration C43-8 in combination with band 7, only has a maximum recoverable scale (MRS) of 410 mas (41 au), smaller than the planetary orbital radius in our radially most extended simulation (50 au). Because we expect observational features such as, e.g., rings on scales comparable to the planetary orbital radius, we also observe the disk with the more compact configuration C43-5 as recommended by the ALMA proposer's guide. The additional configuration increases the MRS in our synthetic observations to 1.94" (194 au), which covers the most relevant angular scales in our simulations.

We set the integration time in the more extended configuration to six hours, and, following the ALMA proposer's guide, set the integration time in the more compact configuration to 79 minutes. For each antenna configuration, we generate a measurement set (MS) with the `simobserve` task contained in the CASA software package for which we set the channel bandwidth to 7.4 GHz, add thermal noise with a random number seed of 1745, adopt a value of 0.475 mm precipitable water vapor, and set the ambient temperature to 269 K. We combine the two measurements sets with the `concat` task, before using the `simanalyze` task to generate the final combined intensity images by applying Briggs weighting to the visibility data (robust=0.5) and setting the `clean` threshold to a value of 50 µJy/beam.

8.3 Results

In this section, we present our results by first qualitatively discussing the three-dimensional dust morphology in the presence of turbulent transport and an embedded planet in Sec. 8.3.1. There, we mainly focus on the simulation containing a Jupiter-mass planet orbiting on a circular orbit at 50 au from the central star and Schmidt number $Sc = 100$. This particular example was chosen because the flow pattern due to planetary mixing is best identified/studied in a background with weak turbulent stirring. In section 8.3.2, we then quantify the level of planetary dust mixing with an effective diffusivity before presenting the synthetic ALMA observations in Sec. 8.3.3.

8.3.1 Three-dimensional Dust Morphology

In the first sub-panel of Fig. 8.3.1, we show the azimuthally averaged dust-to-gas ratio of the `50au` simulation with $Sc = 100$ at time-zero (before inserting the planet). turbulent transport counteracts the vertical settling of the mm-sized dust grains such that, in the absence of resolved turbulent flows and/or additional gravitational forcing, the vertical disk profile does settle in an equilibrium distribution in which downward vertical settling is perfectly balanced by upward turbulent transport. With the term *downward*, we refer to the direction towards the disk midplane, and with *upward* the direction away from the disk midplane. Note that the gas in our radiative simulations is not necessarily vertically isothermal and therefore, the vertical profile of the dust-to-gas ratio does not necessarily follow the equilibrium profile of Eq. 5.24.
We slowly introduce the planetary potential to the protoplanetary disk. The embedded planet, modeled via its gravitational potential, then becomes a source of additional dust mixing besides the background level of turbulent transport (Binkert et al., 2021). In the second sub-panel of Fig. 8.3.1, we show the azimuthally averaged dust-to-gas ratio of the simulation containing a Jupiter-mass planet at 220 orbits ($t = 220\ 2\pi\Omega_p^{-1}$) in the `50au` with $Sc = 100$. The third and fourth sub-panels show vertical cuts at $\phi = \pm 45^\circ$ (the planet is located at $\phi = 0^\circ$). The vertical distribution shows the characteristic vertical plume-like structures to the inside and outside the planetary orbital radius at $r = r_p$ that are a result of dust stirring caused by meridional flows (Szulágyi et al., 2022). Planetary dust stirring in the absence of background turbulence was previously reported in Binkert et al. (2021) and Bi et al. (2021) and further confirmed by Krapp et al. (2021) in vertically isothermal simulations including turbulent transport. As opposed to Bi et al. (2021), who report the vertically puffed up dust distribution to be roughly azimuthally symmetric, we find an asymmetric distribution with respect to the planet, which becomes apparent when comparing the third and fourth sub-panel of Fig. 8.3.1. We find the dust distribution to be azimuthally more symmetric in simulations containing a less massive planet and/or more strongly coupled dust.
Vertical flows in the gas, as part of a meridional circulation, have previously been found in hydrodynamic simulations (Kley et al., 2001; Szulágyi et al., 2014; Fung & Chiang, 2016) and have also been confirmed observationally (Teague et al., 2019). The existence of similar flow structures in the solid disk component (Szulágyi et al., 2022) could have relevant consequences, e.g., on dust grain chemistry as grains experience different chemical and physical environments, or it is relevant for grain growth when flow structures influence the relative velocities of individual dust grains. Further, large-scale dust flows could influence the three-dimensional disk morphology and thus have observational consequences for continuum emissions, which directly trace the spatial distribution of dust grains. To investigate the potential observational impacts of planet-induced dust stirring, we further analyze the origin and spatial structure of the vertical dust features in the remainder of this section.

We still focus on the simulation containing the Jupiter-mass planet with $Sc = 100$ and examine the dust flow structure there, before generalizing our results to different sets of parameters. We find distinct flow structures in the mm-sized dust, which are created by the planet and are inherently three-dimensional and vary strongly in space. Thus, it is difficult to visualize them in two-dimensional plots. We especially found cuts in the r-z-plane or azimuthal averages of density distributions or velocity fields, e.g., like in Fig. 8.3.1, to poorly represent the underlying nature of the dust distribution and flow structure. In order to improve upon previous explanations and visualizations of planet-induced dust stirring, we show vertical cuts along a specific curve (empirically determined) in $r - \phi$ space in Fig. 8.3.2. Specifically, we show the vertical dust density distribution along two curves with the functional dependency

$$\frac{r_i(\phi)}{r_p} = \mathrm{sgn}(\phi) A_i |\phi|_i^b + 1 \tag{8.14}$$

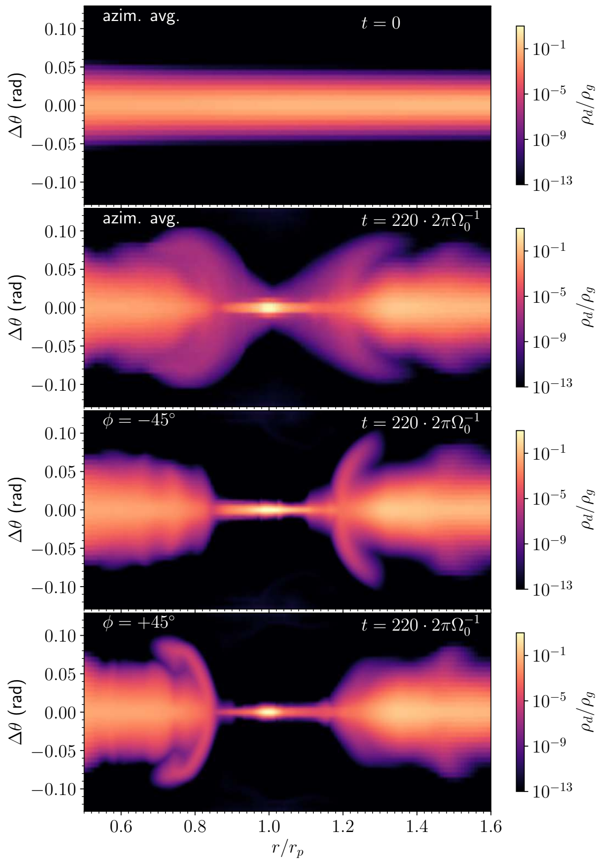

Figure 8.3.1: Dust-to-gas ratio in our fiducial simulation, containing a Jupiter-mass planet orbiting at $r_p = 50$ au from the central star with reduced dust diffusivity compared to the fiducial model ($Sc = 100$). The first subplot shows the azimuthally averaged dust-to-gas ratio at $t = 0$, i.e., before injecting the planet potential. The second subplot shows the azimuthally averaged dust-to-gas ratio at $t = 220 \cdot 2\pi\Omega_0^{-1}$. The third and fourth subplots show a vertical cut at $\phi = -45°$ and $\phi = +45°$. The gap region and the planetary stirring of dust can clearly be identified.

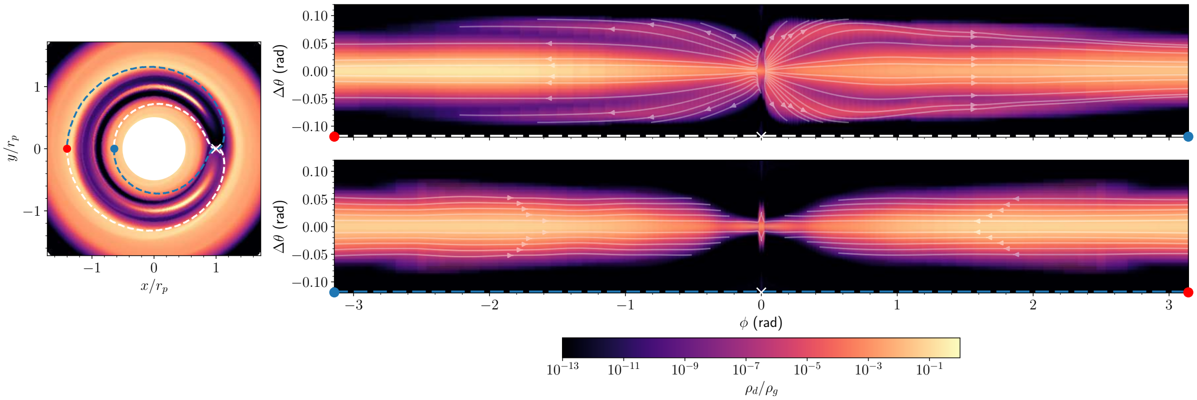

Figure 8.3.2: Visualization of how dust is delivered to the planetary region by the Keplerian flow (bottom right plot), where it is lifted and then transported away from the planet on the opposing side (upper right plot). *Left:* Dust surface density map of the simulation containing a Jupiter-mass planet orbiting at 50 au. The dashed blue and white lines indicate the curves along which we plot the vertical cuts on the r.h.s. *Right:* Vertical cuts along the blue (*top*) and white (*bottom*) curves, which each cover the full azimuthal range of $\pm\pi$. The color map represents the vertical distribution of the local dust-to-gas ratio ρ_d/ρ_g along these curves, with $\phi = 0$ being the position of the planet and positive in the counterclockwise direction. The faint white streamlines visualize the dust velocity components in the polar direction and parallel to the curve in the co-rotation frame of the planet. Note that these streamlines represent the velocity field along a two-dimensional surface and are not fully representative of the three-dimensional flow. For better visualization, the vertical axes of the plots on the r.h.s. are stretched by a factor ~ 4.5.

where $\phi \in (-\pi, \pi)$. For the first curve, we chose $A_1 = -0.24$ and $b_1 = 0.35$ for $\phi \geqslant 0$ and $A_1 = -0.27$ and $b_1 = 0.35$ for $\phi \leqslant 0$. For the second curve, we chose $r_2(\phi) = r_1(-\phi)$. These two curves are represented by a white and blue dashed line respectively in the surface density plot on the l.h.s of Fig. 8.3.2. The r.h.s plots in Fig. 8.3.2 represent the vertical cuts along these two curves and show the dust-to-gas ratio. Moreover, we show the streamlines of the vertical and parallel dust velocity components along the two curves in the co-rotating frame of the planet. Note that these streamlines only represent the velocity field along a two-dimensional surface and do not fully represent the three-dimensional flow. However, they nicely visualize the influence of the planet on the dust flow.

Note that Eq. 8.14 is functionally similar to the spiral wake parametrization of Rafikov (2002), who predict the functional form of planet-generated density waves in a gas disk. For a disk with $c_s \propto r^{-1/4}$, equation (44) of Rafikov (2002) predicts a wake profile of $r \propto \phi^{0.8}$ (for $\phi > 0$) far away from the planet, which is comparable to the profile of the spiral density wakes present in the gas. The profile described by Eq. 8.14 is with $r \propto \phi^{0.35}$ more tightly wound and distinctly different from the spiral wake in the gas (see also the discussion in section 8.3.2, and compare to the tightly wound flow feature in Figure 8.3.3).

Along both, the blue and the white curve, the width of the background distribution narrows as it approaches the location of the planet. In the upper sub-plot on the r.h.s of Fig. 8.3.1, a wing-like structure is superimposed on the smooth background distribution. Such a feature is absent in the lower subplot. It is these wing-like structures that are responsible for the vertical features seen in Fig. 8.3.1. We find that the wing-like structures are caused by vertical flows in the dust that are strongest at the location where the planetary spiral wake intersects with the edge of the gap ($\phi \sim \pm 0.4$). The wing-like features are asymmetric with respect to the planet, with the feature associated with the inner gap edge being more extended in the polar direction. Our simulations are strictly symmetric about the midplane. Therefore, the observed vertical flows are not a direct result of the local gravitational field. Instead, we find the vertical dust flows to be driven by the vertical roll-up motions of the gas in the wake of the planet. These distinct flows in the gas in the presence of a planet were first reported in Szulágyi et al. (2014) and Fung et al. (2015) and are part of the meridional circulation created by the planet. The origin of the vertical upward motion in the gas can be understood by considering the gas flow in the planet's co-rotation frame. In such a frame, gas approaches the planet from two sides on a horseshoe orbit. Away from the planet, this gas is vertically in hydrostatic equilibrium and thus roughly flows with a columnar structure. As the column approaches the planet, it enters the Hill sphere of the planet, where the flow components away from the midplane rapidly accelerate vertically toward the disk midplane because the increased vertical gravity of the planet breaks the vertical hydrostatic equilibrium. Thus, a portion of the gas flow on the horseshoe orbit has lost significant potential energy as it arrives at the turn of the horseshoe (when the flow crosses $r = r_p$ and is closest to the planet) and thus has gained kinetic energy (e.g., see Figure 5 in Fung et al. (2015) for a visualization of the gas flow structure at the horseshoe turn). After the horseshoe turn, the fast-moving gas then radially moves away from the planetary orbital radius close to the midplane. Fung et al. (2015) call this component of gas flow, which is pulled toward the planet from high altitudes and continues radially at midplane, the *transient horseshoe flow*. They call it *transient* because, due to the excess radial speed, the gas flow is no longer part of the recurring horseshoe flow. Instead of following the horseshoe trajectory, the gas flow overshoots and exits the horseshoe region, where it encounters the Keplerian flow that flows along quasi-circular orbits outside the horseshoe region (unless it enters the planet's Bondi sphere where it becomes part of the *atmospheric recycling* flow (e.g., Ormel et al., 2015; Kuwahara et al., 2019). The fast-moving radial flow enters the quasi-Keplerian flow field exactly where the streamlines of the approaching Keplerian flow are bent toward the planet at Lindblad resonances. The result is a convergence of the two flow components at close to 90 degrees (similar to the description in Szulágyi et al. (2014)), which further increases the local gas pressure at this location. This local non-equilibrium build-up of gas pressure decompresses in an upward direction via the vertical roll-up motion, discussed in (Szulágyi et al., 2014; Fung et al., 2015; Szulágyi et al., 2022). The forced upward motion at the location of the convergence of the two flow components is also the origin of the upward-directed part of the meridional circulation. In this work, we find that the fast midplane gas flows which are deflected upwards drag along a substantial amount of mm-sized dust causing the characteristic plumes on two opposing sides of the planet, which we visualize in the upper right sub-plot of Fig. 8.3.2. Note how all the streamlines in this plot originate in a region close to the planet at the midplane. I.e., dust that is lifted to regions above the midplane, mainly originates from a region close to the midplane and the resulting effect is the large-scale vertical planetary dust mixing. The fact that the strong vertical gas flows induced by the embedded planet may also drag along substantial amounts of dust to high-altitude disk regions was already hypothesized by Edgar & Quillen (2008). Vertically, the dust plumes extend roughly a Hill radius $\sim r_H$, in agreement with the predicted scale for the gas (Fung et al., 2015). Downstream, the component of the flow (gas and dust) which has been lifted vertically away from the midplane is carried away from the azimuthal location of the planet by the differentially rotating Keplerian disk flow. We find that away from these particular, spatially very localized, upward gas motions, vertical stirring is not sustained, and the vertically lifted dust settles into its vertical equilibrium distribution. If the dust grains are only marginally coupled, as is the case in our fiducial simulation, they completely settle before they encounter the planet again (see also Szulágyi et al., 2022). The result is a strong asymmetry in the distribution of the mm-sized dust along the orbit of the embedded planet. After this qualitative description of the relevant physics in the example shown in Fig. 8.3.2, we study the planetary dust stirring more quantitatively in the next section.

8.3.2 Effective Diffusivity

In the previous Sec. 8.3.1, we have qualitatively described the vertical dust stirring by a planet embedded in a protoplanetary disk. In this section, we aim to quantify the level of vertical planetary stirring and how it is influenced by turbulent transport, by measuring an effective diffusivity δ_{eff}.

Ultimately, we are interested in how planetary dust stirring is affected by different strengths of dust turbulent transport. The straightforward approach to expose the planetary environment to different levels of turbulent transport is to change the turbulent viscosity ν in the gas because when keeping the Schmidt number at unity (see Eq. 8.1), a change in viscosity will also change the strength of turbulent transport. However, as mentioned in Sec. 8.2.3, we found that lower values of the gas viscosity give rise to additional sources of dust stirring, likely attributed to the VSI and/or vortices at the gap edges generated by the Rossby wave instability. These additional effects make it difficult to isolate and study the sole effects of planetary dust stirring. Therefore, in this study, we keep the gas viscosity fixed at the relatively large fiducial value of $\nu = 10^{-5} r_0^2 \Omega_0$ in order to suppress additional sources of dust stirring. Nonetheless, we aim to explore the effects of different levels of dust turbulent transport and thus alter the value of the dust diffusion coefficient D while keeping the gas viscosity at the fiducial value the same. We thus effectively change the value of the Schmidt number Sc (see Eq. 8.1). Besides our fiducial setups, we ran additional simulations in which we decrease the dust diffusion coefficient by one and two orders of magnitude, respectively, and leave the remaining parameters identical (see Table 8.2.2). Thus, we ran simulations with different levels of dust turbulent transport in which the Schmidt number, as defined in Eq. 8.1, takes values of $Sc = 1, 10, 100$, such that lower levels of dust turbulent transport are associated with a larger Schmidt number.

In Chapter 5, specifically in Eq. 5.24, we showed that, for a given (vertically isothermal) gas distribution, the vertical extent of the dust depends on the ratio between the midplane Stokes number St_{mid} and the dimensionless diffusion coefficient δ, i.e., the diffusivity. In our simulations, we determine the midplane Stokes number St_{mid} and the gas scale height h_g at every coordinate (x, y) and approximate the local vertical dust density profile $\rho_d(z)$ at this location with Eq. 5.24

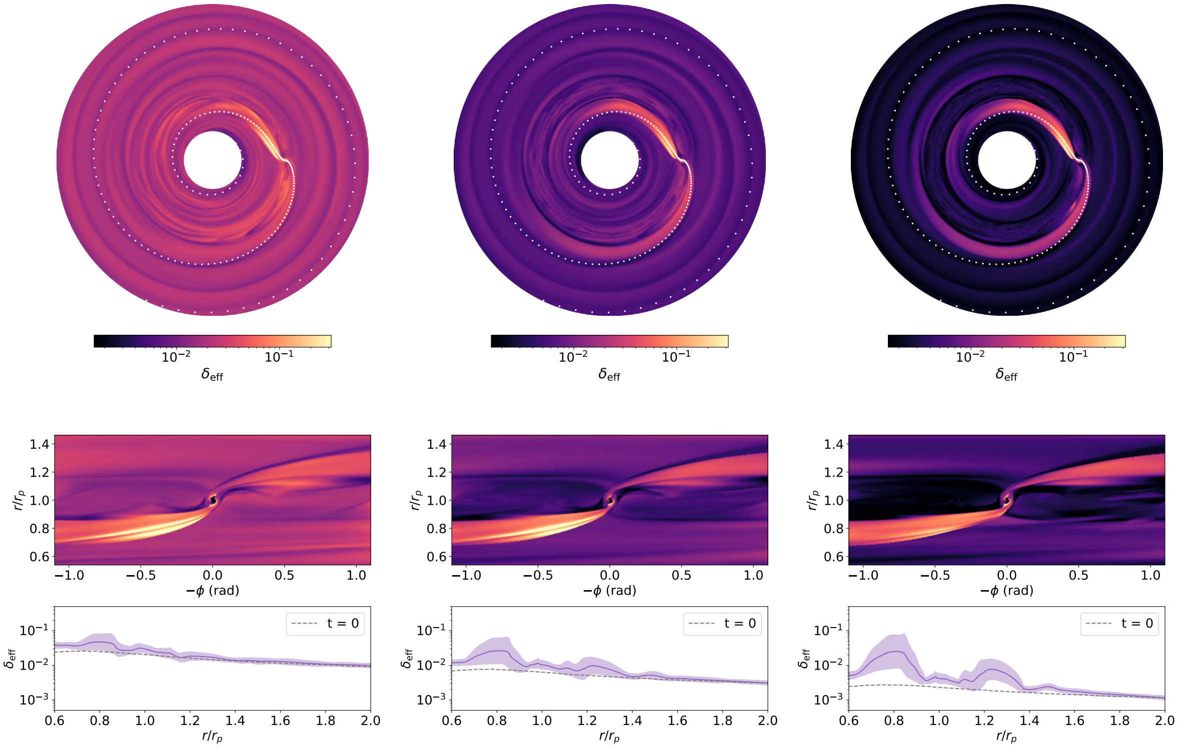

Figure 8.3.3: This figure shows the effective vertical diffusivity $\delta_{\rm eff}$ as found by fitting Eq. 5.24 at every point in the x-y-plane in three simulations of the `50au`-domain containing a Jupiter-mass planet with decreasing strength of turbulent transport from left to right ($Sc = 1, 10, 100$). *Top:* Two-dimensional map of the effective vertical diffusivity $\delta_{\rm eff}$. For comparison, the white dots follow the wake equation of Rafikov (2002) and matches well the spiral wake in gas. The *middle* panels show a zoomed-in view of the region surrounding the planet with increased numerical resolution. *Bottom:* The solid line traces the azimuthal average of the effective vertical diffusivity $\delta_{\rm eff}$. The shaded regions show the one sigma deviation from the average value, and the dashed line is the unperturbed average value at $t = 0$.

and determine an effective diffusivity $\delta_{\text{eff}}(x, y)$ by using a least square fit in log-space. We stress here that the vertical dust density structure is strictly not in a vertical static equilibrium wherever the flow is highly dynamic, e.g., in the planetary wakes. Nonetheless, our approach allows us to quantify the level of vertical stirring with an effective diffusivity δ_{eff}.

We visualize our results in Fig. 8.3.3 where we show two-dimensional maps of the effective diffusivity δ_{eff} in the upper row of each subplot. The sub-panels show, from left to right, simulations with decreasing levels of turbulent transport. While the sub-panels of the left side show the fiducial simulation, the parametrized dust diffusion coefficient is decreased by a factor 10 in the simulation shown in the sub-panels in the middle and decreased by a factor 100 in the sub-panels on the right. All three columns show a simulation containing a Jupiter-mass planet orbiting at 50 au.

The subplots in the second row of Fig. 8.3.3 show a zoomed-in view of the region surrounding the planet with increased numerical resolution (doubled along each dimension). These effective diffusivity maps trace the regions in which planetary dust stirring is strongest. We find two maxima on opposite sides of the planet at the approximate location where the planetary spiral wake intersects with the edge of the planetary gap, i.e., the location where overshooting horseshoe flows and quasi-circular flows converge, as described in Sec. 8.3.1. There, the vertically stirred dust is dragged along with the Keplerian flow and carried away from the planet in two opposing directions on almost circular trajectories. The result is the formation of asymmetric features, i.e., two spiral-like arms, originating at the location of the planet and fading as the dust settles downstream. We note that these spiral arm features have a smaller pitch angle than the spiral arms in the gas and tend to become almost circular away from the location of the planet. For comparison, we trace the spirals in gas with the wake equation of Rafikov (2002) (their equation 44) in the first row of Fig. 8.3.3 with white dots (we use their parameters $\nu = 0.25$ and $h_p = 0.07$).

In addition to the azimuthal asymmetry due to the presence of the planet, we also find an asymmetry with respect to the planet itself, with the effective diffusivity being larger in the inner arm than in the outer arm. Apart from the distinct main feature, we find a background distribution that traces spiral features in the outer disk, but with a significantly smaller contrast than the main spiral.

In the third row of Fig. 8.3.3, we show the corresponding azimuthally averaged effective diffusivity with a solid line and illustrate the one sigma deviations from the average value with the shaded area as a measure of azimuthal variability. In the simulations containing a Jupiter-mass planet with $Sc = 100$ (*right*), we find two maxima in the azimuthally averaged effective diffusivity at $\sim 0.85 r_p$ and $\sim 1.25 r_p$ with an average value of $\delta_{\text{eff}} \sim 3 \cdot 10^{-2}$ and $\delta_{\text{eff}} \sim 7 \cdot 10^{-3}$ respectively. The azimuthal mean of the inner maximum is almost an order of magnitude above the initial value, while the azimuthal mean of the outer maximum is about a factor of three above the initial value. Locally, the effective diffusivity is increased by the planet by almost two orders of magnitude, with values peaking above $\delta_{\text{eff}} > 10^{-1}$. As the strength of the background turbulence increases (decreasing Schmidt number), planetary features in the diffusivity maps become less prominent and are swallowed by the background turbulent mixing. Also, the azimuthal variability decreases. In our simulations with full turbulent transport ($Sc = 1$, *left*), the diffusivity deviates only marginally from the equilibrium value beyond the immediate planetary region.

Influence of the diffusion coefficient

We find the dust flow morphology to be weakly dependent on the level of background turbulence (without changing the gas viscosity). The dust flow, which is the main driver of the planetary dust stirring, only marginally influences the gas flow via the back reaction due to the dust-to-gas ratio generally being below unity. At the same time, we find the flow structure in the planet's Hill sphere to be highly dynamic and far away from an equilibrium distribution, in agreement with the findings of Krapp et al. (2021). Thus, the timescales responsible for the localized vertical stirring are significantly shorter than the diffusion timescales (also compared to the viscous timescale). At the same time, the vertically extended dust flow that approaches the planet is vertically compressed, along with the gas, as it approaches the Hill sphere due to the increased vertical gravity. Thus, the bulk of the dust approaches the planet on a horseshoe trajectory close to the midplane, regardless of the level of background turbulence.

As a result of the flow structure being largely independent of the level of background turbulence, the columnar features visible in the dust density distribution can be drowned in the turbulent background distribution if the background disk is thicker than the dust plumes created by the planet. On the other hand, dust structures caused by planetary stirring become more prominent if the level of background turbulence is small. Similarly, the plumes in the density distribution become indistinguishable from the background distribution if their vertical extent decreases due to e.g., weaker stirring by a less massive planet. Ultimately, whether the asymmetric features due to planetary stirring stand out in the three-dimensional dust density distribution depends on the relative strength of planetary stirring and background turbulence. The features are favored in disks with low levels of background turbulence containing a massive planet.

In our simulations containing a Jupiter-mass planet or below, we find the extent of the vertical dust plumes to be comparable to the planetary Hill radius r_H. Only in the 5 Jupiter-mass case, do we find it to be smaller, which is also the only case in which the Hill radius is significantly larger than the disk scale height ($r_H \simeq 2.4h_g$).

8.3.3 Synthetic Continuum Observations

A natural question that follows from the analysis in the previous sections is, what are the impacts of the discussed dust stirring mechanisms, i.e., planetary stirring and turbulent transport on astronomical observations. In this study, we focus on ALMA continuum observations, which trace the thermal emission of the dust component in the disk, with the goal to analyze the effects of turbulent transport and planetary dust stirring on continuum observations of protoplanetary disks. To isolate the effect of turbulent transport, we first analyze intensity maps of smooth, azimuthally symmetric disks (without an embedded planet) in Sec. 8.3.3, before we analyze disks with an embedded Jupiter-mass planet in Sec. 8.3.3.

Synthetic observations of axisymmetric disks without planetary perturber

In Fig. 8.3.4 and Fig. 8.3.5, we show synthetic ALMA continuum observations of axisymmetric protoplanetary disks (without an embedded planet) with different strengths of turbulent transport (decreasing from top to bottom) and corresponding disks with an embedded Jupiter-mass planet, respectively. We first focus on Fig. 8.3.4, where, from left to right, the inclination of the disk increases from $i = 0^\circ$ in the first column to $i = 90^\circ$ in the fourth column. From top to bottom, we decrease the strength of turbulent transport and show Schmidt numbers of 1, 10, and 100 in the first, second, and third rows, respectively. In the fourth row, we show a disk without prescribed turbulent transport, in which the dust is pressureless and has completely settled.

In the face-on views of the disks in Fig. 8.3.4, the effects of turbulent transport are visible at the inner and outer edges of the disks. With increasing strength of turbulent transport, the outer edge of the disk diffuses radially outward and counteracts the radial inward drift. This is especially apparent in the face-on view ($i = 0^\circ$) and also, but to a lesser degree, in the inclined disks ($i > 0^\circ$). In the inner disk, stellar irradiation increases the disk temperature, which in turn increases the turbulent pressure and its dependence on Eq. 8.3 and the gas sound speed in Eq. 4.1). As a result, dust diffuses radially away from the hot inner edge of the disk, and is also more extended vertically. Since the underlying temperature distribution is almost identical in all the presented models in Fig. 8.3.4, the relative difference in the peak intensities between the models, arises solely from the differences in the radial and vertical dust density distribution.

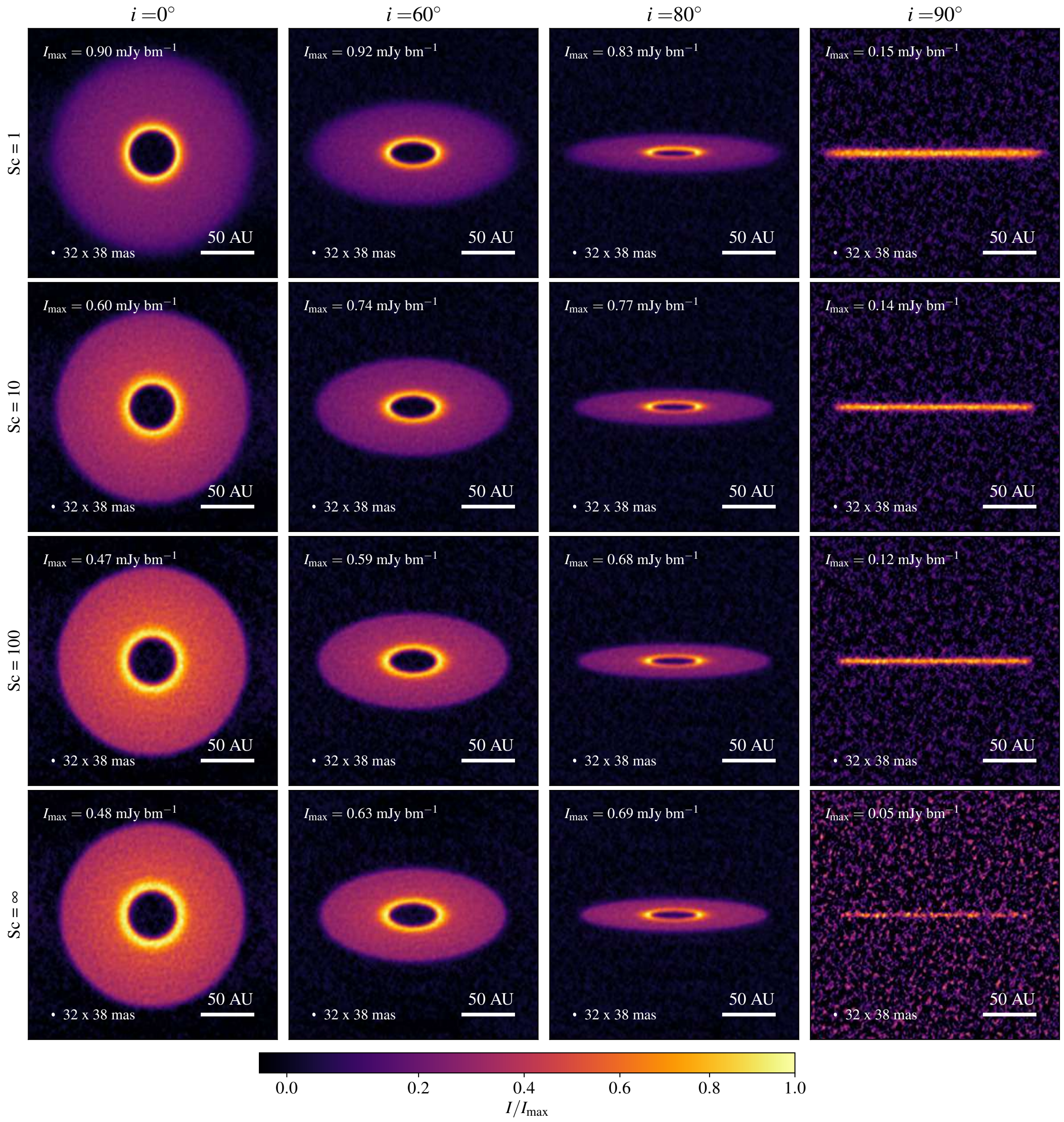

Figure 8.3.4: Synthetic ALMA Band 7 (345 GHz) observations, obtained with the C43-8 + C43-5 antennae configuration, demonstrating the observational influences of turbulent transport and inclination i on axisymmetric disks (`50au`-domain). Each row shows the same disk at different inclinations $i = 0°, 60°, 80°, 90°$. From top to bottom, we show disks with decreasing strength of turbulent transport, with the fourth row displaying a simulation without turbulent transport. The color map is normalized to the peak intensity and stretched with a 0.8-power law. The beam size is indicated in the lower-left corner of each subplot.

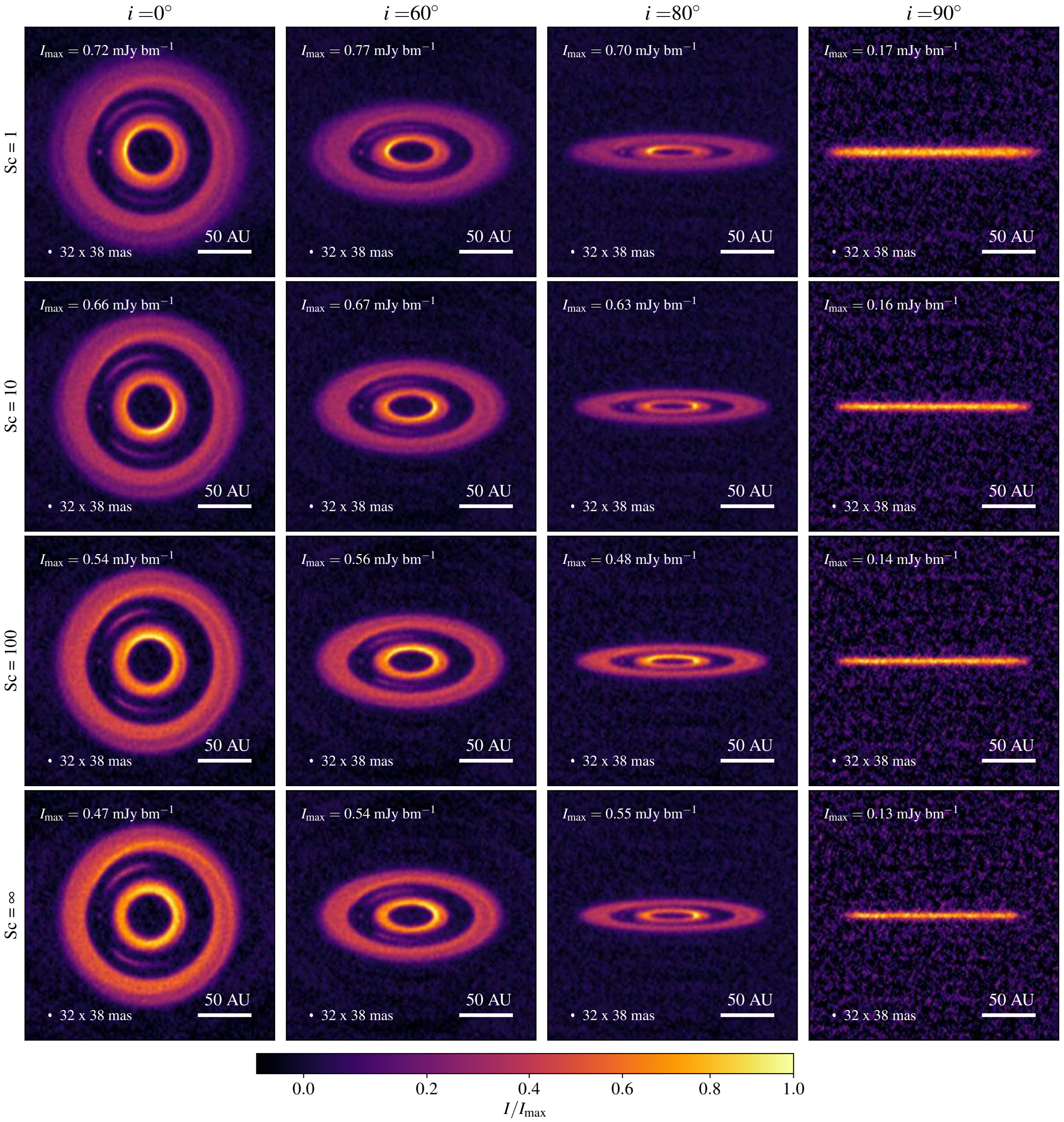

Figure 8.3.5: Synthetic ALMA Band 7 (345 GHz) observations, obtained with the C43-8 + C43-5 antennae configuration, demonstrating the observational influences of turbulent transport and inclination on a disk with an embedded Jupiter-mass planet on a circular orbit at 50 au. Each row shows the same disk at different inclinations $i = 0°, 60°, 80°, 90°$. From top to bottom, we show disks with decreasing strength of turbulent transport, with the fourth row displaying a simulation without turbulent transport. The color map is normalized to the peak intensity and stretched with a 0.8-power law. The beam size is indicated in the lower-left corner of each subplot.

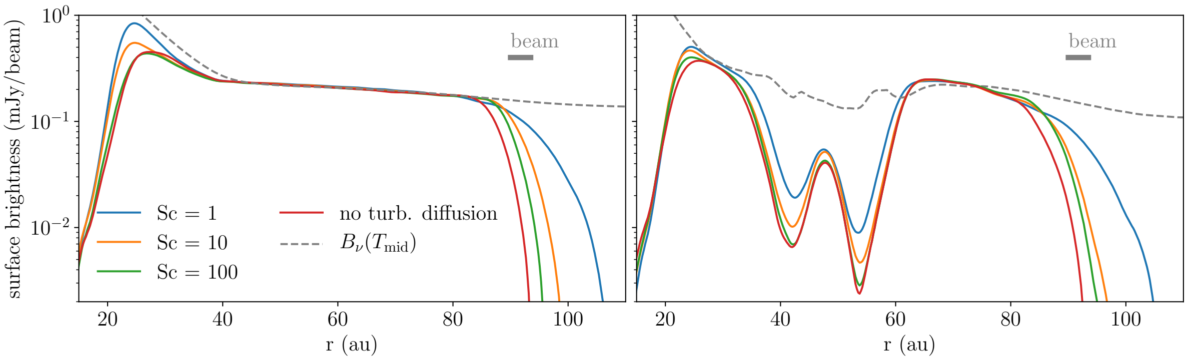

Figure 8.3.6: Azimuthally averaged radial intensity profile of the face-on view ($i = 0°$) of the synthetic ALMA observations of axisymmetric disks (*left*) and disks containing a Jupiter-mass planet at 50 au (*right*) with different strength of turbulent transport ($Sc = 1, 10, 100$). The profiles were obtained from the synthetic observations presented in Fig. 8.3.4 and Fig. 8.3.5. The gray dashed line represents the Planck function $B_\nu(T)$ evaluated at the midplane temperature $T_{\rm mid}$ and $\nu = 345$ GHz (band 7).

Interestingly, differences in the vertical scale height are not apparent in any view besides the edge-on view ($i > 90°$). We will study the edge-on case separately in Sec. 8.3.3. Derived from the intensity maps, we show, in the left sub-plot of Fig. 8.3.6, the azimuthally averaged radial intensity profile of the face-on views ($i = 0°$). The differences at the disk edges become apparent. On the other hand, the observed intensity away from the edges of the disk is very similar between the presented models and is closely matching the blackbody emission shown by the Planck function $B_\nu(T)$ evaluated at the disk midplane temperature $T_{\rm mid}$ and $\nu = 345$ GHz (band 7).

Synthetic observations of disks with an embedded Jupiter-mass planet

In this section, we study the effects of an embedded Jupiter-mass planet on the observed continuum emission of the same disks, as discussed in the previous Sec. 8.3.3. We present the synthetic continuum observation of our models containing a Jupiter-mass planet on a circular orbit at 50 au (orbiting in a counterclockwise direction) in Fig. 8.3.5. Like in the previous section, we present four models with varying strengths of turbulent transport (Sc $= 1,10,100,\infty$) at four different inclinations ($i = 0°, 60°, 80°, 90°$). The images are oriented such that the planet is located at the 9 o'clock position. In this subsection, we focus on the observational disk features caused by the Jupiter-mass planet and aim to link them to the hydrodynamical models. When focusing on the face-on views ($i = 0°$), we notice a wide ring outside the orbit of the planet. Like in the no-planet case, the outer edge of the ring radially diffuses outward when turbulent transport is active. In contrast, the inner edge of the outer ring, i.e., the edge facing the planet, seems to be only marginally affected by turbulent transport and appears equally sharp at different levels of turbulent transport. This is supported by the azimuthally averaged radial intensity profile in the sub-plot on the right-hand-side of Fig. 8.3.6 where the gap width is slightly narrower only for $Sc = 1$.

Moreover, the radial intensity profile just outside the planetary gap is largely flat and does not show the characteristic Gaussian peak which we would expect at the location of the local gas pressure maximum. This indicates that the intensity map traces the dust temperature rather than the dust density distribution, a sign of optically thick emission at the observed wavelength. We confirm this by plotting the Planck function $B_\nu(T)$ to Fig. 8.3.6 evaluated at the midplane

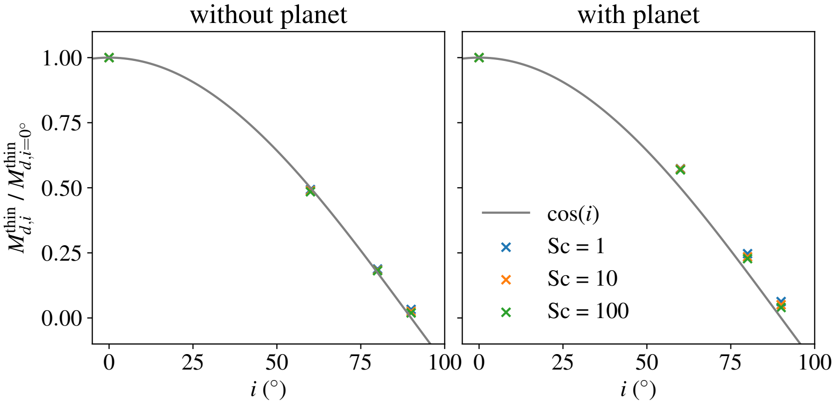

Figure 8.3.7: Visualization of the dependence of the optically thin dust mass $M_{d,i}^{\rm thin}$, obtained with Eq. 8.15 and listed in Table 8.3.1, on the inclination i. The left-hand side shows the values of axisymmetric disks, and the right-hand side shows the values of the disks containing a Jupiter-mass planet at 50 au. The measured values roughly follow the $\cos(i)$-function, which is represented by the solid gray line in the plots. See Sec. 8.3.3 for a discussion.

temperature $T_{\rm mid}$ and $\nu = 345$ GHz (band 7) which represents fully optically thick emissions and roughly traces the observed intensity profiles.

In all four face-on views, we clearly identify the spiral wake of the planet, peaking in intensity at about 60° behind the planet where the spiral arm emerges from the outer gap edge, i.e., the location where shock heating contributes to a local increase in temperature. With this, we also confirm Speedie et al. (2022) and ALMA's potential to detect planetary spirals.

Next, we focus on the emission coming from within the main gap region. We find some emission coming from the location of the planet itself, strongest in the $Sc = 1$ case. However, because we do not fully resolve the planetary potential well in our simulations, emission from the planet's vicinity should be followed up with mesh-refined future simulations, thus we will not comment on it further. The second feature we find is emissions from along the co-rotation radius of the planet, with the majority of the emission coming from the location of the two Lagrange points L4 and L5. The population of co-rotating dust is azimuthally more equally distributed in simulations with increased strength of turbulent transport, but the radial extent seems insensitive to the strength of turbulent transport. This is mainly because the strength of radial turbulent transport is reduced in the gap region, where dust grains are only marginally coupled as a result of angular momentum conservation and epicyclic oscillations. However, we remark that the observational features within the planetary gap should be taken with a grain of salt because marginally coupled dust grains tend to undergo crossing trajectories, an effect that we currently fail to capture using the fluid approach for dust. However, it is worth noting that the existence of a population of co-rotating dust grains is also predicted by three-dimensional particle-based studies (Fouchet et al., 2007; Zhu et al., 2014). Nonetheless, we expect these features to be transient and the planetary co-rotation region away from the two stable Lagrange points to become depleted eventually if we ran the simulations for longer (e.g., Dong et al., 2018).

Similarly to the outer gap edge, the inner gap edge in the intensity maps is not greatly affected by turbulent transport. Unlike in the outer disk, in the synthetic observations in Fig. 8.3.5, we do not identify a prominent planetary spiral in the inner disk.

Table 8.3.1: This table shows the optically thin dust masses of the synthetic ALMA observations as calculated with Eq. 8.15. The upper half of the table shows values obtained from the axisymmetric disk observations shown in Fig. 8.3.4. The bottom half shows the values obtained from synthetic observations of disks with an embedded Jupiter-mass planet, as shown in Fig. 8.3.5. For models with different strengths of turbulent transport, we list, in the third column of the table, the actual dust mass present in the models in units of Earth masses ($M_{\mathrm{d,hydro}}$). The last four columns list the optically thin dust mass retrieved from the observations at different inclinations in units of Earth masses ($M^{\mathrm{thin}}_{d,i}$). The measured optically thin disk dust masses are significantly lower than the actual dust masses present in the disk and decrease with increasing inclination. See Sec. 8.3.3 for a discussion.

	model	$M_{\mathrm{d,hydro}}$ ($M_\oplus$)	$M^{\mathrm{thin}}_{d,i=0^\circ}$ ($M_\oplus$)	$M^{\mathrm{thin}}_{d,i=60^\circ}$ ($M_\oplus$)	$M^{\mathrm{thin}}_{d,i=80^\circ}$ ($M_\oplus$)	$M^{\mathrm{thin}}_{d,i=90^\circ}$ ($M_\oplus$)
without planet	Sc = 1	127	73.4	36.2	13.8	2.40
	Sc = 10	123	65.9	32.2	12.1	1.64
	Sc = 100	122	61.7	29.9	11.2	1.18
	Sc = ∞	119	60.1	32.9	12.0	0.34
with planet	Sc = 1	127	49.0	28.1	12.1	3.08
	Sc = 10	123	43.0	24.6	10.1	2.18
	Sc = 100	121	42.2	24.0	9.61	1.69
	Sc = ∞	116	38.2	22.1	8.81	1.35

Optically thin dust masses derived from the ALMA mock images

From both sets of observations (without and with an embedded planet), we retrieve the optically thin dust mass M^{thin}_d , as routinely done in observational surveys of protoplanetary disks (e.g., Ansdell et al., 2016; Tychoniec et al., 2020). Here, we aim to study the influence of turbulent transport, the presence of a planet and its inclination. From the observed fluxes $F_{\nu=345GHz}$ integrated over the entire disk, we calculate the optically thin dust mass as (Hildebrand, 1983)

$$M^{\mathrm{thin}}_d = \frac{F_\nu d^2}{\kappa_\nu B_\nu(T_d)} \tag{8.15}$$

where $d = 100$ pc is the distance to the source, $\kappa_\nu = 10.1\,\mathrm{cm}^2/\mathrm{g}$ the absorption opacity (identical to the one used in the radiative transfer calculation), and B_ν the Planck function at the observed frequency $\nu = 345$ GHz. We set the dust temperature T_d equal to 7.9 K, the mass-averaged midplane temperature in our models. We summarize our results in Table 8.3.1 and list the total dust mass present in the model ($M_{\mathrm{d,hydro}}$) in the third column in units of Earth mass. In columns four to seven of Table 8.3.1, we list the optically thin dust masses, calculated with Eq. 8.15, for the 2×16 synthetic observations presented above. As a result of the marginally optically thick emission in the models, we find the optically thin dust mass M^{thin}_d to underestimate the actual dust mass by a factor of 1.7 to 3.0 for the face-on views. Further, we find the optically thin dust mass M^{thin}_d to generally decrease with decreasing strength of turbulent transport. This is mainly because dust contained in dense optically thick regions diffuses into less dense optically thin disk regions, which increases the observed flux from these regions. We also find the optically thin dust mass M^{thin}_d to decrease with increasing inclination i. Based on geometrical arguments, one can show that the optically thin dust mass M^{thin}_d, in an optically thick and geometrically thin disk, decreases with increasing inclination like $\cos(i)$. In Fig. 8.3.7, we plot the normalized optically thin disk dust masses $M^{\mathrm{thin}}_{d,i}$ as a function of the inclination i. The gray line follows the cosine of

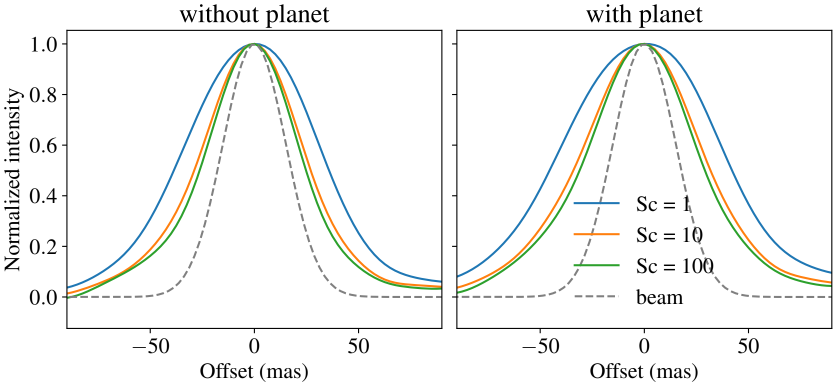

Figure 8.3.8: Normalized and average minor axis profiles of axisymmetric disks (*left*) and disks containing a Jupiter-mass planet (*right*) obtained from the synthetic observations of the `50au`-domain in edge-on view ($i = 90°$). The different colored profiles represent disks with different strengths of turbulent transport. The dashed line indicates a Gaussian profile with FWHM equivalent to the beam size in the synthetic observations.

the inclination ($\cos(i)$). The left subplot of Fig. 8.3.7 shows the normalized optically thin disk dust masses of the disks without an embedded planet. The results agree well with the cosine function, indicating that the disk aspect ratio is small, and the disk is mainly optically thick. Only in the edge-on view ($i = 90°$), the measured dust masses lie above the cosine function. This is because for very inclined disks, edge effects and the fact that the observed disk is not perfectly geometrically thin become important. Overall, this is an important result, especially for the dust-mass measurement in unresolved, optically thick disks in which the inclination can not be determined. Due to inclination effects, the measured optically thin dust mass in inclined disks is underestimated by a factor $\cos(i)$ with respect to the face-on view.
In the right subplot of Fig. 8.3.7, we plot the optically thin dust masses of the disks containing a Jupiter-mass planet. Like the dust masses in the disk without a planet, the normalized dust masses in the disk with an embedded planet follow the cosine function. However, unlike in the no-planet case, the results for inclined disks are shifted slightly above the cosine line. We expect the difference to arise from optically thin dust in the gap region or a more vertically extended disk structure caused by the planet stirring.

Synthetic observations of edge-on protoplanetary disks

In the previous sections, we have discussed how turbulent transport affects the inner and outer edges of the disks, where sharp edges are radially smeared out, which has a direct impact on optically thin dust masses. However, the effects of turbulent transport on the vertical extent of the disk are hardly discernible in the disks with low inclinations ($i < 90°$). We now focus on the edge-on observations ($i = 90°$) presented in Fig. 8.3.4 and Fig. 8.3.5 in which we aim to analyze the effects of turbulent transport and planetary stirring in the vertical direction. Because the effective diffusivity δ_{eff} is closely related to the vertical dust scale height h_d, we aim to infer the vertical extent of the disk from the edge-on observations and relate it to the strength of vertical stirring (similar to the procedures presented in Villenave et al. (2020, 2022)). For this, we first estimate the resolution required to resolve the dust scale height h_d along the minor axis of a disk in an edge-on view. Assuming the dust scale height is approximately Gaussian with scale height h_d, the FWHM, i.e., the beam size of the observing beam, must be smaller than $\sim 2.355 h_d$ (to fully resolve the scale height, the beam should sample this value at least

Table 8.3.2: Summary of the vertical disk thickness of the axisymmetric disks (*upper half*) and disks with a Jupiter-mass planet (*lower half*) with different strengths of turbulent transport (decreasing from top to bottom). The third column lists the measured deconvolved disk scale heights (w_m) of the underlying disk profile as measured in the edge-on view ($i = 90^\circ$) of the synthetic observations and are calculated with Eq. 8.17. The fourth column lists the corresponding scale heights ($w_{\rm rt}$) measured directly after the radiative transfer calculation, i.e., before the convolution with the ALMA beam and the addition of the thermal noise. The second to last column lists the azimuthally averaged dust scale height ($h_{d,80\,\rm au}$) measured in the underlying hydrodynamic simulation at a heliocentric distance of 80 au. The last column lists the ratio of the true underlying scale height with the hydrodynamic scale height ($w_{\rm rt}/h_{d,80\,\rm au}$). The former values are generally larger by a factor of a few.

	Sc	w_m (au)	$w_{\rm rt}$ (au)	$h_{d,80\,\rm au}$ (au)	$\frac{w_{\rm rt}}{h_{d,80\,\rm au}}$
without planet	1	2.96	2.99	1.20	2.49
	10	1.81	1.97	0.73	2.70
	100	1.54	1.40	0.52	2.70
	∞	1.18	0.43	0.44	0.97
with planet	1	3.83	3.23	1.34	2.69
	10	2.27	2.17	0.80	2.97
	100	2.00	1.55	0.55	2.98
	∞	1.92	1.19	0.45	2.70

twice). In the observations presented in Fig. 8.3.4 and Fig. 8.3.5, using the ALMA configuration C43-8 concatenated with C43-5, the mean beam size is 35 mas. Therefore, based on this rough estimate, at a distance of 100 pc, dust scale heights above $h_d \gtrsim 1.5$ au can be properly resolved. Assuming that the optical surface that we observe in the edge-on view lies at about 80 au from the central star, this corresponds to a disk aspect ratio of $h_d/r = 0.019$. In our models, the gas disk has an aspect ratio $h_g/r \sim 0.05$ at 80 au. We then use (Youdin & Lithwick, 2007)

$$h_d^2 = \frac{\delta}{St + \delta} h_g^2 \tag{8.16}$$

to obtain an approximate lower limit of the ratio between diffusivity δ and the Stokes number St that are required for us to resolve the disk vertically. We find $\delta/St > 0.14$. At 80 au, the midplane Stokes number in our models is $St_{\rm mid} \sim 0.065$. Hence, we expect the disk to be resolved along its minor axis in the edge-on view if $\delta > 9.1 \cdot 10^{-3}$. Therefore, we expect the disk scale height in the models with $Sc \leqslant 10$ to be properly resolved in ALMA observations. This might be improved when a new generation of radio interferometers with even better angular resolution becomes available. For example, ngVLA is expected to resolve sub-mas-scales (Selina et al., 2018), i.e., an order of magnitude better compared to the capabilities of ALMA. Thus, as long as the upper end of the dust size distribution remains comparable or smaller than ALMA wavelengths, we expect to observe more optically thin emissions at a higher angular resolution with ngVLA compared to ALMA. However, if the upper end of the dust size distribution extends into the regime comparable to ngVLA wavelengths $\lambda_{\rm obs.}$ ($6-300$ mm compared to $0.3-3$ mm for ALMA), the advantage might only be marginal at best. This is because, assuming the observed particle size is proportional to the observed wavelength, the scale height of the observed particles scales inversely with the observed wavelength $h_d \propto \lambda_{\rm obs.}^{-1}$ and thus, the larger particles probed at ngVLA wavelengths are more settled compared to the particles probed with ALMA.

In Fig. 8.3.8, we present the average brightness profiles (averaged along the central 0.5 as) along the minor axis of the synthetic edge-on disk observations without a planet (left) and with an embedded Jupiter-mass planet (right). The dashed line corresponds to a Gaussian beam profile with FWHM = 35 mas. We measure the scale height of the observed minor axis σ_m by fitting a Gaussian to the profiles. Because the profiles have been convolved with the ALMA beam, we have to deconvolve them to obtain the true scale height of the underlying profile w_m. Assuming the underlying profile is also Gaussian, the true scale height of the underlying minor axis profile can be found using the formula

$$w_m = \sqrt{\sigma_m^2 - \sigma_b^2} \tag{8.17}$$

where σ_b is the standard deviation of the beam. We list the values of the deconvolved scale height w_m in Table 8.3.2. Comparing them to the beam size (1.5 au), only the minor axis of the model in which turbulent transport is strongest ($Sc = 1$) and contains an embedded planet is sampled by the beam at least twice. All the other models are vertically not well resolved. But, only the model without prescribed turbulent transport ($Sc = \infty$) vertically extends less than one beam. Nevertheless, we evaluate the influence of the convolution/deconvolution and also measure the average FWHM of the minor axis profile in the output of the radiative transfer calculation ($\mathrm{FWHM_{rt}}$) to estimate the actual underlying scale height with $w_{\mathrm{rt}} = \mathrm{FWHM_{rt}}/2.355$. We list the values of the estimated underlying scale heights w_{rt} in the third column of Table 8.3.2. We find the measured scale heights w_m to agree well with the true underlying scale heights w_{rt} if they are comparable or larger than the beam size (1.5 au). However, the measured scale heights w_{rt} are larger by a factor of 2.49-2.98 compared to the hydrodynamical scale heights evaluated at 80 au $h_{d,80\,au}$ (obtained from the FWHM). We list the detailed value for each model in the sixth column of Table 8.3.2. The difference between the two values is a result of the large optical depths along the line of sight in the edge-on view.

8.4 Discussion, Summary, and Conclusion

8.4.1 Caveats

In this work, we incorporate a large amount of the relevant physics important for studying the underlying problem. More specifically, we study the problem in three dimensions and model the main thermodynamic processes that account for the heating and cooling of the protoplanetary disk (radiative, viscous, adiabatic). Further, we model the dynamics of the gas and solid components independently and let them interact via aerodynamic drag. In the solids, we include a linear and angular momentum-conserving subgrid model for the turbulent stirring of dust grains. The subsequent radiative transfer step accounts for the frequency-dependent interaction between the protoplanetary disk material and radiation. Nonetheless, our approach can benefit from a few improvements, of which some were already listed in section 4.2 of Binkert et al. (2021). Among the most relevant is the fact that we use only a single dust grain size and do not incorporate other grain sizes or the effects of grain growth. We aim to overcome this drawback in a subsequent study.

We also highlight that the low mass-averaged midplane temperature of 7.9 K, as stated in Sec. 8.3.3, is a result of efficient cooling via the disk surface to the 2.7 K background (i.e., the cosmic microwave background). The background radiation in a molecular cloud is likely closer to ~ 10 K (e.g., Schnee et al., 2009). Thus, disks embedded in a molecular cloud core are likely warmer and thus thicker and more strongly flared than the isolated disks considered in this work.

Further, we keep the planet in our simulations on a fixed circular orbit. In reality, planets are likely to undergo migration, an effect that we do not capture in this work. As outlined in Binkert et al. (2021) and Chapter 7, especially the rapid type III migration could be of importance (Masset & Papaloizou, 2003) and potentially affect the disk morphology (e.g., Weber et al., 2019). Moreover, the presence of multiple planets could also affect the disk morphology.

8.4.2 Summary

Using three-dimensional radiative two-fluid (gas + 1 mm size dust) hydrodynamic simulations of protoplanetary disks with an embedded planet, we investigate planet-induced dust stirring in a turbulent background. We model turbulent transport as a pressure-like term in the otherwise pressureless dust fluid, as discussed in Chapter 5. This approach has the advantage that, as opposed to adding the turbulent transport flux only to the mass conservation equation, fully conserves linear and angular momentum, a vital property to study the protoplanetary disk problem. As a result of the angular momentum conservation, the turbulent transport model implicitly captures the effects of in-plane epicyclic oscillations as predicted by Youdin & Lithwick (2007), i.e., the weakening of dust turbulent transport in moderately coupled environments ($St \gtrsim 1$). Due to the implicit nature, this is also the case if the flow deviates from being purely Keplerian, e.g., inside the Hill sphere of an embedded planet. As a result, we also accurately capture the turbulent redistribution of dust mass and angular momentum (i.e., the dust accretion behavior) inside the planetary Hill sphere and a potential circumplanetary disk (CPD), in moderately coupled environments of a gap-opening planet. A property that the gradient diffusion approach does not have. Our model also correctly reproduces the dust distribution in the vertical equilibrium solution in both the strong-coupling limit ($St \ll 1$) and the weak coupling limit ($St \gg 1$). In practice, modeling the dust component as a fluid with non-zero pressure also simplifies the numerical treatment because specialized pressureless solvers can be omitted and standard (gas) fluid solvers can be used instead. Using this approach, we studied observational signatures of planet-induced dust stirring and turbulent transport in synthetic ALMA (sub-)mm-continuum observations. Our main findings are the following:

- In our three-dimensional radiative hydrodynamic simulations, we identify distinct flow structures in the millimeter-size dust in the surroundings of a giant planet, which are driven by the meridional circulation of the gas. These dust flow structures are inherently three-dimensional, vary strongly in space, leading to disk asymmetries. We find these distinct flow structures to be only marginally affected by background turbulence.

- We quantify the planetary dust stirring by measuring an effective diffusivity δ_{eff} and find it to vary strongly both radially and azimuthally, with two distinct maxima at two opposing sides of the planet. We find the planetary mixing to produce azimuthally averaged values in the range $\delta_{\mathrm{eff}} \sim 5 \cdot 10^{-3} - 2 \cdot 10^{-2}$ and local peaks with values up to $\delta_{\mathrm{eff}} \sim 3 \cdot 10^{-1}$ for a Jupiter-mass planet. The effective diffusivity scales with the planet mass and if the diffusivity of the background turbulence is large enough in relation to the planet mass, i.e., the turbulent alpha is larger than the effective diffusivity ($\alpha > \delta_{\mathrm{eff}}$), the effect of planetary stirring on the vertical dust scale height is *drowned* in the turbulent background.

- In our synthetic ALMA continuum observations, we find the angular resolution of ALMA to only be sufficient to resolve the vertical structure of our model if turbulent transport is relatively strong. We were unable to make the planetary-induced vertical dust structures visible in the synthetic observations because we found the requirements on angular resolution and contrast/sensitivity to be too stringent for ALMA. In near face-on observations, we confirm Speedie et al. (2022) and the capability of ALMA to detect planetary spirals, at least the outer arm.

- We find the total disk mass observationally obtained from using the optically thin approximation to be only weakly affected by the strength of turbulent transport. However, as a result of the disks being marginally optically thick, the optically thin dust masses decrease with inclination i and is roughly proportional to $\cos(i)$.

- In an edge-on observation ($i = 90^\circ$), the observed vertical disk scale height of the millimeter continuum emission of the disk overestimates the underlying hydrodynamic scale height by a factor of $\sim 2.5 - 3$. Not accounting for this difference could result in an overestimation of the vertical strength of turbulent transport in real observations.

Chapter 9

Summary and Outlook

In this thesis, we studied the dynamics and distribution of dust grains in protoplanetary disks and their influence on astronomical observations. In recent years, astronomers have captured images of protoplanetary disks at unprecedented resolutions, uncovering a wealth of details. Since these observations often probe the distribution of dust, their interpretation requires accurate models of dust dynamics beyond the capabilities of simple stationary and axisymmetric analytical disk models. The models and results presented in this thesis allow for drawing more accurate conclusions about the detailed physical conditions in protoplanetary disks and help to constrain the initial and boundary conditions for planet formation. Moreover, our results provide insights into the observational signatures of yet undetected forming planets. In detail, our findings are the following:

- Motivated by limitations of earlier gradient diffusion models, we present in Chapter 5 a novel model for dust turbulent transport in protoplanetary disks. We propose new dynamical equations that allow for non-local turbulent dust transport in a background of homogeneous and isotropic turbulence. The presented model improves upon earlier models by conserving angular momentum, implicitly capturing orbital effects, and removing the ambiguity of whether turbulence causes diffusion of either the absolute dust density or the dust concentration. Furthermore, we recover earlier models in special limiting cases, setting them into context and thus improving the understanding of turbulent dust dynamics in protoplanetary disks. Future work should focus on generalizing the approach to more realistic inhomogeneous and anisotropic turbulence. As elaborated in Sec. 3.5, detailed models of turbulence beyond the α-disk model are highly desirable to advance the field. Because of the complexity of realistic disk turbulence, we expect analytical approaches in this direction to likely be futile. Thus, we propose a data-driven approach that makes use of our mean-field formalism and infers model quantities like the turbulent pressure tensor via statistical analysis of resolved (local) hydrodynamic simulations of turbulent protoplanetary disks. Such an approach would allow for global simulations of protoplanetary disks with realistic physics of turbulence, while significantly reducing computational requirements compared to fully resolved simulations.
- In Chapter 6, we use an analytical disk model incorporating dust dynamics to explain the lack of refractory carbon in the inner regions of the Solar System today. We analyze various decomposition mechanisms, such as photolysis and irreversible sublimation, and constrain the conditions of the early solar disk which lead to depletion as observed today. We present an explicit timescale for carbon depletion as a function of disk parameters. We find the depletion timescale to be as short as $\tau_c^{\mathrm{eff}} = 158$ kyr at 1 au, which coincides with the optimistic upper limit needed to reproduce today's refractory carbon abundance with the aforementioned mechanisms alone. However, we also find periodic stellar luminosity

outbursts to further decrease the carbon mass fraction by a factor of ten in the inner disk up to about four astronomical units and thus compensate for the inhibiting effects of dust transport. In conclusion, we demonstrate that under certain conditions, photo- and thermally-induced decomposition in combination with stellar luminosity outbursts in the first million years of Solar System formation, can reproduce the carbon abundances observed today. Future studies should build on our findings to improve our understanding of the early evolution of the Solar System. We highlight the work of Vaikundaraman et al. (2022), who study the depletion of carbonaceous material numerically, using a Monte Carlo approach and additionally include dust evolution and explicit turbulent transport, improving the physics of the model.

- In Chapter 7 and Chapter 8, we focus on observable signatures of a giant planet in millimeter continuum observations of protoplanetary disks. In recent years, advanced radio interferometers have revealed a wealth of substructures in protoplanetary disks. Such substructures can potentially be explained by the presence of planets. However, so far only very few planets have actually been linked to substructures in disks. The goal of our work is to provide novel insights regarding the morphology of substructures caused by a planet to better identify substructures that are indeed caused by a planet. We do this by means of novel three-dimensional radiative two-fluid (gas + 1 mm size dust) hydrodynamic simulations with an embedded giant planet, which have not been carried out to study protoplanetary disks before. We then produce synthetic millimeter continuum observations of our simulations that allow for the analysis of observable disk features caused by an unseen giant planet.
  Our first study, which we present in Chapter 7, reveals that planets above the mass of Neptune, open up an annular gap in the dust distribution. We quantified the width of the gap by establishing an empirical relation between the gap width and the planet mass, helping to constrain the mass of a potential planet in observed protoplanetary disks. Furthermore, we find that giant planets cause significant vertical dust stirring, lifting dust far above the disk midplane, resulting in a thicker dust disk compared to disks without a planet. Moreover, we point out that relying on the optically thin approximation for the determination of disk masses can underestimate the total disk mass by a factor of a few up to a factor of ten. This has important consequences for planet formation because the total disk mass provides the mass reservoir from which planets can form.
  For the study in Chapter 8, we combine the turbulent dust transport model presented in Chapter 5 with the hydrodynamical simulations in Chapter 7, and we study the three-dimensional dust morphology in protoplanetary disks under the influence of both turbulent and planetary stirring. We find distinct flow structures caused by the presence of a planet, revealing the three-dimensional nature of dust flows around a planet in protoplanetary disks. We quantify the planet's potential for dust stirring by measuring an effective diffusivity. While we find the effective diffusivity to vary strongly in space, we find azimuthally averaged values in a range $\delta_{\mathrm{eff}} \sim 5 \cdot 10^{-3} - 2 \cdot 10^{-2}$ for a Jupiter-mass planet. We also investigated whether the increase of the dust disk thickness caused by either turbulence or the planet is resolvable in millimeter continuum observations. We find an observable effect only at the highest levels of turbulence $\alpha \gtrsim 4 \cdot 10^{-3}$, but not at lower values. Signatures of planetary dust stirring were all below the resolution or sensitivity limits.
  Overall, we provide detailed insights into the mechanism of planetary dust stirring and possible observational consequences, helping to interpret astronomical observations. In the future, our study should be extended to cover a larger parameter space. Furthermore, the physical accuracy of the hydrodynamic simulations would benefit from incorporating even more physics, like a realistic dust size distribution, more advanced temperature calculation, or chemistry. However, considering the limitations set by the currently available computational resources, improved methods are highly desirable when incorporating more

complex physics and/or chemistry.

Bibliography

Adams, F. C., Lada, C. J., & Shu, F. H. 1987, Astrophysical Journal, 312, 788

Alata, I., Cruz-Diaz, G. A., Muñoz Caro, G. M., & Dartois, E. 2014, Astronomy and Astrophysics, 569, 119

Alata, I., Jallat, A., Gavilan, L., et al. 2015, Astronomy and Astrophysics, 584, 123

Alessio, P. D., & Woolum, D. S. 2005, Chondrites and the Protoplanetary Disk, 341, 353

Alexander, C. M., Nittler, L. R., Davidson, J., & Ciesla, F. J. 2017, Meteoritics and Planetary Science, 52, 1797

Alexander, R., Pascucci, I., Andrews, S., Armitage, P., & Cieza, L. 2014, in Protostars and Planets VI, ed. H. Beuther, R. S. Klessen, C. P. Dullemond, & T. Henning (University of Arizona Press, Tucson, AZ), 475–496

Allegre, C., Manhes, G., & Lewin, E. 2001, Earth and Planetary Science Letters, 185, 49

ALMA Partnership, Brogan, C. L., Pérez, L. M., et al. 2015, Astrophysical Journal Letters, 808, L3

Altwegg, K., Balsiger, H., Bar-Nun, A., et al. 2015, Science, 347, 3

Anderson, D. E., Bergin, E. A., Blake, G. A., et al. 2017, The Astrophysical Journal, 845, 13

Andrews, S. M. 2020, Annual Review of Astronomy and Astrophysics, 58, 483

Andrews, S. M., Rosenfeld, K. A., Kraus, A. L., & Wilner, D. J. 2013, The Astrophysical Journal, 771, 129

Andrews, S. M., Terrell, M., Tripathi, A., et al. 2018a, The Astrophysical Journal, 865, 157

Andrews, S. M., Huang, J., Pérez, L. M., et al. 2018b, The Astrophysical Journal, 869, L41

Ansdell, M., Williams, J. P., Marel, N. v. d., et al. 2016, The Astrophysical Journal, 828, 46

Ansdell, M., Williams, J. P., Trapman, L., et al. 2018, The Astrophysical Journal, 859, 21

Arlt, R., & Urpin, V. 2004, Astronomy and Astrophysics, 426, 755

Armitage, P. J. 2010, Astrophysics of planet formation (Cambridge, UK: Cambridge University Press)

—. 2011, Annual Review of Astronomy and Astrophysics, 49, 195

Ataiee, S., Baruteau, C., Alibert, Y., & Benz, W. 2018, Astronomy and Astrophysics, 615, 1

Audard, M., Ábrahám, P., Dunham, M. M., et al. 2014, in Protostars and Planets VI, ed. H. Beuther, R. S. Klessen, C. P. Dullemond, & T. Henning (University of Arizona Press, Tucson, AZ)

Avenhaus, H., Quanz, S. P., Garufi, A., et al. 2018, The Astrophysical Journal, 863, 44

Ayliffe, B. A., Laibe, G., Price, D. J., & Bate, M. R. 2012, Monthly Notices of the Royal Astronomical Society, 423, 1450

Bae, J., Zhu, Z., & Hartmann, L. 2017, The Astrophysical Journal, 850, 201

Bai, X. N., & Stone, J. M. 2013, Astrophysical Journal, 769, 76

Balbus, S. A., & Hawley, J. F. 1991, The Astrophysical Journal, 376, 214

—. 1998, Reviews of Modern Physics, 70, 1

Balbus, S. A., & Papaloizou, J. C. B. 1999, The Astrophysical Journal, 521, 650

Ballering, N. P., & Eisner, J. A. 2019, The Astronomical Journal, 157, 144

Barge, P., Ricci, L., Carilli, C. L., & Previn-Ratnasingam, R. 2017, Astronomy and Astrophysics, 605

Barranco, J. A., & Marcus, P. S. 2005, The Astrophysical Journal, 623, 1157

Barraza-Alfaro, M., Flock, M., Marino, S., & Pérez, S. 2021, Astronomy and Astrophysics, 653, A113

Beckwith, S. V. W., Chini, R. S., & Güsten, R. 1990, The Astronomical Journal, 99, 924

Bell, K. R., & Lin, D. N. C. 1994, The Astrophysical Journal, 427, 987

Benítez-Llambay, P., Krapp, L., & Pessah, M. E. 2019, The Astrophysical Journal Supplement Series, 241, 25

Bergin, E. A., Blake, G. A., Ciesla, F., Hirschmann, M. M., & Li, J. 2015, Proceedings of the National Academy of Sciences of the United States of America, 112, 8965

Bergin, E. A., & Tafalla, M. 2007, Annual Review of Astronomy and Astrophysics, 45, 339

Bergin, E. A., & Williams, J. P. 2017, in Formation, Evolution, and Dynamics of Young Solar Systems (Springer), 1–38

Bergin, E. A., Cleeves, L. I., Gorti, U., et al. 2013, Nature, 493, 644

Bertrang, G. H., & Wolf, S. 2017, Monthly Notices of the Royal Astronomical Society, 469, 2869

Bi, J., Lin, M.-K., & Dong, R. 2021, The Astrophysical Journal, 912, 107

Biferale, L., Crisanti, A., Vergassola, M., & Vulpiani, A. 1995, Physics of Fluids, 7, 2725

Binkert, F. 2019, Master's thesis, ETH Zurich

Binkert, F., Szulágyi, J., & Birnstiel, T. 2021, Monthly Notices of the Royal Astronomical Society, 506, 5969

—. 2023, Monthly Notices of the Royal Astronomical Society, 523, 55

Birnstiel, T. 2011, PhD thesis, University of Heidelberg

Birnstiel, T., & Andrews, S. M. 2014, Astrophysical Journal, 780, 153

Birnstiel, T., Dullemond, C. P., & Brauer, F. 2010, Astronomy and Astrophysics, 513, A79

Birnstiel, T., Klahr, H., & Ercolano, B. 2012, Astronomy and Astrophysics, 539, 148

Birnstiel, T., Ormel, C. W., & Dullemond, C. P. 2011, Astronomy and Astrophysics, 525, A11

Birnstiel, T., Dullemond, C. P., Zhu, Z., et al. 2018, The Astrophysical Journal, 869, L45

Bitsch, B., Crida, A., Morbidelli, A., Kley, W., & Dobbs-Dixon, I. 2013, Astronomy and Astrophysics, 549, A124

Bitsch, B., Morbidelli, A., Johansen, A., et al. 2018, Astronomy and Astrophysics, 612, 1

Bitsch, B., Morbidelli, A., Lega, E., & Crida, A. 2014, Astronomy and Astrophysics, 564, A135

Blackman, E. G., & Field, G. B. 2003, Physics of Fluids, 15, 1

Blum, J. 2010, Research in Astronomy and Astrophysics, 10, 1199

Blum, J., Gundlach, B., Krause, M., et al. 2017, Monthly Notices of the Royal Astronomical Society, 469, S755

Bodenheimer, P., & Pollack, J. B. 1986, Icarus, 67, 391

Bohren, C. F., & Huffman, D. R. 1984, Nature, 307, 575

Boss, A. P. 1997, Science, 276, 1836

Bouchut, F., Jin, S., & Li, X. 2003, SIAM Journal on Numerical Analysis, 41, 135

Boudet, N., Mutschke, H., Nayral, C., et al. 2005, The Astrophysical Journal, 633, 272

Bowler, B. P. 2016, Publications of the Astronomical Society of the Pacific, 128, 1

Carballido, A., Bai, X. N., & Cuzzi, J. N. 2011, Monthly Notices of the Royal Astronomical Society, 415, 93

Carballido, A., Cuzzi, J. N., & Hogan, R. C. 2010, Monthly Notices of the Royal Astronomical Society, 405, 2339

Carballido, A., Fromang, S., & Papaloizou, J. 2006, Monthly Notices of the Royal Astronomical Society, 373, 1633

Cassan, A., Kubas, D., Beaulieu, J. P., et al. 2012, Nature, 481, 167

Chambers, J. E. 2004, Earth and Planetary Science Letters, 223, 241

Champney, J. M., & Cuzzi, J. N. 1990, 28th Aerospace Sciences Meeting, 1990

Charnoz, S., Fouchet, L., Aleon, J., & Moreira, M. 2011, Astrophysical Journal, 737, 33

Chen, K., & Lin, M.-K. 2020, The Astrophysical Journal, 891, 132

Chiang, E., Lithwick, Y., Murray-Clay, R., et al. 2007, in Protostars and Planets V, ed. B. Reipurth, D. Jewitt, & K. Keil (University of Arizona Press, Tucson, AZ), 895

Chiang, E. I., & Goldreich, P. 1997, The Astrophysical Journal, 490, 368

Christiaens, V., Cantalloube, F., Casassus, S., et al. 2019, The Astrophysical Journal, 877, L33

Chyba, C. F., Thomas, P. J., Brookshaw, L., & Sagan, C. 1990, Science, 249, 366

Ciesla, F. J. 2005, in Chondrites and the Protoplanetary Disk, ed. A. N. Krot, E. R. D. Scott, & B. Reipurth, Vol. 341 (Astronomical Society of the Pacific), 811–820

—. 2009, Icarus, 200, 655

—. 2010, Astrophysical Journal, 723, 514

Cieza, L. A., Casassus, S., Tobin, J., et al. 2016, Nature, 535, 258

Cieza, L. A., Ruíz-Rodríguez, D., Hales, A., et al. 2019, Monthly Notices of the Royal Astronomical Society, 482, 698

Commerçon, B., Teyssier, R., Audit, E., Hennebelle, P., & Chabrier, G. 2011, Astronomy and Astrophysics, 529, A35

Connelly, J. N., Bollard, J., & Bizzarro, M. 2017, Geochimica et Cosmochimica Acta, 201, 345

Crida, A., Morbidelli, A., & Masset, F. 2006, Icarus, 181, 587

Cumming, A., Butler, R. P., Marcy, G. W., et al. 2008, Publications of the Astronomical Society of the Pacific, 120, 531

Cuzzi, J. N., Dobrovolskis, A. R., & Champney, J. M. 1993, Icarus, 106, 102

D'Angelo, G., & Lissauer, J. J. 2018, Formation of giant planets, ed. H. J. Deeg & J. A. Belmonte (Springer), 140

de Val-Borro, M., Edgar, R. G., Artymowicz, P., et al. 2006, Monthly Notices of the Royal Astronomical Society, 370, 529–558

Dipierro, G., & Laibe, G. 2017, Monthly Notices of the Royal Astronomical Society, 469, 1932

Dipierro, G., Laibe, G., Price, D. J., & Lodato, G. 2016, Monthly Notices of the Royal Astronomical Society: Letters, 459, L1

Dipierro, G., Ricci, L., Pérez, L., et al. 2018, Monthly Notices of the Royal Astronomical Society, 475, 5296

Dobrovolskis, A. R., Dacles-Mariani, J. S., & Cuzzi, J. N. 1999, Journal of Geophysical Research: Planets, 104, 30805

Dong, R., & Fung, J. 2017, The Astrophysical Journal, 835, 146

Dong, R., Li, S., Chiang, E., & Li, H. 2017, The Astrophysical Journal, 843, 127

—. 2018, The Astrophysical Journal, 866, 110

Dong, R., Zhu, Z., Rafikov, R. R., & Stone, J. M. 2015a, Astrophysical Journal Letters, 809, L5

Dong, R., Zhu, Z., & Whitney, B. 2015b, Astrophysical Journal, 809, 93

Dong, S., & Zhu, Z. 2013, Astrophysical Journal, 778, 53

Draine, B. T. 2003, The Astrophysical Journal, 598, 1026

—. 2006, The Astrophysical Journal, 636, 1114

Drake, M. J., & Righter, K. 2002, Nature, 416, 39

Drążkowska, J., Li, S., Birnstiel, T., Stammler, S. M., & Li, H. 2019, The Astrophysical Journal, 885, 91

Drążkowska, J., Bitsch, B., Lambrechts, M., et al. 2022, arXiv e-prints, arXiv:2203.09759

Dubrulle, B., Morfill, G., & Sterzik, M. 1995, Icarus, 114, 237

Dullemond, C. P., & Dominik, C. 2004, Astronomy and Astrophysics, 421, 1075

Dullemond, C. P., Juhasz, A.; Pohl, A., Sereshti, F.; Shetty, R., et al. 2012, RADMC-3D: A multi-purpose radiative transfer tool

Dullemond, C. P., & Penzlin, A. B. 2018, Astronomy and Astrophysics, 609, 50

Dullemond, C. P., Birnstiel, T., Huang, J., et al. 2018, The Astrophysical Journal, 869, L46

Duncan, M. J., & Levison, H. F. 1997, Science, 276, 1670

Dürmann, C., & Kley, W. 2015, Astronomy and Astrophysics, 574, A52

Duschl, W. J., Gail, H.-P., & Tscharnuter, W. M. 1996, Astronomy & Astrophysics, 312, 624

Edgar, R. G., & Quillen, A. C. 2008, Monthly Notices of the Royal Astronomical Society, 387, 387

Einstein, A. 1905, Ann. d. Phys., 322, 549–560

Ercolano, B., & Pascucci, I. 2017, Royal Society Open Science, 4, 170114

Evans, N. J. 1999, Annual Review of Astronomy and Astrophysics, 37, 311

Fan, L.-S., & Chao, Z. 1998, Principles of Gas–Solid Flows (Cambridge University Press)

Favre, A. J. 1965, The Equations of Compressible Turbulent Gases, Tech. rep., INSTlTUT DE MECANIQUE STATISTlQUE DE LA TURBULENCE, Marseille, France

Fedele, D., Van Den Ancker, M. E., Henning, T., Jayawardhana, R., & Oliveira, J. M. 2010, Astronomy and Astrophysics, 510, 72

Fedele, D., Carney, M., Hogerheijde, M. R., et al. 2017, Astronomy & Astrophysics, 600, A72

Finocchi, F., Gail, H.-P., & Duschl, W. 1997, Astronomy and Astrophysics, 325, 1264

Fischer, D. A., & Valenti, J. 2005, The Astrophysical Journal, 622, 1102

Fischer, R. A., Cottrell, E., Hauri, E., Lee, K. K., & Le Voyer, M. 2020, Proceedings of the National Academy of Sciences of the United States of America, 117, 8743

Flaherty, K., Hughes, A. M., Simon, J. B., et al. 2020, The Astrophysical Journal, 895, 109

Flaherty, K. M., Hughes, A. M., Rosenfeld, K. A., et al. 2015, Astrophysical Journal, 813, 99

Flaherty, K. M., Hughes, A. M., Teague, R., et al. 2018, The Astrophysical Journal, 856, 117

Flaherty, K. M., Hughes, A. M., Rose, S. C., et al. 2017, The Astrophysical Journal, 843, 150

Flock, M., Nelson, R. P., Turner, N. J., et al. 2017, The Astrophysical Journal, 850, 131

Flock, M., Ruge, J. P., Dzyurkevich, N., et al. 2015, Astronomy and Astrophysics, 574, 1

Fomenkova, M. N., Chang, S., & Mukhin, L. M. 1994, Geochimica et Cosmochimica Acta, 58, 4503

Fouchet, L., Gonzalez, J.-F., & Maddison, S. T. 2010, Astronomy & Astrophysics, 518, A16

Fouchet, L., Maddison, S., Gonzalez, J.-F., et al. 2007, Astronomy & Astrophysics, 474, 1037–1047

Fox, R. O. 2003, Computational Models for Turbulent Reacting Flows, 1st edn. (Cambridge: Cambridge University Press)

Frank, J., King, A. R., & Raine, D. J. 2002, Accretion Power in Astrophysics (Cambridge University Press)

Fressin, F., Torres, G., Charbonneau, D., et al. 2013, Astrophysical Journal, 766, 81

Fromang, S., & Nelson, R. P. 2009, Astronomy and Astrophysics, 496, 597

Fromang, S., & Papaloizou, J. 2006, Astronomy and Astrophysics, 452, 751

Fulton, B. J., Petigura, E. A., Howard, A. W., et al. 2017, The Astronomical Journal, 154, 109

Fulton, B. J., Rosenthal, L. J., Hirsch, L. A., et al. 2021, The Astrophysical Journal Supplement Series, 255, 14

Fung, J., Artymowicz, P., & Wu, Y. 2015, Astrophysical Journal, 811, 101

Fung, J., & Chiang, E. 2016, The Astrophysical Journal, 832, 105

Gail, H.-P. 2001, Astronomy & Astrophysics, 378, 192

Gail, H. P., & Trieloff, M. 2017, Astronomy and Astrophysics, 606, A16

Galametz, M., Maury, A. J., Valdivia, V., et al. 2019, Astronomy and Astrophysics, 632, A5

Garaud, P., Barriere-Fouchet, L., & Lin, D. N. C. 2004, The Astrophysical Journal, 603, 292

Garufi, A., Benisty, M., Pinilla, P., et al. 2018, Astronomy and Astrophysics, 620, 1

Gaudi, B. S., Meyer, M., & Christiansen, J. 2021, in ExoFrontiers; Big Questions in Exoplanetary Science, ed. N. Madhusudhan (IOP Publishing), 2–1

Geiss, J. 1987, Astronomy and Astrophysics, 187, 859

Goldreich, P., & Lynden-Bell, D. 1965, Monthly Notices of the Royal Astronomical Society, 130, 97

Goldreich, P., & Tremaine, S. 1980, The Astrophysical Journal, 241, 425

Goldreich, P., & Ward, W. R. 1973, The Astrophysical Journal, 183, 1051

Gole, D. A., Simon, J. B., Li, R., Youdin, A. N., & Armitage, P. J. 2020, The Astrophysical Journal, 904, 132

Gonzalez, J. F., Laibe, G., Maddison, S. T., Pinte, C., & Ménard, F. 2015, Monthly Notices of the Royal Astronomical Society: Letters, 454, L36

Gonzalez, J. F., Pinte, C., Maddison, S. T., & Ménard, F. 2012, Astronomy & Astrophysics, 547, A58

Goodman, J., & Pindor, B. 2000, Icarus, 148, 537

Gradie, J., & Tedesco, E. 1982, Science, 216, 1405

Grevesse, N., Asplund, M., Sauval, A. J., & Scott, P. 2010, Astrophysics and Space Science, 328, 179

Guilloteau, S., Dutrey, A., Wakelam, V., et al. 2012, Astronomy and Astrophysics, 548, 70

Güttler, C., Blum, J., Zsom, A., Ormel, C. W., & Dullemond, C. P. 2010, Astronomy and Astrophysics, 513, 57

Haffert, S. Y., Bohn, A. J., de Boer, J., et al. 2019, Nature Astronomy, 3, 749

Hartmann, L., & Kenyon, S. J. 1996, Annual Review of Astronomy and Astrophysics, 34, 207

Hayashi, C. 1981, Progress of Theoretical Physics Supplement, 70, 35

He, M. Y., Ford, E. B., & Ragozzine, D. 2019, Monthly Notices of the Royal Astronomical Society, 490, 4575

—. 2021, The Astronomical Journal, 161, 16

Hendler, N., Pascucci, I., Pinilla, P., et al. 2020, The Astrophysical Journal, 895, 126

Henning, T., & Semenov, D. 2013, Chemical Reviews, 113, 9016

Henning, T., & Stognienko, R. 1996, Astronomy and Astrophysics, 211, 291

Herbig, G. H. 1966, Vistas in Astronomy, 8, 109

Hildebrand, R. H. 1983, Quarterly Journal of the Royal Astronomical Society, 24, 267

Hillenbrand, L. A. 2005, arXiv e-prints, astro-ph/0511083

Hinze, J. 1959, Turbulence, 2nd edn. No. 03 (New York: McGraw Hill)

Hirschmann, M. M. 2018, Earth and Planetary Science Letters, 502, 262

Howard, A. W., Marcy, G. W., Bryson, S. T., et al. 2012, Astrophysical Journal, Supplement Series, 201, 4

Huang, J., Andrews, S. M., Pérez, L. M., et al. 2018, The Astrophysical Journal, 869, L43

Huang, P., & Bai, X.-N. 2022, Astrophysical Journal Supplement Series, 262, 11

Hughes, A. M., Wilner, D. J., Andrews, S. M., Qi, C., & Hogerheijde, M. R. 2011, Astrophysical Journal, 727, 85

Humphries, J., & Nayakshin, S. 2018, Monthly Notices of the Royal Astronomical Society, 477, 593

—. 2019, Monthly Notices of the Royal Astronomical Society, 489, 5187

Ida, S., & Lin, D. N. C. 2004, The Astrophysical Journal, 604, 388

Isella, A., Benisty, M., Teague, R., et al. 2019, The Astrophysical Journal, 879, L25

Isella, A., & Turner, N. J. 2018, The Astrophysical Journal, 860, 27

Jewitt, D. 2002, The Astronomical Journal, 123, 1039

Jin, S., Li, S., Isella, A., Li, H., & Ji, J. 2016, The Astrophysical Journal, 818, 76

Johansen, A., & Klahr, H. 2005, The Astrophysical Journal, 634, 1353

Johansen, A., & Lambrechts, M. 2017, Annual Review of Earth and Planetary Sciences, 45, 359

Johansen, A., Oishi, J. S., Low, M. M. M., et al. 2007, Nature, 448, 1022

Johansen, A., Youdin, A., & Klahr, H. 2009, Astrophysical Journal, 697, 1269

Jones, R. H., Lee, T., Connolly Jr., H. C., Love, S. G., & Shang, H. 2000, in Protostars and planets IV, ed. V. Mannings, A. P. Boss, & S. S. Russell (University of Arizona Press, Tucson, AZ), 927–962

Jura, M. 2006, The Astrophysical Journal, 653, 613

Kalas, P., Graham, J. R., Chiang, E., et al. 2008, Science, 322, 1345

Kanagawa, K. D., Muto, T., Tanaka, H., et al. 2016, Publications of the Astronomical Society of Japan, 68, 1

Kanagawa, K. D., Tanaka, H., Muto, T., & Tanigawa, T. 2017, Publications of the Astronomical Society of Japan, 69, 97

Kane, S. R. 2011, Icarus, 214, 327

Keppler, M., Benisty, M., Müller, A., et al. 2018, Astronomy and Astrophysics, 617, A44

Klahr, H., & Bodenheimer, P. 2006, The Astrophysical Journal, 639, 432

Klahr, H., & Hubbard, A. 2014, Astrophysical Journal, 788

Klahr, H., & Schreiber, A. 2021, The Astrophysical Journal, 911, 9

Klarmann, L., Ormel, C. W., & Dominik, C. 2018, Astronomy and Astrophysics, 618, L1

Kley, W. 1989, Astronomy and Astrophysics, 208, 98

Kley, W., & Dirksen, G. 2006, a&a, 447, 369

Kley, W., D'Angelo, G., & Henning, T. 2001, The Astrophysical Journal, 547, 457

Kley, W., & Nelson, R. P. 2012, Annual Review of Astronomy and Astrophysics, 50, 211

Kokubo, E., & Ida, S. 1998, Icarus, 131, 171

Krapp, L., Kratter, K. M., & Youdin, A. N. 2021, The Astrophysical Journal, 928, 156

Kratter, K., & Lodato, G. 2016, Annual Review of Astronomy and Astrophysics, 54, 271

Kress, M. E., Tielens, A. G., & Frenklach, M. 2010, Advances in Space Research, 46, 44

Kretke, K. A., & Lin, D. N. C. 2007, The Astrophysical Journal, 664, L55

Krijt, S., & Ciesla, F. J. 2016, The Astrophysical Journal, 822, 111

Krot, A. N., Amelin, Y., Cassen, P., & Meibom, A. 2005, Nature, 436, 989

Kunimoto, M., & Matthews, J. M. 2020, The Astronomical Journal, 159, 248

Kuwahara, A., Kurokawa, H., & Ida, S. 2019, Astronomy and Astrophysics, 623, A179

Laibe, G., Bréhier, C. E., & Lombart, M. 2020, Monthly Notices of the Royal Astronomical Society, 494, 5134

Lambrechts, M., & Johansen, A. 2014, Astronomy and Astrophysics, 572, A107

Laplace, P. 1798, Traité de mécanique céleste (Paris: De L'Imprimerie de Crapelet)

Lee, J.-E., Bergin, E. A., & Nomura, H. 2010, The Astrophysical Journal Letters, 710, 21

Lenz, C. T., Klahr, H., Birnstiel, T., Kretke, K., & Stammler, S. 2020, Astronomy and Astrophysics, 640, A61

Lesieur, M. 1997, Turbulence in Fluids (Dordrecht: Springer)

Lesur, G., Ercolano, B., Flock, M., et al. 2022, arXiv e-prints, arXiv:2203.09821

Lesur, G. R., & Latter, H. 2016, Monthly Notices of the Royal Astronomical Society, 462, 4549

LeVeque, R. J. 2002, Finite Volume Methods for Hyperbolic Problems (Cambridge University Press)

—. 2004, Journal of Hyperbolic Differential Equations, 01, 315

Li, A., & Greenberg, J. M. 1997, Astronomy & Astrophysics, 323, 566

Li, J., Bergin, E. A., Blake, G. A., Ciesla, F. J., & Hirschmann, M. M. 2021, Science Advances, 7, eabd3632

Lichtenberg, T., Drążkowska, J., Schönbächler, M., Golabek, G. J., & Hands, T. O. 2021, Science, 371, 365

Lichtenberg, T., & Krijt, S. 2021, The Astrophysical Journal Letters, 913, L20

Lin, D. N. C., & Papaloizou, J. 1979, Monthly Notices of the Royal Astronomical Society, 186, 799

Lin, D. N. C., & Papaloizou, J. 1986, The Astrophysical Journal, 309, 846

Lin, D. N. C., & Papaloizou, J. C. B. 1984, The Astrophysical Journal, 285, 818

—. 1993, in Protostars and Planets III, ed. E. Levy & J. Lunine (University of Arizona Press), 749

Lin, J. W., Lee, E. J., & Chiang, E. 2018, Monthly Notices of the Royal Astronomical Society, 480, 4338

Lin, M. K. 2019, Monthly Notices of the Royal Astronomical Society, 485, 5221

Lissauer, J. J. 1993, Annual Review of Astronomy and Astrophysics, 31, 129

Liu, B., Ormel, C. W., & Johansen, A. 2019, Astronomy & Astrophysics, 624, A114

Liu, H. B. 2019, The Astrophysical Journal, 877, L22

Lynden-Bell, D., & Pringle, J. E. 1974, Monthly Notices of the Royal Astronomical Society, 168, 603

Lyra, W. 2014, Astrophysical Journal, 789, 1

Mamajek, E. E., Meyer, M. R., Hinz, P. M., et al. 2004, The Astrophysical Journal, 612, 496

Manger, N., Klahr, H., Kley, W., & Flock, M. 2020, Monthly Notices of the Royal Astronomical Society, 499, 1841

Marois, C., Macintosh, B., Barman, T., et al. 2008, Science, 322, 1348

Martin, R. G., & Livio, M. 2012, Monthly Notices of the Royal Astronomical Society: Letters, 425, 1

Marty, B. 2012, Earth and Planetary Science Letters, 313-314, 56

Masset, F. S., & Papaloizou, J. C. B. 2003, The Astrophysical Journal, 588, 494

Mathis, J. S., Rumpl, W., & Nordsieck, K. H. 1977, The Astrophysical Journal, 217, 425

Mayor, M., & Queloz, D. 1995, Nature, 378, 355

Mayor, M., Marmier, M., Lovis, C., et al. 2011, eprint: arXiv:1109.2497

McKee, C. F., & Ostriker, E. C. 2007, Annual Review of Astronomy and Astrophysics, 45, 565

Mcmullin, J. P., Waters, B., Schiebel, D., Young, W., & Golap, K. 2007, Astronomical Data Analysis Software and Systems XVI, 376, 127

Meheut, H., Meliani, Z., Varniere, P., & Benz, W. 2012, Astronomy and Astrophysics, 545, 1

Mignone, A., Flock, M., & Vaidya, B. 2019, The Astrophysical Journal Supplement Series, 244, 38

Miotello, A., Kamp, I., Birnstiel, T., Cleeves, L. I., & Kataoka, A. 2022, arXiv e-prints, arXiv:2203.09818

Miotello, A., van Dishoeck, E. F., Williams, J. P., et al. 2017, Astronomy and Astrophysics, 599, A113

Morbidelli, A., Lunine, J. I., O'Brien, D. P., Raymond, S. N., & Walsh, K. J. 2012, Annual Review of Earth and Planetary Sciences, 40, 251

Mulders, G. D. 2018, Planet Populations as a Function of Stellar Properties, ed. H. J. Deeg & J. A. Belmonte (Springer International Publishing AG), 153

Mulders, G. D., Pascucci, I., & Apai, D. 2015, Astrophysical Journal, 814, 130

Mulders, G. D., Pascucci, I., Manara, C. F., et al. 2017, The Astrophysical Journal, 847, 31

Müller, A., Keppler, M., Henning, T., et al. 2018, Astronomy & Astrophysics, 617, L2

Nakagawa, Y., Sekiya, M., & Hayashi, C. 1986, ICARUS, 67, 375

Nakano, H., Kouchi, A., Tachibana, S., & Tsuchiyama, A. 2003, The Astrophysical Journal, 592, 1252

Narang, M., Manoj, P., Furlan, E., et al. 2018, The Astronomical Journal, 156, 221

Nelson, R. P., Gressel, O., & Umurhan, O. M. 2013, Monthly Notices of the Royal Astronomical Society, 435, 2610

Oba, M., Mita, H., & Shimoyama, A. 2002, Geochemical Journal, 36, 51

O'dell, C. R., Wen, Z., & Hu, X. 1993, Astrophysical Journal, 410, 696

Ormel, C. W. 2017, The Emerging Paradigm of Pebble Accretion, ed. M. Pessah & G. Oliver (Cham: Springer), 197–228

Ormel, C. W., & Cuzzi, J. N. 2007, Astronomy and Astrophysics, 466, 413

Ormel, C. W., & Liu, B. 2018, Astronomy and Astrophysics, 615, A178

Ormel, C. W., Shi, J. M., & Kuiper, R. 2015, Monthly Notices of the Royal Astronomical Society, 447, 3512

Owen, J. E., & Wu, Y. 2017, The Astrophysical Journal, 847, 29

Paardekooper, S.-J., & Mellema, G. 2004, Astronomy & Astrophysics, 425, L9–L12

—. 2006, Astronomy & Astrophysics, 453, 1129

Paneque-Carreño, T., Miotello, A., Van Dishoeck, E. F., et al. 2023, Astronomy and Astrophysics, 669, 1

Papaloizou, J. C. B., & Pringle, J. E. 1984, Monthly Notices of the Royal Astronomical Society, 208, 721

Patisson, F., Lebas, E., Hanrot, F., Ablitzer, D., & Houzelot, J. L. 2000, Metallurgical and Materials Transactions B: Process Metallurgy and Materials Processing Science, 31, 381

Pavlyuchenkov, Y., & Dullemond, C. P. 2007, Astronomy and Astrophysics, 471, 833

Peña, C. C., Naylor, T., & Morrell, S. 2019, Monthly Notices of the Royal Astronomical Society, 486, 4590

Pérez, L. M., Carpenter, J. M., Andrews, S. M., et al. 2016, Science, 353, 1519

Perez, S., Dunhill, A., Casassus, S., et al. 2015, Astrophysical Journal Letters, 811, L5

Persson, M. 2014a, Current view of protostellar evolution (ENG), doi:https://doi.org/10.6084/m9.figshare.654555.v7

—. 2014b, SEDs of the different protostellar evolutionary stages, doi:https://doi.org/10.6084/m9.figshare.1121574.v2

Petigura, E. A., Howard, A. W., & Marcy, G. W. 2013, Proceedings of the National Academy of Sciences of the United States of America, 110, 19273

Petigura, E. A., Marcy, G. W., Winn, J. N., et al. 2018, The Astronomical Journal, 155, 89

Picogna, G., & Kley, W. 2015, Astronomy & Astrophysics, 584, A110

Pineda, J. E., Szulágyi, J., Quanz, S. P., et al. 2019, ApJ, 871, 48

Pineda, J. E., Arzoumanian, D., André, P., et al. 2022, arXiv:2205.03935

Pinilla, P., Benisty, M., & Birnstiel, T. 2012, Astronomy and Astrophysics, 545, 81

Pinilla, P., Pohl, A., Stammler, S. M., & Birnstiel, T. 2017, The Astrophysical Journal, 845, 68

Pinte, C., Dent, W. R. F., Ménard, F., et al. 2016, The Astrophysical Journal, 816, 25

Pinte, C., Price, D. J., Ménard, F., et al. 2018, The Astrophysical Journal Letters, 860, L13

Pohl, A., Sissa, E., Langlois, M., et al. 2017, Astronomy and Astrophysics, 605, 1

Pollack, J. B., Hubickyj, O., Bodenheimer, P., et al. 1996, Icarus, 124, 62

Rafikov, R. R. 2002, The Astrophysical Journal, 569, 997

—. 2006, The Astrophysical Journal, 648, 666

—. 2017, The Astrophysical Journal, 837, 163

Raymond, S. N., Kokubo, E., Morbidelli, A., Morishima, R., & Walsh, K. J. 2014, in Protostars and Planets VI, ed. H. Beuther, R. S. Klessen, C. P. Dullemond, & T. Henning (University of Arizona Press, Tucson, AZ), 595–618

Regály, Z., Juhász, A., Sándor, Z., & Dullemond, C. P. 2012, Monthly Notices of the Royal Astronomical Society, 419, 1701

Reynolds O. 1895, Philosophical Transactions of the Royal Society of London, 123

Ricci, L., Liu, S.-F., Isella, A., & Li, H. 2018, The Astrophysical Journal, 853, 110

Rice, W. K., Armitage, P. J., Wood, K., & Lodato, G. 2006, Monthly Notices of the Royal Astronomical Society, 373, 1619

Rice, W. K., Lodato, G., Pringle, J. E., Armitage, P. J., & Bonnell, I. A. 2004, Monthly Notices of the Royal Astronomical Society, 355, 543

Riols, A., & Lesur, G. 2018, Astronomy and Astrophysics, 617, A117

Rosotti, G. P., Juhasz, A., Booth, R. A., & Clarke, C. J. 2016, Monthly Notices of the Royal Astronomical Society, 459, 2790

Rosotti, G. P., Tazzari, M., Booth, R. A., et al. 2019, Monthly Notices of the Royal Astronomical Society, 486, 4829

Rosotti, G. P., Teague, R., Dullemond, C., Booth, R. A., & Clarke, C. J. 2020, Monthly Notices of the Royal Astronomical Society, 495, 173

Ruge, J. P., Flock, M., Wolf, S., et al. 2016, Astronomy and Astrophysics, 590

Rybicki, G. B., & Lightman, A. P. 1979, Radiative processes in astrophysics (Wiley)

Safronov, V. 1972, Evolution of the protoplanetary cloud and formation of the earth and the planets (Nerusalem: Keter Publishing House)

Santos, N. C., Israelian, G., & Mayor, M. 2004, Astronomy and Astrophysics, 415, 1153

Schäfer, U., Johansen, A., & Banerjee, R. 2020, Astronomy and Astrophysics, 635, A190

Schäfer, U., Yang, C. C., & Johansen, A. 2017, Astronomy and Astrophysics, 597, 1

Schnee, S., Rosolowsky, E., Foster, J., Enoch, M., & Sargent, A. 2009, Astrophysical Journal, 691, 1754

Schrapler, R., & Henning, T. 2004, The Astrophysical Journal, 614, 960

Scott, E. R. 2007, Annual Review of Earth and Planetary Sciences, 35, 577

Scott, E. R., & Krot, A. N. 2014, in Meteorites and Cosmochemical Processes, ed. A. M. Davis, Vol. 1 (Elsevier), 65–137

Selina, R., McKinnon, M., Beasley, A. J., et al. 2018, SPIE Astronomical Telescopes & Instrumentation, 107001O

Semenov, D., Henning, T., Helling, C., Ilgner, M., & Sedlmayr, E. 2003, Astronomy and Astrophysics, 410, 611

Shakura, N. I., & Sunyaev, R. A. 1973, Symposium - International Astronomical Union, 55, 155

Shariff, K., & Cuzzi, J. N. 2011, Astrophysical Journal, 738, 73

Shu, F. H. 1992, The physics of astrophysics: Gas Dynamics, ed. A. Kelly (Mill Valley, CA 94941: University Science Books)

Siebenmorgen, R., & Heymann, F. 2012, Astronomy and Astrophysics, 543, A23

Siebenmorgen, R., & Krügel, E. 2010, Astronomy and Astrophysics, 511, 6

Siess, L., Dufour, E., & Forestini, M. 2000, Astronomy and Astrophysics, 358, 593

Speedie, J., Booth, R. A., & Dong, R. 2022, The Astrophysical Journal, 930, 40

Stammler, S. M., Birnstiel, T., Panić, O., Dullemond, C. P., & Dominik, C. 2017, Astronomy and Astrophysics, 600, 1

Stevenson, D. J. 1982, Planetary and Space Science, 30, 755

Stevenson, D. J., & Lunine, J. I. 1988, Icarus, 75, 146

Stoll, M. H., & Kley, W. 2014, Astronomy and Astrophysics, 572, 1

Stoll, M. H., Kley, W., & Picogna, G. 2017, Astronomy and Astrophysics, 599, 4

Stone, J. M. 1997, The Astrophysical Journal, 487, 271

Struve, O. 1952, The Observatory, 72, 199

Surville, C., Mayer, L., & Lin, D. N. C. 2016, The Astrophysical Journal, 831, 27

Szulágyi, J. 2017, The Astrophysical Journal, 842, 103

Szulágyi, J., Binkert, F., & Surville, C. 2022, The Astrophysical Journal, 924, 1

Szulágyi, J., Dullemond, C. P., Pohl, A., & Quanz, S. P. 2019, Monthly Notices of the Royal Astronomical Society, 487, 1248

Szulágyi, J., & Garufi, A. 2021, Monthly Notices of the Royal Astronomical Society, 506, 73

Szulágyi, J., Masset, F., Lega, E., et al. 2016, Monthly Notices of the Royal Astronomical Society, 460, 2853

Szulágyi, J., Morbidelli, A., Crida, A., & Masset, F. 2014, Astrophysical Journal, 782, 65

Szulágyi, J., van der Plas, G., Meyer, M. R., et al. 2018, Monthly Notices of the Royal Astronomical Society, 473, 3573

Takeuchi, T., & Lin, D. N. C. 2002, ApJ, 581, 1344

Takeuchi, T., & Lin, D. N. C. 2005, The Astrophysical Journal, 623, 482

Tanaka, H., Takeuchi, T., & Ward, W. R. 2002, The Astrophysical Journal, 565, 1257

Taylor, G. I. 1920, Proceedings of the London Mathematical Society, 196

Tchen, C.-M. 1947, PhD thesis, Delft University

Teague, R., Bae, J., & Bergin, E. A. 2019, Nature, 574, 378

Teague, R., Bae, J., Bergin, E. A., Birnstiel, T., & Foreman-Mackey, D. 2018a, The Astrophysical Journal Letters, 860, L12

Teague, R., Guilloteau, S., Semenov, D., et al. 2016, Astronomy and Astrophysics, 592, 49

Teague, R., Henning, T., Guilloteau, S., et al. 2018b, The Astrophysical Journal, 864, 133

Tominaga, R. T., Takahashi, S. Z., & Inutsuka, S.-I. 2019, The Astrophysical Journal, 881, 53

Toomre, A. 1964, The Astrophysical Journal, 129, 1217

Toro, E. F. 2009, Riemann solvers and numerical methods for fluid dynamics: A practical introduction (Springer), 1–724

Trapman, L., Rosotti, G., Bosman, A. D., Hogerheijde, M. R., & Van Dishoeck, E. F. 2020, Astronomy and Astrophysics, 640, 1

Tripathi, A., Andrews, S. M., Birnstiel, T., & Wilner, D. J. 2017, The Astrophysical Journal, 845, 44

Turner, N. J., Fromang, S., Gammie, C., et al. 2014, in Protostars and Planets VI, ed. H. Beuther, R. S. Klessen, C. P. Dullemond, & T. Henning (University of Arizona Press, Tucson, AZ), 411–432

Tychoniec, L., Manara, C. F., Rosotti, G. P., et al. 2020, Astronomy & Astrophysics, 640, A19

Uhlenbeck, G. E., & Ornstein, L. S. 1930, Physical Review, 36, 823

Umurhan, O. M., Estrada, P. R., & Cuzzi, J. N. 2020, The Astrophysical Journal, 895, 4

Urpin, V. 2003, Astronomy and Astrophysics, 404, 397

Vaikundaraman, V., Drążkowska, J., Binkert, F., Birnstiel, T., & Miotello, A. 2022, in European Planetary Science Congress, 2022–647

Van Der Marel, N., Van Dishoeck, E. F., Bruderer, S., et al. 2013, Science, 340, 1199

Van 't Hoff, M. L. R., Bergin, E. A., Jørgensen, J. K., & Blake, G. A. 2020, Astrophysical Journal, 897, L38

Van Zadelhoff, G. J., Aikawa, Y., Hogerheijde, M. R., & Van Dishoeck, E. F. 2003, Astronomy and Astrophysics, 397, 789

Vigan, A., Fontanive, C., Meyer, M., et al. 2021, Astronomy and Astrophysics, 651, 1

Villenave, M., Ménard, F., Dent, W. R., et al. 2020, Astronomy and Astrophysics, 642, A164

Villenave, M., Stapelfeldt, K. R., Duchene, G., et al. 2022, The Astrophysical Journal, 930, 11

Visser, A. W. 1997, Mar Ecol Prog Ser, 158, 275

Voelk, H. J., Jones, F. C., Morfill, G. E., & Roeser, S. 1980, Astronomy and Astrophysics, 85, 316

Vorobyov, E. I., Matsukoba, R., Omukai, K., & Guedel, M. 2020, Astronomy & Astrophysics, 638, A102

Wade, J., & Wood, B. J. 2005, Earth and Planetary Science Letters, 236, 78

Wafflard-Fernandez, G., & Baruteau, C. 2020, Monthly Notices of the Royal Astronomical Society, 493, 5892

Warren, S. G., & Brandt, R. E. 2008, Journal of Geophysical Research Atmospheres, 113, 1

Weber, P., Benítez-Llambay, P., Gressel, O., Krapp, L., & Pessah, M. E. 2018, The Astrophysical Journal, 854, 153

Weber, P., Pérez, S., Benítez-Llambay, P., et al. 2019, The Astrophysical Journal, 884, 178

Wehrstedt, M., & Gail, H. P. 2002, Astronomy and Astrophysics, 385, 181

Weidenschilling, S. J. 1977a, Monthly Notices of the Royal Astronomical Society, 180, 57

—. 1977b, Astrophysics and Space Science, 51, 153

—. 1980, Icarus, 44, 172

—. 1997, in Astronomical Society of the Pacific Conference Series, ed. Y. J. Pendleton, 281

Wetherill, G. W., & Stewart, G. R. 1989, Icarus, 77, 330

Whipple, F. L. 1972, in From Plasma to Planet, Proceedings of the Twenty-First Nobel Symposium held 6-10 September, 1971 at Saltsjöbaden, near Stockholm, Sweden., ed. A. Evlius (Wiley), 211

Woitke, P., Arabhavi, A. M., Kamp, I., & Thi, W.-F. 2022, Astronomy & Astrophysics, 688, A164

Woitke, P., Kamp, I., & F. Thi, W. 2009, Astronomy and Astrophysics, 501, 383

Wolf, S., & D'Angelo, G. 2005, The Astrophysical Journal, 619, 1114

Wolszczan, A., & Frail, D. 1992, Nature, 255, 145

Wood, B. J., Li, J., & Shahar, A. 2013, Reviews in Mineralogy and Geochemistry, 75, 231

Wright, J. T., Marcy, G. W., Howard, A. W., et al. 2012, Astrophysical Journal, 753, 1

Xu, S., Dufour, P., Klein, B., et al. 2019, The Astronomical Journal, 158, 242

Xu, S., Jura, M., Koester, D., Klein, B., & Zuckerman, B. 2014, Astrophysical Journal, 783, 1

Yang, C.-C., & Johansen, A. 2016, The Astrophysical Journal Supplement Series, 224, 39

Youdin, A., & Johansen, A. 2007, The Astrophysical Journal, 662, 613

Youdin, A. N. 2011a, Astrophysical Journal, 731, 99

—. 2011b, Astrophysical Journal, 742, 38

Youdin, A. N., & Goodman, J. 2005, The Astrophysical Journal, 620, 459

Youdin, A. N., & Lithwick, Y. 2007, Icarus, 192, 588

Zhang, K., Bergin, E. A., Blake, G. A., et al. 2016, The Astrophysical Journal, 818, L16

Zhang, K., Blake, G. A., & Bergin, E. A. 2015, Astrophysical Journal Letters, 806, L7

Zhang, S., & Zhu, Z. 2020, Monthly Notices of the Royal Astronomical Society, 493, 2287

Zhang, S., Zhu, Z., Huang, J., et al. 2018, The Astrophysical Journal Letters, 869, L47

Zhu, Z., Hartmann, L., Calvet, N., et al. 2007, The Astrophysical Journal, 669, 483

Zhu, Z., Nelson, R. P., Dong, R., Espaillat, C., & Hartmann, L. 2012, Astrophysical Journal, 755, 6

Zhu, Z., Stone, J. M., & Bai, X. N. 2015, Astrophysical Journal, 801, 81

Zhu, Z., Stone, J. M., Rafikov, R. R., & Bai, X. N. 2014, Astrophysical Journal, 785, 122

Zhu, Z., Zhang, S., Jiang, Y. F., et al. 2019, The Astrophysical Journal, 877, L18

Ziampras, A., Kley, W., & Dullemond, C. P. 2020, Astronomy & Astrophysics, 637, A50

Zsom, A., & Dullemond, C. P. 2008, Astronomy and Astrophysics, 489, 931

Zsom, A., Ormel, C. W., Dullemond, C. P., & Henning, T. 2011, Astronomy and Astrophysics, 534, 1

Zubko, V., Dwek, E., & Arendt, R. G. 2004, The Astrophysical Journal Supplement Series, 152, 211

Zubko, V. G., Krelowski, J., & Wegner, W. 1996, Monthly Notices of the Royal Astronomical Society, 283, 577

Acknowledgments

I would like to express my deepest appreciation to my supervisor, Prof. Til Birnstiel, for his guidance, and support throughout this research journey. Without your patience, feedback, and countless discussions, this work would not have been possible.

I am also deeply thankful to my co-supervisor, Prof. Judit Szulágyi, whose feedback and challenging questions significantly improved the depth and quality of this work. I also appreciate your patience and diligence in reviewing my countless drafts.

Many thanks go to all the past and present members of Til's group who have been a part of this journey with me and made this time less daunting and more enjoyable. Our group meetings, SPF lunches, and Fabulous Friday lunches will be missed. A special mention goes to Christiane, Luca, Thomas, and Tommy for the unforgettable trip to Japan.

I am endlessly grateful to my family for your constant encouragement and for always having my back. Special mention goes to Dominic. You consistently made sure there was enough *life* in my work-life balance, especially when I needed it most.

Lastly, I want to thank Nele. Your love and support have meant the world to me during this journey.

This thesis would not have been possible without the support of all of you.